Lymphocyte receptor *cis* interactions in immune cell signaling



Alexander Mørch

Lincoln College, University of Oxford

DPhil Programme in Infection, Immunology and Translational Medicine

Primary supervisor: Michael L. Dustin

Secondary supervisor: Simon J. Davis

Thesis submitted for the degree of Doctor of Philosophy

Hilary Term, 2023

For Dad

COVID-19 impact statement

The impact of the COVID-19 pandemic and the restrictions that followed affected progress on this thesis in two ways. First, access to a central piece of equipment (a Zeiss microscope located in a building different to my own) was limited both by the initial university-wide closure and then by the subsequent access restrictions due to limits on room occupancy. The total affected period was 172 days in 2020 (97 from closure, 75 from access limitations) and 65 days in 2021 (from secondary effects including servicing delays) in which development and application of the main tool in this thesis, FCCS, could not proceed. Secondly, indirect effects of the pandemic caused the early departure of my postdoctoral supervisor, Dr. Štefan Bálint, from the lab in early 2022. In addition to the loss of his support, this also resulted in the abandonment of what was originally the second half of the project: applying super-resolution microscopy to investigate TCR triggering in T cells.

For these reasons, the scope of the dissertation was expanded to include data from two closely related projects that I had been contributing to throughout my DPhil. Parts of the collaboration with the Kong group (Department of Biochemistry and Molecular Pharmacology, NYU School of Medicine, USA) formed the basis for **Chapter 4** and parts of the collaboration with the Higgins group (Department of Biochemistry, University of Oxford, UK) formed the basis for **Chapter 6**. In both cases, my contribution was the method developed initially to study T-cell coreceptors applied to different instances of lymphocyte receptor *cis* interactions, providing important validation of the method and demonstrating its utility in other areas of molecular immunology.

Declaration of authorship

I hereby declare that, except where specific reference is made, the contents of this dissertation are original and have not been submitted in whole or in part for consideration for any other degree or qualification in this, or any other university. This dissertation is my own work and contains nothing which is the outcome of collaborations with others, except as specified in the text and in the instances listed below:

- **Chapter 4**: PD-1 experiments were conceptualized by Elliot Philips and Xiang-Peng Kong, flow-FRET was performed by Elliot Philips (flow-FRET), FLIM-FRET was performed by Yong Zhou, *in vivo* experiments were performed by Elliot Philips and Jia Liu
- **Chapter 5**: Ca^{2+} triggering experiments were performed by Edward Jenkins, MLE analysis was performed by Falk Schneider
- **Chapter 6**: RIFIN/LILRB1 experiments were conceptualized by Matthew Higgins, structural studies were performed by Tom Harrison and Samuel Chamberlain, NFAT-GFP assays were performed by Akihito Sakoguchi

Abstract

Lymphocytes express a wide range of surface receptors that transduce important signals, including by binding to other proteins expressed at the same membrane (in *cis*). Such interactions are typically studied with biochemical tools like immunoprecipitation, in which interaction equilibria are disturbed by cell lysis, or through fixed high-resolution imaging, in which all dynamics are lost. Here, we adapt and implement a form of fluctuation spectroscopy, called scanning fluorescence cross-correlation spectroscopy (sFCCS), to study the diffusion and interactions of proteins expressed at the surface of living cells. This system is used to test three different instances of important receptor *cis* interactions. In Chapter 4, we demonstrate the presence of intermolecular PD-1/PD-1 *cis* binding (*i.e.,* transient dimerization) and validate this novel and unexpected finding with other biophysical methods. Using genetic engineering and *in vivo* models of disease, we find that PD-1 dimers are important for the functional inhibition of T cells. Next, in Chapter 5, we address the controversy surrounding the coupling between T-cell coreceptors (CD4 and CD8αβ) and the signal-initiating kinase Lck at the cell surface. sFCCS experiments show that coreceptor/Lck occupancy is much higher than claimed by previous reports. In addition, we find that differences between CD4 and CD8αβ are especially pronounced when they are co-expressed and need to compete for limiting amounts of Lck, which may be relevant for models of thymopoiesis. Finally, in Chapter 6, we turn to the study of *cis* interactions between an inhibitory NK-cell receptor and class I MHC molecules. Guided by structural biology, we determine how novel malarial surface antigens have evolved to bind inhibitory molecules even when 'masked' by MHC-I binding in *cis*. Together, our results shed light on this puzzling class of receptor interactions and provide important context for understanding lymphocyte signaling in infection, immunology and translational biology.

Lay summary

Immune cells sense signs of danger, like infections or cancers, through proteins called receptors which are located at the outer membrane of the cell. Receptors normally work by detecting specific chemicals that float around the cell (“in solution”) or on other cells (“in *trans*”). Recently, however, it was discovered that receptors can also detect molecules on the same immune cell (“in *cis*”), challenging our original definitions. In this thesis, we develop a system to study receptor *cis* interactions with very high precision and investigate different biological scenarios in which these interactions are important for the normal functions of immune cells. An improved understanding of this process will aid in the development and application of therapeutics that harness our immune systems to fight disease.

Acknowledgements

First and foremost, I need to thank my supervisors Mike Dustin and Simon Davis for taking me on as a student in their groups. Simon took a chance on me as I was just starting my scientific journey and I am very grateful for the principles of experimental rigor he instilled. Mike provided invaluable mentoring through my DPhil and I would particularly like to thank him for helping me to maintain the momentum and motivation to complete graduate school during a global pandemic. Science is built on the shoulders of giant but it's a little easier if you're directly supervised by them too.

I also owe a huge debt of gratitude to our collaborators, Matt Higgins from Oxford's Department of Biochemistry and Xiang-Peng Kong from NYU School of Medicine, for allowing me to contribute to their engaging and exciting projects. These experiences proved important opportunities to learn about other areas of immunology, they helped my scientific education and they also helped with the structuring of this thesis.

I would like to thank my post-doctoral supervisors, both official and unofficial, who all provided valuable support in the relay race to finish. James, for being my entry point into science and always challenging me to better myself. Mafalda, for teaching me everything that I know. Štefan, for demonstrating how to think critically to improve my work. Falk, for setting the highest possible standard of a scientist I have yet to see broken.

Nothing in this thesis would have been possible without the large and helpful lab communities that I was fortunate to be a part of. There are too many people to thank here but suffice it to say that you can't go wrong with supportive people at both levels: in managing science (Elke, Lina, Salvo, Mafalda and Mai) and executing it (Erdinc, Falk, Nicole, Ed, Caitlin, James, Enas, Pablo, Shams, Tom, Sam, Ashwin and Dan). I am grateful also to the scientific and administrative staff whose help I have benefited from greatly at different stages of my DPhil. A special thanks goes to Chris Lagerholm and Jana Koth for their imaging expertise,

Dawn Gibbons and Chris Tang from IITM for their continued support and the staff at the Huntington Library for allowing me to do most of my writing in actual, non-figurative heaven.

Lastly, I need to express gratitude to my friends. Nicole, for being the first person I could confide in and seek support from. Ed, for all of his antics (occasionally abroad) and his inspiring penchant for science. Caitlin, for teaching me perseverance and also teaching me the lyrics to Man's Not Hot (Big Shaq, the one and only). Joao, because we all need an arch rival and mine sets the bar high. Rob, for reconnecting during lockdown and introducing me to your friends. Midge, for being compassionate and understanding when I was starting at the Kennedy. Ashwin, for your kindness and friendship. Gudde, Rail and the rest of the crew for the camaraderie. Kirsty, with whom I share this achievement.

Endeligt skal jeg også sige tak til min familie, som jeg har set alt for lidt de sidste fire år. Danny og Amalie, som har vist at man kan have det hele. Misse og Tau, som har vist at det er vigtigt at være mærkelig (mest Tau). Cassie, som konstant minder mig om at der er mere i livet end arbejde—som f.eks. sushi og bekæmpelsen af patriarkatet. Jeg skylder, selvfølgelig, det hele til mine forældre: mor, som aldrig tvivler mig (selv når jeg tvivler mig selv), og far, som afhandlingen er dedikeret til.

List of DPhil Publications

The results, techniques and data presented in this thesis have in part been communicated before in the manuscripts below:

Publications

1. Harrison TE, Mørch AM, Felce JH, Sakoguchi A, Reid AJ, Arase H, Dustin ML and Higgins MK (2020) Structural basis for RIFIN-mediated activation of LILRB1 in malaria. **Nature**. https://doi.org/10.1038/s41586-020-2530-3
2. Mørch AM, Schneider F, Jenkins E, Santos AM, Fraser SE, Davis SJ and Dustin ML (2022) The kinase occupancy of T cell coreceptors reconsidered. **Proc Natl Acad Sci** 119:2022.08.01.502332. https://doi.org/10.1073/PNAS.2213538119

Manuscripts in preparation

1. Philips EA, Liu J, Kvalvaag A, Mørch AM, Tocheva AS, Ng C, Liang H, Ahearn IA, Ruimin P, Luo C, Qin Z, Zhou Y, Garcia-Espana A, Mor A, Littman DR, Dustin ML, Wang J and Kong XP (2022) PD-1 dimers mediate T cell inhibition. *Under review*

Table of Contents

1. Introduction 1

1.1 Principles of immunity 1

1.1.1 Innate and adaptive immune responses 2

1.1.2 Lymphocyte maturation and selection 6

1.1.3 Lymphocyte functions in health and disease 11

1.2 Lymphocyte receptors 13

1.2.1 Lymphocyte receptor families and functions 16

1.2.2 Lymphocyte receptor signaling 19

1.2.3 Lymphocyte receptor *cis* interactions 24

1.3 Methods to study *cis* interactions 28

1.3.1 *In vitro* approaches 29

1.3.2 *In situ* approaches 32

1.4 Aims of the thesis 37

2. Methods and materials 39

2.1 Cell culture 39

2.2 Flow cytometry 40

2.3 Cloning 41

2.4 Supported lipid bilayers 41

2.5 Microscopy and image acquisition 42

2.6 sFCCS and image processing 43

3. Establishing the FCS method for correlative measurements 44

3.1 Introduction 44

3.2 Methods 48

3.3 Results 50

3.3.1 Comparing pFCS, sFCS and imaging FCS 50
3.3.2 Cross-correlation measurements 54
3.3.3 Membrane environment affects diffusion behavior 56
3.4 Discussion 58
3.4.1 sFCS balances rapid and multiplexed acquisition 58
3.4.2 New technologies enable correlative measurements 59
4. PD-1 dimerization drives inhibitory signaling 61
4.1 Introduction 61
4.2 Methods 63
4.3 Results 66
4.3.1 Intermolecular PD-1 interactions in *cis* at the cell surface 66
4.3.2 Transmembrane-driven dimerization 69
4.3.3 PD-1 dimers inhibit T-cell function 73
4.4 Discussion 78
4.4.1 Biophysical techniques reveal cell-surface *cis* interactions 78
4.4.2 Generalizing transmembrane-driven interactions 80
4.4.3 A new paradigm for PD-1 signaling 81
5. Reconsidering the kinase occupancy of T-cell coreceptors 83
5.1 Introduction 83
5.2 Methods 85
5.3 Results 88
5.3.1 Biochemical measurements of coreceptor/Lck occupancy 88
5.3.2 Analysis of CD4/Lck occupancy in live cells 93
5.3.3 The CD4 amphipathic helix contributes to Lck association 100
5.3.4 Competition for Lck in dual coreceptor-expressing cells 105
5.3.5 TCR triggering does not affect CD4/Lck occupancy 108
5.4 Discussion 114

5.4.1 Discrepancies between past reports of occupancy 114
5.4.2 Analysis of CD4 C-terminal secondary structure elements 115
5.4.3 Coreceptor occupancy in positive and negative selection 116
5.4.4 Coreceptor/Lck interactions during early TCR signaling 117
6. Malaria antigens and host LILRB1/HLA *cis* interactions 119
6.1 Introduction 119
6.2 Methods 120
6.3 Results 123
6.3.1 Structural characterization of a LILRB1-binding RIFIN 123
6.3.2 RIFIN binding produces functional inhibition of NK cells 126
6.3.3 MHC-I/LILRB1 *cis* interactions are modulated by RIFINs 129
6.4 Discussion 135
6.4.1 RIFIN variable domains form novel α-helical bundles 135
6.4.2 Supported lipid bilayer mimetics of infected erythrocytes 136
6.4.3 Bending over backwards to bind RIFINs 138
7. General discussion 141
7.1 Summary of findings 142
7.2 Defining lymphocyte receptor *cis* interactions 143
7.2.1 Structural biology and the ‘tyranny of the lattice’ 144
7.2.1 Assaying *cis* binding *in vitro* 147
7.2.2 Are receptor *cis* interactions physiologically relevant? 149
7.3 Concluding remarks 153
Bibliography 154

List of Figures

1. Figure 1.1. **Stages in early T-cell development** 9
2. Figure 1.2. **Features of lymphocyte receptor families.** 15
3. Figure 1.3. **The αβTCR signaling network.** 21
4. Figure 1.4. **Example of homotypic *cis-trans* engagement by the inhibitory receptor LILRB1.** 25
5. Figure 1.5. **Schematic of the FC-IP method used to study coreceptor/Lck *cis* interactions *in vitro*** 31
6. Figure 1.6. **The basis of FC(C)S auto- and cross-correlation functions.** 36
7. Figure 3.1 **Comparisons of point-FCS (pFCS), scanning-FCS (sFCS) and imaging FCS (imFCS).** 53
8. Figure 3.2 **Cross-correlation measurements performed by pFCS and sFCS.** 55
9. Figure 3.3 **Positioning of the sFCS line-scan affects measurement quality.** 57
10. Figure 4.1 **Robust PD-1 dimerization at the cell surface.** 68
11. Figure 4.2 **TOXGREEN assays reveal key transmembrane domain residues that drive PD-1 dimerization.** 70
12. Figure 4.3 **Biophysical validation of hPD-1 mutations that modulate dimerization.** 72
13. Figure 4.4 **PD-1 dimerization drives inhibitory signaling in Jurkat T cells.** 74
14. Figure 4.5 **Functional modulation of T cells in models of cancer and autoimmune disease through controlling PD-1 dimerization.** 77
15. Figure 5.1 **CD4/Lck and CD8/Lck occupancies in SP and DP cells in the thymus and periphery.** 90
16. Figure 5.2 **CD4/Lck occupancy in Jurkat $CD4^+$ T cells measured with FC-IP** 92
17. Figure 5.3 **sFCCS measurements of CD4-mCherry2 and Lck-mEGFP in HEK293T cells.** 95
18. Figure 5.4 **CD4 and Lck co-diffuse stoichiometrically in a Zn^{2+}-clasp-dependent manner at the surface of live cells.** 97
19. Figure 5.5 **Increases in diffusion speed on CD4/Lck dissociation.** 99
20. Figure 5.6 **A panel of CD4 mutants to probe secondary structure elements in the CD4 ICD in associating with Lck.** 102
21. Figure 5.7 **Mutation of the CD4 intracellular domains did not substantially alter protein diffusion or surface density.**. 104
22. Figure 5.8 **Coreceptor/Lck occupancy is regulated by Lck availability in dual coreceptor-expressing cells.** 107
23. Figure 5.9 **Signaling-competent and -deficient Jurkat T cells on supported lipid bilayers.** 109
24. Figure 5.10 **sFCCS indicates high-occupancy CD4/Lck complexes are not disrupted by early TCR signaling.** 111
25. Figure 5.11 **Statistical analysis of CD4/Lck diffusion and oligomerization.** 113
26. Figure 6.1 **Structural characterization of a LILRB1-binding RIFIN.**. 125
27. Figure 6.2 **RBL1D2 induces LILRB1-mediated signaling and inhibits NK cell activity**. 128
28. Figure 6.3 **A LILRB1 D3-binding RIFIN interacts with a bent receptor.** 131
29. Figure 6.4 **Cis measurements of LILRB1/MHC-I interactions with sFCCS.** 133
30. Figure 6.5 **Functional effects of RBL1D2 vs. RBL1D3 on primary NK cells in the bilayer assay.** 134

Abbreviations

ACF	Auto-correlation function
ADCC	Antibody-dependent cellular cytotoxicity
AF	Alexa Fluor
AIRE	Autoimmune regulator
ALR	AIM-like receptor
ANOVA	Analysis of variance
APC	Antigen-presenting cell
β2m	Beta-2 microglobulin
BCR	B cell receptor
BHK	Baby hamster kidney
BLNK	B-cell linker
BMP	Bone marrow progenitor
BRR	Basic-rich region
BSA	Bovine serum albumin
CAR	Chimeric antigen receptor
CAT	Chloramphenicol acetyl transferase
CCF	Cross-correlation function
CD	Circular dichroism
CD	Cluster of differentiation
CDR	Complementarity determining region
CFP	Cyan fluorescent protein
CHMI	Controlled human malaria infections
CHO	Chinese hamster ovary
CLP	Common lymphoid progenitor
CLR	C-type lectin receptor
CML	Carboxylate-modified latex
CMP	Common myeloid progenitor
Co-IP	Co-immunoprecipitation
CRISPR	Clustered regularly interspaced short palindromic repeat
Cryo-EM	Cryogenic electron microscopy
cSMAC	Central supramolecular activation cluster
CTL	Cytotoxic T lymphocyte
CTLA-4	Cytotoxic T-lymphocyte-associated protein 4
DAG	Diacyl glycerol
DC	Dendritic cell
DMEM	Dulbecco's Modified Eagle Medium
DN	Double-negative
DOPC	1,2-Dioleoyl-sn-glycero-3-phosphocholine
DP	Double-positive
dSMAC	Distal supramolecular activation cluster
EDTA	Ethylenediaminetetraacetic acid
EMCCD	Electron-multiplying charge-coupled device
Fab	Fragment, antigen binding
FACS	Fluorescence activated cell sorting
FBS	Fetal bovine serum
Fc	Fragment, crystallizable
FCCS	Fluorescence cross-correlation spectroscopy
FC-IP	Flow cytometric IP
FCS	Fluorescence correlation spectroscopy
FP	Fluorescent proteins
FRET	Förster resonance energy transfer
gMFI	geometric mean fluorescence intensity
GC	Germinal center
GPCR	G protein-coupled receptor
GPI	Glycosylphosphatidylinositol
HBS	HEPES-buffered saline
HEK293T	Human embryonic kidney 293T
HEPES	4-(2-hydroxyethyl)-1-piperazineethanesulfonic acid
HLA	Human leukocyte antigen
HSA	Human serum albumin
ICAM-1	Intercellular adhesion molecule 1
ICOS	Inducible T-cell costimulator
ICS	Image correlation spectroscopy
Ig	Immunoglobulin
IgSF	Immunoglobulin superfamily
ILC	Innate lymphoid cell
IP3	Inositol trisphosphate
IRM	Interference reflection microscopy
ITIM	Immunoreceptor tyrosine-based activation motif
ITIM	Immunoreceptor tyrosine-based inhibition motif
ITSM	Immunoreceptor tyrosine-based switch motif
K_D	Dissociation constant
KIR	Killer cell immunoglobulin-like receptor
k_{off}	Dissociation rate constant
k_{on}	Association rate constant
LAG3	Lymphocyte-activation gene 3
LAIR1/2	Leukocyte-associated immunoglobulin-like receptor 1/2
LAT	Linker for activation of T cells

LCMV	Lymphocytic choriomeningitis
LFA-1	Lymphocyte function-associated antigen 1
LILR	Leukocyte immunoglobulin-like receptor
LILRB1/2	Leukocyte Ig-like receptor subfamily B member 1/2
LPS	Lipopolysaccharide
LRC	Leukocyte receptor complex
LSM	Laser-scanning microscope
MAPK	Mitogen-activated protein kinase
MBP	Maltose binding protein
MBS	Main beam splitter
mEGFP	Monomeric enhanced green fluorescent protein
MESF	Molecules of equivalent soluble fluorescence
MFI	Mean fluorescence intensity
MHC	Major histocompatibility complex
MLE	Maximum likelihood estimation
NA	Numerical aperture
NFAT	Nuclear factor of activated T cells
NK	Natural killer
NKC	Natural killer complex
NLR	Nod-like receptor
NMR	Nuclear magnetic resonance
OLR	OAS-like receptor
PAMP	Pathogen-associated molecular pattern
PBC	Photobleaching correction
PBS	Phosphate-buffered saline
PCC	Pearson's correlation coefficient
PD-1	Programmed cell death protein 1
PDB	Protein Data Bank
PD-L1/2	Programmed death-ligand 1/2
PE	Phycoerythrin
PFA	Paraformaldehyde
PfEMP1	*P. falciparum* erythrocyte membrane protein 1
PMA	Phorbol 12-myristate 13-acetate
PRR	Pattern recognition receptor
pSMAC	Peripheral supramolecular activation cluster
RAG	Recombination-activating gene
RBL1D2	RIFIN that binds LILRB1 at D1-D2
RBL1D3	RIFIN that binds LILRB1 at D3
RICS	Raster image correlation spectroscopy
RIFINs	Repetitive interspersed families of polypeptides
RLR	RIG-I-like receptor
R-M	Restriction-modification
ROI	Region-of-interest
RPMI	Roswell Park Memorial Institute medium
RTK	Receptor tyrosine kinase
SCF	Stem cell factor
scFv	Single-chain variable fragment
sCMOS	Scientific complementary metal oxide semiconductor
SD	Standard deviation
SEC	Size exclusion chromatography
SEM	Standard error of the mean
sfGFP	superfolder GFP
SH1/2/3	Src homology 1/2/3 domain
SHP-1/2	SH2-containing tyrosine phosphatases 1 and 2
Siglec	Sialic acid-binding Ig-type lectin
SLB	Supported lipid bilayer
smFRET	Single-molecule FRET
SP	Single-positive
SPT	Single-particle tracking
STAT	Signal transducer and activator of transcription
STED	Stimulated emission depletion
STEVOR	Subtelomeric variant open reading frame
T1D	Type I diabetes
TCCD	Two-color coincidence detection
TCR	T cell receptor
TEC	Thymic epithelial cell
TIRF	Total internal reflection fluorescence
TLR	Toll-like receptor
TM	Transmembrane
TNFR	Tumor necrosis factor receptor
TPEN	N,N,N′,N′-tetrakis(2-pyridinylmethyl)-1,2-ethanediamine
VLR	Variable lymphocyte receptor
VSA	Variant surface antigen
WT	Wild-type
YFP	Yellow fluorescent protein

1. Introduction

1.1 Principles of immunity

The earliest evidence for intrinsic biological defense mechanisms—immune systems—comes from the prokaryotic kingdom. The microbial arms race between single-celled prokaryotes and invading bacteriophages led to the evolution of nucleic acid-based defenses like restriction-modification (R-M) enzymes[1] and clustered regularly interspaced short palindromic repeat (CRISPR)/Cas systems[2,3]. A striking feature of these primordial defenses, which existed well before multicellular life developed ~1500 million years ago[4], is that they share a key principle with the much more complex immune system that later evolved in jawed vertebrates: a pathogen-specific, fast-acting 'innate' response (*i.e.,* R-M) working synergistically with, and complementary to, an 'adaptive' system capable of molecular memory (*i.e.,* CRISPR/Cas)[5]. Primitive immune behaviors began emerging with protozoan eukaryotes including phagocytosis[6] (engulfing and degrading foreign entities), secretory antimicrobials[7], and the evolution of cell-surface receptors capable of discriminating between self and non-self[8]. Rising oxygen levels brought the origin of metazoans some 800 million years ago[9], and with them the immune system flourished into a sophisticated and interconnected network of physical barriers, diverse cell types, and complex behaviors. The coevolutionary arms race between hosts and parasites has also heavily shaped the architecture of immune defense systems in higher vertebrates. Two important phenomena specifically are thought to have emerged from host-parasite competition on evolutionary timescales. First is the intricate and extensive communication between innate and adaptive immunity in the host, which is relatively well characterized[10]. Second is the complex evasion and cloaking strategies in the parasite, about which much less is known[11].

A vital function of the immune system is the ability to efficiently discriminate self from non-self. In the innate branch of immunity, this discrimination is performed by germline-encoded and broadly expressed receptors which recognize signs of infection. This group of surface molecules consists mainly of the pattern recognition receptors (PRRs) which bind to conserved microbial structures or 'patterns' in both extracellular and intracellular environments[12]. Other members include the 'missing self' receptors, a strategy primarily used by natural killer (NK) cells, in which inhibitory receptors containing immunoreceptor tyrosine-based inhibitory motifs (ITIMs) sense infected cells through reduction of surface major histocompatibility complex (MHC) class I molecules[13]. In the adaptive branch of immunity, it is the somatically rearranged and clonally expressed antigen receptors of T and B lymphocytes, the T and B cell receptor (TCR/BCR), which mediate antigen discrimination. Each receptor binds to a small, specific portion of a foreign molecule and allows a highly targeted and efficient search-and-destroy tactic to be launched against the offending pathogen. This reaction is powerful and efficient but comes with considerable risk to the host in the form of collateral damage, *i.e.,* autoimmunity. Despite the extensive central and peripheral quality-control mechanisms that exist to mitigate lymphocyte self-reactivity[14], autoimmune reactions and disorders are common in the human population[15]. A prime directive of modern immunologists is to understand how these mechanisms work, how they go wrong, and how to harness this knowledge for therapeutic benefit.

1.1.1 Innate and adaptive immune responses

Innate immunity

Phagocytosis, a basal function of innate immune cells, is an evolutionarily ancient form of predation often associated (either causally or consequentially) with the acquisition of the ancestral mitochondrion[16]. Genetic studies of *Drosophila*-derived phagocytes were the first to reveal how defensive phagocytosis requires proteins capable of differentiating 'foreign' from

'self' entities[17]. The ability of phagocytes and other innate immune cells to clearly differentiate between the identities of target cells led to the proposal of the 'pattern recognition' paradigm in 1989[18] and the 'missing self' hypothesis just one year later[19].

For pattern recognition, germline-encoded PRRs detect structurally conserved pathogen-associated molecular patterns (PAMPs) such as components of the bacterial or fungal cell wall. Recognition of PAMPs leads to the induction of pro-inflammatory signaling pathways, drives cytokine and interferon production and, eventually, activation of the adaptive immune response. Together with the recruitment of effector cells like neutrophils, secretion of lytic compounds and antimicrobials, and the polarization of macrophages, the innate host defenses can deliver an effective immune reaction within minutes of a stimulus, *i.e.,* within the same timeframe as bacterial growth[20,21]. The PRRs comprise six families of receptors of which the Toll-like receptors (TLRs) are the most extensively studied. The TLRs were discovered in 1997 and named on the basis of homology to a *D. melanogaster* receptor, Toll, that mediates anti-fungal responses[22]. Toll, which is German vernacular ("amazing" or "cool"), is thought to have been coined because of the exclamation made by one of its discoverers, Nüsslein-Volhard, when the malformed ventral body of the Toll-deficient fruit fly was first observed[23]. TLR family members are expressed at both the cell surface and in intracellular compartments and recognize a diverse array of microbial ligands including cell wall components (TLR2), lipopolysaccharide (LPS; TLR4) and CpG DNA (TLR9)[24]. Other PRR families include the C-type lectin receptors (CLRs), the RIG-I-like receptors (RLRs), the AIM-like receptors (ALRs), the Nod-like receptors (NLRs) and the OAS-like receptors (OLRs)[25]. The receptors of pattern recognition constitute effective defenses because their ligands are generally shared across large classes of microbial pathogens and mutations that diminish PRR-ligand recognition mainly produce negative impacts on bacterial fitness.

'Missing self' recognition is an alternative strategy by which innate immune cells can discriminate between self and non-self, analogous to the R-M systems of bacteria[26]. NK cells, for instance, express inhibitory immune receptors (*e.g.,* Killer cell immunoglobulin-like receptor

[KIRs] and leukocyte immunoglobulin-like receptors [LILRs]) that recognize polymorphic MHC-I molecules which allow them to monitor MHC expression levels on host cells. A reduction in MHC-I proteins, caused either by viral infections or environmental stressors, acts as a signal for NK-mediated lysis of the target cell[27]. Some of these inhibitory receptors are also expressed by phagocytes and prevent phagocytic attack and lysis of healthy cells[28]. Missing-self recognition pathways often inhibit classic functions of innate immunity like phagocytosis, killing and complement activation, suggesting that these pathways evolved to complement and regulate the more evolutionary ancient effector mechanisms of innate immune cells. Although the precise physiological functions of pattern- and missing self-recognition as it occurs with different infectious organisms in different anatomical locations continues to be studied, a key principle is clear: pathogen sensing by innate immunity provides crucial information about pathogen origin, location and type to instruct adaptive immunity[26].

Adaptive immunity

The modern form of adaptive immunity, or acquired immunity, traces its roots back more than 500 million years ago to agnathans (jawless fish). Although early studies showed that these species could reject allogeneic skin grafts and produce antigen-specific agglutinations, suggestive of adaptive immunity, transcriptional profiling revealed that there were no genes with significant similarity to MHC, TCR or immunoglobulin (Ig) genes[29]. Instead, the lymphoid cells of jawless fish express variable lymphocyte receptors (VLRs), composed of modular leucine-rich repeat domains, generated through an unusual mechanism called somatic diversification[30]. In this process, the incomplete genomic *VLR* sequence is 'filled in' stochastically in individual lymphocytes through the insertion of donor cassette sequences. It is only much later, in jawed fish, that the adaptive immune system begins to more closely resemble that of our own: clonally distributed antigen receptors generated by somatic recombination by the action of recombination-activating gene (RAG) proteins[31]. According to the RAG transposon hypothesis, the somatic recombination mechanism evolved through the

insertion of RAG-encoding transposons into an Ig superfamily (IgSF) exon followed by two whole genome duplication events[32]. This paradigm-shifting event produced the three distinct antigen receptor families in gnasthosomes (*i.e.,* all jawed vertebrates) that most immunologists are familiar with today: the αβ/γδ TCRs (equivalent to VLR-A and -C), BCRs (equivalent to VLR-B) and MHCs (whose evolutionary origin remains enigmatic[33,34]).

The defining feature of a classical adaptive response is the coordination and synergy between T cells, mediating cellular immunity, and B cells, mediating humoral immunity. T cells recognize small (8-20 residue) linear polypeptides presented either on MHC-I proteins, expressed on all nucleated somatic cells, or MHC-II proteins, expressed on specialized antigen-presenting cells (APCs) which include dendritic cells (DCs), B cells and macrophages[35]. Activation of T cells through the recognition of cognate peptide-MHC (pMHC) complexes leads to different outcomes depending on the ontogeny of the cell: $CD8^+$ (Cluster of differentiation 8) cytotoxic T lymphocytes (CTLs; 'killer T cells') destroy their targets by delivering a lethal payload of lytic compounds[36] while $CD4^+$ helper T (T_H) cells produce immunomodulatory cytokines that aid antibody-producing B cells[37]. The BCR, in contrast to the TCR, binds to unprocessed and conformational antigen epitopes presented either in solution or by follicular dendritic cells (fDCs)[38]. Activated B cells differentiate into plasma cells which produce swathes of antibodies capable of binding their epitopes with high avidity, either neutralizing their activity, coating microbes for opsonization or recruiting complement. Perhaps the most important feature of adaptive immune responses is the capacity for memory; both T and B cell subsets exist which retain molecular information of previous infections and are poised to reinitiate a response. This mechanism is the basis for immunization, which has become the most powerful and effective method at reducing disease burdens around the world[39].

1.1.2 Lymphocyte maturation and selection

Mature leukocytes that derive from the common lymphoid progenitors (CLPs) or common myeloid progenitors (CMPs) form the frontline of cellular immunity. Lymphopoiesis gives rise to T cells, B cells and NK cells while myelopoiesis gives rise primarily to eosinophils, basophils, neutrophils and monocytes (from which macrophages and DCs can also derive). It is primarily cells of the lymphoid system which orchestrate and manage an adaptive immune response, although there is a growing appreciation for the role of innate lymphoid cells (ILCs), like NK cells, which straddle both arms of immunity[40]. T cells and B cells develop in specialized immunological organs, the primary lymphoid tissues, where the diversity in their antigen receptor repertoires are created through an extensive genomic rearrangement program called V(D)J recombination[41,42]. The terms of NK-cell development, in contrast to that of T and B cells, are less clearly defined but it is thought to involve both an 'education' or selection process in the bone marrow alongside a continuous 'tuning' of receptor sensitivity in the periphery[43].

T-cell development

T-cell lineage commitment occurs in the thymus, where a series of irreversible selection processes ensure the generation of mature T cells which are appropriately MHC-restricted and self-tolerant (**Figure 1.1**). The earliest progenitors of mature T cells are called prothymocytes and derive from bone marrow progenitor (BMP) cells. Prothymocytes exit the bone marrow and migrate towards the thymus in response to signals secreted by thymic epithelial cells (TECs). Double-negative (DN) thymocytes, *i.e.,* lacking both CD4 and CD8 coreceptors, proceed through four developmental substages (DN1-4) in the cortex to test for the successful rearrangement of the TCRβ chain in a process called β-selection. Here, a V(D)J-rearranged β-chain is paired with an invariant TCRα-chain to form the pre-TCR. Functional pre-TCR expression, assembly and signaling leads to downregulation of *Rag1/2*

genes, terminating TCRβ rearrangement and allelically excluding the expression of more than one β-chain per thymocyte[44]. Permissive pre-TCR signaling allows DN4 thymocytes to proceed to the $CD4^+$ $CD8^+$ double-positive (DP) stage where the TCRα chain is subsequently rearranged, increasing the diversity of the αβTCR[45].

After successful completion of β-selection, DP cells are tested for the ability to recognize self-MHC ligands with a low affinity (positive selection). The failure of a clonotypic αβTCR to recognize a pMHC ligand expressed on cortical TECs (cTECs) leads to passive cell death ('death by neglect') through the lack of proliferative cues. cTECs express unique components of the proteolytic machinery that generates peptides for both MHC class I (*e.g.,* β5t subunit of the proteasome) and MHC class II (*e.g.,* thymus-specific serine protease), indicating that they display a unique set of self-peptides for positive selection[46]. Since an individual will only express a small subset of the MHC haplotypes that occur in the population, positive selection likely endows the TCR repertoire with specificity for host MHC. Coupling of the effector mechanisms of 'help' and 'killing' to different MHC classes is mediated by the coreceptor proteins, which bind and sequester Lck to ensure that only $CD4^+$ thymocytes receive MHC-II-dependent signals and $CD8^+$ thymocytes receive MHC-I-dependent signals[47,48].

Positively selected DP thymocytes cease TCRα rearrangement, become $CD4^-$ $CD8^+$ or $CD4^+$ $CD8^-$ single-positive (SP) cells and move to the thymic medulla to screen out cells with strong affinity for self-antigens (negative selection)[46]. This process is mediated primarily by medullary TECs (mTECs), but also DCs and macrophages, which exhibit a highly promiscuous gene expression profile displaying a diverse array of self-antigens from different tissues. The transcriptional 'smorgasbord' of mTECs is driven by a single transcription factor, autoimmune regulator (AIRE), the deficiency of which causes extreme autoimmune disease in humans[49,50]. Apoptosis is directly induced in cells that bind to self-antigens with high affinity, deleting potentially self-reactive thymocytes[51]. Cells that successfully navigate β-selection, positive selection and negative selection egress from the thymus and enter the circulatory

system as peripheral, mature T cells. Only 1 in every 10 thymic progenitor cells is estimated to survive this immunological bootcamp, highlighting the advantages T-cell immunity must provide to the organism given the significant energetic cost of a cellular training program with an extremely high failure rate[52].

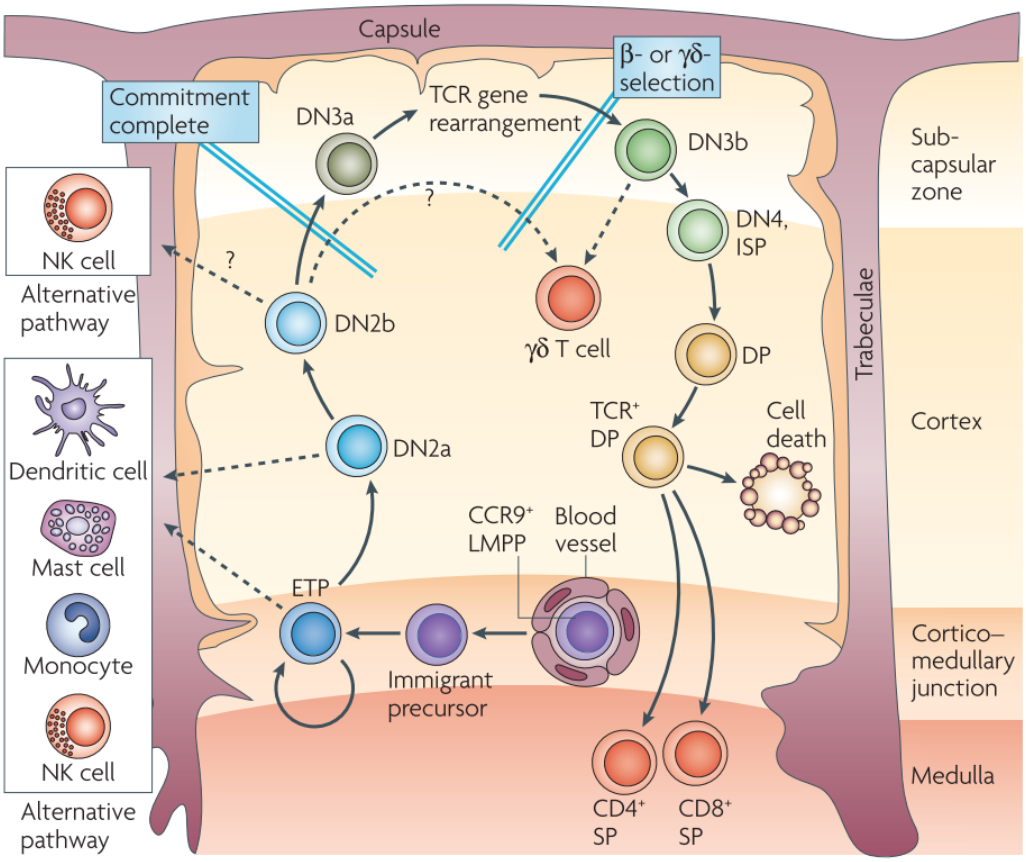


Figure 1.1. **Stages in early T-cell development**. Early T-cell precursors (ETP) arrive in the thymus and proceed through DN, DP and SP stages in different thymic microenvironments (depicted by solid arrows). The gene segments of TCRβ and TCRα chains are rearranged during the DN stages and tested for self-MHC-reactivity (*i.e.,* β-selection and positive selection) which primarily takes place in the cortex. Progressing DP thymocytes that bind too strongly to self-antigens are deleted to prevent autoimmunity (*i.e.,* negative selection) and move to the medulla as $CD4^+$ or $CD8^+$ SP cells followed by egress to the periphery. Adapted from ref. [53].

B-cell development

B-cell development begins in the fetal liver and occurs continuously in the bone marrow throughout the rest of life. CLPs which receive specific signals from bone marrow stromal cells, like stem cell factor (SCF) and IL-7, begin progressing through various stages of development. These stages (early pro-B, late pro-B, large pre-B, small pre-B, immature B), each correspond to a different phase of V(D)J-joining of H and L chain gene segments, ultimately producing a mature B cell expressing membrane IgM and IgD. H chains are rearranged in early and late pro-B cells while L chains are rearranged at the small pre-B and immature B-cell stages. Tonic signaling by the unligated BCR in small pre-B cells leads to positive selection and proliferation, whereas BCR engagement of self-antigens promotes negative selection, analogously to thymic education. Unlike T cells, mature B cells have the capability of increasing their receptors' affinity for antigen via the process of affinity maturation, which occurs in specialized germinal center (GC) structures of the lymph nodes[54,55].

NK-cell development

NK cells share many attributes with T and B cells: NK precursors undergo a selection process in primary lymphoid organs, their receptors have some degree of antigen specificity, they undergo clonal expansion, and can even generate memory cells that persist beyond the initial immune response. NK-cell development primarily occurs in the bone marrow in a process called 'education' which is essential for the establishment of missing-self recognition. Inhibitory receptors expressed on NK-cell precursors like the KIRs must engage with cognate MHC-I molecules to generate functional NK cells in the periphery, analogously to positive selection in T cells. There is also an additional layer of 'tuning' of NK-cell responsiveness by varying the number of inhibitory receptors expressed for autologous MHC-I molecules. Although NK cells do not undergo 'death by neglect' to filter out non-interacting receptors, there is evidence from transplant studies that mature NK cells receive continuous signals from host MHC-I molecules

to modulate responsiveness. This suggests that, while T-cell sensitivity thresholds are set largely in the thymus, NK-cell thresholds are continuously shaped by the expression pattern of host human leukocyte antigen (HLA) molecules[56].

1.1.3 Lymphocyte functions in health and disease

In the absence of infection, mature T cells continuously migrate around the body and patrol peripheral and lymphoid tissues for signs of peptide-, lipid- or metabolite-derived antigens. Recognition of cognate antigens initiates transcriptional programs that promote cellular proliferation, and T cells can differentiate into a range of specialized subsets depending on the nature of the threat. Conventional T cell responses are shaped by at least three signals: 1) antigen-specific TCR-pMHC binding, 2) co-stimulatory molecules which provide evidence of an ongoing infection, and 3) contextual signals (*e.g.,* immunomodulatory cytokines) which influence T-cell polarization according to the type of pathogen encountered by innate immunity. $CD4^+$ helper T cells can differentiate into T_H1, T_H2, T_H9, T_H17, T_H22, follicular helper T cells (T_{FH}) and regulatory T cells (T_{regs}), characterized by differences in cytokine secretion profile and surface marker expression[57]. The conventional effector $CD4^+$ T cell subsets are T_H1, T_H2 and T_H17 cells which produce cytokines that enhance immune responses towards intracellular, helminth and extracellular pathogens, respectively. T_H9 and T_H22 cells are unconventional polarizations with less clearly defined roles but are thought to mediate helminth defenses and epidermal wound healing, respectively (see reviews in ref. [58]). T_{FH} cells reside in germinal centers and manage humoral immune responses by interacting with B cells. T_{regs}, which can either be generated in the thymus during negative selection or induced peripherally[59], dampen the immune responses by producing anti-inflammatory cytokines like TGF-β. $CD8^+$ CTLs either become short-lived effector cells capable of serial killing or long-lived memory cells that persist for years[60]. Studies of physiological T-cell responses have

shown that the borders between these subsets are relatively fluid, and there is a remarkable amount of plasticity in T-cell differentiation[61].

After an initial encounter with antigen the immune system predominantly produces IgM antibodies at a steady rate, peaking at ~2 weeks post-exposure. When rechallenged with the same antigen, antibodies are produced at a much higher rate and reach levels orders-of-magnitude greater than before. Most antibodies in this secondary response are also class-switched to IgG and have acquired a greatly increased avidity for antigen through affinity maturation[62]. This process lies at the center of humoral immune responses and depends on efficient B-cell activation in the follicles of lymph nodes. Here, naïve B cells encounter cognate antigens on the surface of resident APCs, like fDCs, which triggers antigen internalization and processing for presentation to T_{FH} cells via MHC-II. This occurs at the edges of B-cell follicles and prompts isotype switching to begin in the now rapidly proliferating B cells. Activated B cells have one of three fates: they can become GC B cells and undergo affinity maturation by cycling between GC dark and light zones, they can become short-lived plasma cells which are responsible for antibody production, or they can differentiate into long-lived memory B cells[63].

Mature NK cells that have left the bone marrow patrol the blood, spleen and liver for signs of infections and tumors, similar to T cells, although they do not appear to access lymph nodes in significant numbers. In response to a viral outbreak, NK cells are activated and expand robustly, interacting with both innate and adaptive immune systems[64]. NK-cell activation can occur in an antigen-specific manner, via activating receptors that recognize pathogens (*e.g.,* the LY49H receptor which binds a viral glycoprotein), or an antigen-nonspecific manner, via cytokines like IL-12 and type I interferons[56]. Missing-self recognition, in contrast, occurs exclusively by the (lack of) ligation of inhibitory receptors that bind MHC-I proteins. Both pathways that drive NK-cell activation lead to aggressive cellular cytotoxicity directed at the target cell through the release of cytolytic proteins like perforin and granzyme B. There is some evidence that subsets of NK cells persist long-term post-infection, capable of recall responses and more potent effector functions—hallmarks of immunological memory.

However, there are two arguments for why these subsets are not considered conventional immune memory cells: they seem to persist for much shorter periods of time than central memory T and B cells, and their capacity to traffic back to the original sites of infection appears limited[56].

1.2 Lymphocyte receptors

The behaviors of T cells and B cells are, in large part, controlled by signaling through a single clonotypic antigen receptor—the TCR or BCR—expressed at their surface (**Figure 1.2**). These receptors elicit highly specific and sensitive cellular responses, endowing the immune system with the ability to detect minute amounts of foreign antigen[65,66] while remaining tolerant to an abundance of self-molecules. Although it is still debated how antigen discrimination arises *in vivo*, the evolving view is that it is an emergent property of the receptors themselves and/or their proximal signaling complexes[67]. These complexes comprise a central, ligand-binding element (α/β receptor chains for the TCR, IgH/IgL chains for the BCR), surrounded by accessory signaling chains (CD3 for the TCR, Igα/β for the BCR), assisted by coreceptor proteins (CD4/CD8 for the TCR, CD19/21 for the BCR) and a cytoplasmic Src-family kinase that phosphorylates special receptor motifs (Lck for the TCR, Syk for the BCR)[68,69].

The large, multi-component machinery of the antigen receptors stands in contrast to the relatively simple but numerous NK-cell receptors (**Figure 1.2**). Triggering of NK cells is governed by a balance of activatory and inhibitory signaling delivered by a battery of polygenic and polymorphic receptors expressed at the cell surface. Unlike the TCR and BCR, NK-cell receptors bind to a very narrow range of conserved ligands—typically binding to monomorphic regions of MHC or MHC-like proteins—and require many receptors to be engaged in order to activate. Decision-making in NK cells occurs through integration of signals from both activating and inhibiting receptor types to determine whether or not to initiate effector activity. Mammalian activating receptors include the Fc receptor CD16 (FcγRIIIa), the Ly49 family of

C-type lectins and the NCRs. Mammalian inhibitory receptors include the KIRs, the CD94/NKG2 family of C-type lectins and the leukocyte Ig-like receptors subfamily B (LILRBs) (**Figure 1.2**). NK-cell receptors, particularly those for classical MHC-I molecules, have evolved multiple, independent times which emphasizes the functional importance of being able to sense the presence of intact class I proteins on somatic cells[70,71].

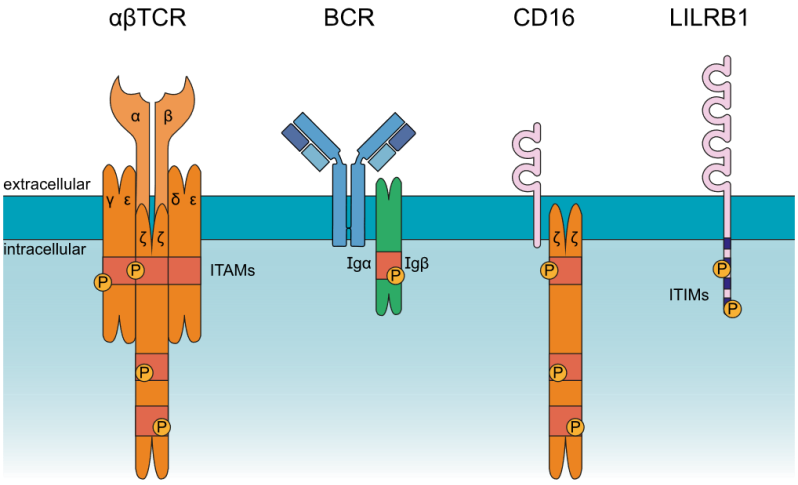


Figure 1.2. **Features of lymphocyte receptor families.** Structures of lymphocyte receptor examples depicting the primary features of the TCR and CD3 signaling chains, the BCR and associated Igα/β chains, CD16 and the associated ζ chains and LILRB1, a 4-Ig domain single-pass transmembrane protein with cytosolic ITIMs. TCR and BCR models adapted from ref.[72]. ITAM = Immunoreceptor tyrosine-based activation motif. ITIM = Immunoreceptor tyrosine-based inhibition motif.

1.2.1 Lymphocyte receptor families and functions

The T-cell receptor

A seminal finding in the study of T-cell biology was that T-cell activation required simultaneous recognition of both foreign peptide fragments and self-MHC molecules, as reported by Rolf Zinkernagel and Peter Doherty[73]. With the advent of advanced structural methods, we now know that the molecular basis for this unique receptor-ligand recognition event is the dual interaction of the αβTCR with both the peptide and the MHC protein on which it is presented. A fully assembled TCR is expressed at the surface of T cells as a complex of an antigen-binding heterodimer (TCRα and TCRβ) and three CD3 signaling dimers (CD3δε, CD3γε + CD247/CD3ζζ) forming an octameric assembly[74,75]. The docking site of the αβTCR that binds pMHC ligands is composed of three flexible complementarity determining region (CDR) loops: CDR1 and CDR2, which primarily make contacts with the MHC molecule, and the hypervariable CDR3 loop, which is responsible for peptide recognition by making extensive contacts directly with the peptide. Structural studies of the ~173 TCR-pMHC complexes currently deposited in the Protein Data Bank (PDB) have yielded insights into various aspects of TCR-pMHC binding geometry including: biased TCR usage, autoreactive TCRs, MHC polymorphism, molecular mimicry influencing TCR cross-reactivity and even an example of a TCR with reactivity towards both class I and class II proteins[76]. This last example highlights the highly conserved binding orientation mode of the TCR to its ligands, termed docking polarity.

The B-cell receptor

The B-cell receptor is a membrane-bound antibody (IgM and IgD) associated with two accessory ITAM-containing signaling chains called Igα and Igβ, equivalent to the CD3 chains of the TCR. IgM and IgD are splicing isoforms of the same heavy chain precursor and have identical antigen-binding domains but different structures; IgM has a shorter and more rigid

hinge region and is speculated primarily to bind monovalent antigens while both isotypes can bind multivalent antigens[77]. Although early studies revealed that the domains of the BCR were arranged in the characteristic Y-shape of antibodies, with two Fab 'arms' connected through hinges to two Fc 'legs', how these ectodomains connected to the membrane and Igα/β has only very recently been resolved with cryogenic electron microscopy (cryo-EM)[78]. Like the TCR, the BCR binds antigen via CDR loops on both chains of the receptor. While all three loops form contacts with antigen, it is often the CDR3 loop of the heavy chain which is considered the most important. The BCR CDR loops are substantially more rigid than those of the TCR and this structural rigidity has been proposed to aid in focusing the evolution of the receptor paratope during affinity maturation[79]. This process involves the selection of B cells with the highest affinity for antigen, with changes to antibody sequences driven by a rapid increase in mutation of genomic Ig genes (somatic hypermutation). BCR affinity dictates the quality of B-cell responsiveness, with higher affinities leading to faster and more efficient activation, proliferation and terminal differentiation[63]. Although this mechanism has been considered the *de facto* method for B cells to increase their affinity for antigen molecules, in 2016 it was shown that they can also generate better binding through insertion of entire protein-binding domains directly into the CDR loops. Antibodies that contain an insert of the LAIR1 receptor bind to a malarial surface antigen, a member of the repetitive interspersed families of polypeptides (RIFIN) family, expressed on the surface of infected erythrocytes[80,81].

NK-cell receptors

In humans, the NK-cell receptor genes reside in two distinct chromosomal complexes: the natural killer complex (NKC) which encodes C-type lectin receptors (*i.e.,* the NKG2 receptors), and the LRC which contain genes for the Ig-like receptors, primarily the KIRs and LILRs. The C-type lectin receptor genes include the activating NKG2C/E/D, the inhibiting NKG2A and a single Ly49 pseudogene, an evolutionary relic from the last common ancestor of primates and rodents[82]. The NKG2 receptors form signaling-competent heterodimers with the invariant

CD94 chain at the cell surface, except for NKG2D which associates with DAP10. The known ligands for conventional NKG2 receptors are conserved HLA proteins; NKG2C binds HLA-E, for instance, which presents signal peptides from classical HLA-A/B/C molecules, allowing for a simple detection mechanism of gross class I expression. Although NKG2D bears little sequence homology to the other NKG2 receptors, it also recognizes MHC-like stress-induced ligands (*e.g.,* MHC class I polypeptide–related sequence A/B [MICA/MICB]), typically upregulated following infection or oncogenic transformation.

In humans, the primary sensors of class I proteins on NK cells are members of the leukocyte receptor complex (LRC): the KIRs and LILRs but also leukocyte-associated immunoglobulin-like receptor (LAIR) 1, LAIR2, FcαR and NKp46, all of which descend from a common ancestral sequence[82]. KIRs are named according to the number of extracellular Ig domains (2 or 3) they contain, as well as whether they have a short (S) or long (L) cytoplasmic tail (*e.g.,* KIR2DS1 or KIR3DL). Inhibitory KIRs normally have long tails that contain ITIMs while activatory KIRs have short tails and associate with the ITAM-containing adaptor proteins like DAP-12. The KIR loci exhibit a very high degree of homology, with genes arranged in a continuous head-to-tail orientation in a single, tight cluster. This genetic organization is hypothesized to have facilitated many cross-overs, insertions and deletions over the course of rapid KIR evolution, producing a large number of KIR proteins (>15 in humans) that are very closely related in structure and function[83]. The LILRs, which are evolutionarily older and appear to be more stable than KIRs, consist of either two or four Ig-like domains with either a long cytoplasmic tail with ITIMs (subfamily B, inhibitory) or a short cytoplasmic tail and associate with an ITAM-containing FcRγ chain (subfamily A, activatory). Their interactions with class I MHC proteins occurs through various binding modes, the best characterized of which is LILRB1 which binds β_2m directly and therefore recognizes virtually all HLA-I proteins[84]. LILRB1 is also bound by pathogen-derived molecules like human cytomegalovirus UL18[85] and *Plasmodium falciparum* RIFINs[86], likely as part of immune evasion strategies.

1.2.2 Lymphocyte receptor signaling

TCR signaling

TCR signaling begins with the increase in net phosphorylation of CD3 ITAMs by Lck which is recruited to ligand-engaged receptors (**Figure 1.3**). There are a total of 10 ITAMs in the cytoplasmic domains of the TCR, each of which contains two precisely-spaced tyrosines in the consensus sequence: YxxI/L$x_{6\text{-}12}$YxxI/L that are phosphorylated by Src-family kinases Lck and, to a lesser extent, Fyn. Phosphorylated ITAMs serve as docking sites for the tandem SH2 domains of another kinase, zeta-chain-associated protein kinase 70 (ZAP70), which is recruited and activated by both Lck and trans-autophosphorylation[87]. Activated ZAP70 phosphorylates signaling adaptor proteins Linker for activation of T cells (LAT), acting as multivalent signaling scaffolds that are probably bridged and oligomerized by adaptors like Grb2 and SOS, which can bind multiple phosphorylated LAT proteins (**Figure 1.3**). The major downstream signaling effects of LAT-recruited adaptor proteins are Ca^{2+} flux, activation of the Ras-mitogen-activated protein kinase (MAPK) cascade and Rho-family GTPase activity which collectively lead to cytoskeletal changes, metabolic remodeling and gene expression programs which drive proliferation and differentiation[88,89].

What produces TCR phosphorylation (*i.e.,* triggering) in the first instance? Several theories have been proposed and are generally categorized as oligomerization-, conformational- or segregation-based models[89,90]. One source of controversy has been the valency of the TCR which has been exceptionally difficult to probe *in situ*. Initial reports suggested that the TCR might be pre-clustered into oligomers that 'poise' the receptor to detect sparse antigens[91,92]. It later became apparent that clustered receptors were artefacts of imaging setups that produced low levels of TCR triggering[93] or analyses which overcounted molecules (*i.e.,* blinking effects)[94,95], and biophysical studies have since confirmed that TCR is monovalent and monomeric in the absence of stimulus[96–99]. The most recent evidence would suggest that initial TCR triggering is produced either by mechanotransduction, where the TCR intrinsically senses ligand quality through the types of bonds formed[100], or by kinetic

segregation, in which antigen discrimination is constrained by T-cell topography and relies only on receptor dwell-times in close contacts[101].

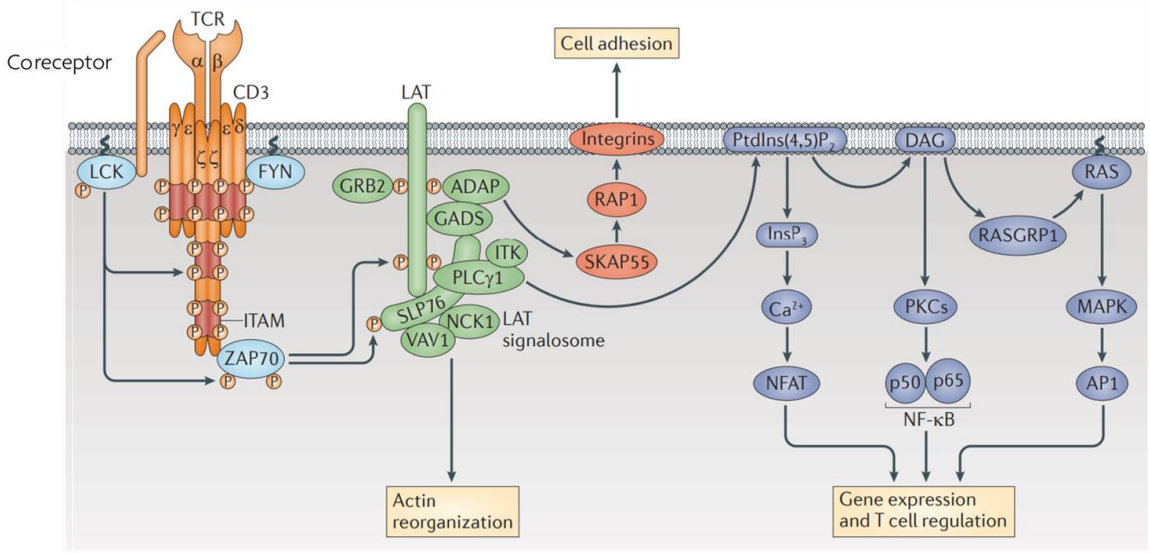


Figure 1.3. **The αβTCR signaling network.** The recognition of cognate pMHC molecules by the TCR leads to phosphorylation of cytoplasmic ITAMs on the CD3 chains by both free Lck and coreceptor-bound Lck. ZAP70 is recruited to pITAMs and is activated by Lck through phosphorylation. ZAP70 phosphorylates LAT which functions as a signaling hub for the recruitment of adaptors from which downstream signaling pathways emanate and impinge on cytoskeletal rearrangements (via Vav1 and Rac), Ras-MAPK signaling (via PLCγ1) and Ca^{2+} flux (via PLCγ1 and IP_3). Image taken from ref.[102].

BCR signaling

The BCR, like the TCR, is sensitive to the quality of ligands it encounters and must discriminate between them. Upon binding to a cognate antigen, it initiates signaling cascades that remodel the cytoskeleton, metabolism and transcriptional profile. The BCR must also internalize bound antigens for processing and loading onto MHC-II proteins to present to T cells. Studies of BCR signaling have revealed that while these two functions are interrelated, full B-cell activation (including differentiation into plasma cells) requires both a primary antigenic signal (*i.e.,* antigen binding) and a secondary co-stimulatory signal (*e.g.,* CD40L, complement receptors, PRRs) as evidence of the presence of a pathogen.

BCR signaling begins much like the TCR with the increase in net phosphorylation of receptor-associated ITAMs by a Src-family kinase, which leads to the recruitment of a Syk-family kinase that phosphorylates a multivalent adaptor protein. In the case of the BCR, it is Lyn kinase that phosphorylates Igα/Igβ-associated ITAMs and Syk kinase that is recruited to the receptor. Syk phosphorylates an adaptor called B-cell linker (BLNK) which recruits downstream effector proteins like PLCγ2 (which releases the second messengers inositol trisphosphate [IP_3] and diacyl glycerol [DAG]), Grb2/SOS (which activates the Ras-MAPK cascade) and Nck (which causes cytoskeletal remodeling)[103,104].

Much like the TCR, the mechanism by which the BCR is triggered has been an enigma[105]. Originally, the BCR was thought to be activated by simple aggregation through binding to multivalent antigens (*i.e.,* conformation-induced oligomerization). This proposal was overturned by the observation that ITAM phosphorylation could spread to non-engaged BCRs, prompting the view that BCRs are oligomeric in the resting state only (*i.e.,* dissociation-activation). Finally, it has also been suggested that triggering is controlled by lateral diffusion in the plasma membrane; either by collision with activating factors (*i.e.,* collision-coupling) or by segregation from inhibitory factors (*i.e.,* kinetic segregation)[106,107].

NK-cell receptor signaling

Activation of NK cells is controlled by the balance between activatory signaling from ITAM-containing receptors and inhibitory signaling from ITIM-containing receptors. Most NK-cell activatory receptors signal in a manner reminiscent of the antigen receptors of T cells and B cells; the ITAMs of engaged receptors are phosphorylated by Src-family kinases (Lck and Fyn), leading to the recruitment and activation of Syk-family kinases (ZAP70 and Syk). Adaptor proteins like LAT and Slp76 are phosphorylated and form signaling 'hubs', upon which signal quality and quantity from multiple receptors are integrated[108]. NKG2D, which forms a heterodimer with adaptor protein DAP10, is the only receptor that elicits ITAM-independent signaling and is thought to interact directly with downstream adaptors like Grb2 and PI3K without the need for Syk-family kinases. Both ITAM- and DAP10-dependent signaling converges on the MAPK signaling cascade which activate effector functions like cytotoxicity and cytokine secretion, primarily interferon-γ.

Inhibitory ITIM signaling occurs through the recruitment of tandem SH2-containing tyrosine phosphatases 1 and 2 (SHP-1 and -2) to the tails of triggered receptors. ITAM- and ITIM-signaling is saturable and proportional to the magnitude of receptor engagement, meaning that the relative balance between activatory and inhibitory ligands is relayed into the cell and converges on tyrosine phosphorylation of critical signaling molecules which serve as targets for both Syk-family kinases and SHP-1/2, like Vav1[109].

Additionally, accessory receptors like adhesion proteins, cytokine receptors and PRRs are also able to feed into the dynamic activation-inhibition equilibrium in NK cells, acting as co-stimulations of cytotoxicity. β_2-integrin signaling, via lymphocyte function-associated antigen 1 (LFA-1), is linked to perforin degranulation via CD16-mediated antibody-dependent cellular cytotoxicity (ADCC), for instance[110].

1.2.3 Lymphocyte receptor *cis* interactions

Conventional binding interactions between receptors and their ligands occur in *trans* (*i.e.,* between molecules not co-expressed in the same cell membrane). However, an increasing number of surface receptors are being reported to have binding partners in *cis* (*i.e.,* within the same membrane), especially in mechanisms of signal regulation (**Figure 1.4**). This phenomenon was first observed for CD22, a Siglec (sialic acid-binding Ig-type lectin) that functions as an inhibitory coreceptor for B cells, whose ability to bind soluble sialic acids was found to be 'masked' by glycan-linked sialic acid residues on the same cell[111]. Although the identity of the *cis* ligand is not clear, functional and biochemical studies suggest that the role of the *cis* interaction is to competitively inhibit ligand-binding in *trans*, thus regulating the sensitivity of CD22 to sialic acids[112,113]. This mechanism is thought be one way of adjusting the signaling threshold of the BCR, preventing overstimulation after cross-linking by multivalent antigens[114]. Several receptors have since been reported to bind either the same or different ligands in *cis* at the cell surface. When the *cis* and *trans* ligands are distinct, the interaction can be classed as heterotypic: this is the case for the proposed binding of CD80, which conventionally binds *trans* CD28, to programmed death-ligand 1 (PD-L1) in *cis* on T cells as part of a co-stimulatory signaling mechanism[115]. Alternatively, when the *cis* and *trans* ligands are identical, the *cis* interaction is referred to as homotypic[116]; these include the proposed binding of some NK-cell receptors to class I proteins[117] and adhesive CD2-CD58 interactions that control T-cell sensitivity[118]. Additionally, PD-L1 was also recently reported to be capable of engage its *trans* receptor in *cis*[119], suggesting that and heterotypic *cis* interactions are not mutually exclusive—it remains to be seen whether this is unique to PD-L1, however.

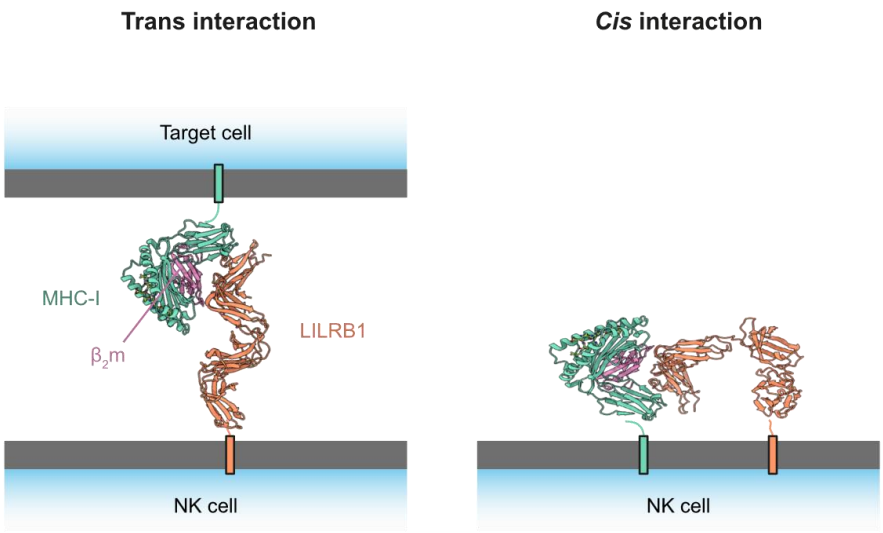


Figure 1.4. **Example of homotypic *cis-trans* engagement by the inhibitory receptor LILRB1.** For the *trans* interaction (left), LILRB1 extends vertically from the cell surface to make contacts with the β_2m domain of MHC-I via a flexible loop in the D1-D2 hinge. For the *cis* interaction (right), LILRB1 needs to deform and adopt an extensively bent conformation in order to engage membrane-proximal β_2m domains with the same loop. This bending is hypothesized to occur at the most flexible region of the protein, the D2-D3 hinge[120]. Crystal models generated by S. Chamberlain.

The original definition of cell-surface binding in *cis* was restricted only to homotypic *cis* interactions between receptor proteins and their ligands (*i.e.,* exclusively considering integral membrane proteins[121]). However, this definition is restricted only to the relatively rare instances when the ligand for a given receptor is present on the same cell surface. The discovery of heterotypic *cis* interactions[122] demonstrate the need for a revised classification. We propose that any laterally-occurring, non-covalent interaction between molecules constrained to a membrane can be categorized as a *cis* interaction. As these interactions will be specific they will most likely have a regulatory effect (*e.g.,* enhances/hinders signaling), although this is not a strict requirement. This expanded definition therefore includes both heterotypic interactions (*e.g.,* PD-L1/CD80 binding)[122], transient receptor dimerization (*e.g.,* GPCR oligomerization) and pseudo-trans interactions which require bending of the membrane. This approach is deliberately broad to allow us to consider receptors which might otherwise not have been deemed of interest for *cis* interaction studies. An important example of this is the recently reported *cis* interaction between CD2 (a transmembrane protein) binding to CD58 (a glycosylphosphatidylinositol [GPI]-anchored protein)[123]. Membrane-associated proteins are effectively confined to the bilayer through hydrophobic moieties, restricting their interactions with membrane-embedded receptors to 2D. Many membrane-associated enzymes (*e.g.,* G proteins, phosphatases and kinases) interact non-covalently with their respective receptors to regulate signal transduction, much like *cis* interactions between receptors. Examples of three distinct categories of *cis* interactions between lymphocyte receptors are presented below, and their relevance to this thesis is discussed further in section 1.4.

Transient dimerization of a co-signaling molecule

PD-1 is a co-inhibitory receptor expressed broadly on activated lymphocytes and is the target for several checkpoint inhibitor therapies[124]. A recent report[125] describing a secreted form of its ligand, secPD-L1, has led to speculation that dimerization of the receptor might regulate

inhibitory signaling[126]. However, PD-1 is strictly monomeric in crystal lattices[127,128] suggesting that dimerization might be a transient event, requiring studies of membrane-bound receptors to determine.

Zn^{2+}-mediated coreceptor/kinase interactions in the initiation of T-cell signaling

CD4 and CD8 each associate with an Lck molecule at the inner cytoplasmic leaflet via a Zn^{2+} 'clasp' interaction[129,130]. This heterotypic *cis* interaction is required for the ability of coreceptors to amplifying T-cell antigen sensitivity through recruitment of kinase activity to the TCR[131]. The coreceptor/Lck coupling ratio (also known as the occupancy) is a core component of some TCR signaling models[132–134] but biochemical investigations disagree on how much kinase is bound to the coreceptors[135–138]. Thus, there is no current consensus on coreceptor/Lck coupling levels *in situ*[139,140] as this is challenging to measure.

Cis interactions of an inhibitory receptor in malaria

The inhibitory immune receptor LILRB1 is expressed broadly on leukocytes where it transduces negative regulatory signals on binding of class I HLA molecules[141]. Early studies of LILRB1 suggested that it can also interact with MHC-I proteins in *cis*[142], potentially to 'mask' the binding of *trans* ligands. In 2017, the discovery of malarial surface antigens that bound LILRB1 indicated a role for these proteins (called RIFINs) in evading host immunity[143]. However, it remains unclear exactly how RIFINs engage LILRB1 especially if the receptor is mostly bound to MHC-I in *cis*. Measurements of LILRB1/MHC-I interactions in the presence of different RIFINs might reveal whether these homotypic *cis* interactions can be 'unmasked' or co-opted by the malaria parasite.

1.3 Methods to study *cis* interactions

A major obstacle to the study of receptor *cis* interactions is the lack of accessible, robust and specific methods to measure protein/protein interactions occurring in *cis* only (*i.e.,* direct methods)[121]. Most studies have instead used indirect methods where functional consequences of the putative *cis* interactions are determined by disrupting them via *e.g.,* blocking antibodies or enzymatic treatment[123,144,145]. Since these assays are often performed on bulk populations of cells, it can be difficult to distinguish true *cis* interactions from confounding variables. For instance, extracellular particles released by many immune cells contain proteins that could bind cell-surface receptors in any orientation[146]. A large number of receptors are also proteolytically cleaved by membrane-bound proteases to shed their ectodomains which can be active in a soluble form[147]. In addition, *trans* interactions might also occur both between cells (intermembrane) and on the same cell (intramembrane) due to roughness and irregularities of the cell surface like membrane ruffles and undulations[148].

Direct methods to study receptor *cis* interactions come in two forms: *in vitro* and *in situ*. *In vitro* approaches involves extracting proteins from cells and assaying them in a purified system, isolated from cellular context. These methods are typically normal biochemical or biophysical binding assays in which the analytes are either known only to interact in *cis* or have been modified such that *trans* interactions cannot occur. For this reason, *in vitro* approaches cannot be used to study to homotypic *cis* interactions that occur via the same interfaces because of the inability to distinguish between the two binding modes. *In situ* approaches are more difficult to implement and calibrate than *in vitro* methods but have the advantage of reporting on protein/protein interactions as they occur in a native context, at the surface of live cells. To perform *in situ* measurements, the target proteins are selectively visualized by fluorescent labels and then tracked at the cell surface over time. For these approaches the primary challenge is to deconvolve signals (*i.e.,* mobile, properly assembled

proteins/complexes with appropriate labeling density) from noise (*e.g.,* protein aggregates/clusters, free dye molecules, intracellular species) during acquisition and analysis.

1.3.1 *In vitro* approaches

Co-immunoprecipitation (co-IP)

Immunoprecipitation, as the name suggests, relies on the principle of high-affinity antibody/antigen binding to selectively precipitate a target protein (the primary analyte) from crude mixture of proteins and other biomolecules. Co-IPs are used to analyze the binding of other proteins (secondary analytes) to the target under the hypothesis that, if two proteins interact in a specific manner, and at a substantial level, they will co-precipitate. Co-IP experiments are available in two fundamental strategies. First, they can be used to search for unknown components of a protein complex through precipitation of the primary analyte followed by analysis by gel electrophoresis and autoradiography or sequencing to identify binding partners. The second strategy involves testing and quantifying the binding of two proteins known to interact, requiring antibodies to each protein[149].

The primary advantage of using co-IP to study and quantify receptor interactions in *cis* is that the sample is instantaneously solubilized with mild detergents, stabilizing membrane proteins in lipid micelles for analysis without the need to make extensive modifications or truncations to stabilize proteins. It is therefore easily applicable to primary cells without the need for modification and treatment which is useful when only small amounts of material are available (*e.g.,* rare cell subsets). Extracted proteins, immobilized to beads via antibodies, can then be analyzed and quantitated by Western blotting to determine the extent of the interaction. However, since the proteins are boiled and linearized before gel electrophoresis it is not possible to determine protein integrity and whether some of the analyte is bound non-specifically due to *e.g.,* sticky/misfolded protein aggregates. To overcome this problem, a variant of co-IP has been developed in which analytes are detected using flow cytometry rather

than gel electrophoresis. In flow cytometric (FC)-IPs, antibodies specific for conformational epitopes can be used to ensure that only correctly folded proteins are measured (**Figure 1.5**)[150].

Co-IPs, like all biochemical methods, are necessarily disruptive to the system under study and there are therefore several caveats of using IPs for making quantitative measurements. The use of detergents may unphysiologically stabilize or disrupt some protein/protein interactions, biasing the signals measured in precipitates. Additionally, the plasma membrane is not perfectly solubilized and proteins from internal membranes (*e.g.,* vesicles, endosomes, lysosomes and trafficking compartments) can also contribute to the measurements. Another possibility is that excessive dilutions during washing steps shifts the equilibrium of the complex towards dissociation, resulting in loss of material over time.

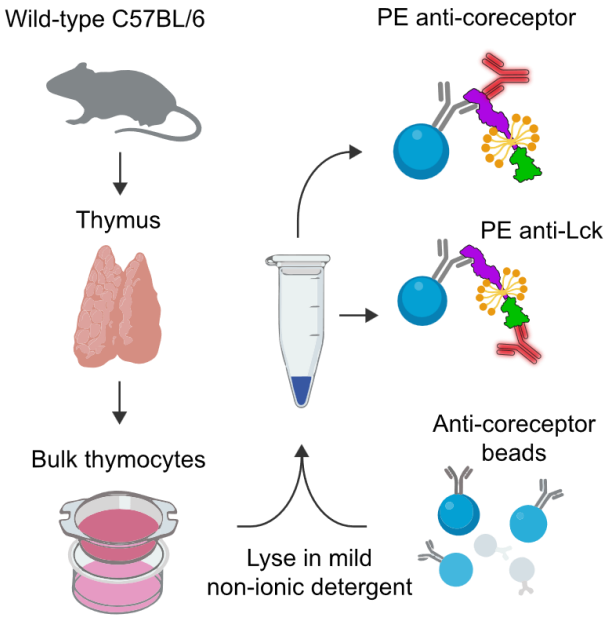


Figure 1.5. **Schematic of the FC-IP method used to study coreceptor/Lck *cis* interactions *in vitro***. FC-IPs are a variation of traditional co-IP methods in which the analytes are detected using flow cytometry, instead of Western blotting, to ensure that only correctly folded proteins are measured. A capture antibody is used to precipitate the primary analyte from the sample followed by washing and staining for either the primary or secondary analyte using fluorescent antibodies. In this schematic, a coreceptor (CD4) is shown in purple and Lck is shown in green as an example of a heterotypic *cis* interaction studied with FC-IP.

Surface plasmon resonance (SPR)

SPR is a form of optical spectroscopy that utilizes the principle of resonance to detect changes in refractive index at a thin metal surface. For biological applications, a microflow system is usually coupled to an SPR sensor in a Kretschmann configuration. The primary analyte (the 'bait') is conjugated to a chip and a secondary analyte (the 'prey') is then injected into the flow cell. Localized changes in mass cause changes in refractive index, which changes the SPR angle, and is measured by detecting intensity fluctuations of the reflected light producing a sensorgram, a readout of binding. Rates of change can then by analyzed to yield apparent association/dissociation rate constants from which the equilibrium constant (K_D) can be determined. Since the SPR signal is directly proportional to changes in mass, stoichiometry can be interpreted if the molecular size of the proteins is known[151].

The main advantages of SPR is that only relatively small amounts of material (< 5 µg) are needed to determine accurate kinetic constants of any interaction without the need for labels. The limitation of SPR is that equipment only measures changes in mass, so small polypeptides or molecules have poor signal-to-noise ratios. Additionally, the analytes need to be soluble proteins so hydrophobic regions of receptors or membrane-associated proteins need to be removed or mutated to prevent aggregation. Advances in SPR chip technology have alleviated some of these issues with *in vitro* reconstituted membrane systems used to study native receptor-ligand binding[152].

1.3.2 *In situ* approaches

Fluorescence colocalization and single-particle tracking (SPT)

Fluorescence imaging methods rely on the selective excitation and detection of fluorescent dyes which emit light at particular wavelengths, collecting and splitting the illumination through dichroic mirrors, to obtain high-resolution images of biological specimens invisible to the naked eye. Conventionally, imaging is performed in microscopes configured either in epifluorescence

mode (where the same objective lens is used for illumination and transmitted light), confocal (where out-of-focus light is blocked with a pinhole) or total internal reflection fluorescence (TIRF; where a thin evanescent wave is used to selectively illuminate fluorophores close to the surface).

The simplest use of fluorescence imaging to study interactions is through co-localization analysis, where the co-occurrence of fluorescence signal at the same subcellular locations is used to infer information about the interactions of two or more spectrally distinct species. Rigorous co-localization is normally assessed statistically using colocalization metrics—such as Pearson's correlation coefficient or Manders overlap coefficient—which can be useful since co-localization manifests in different ways depending on how the proteins distribute and how they interact (*e.g.,* signal co-occurrence vs. signal proportionality)[153]. The main problem with a conventional imaging approach is that it is inappropriate for direct measurements of molecular interactions due to the diffraction limit—a spatial limit (~200 nm in xy) on how close two point-emitters can be before they become unresolvable due to the diffraction of light.

An interesting solution to the problem of studying single-molecule interactions in living systems without super-resolved imaging that has gained popularity is single-particle tracking. SPT was made possible with significant advancements in fluorescent probe technology, such as increasingly bright and photostable labeling moieties, enabling the fluorescence of single molecules to be localized, visualized and tracked for substantial periods of time[154]. Variants of the SPT method have also been designed specifically to detect biomolecular association such as two-color coincidence detection (TCCD), in which spectrally separated photons are measured simultaneously as they move through overlapping observation volumes[155].

Caveats of SPT methods are that individual localizations are still diffraction-limited, making it difficult to distinguish a binding event from random collision, photobleaching from sustained excitation of the same dyes, and the possibility that labeling of proteins with fluorescent adducts might perturb their function (*e.g.,* blocking an interaction epitope).

Measuring interactions of biomolecules can be especially challenging since the number of fluorescent particles must be sufficiently low to resolve individual tracks and this is typically achieved either by a very low labeling density (which decreases probability of detecting heterodimers) or a very low expression density (which shifts the binding equilibrium towards monomers according to the law of mass action[156]).

Biophysical methods: FRET and FCCS

A key development in the quest to study intermolecular protein interactions was the application of Förster resonance energy transfer (FRET) to biological macromolecules. FRET relies on the non-radiative the transfer of energy between certain fluorophores only when they are within a very short (< 6 nm) distance, allowing molecular binding events to be detected using a conventional microscope with less technical complexity than super-resolved imaging methods[157]. As a result, FRET has seen widespread use for the study of many protein/protein interactions *in situ*. However, FRET signals measure changes in proximity, rather than the interactions themselves, and careful consideration needs to be given in the design of FRET constructs since the FPs normally used have non-negligible sizes. As a result, FRET between randomly distributed membrane proteins will arise non-specifically at physiological expression densities (100-200 molecules/μm^2) because of forced proximity even of non-interacting proteins[158]. The primary limitation of conventional FRET is poor signal-to-noise, partly because of bleaching and energy loss, and several technologies have been developed to address this problem including, for example, fluorescence lifetime imaging (FLIM)-FRET. The use of FLIM as a readout for FRETing molecules is based on the principle that the fluorescence lifetime of a donor molecule changes when it undergoes FRET with an acceptor. Since only the donor needs to be directly excited (since only donor lifetime is measured), signals can be greatly improved over intensity-FRET since lower laser powers and wider emission filters can be used[159]. Finally, single-molecule FRET (smFRET) has also seen a gain in popularity because of its ability to determine interaction kinetics between individual fluorophores in real-time[160].

However, the sensitivity of this technique means that a great deal of caution is required in sample preparation and data interpretation to exclude artefactual signals. Moreover, as a single-molecule approach, smFRET suffers from the same label/expression density issues as SPT in resolving individual fluorophores to study membrane protein interactions.

Fluorescence correlation spectroscopy (FCS) is a form of fluctuation spectroscopy in which the random movement of fluorescent particles through an observation volume is used to extract information about molecular diffusion and dynamics (**Figure 1.6a**). Fluctuating particles that diffuse into a confocal spot produce bursts of fluorescence recorded as intensity traces which are correlated in time yielding auto-correlation functions (ACFs)[161]. In fluorescence cross-correlation spectroscopy (FCCS), two spectrally distinct labels are measured and their movement cross-correlated to determine the extent of co-diffusion, indicative of binding[162] (**Figure 1.6b**). The molecular applications of conventional single point-FCCS, also called pFCCS, are mainly limited by photobleaching effects since slowly diffusing species, like receptors and other membrane proteins, experience prolonged exposure to the laser which continuously illuminates one location[163]. Efforts to improve the signal-to-noise and applicability of FCS to biological samples has led to the development of several variants of the method including scanning-FCS and imaging-FCS. In the former, samples are scanned along a line using a laser-scanning microscope (LSM), reducing bleaching at any single point. In the latter, a field of pixels is illuminated simultaneously using TIRF microscopy for multiplexed analysis, allowing for both increased sample size and integration of spatial information.

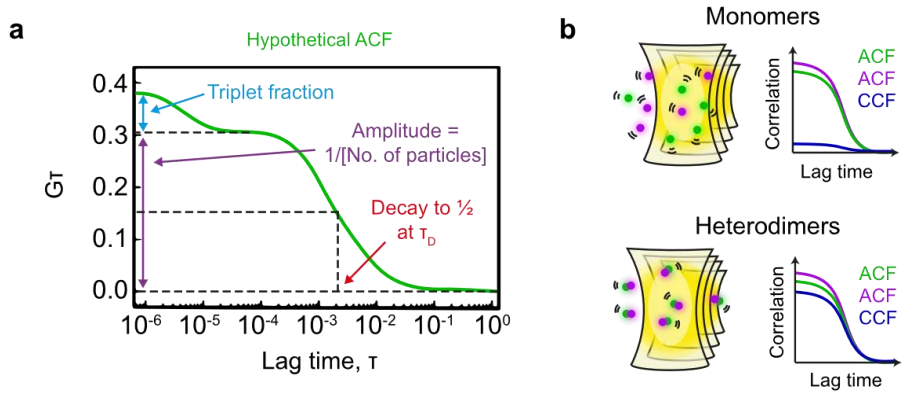


Figure 1.6. **The basis of FC(C)S auto- and cross-correlation functions. a.** A schematic ACF curve over a large lag time range (τ) with the effects of photophysical or diffusive processes contributing to the shape of the curve indicated with arrows. At very fast lag times, triplet state fluorescence (blue) affects the y-axis intercept. The amplitude (purple) is inversely proportional to the number of particles in the observation volume. The half-life of the diffusion curve decays at the transit time (τ_D), which is used to obtain the diffusion coefficient for the system. Adapted from ref.[164]. **b.** A diagram of FCCS in which the ACF for each fluorescent species is cross-correlated to obtain the CCF (blue), the amplitude of which is directly proportional to the fraction of heterodimeric (*i.e.,* green-red) particles. ACF = auto-correlation function. CCF = cross-correlation function.

1.4 Aims of the thesis

Although our understanding of the capacity for lymphocyte receptors to engage in physiologically important *cis* interactions has grown, it is still challenging to study and document these interactions in environments that closely resemble their native states. This thesis proposes to adapt and extend conventional FCCS techniques to the study of lymphocyte receptor *cis* interactions as they occur in live cells. We will establish a suitable FCCS methodology for reliable *in situ* measurements of co-diffusion as a proxy for *cis*-interacting proteins. To verify our system, we will apply FCCS to receptors that either are known or have been proposed to engage in important *cis* interactions. As described before, *cis* interactions have been defined broadly in this thesis to include virtually any regulatory interaction between proteins expressed within a 2D plane. To this end, we have chosen three distinct examples of putative *cis* interactions to study using FCCS:

1. First, we aim to study *cis* interactions between PD-1 receptors, a molecule normally considered monomeric, in an effort to determine whether oligomeric state might regulate signaling through the receptor. Although some groups use the term 'receptor/receptor *cis* interactions', this type of binding is effectively just transient homodimerization and is known to occur for other lymphocyte receptors (*e.g.,* the dynamic dimer CD80 which equilibrates between monomeric and dimeric forms).
2. Second, we aim to study the role of coreceptor proteins CD4 and CD8 in the initiation of TCR signaling. Coreceptors bind to the small, membrane-anchored protein Lck in *cis* and cause localization of the kinase to the TCR. Although not a conventional *cis* interaction, these interactions are constitutive, regulatory and constrained to the cell surface. Additionally, no prior attempts have succeeded in quantifying their occupancy in live cells.
3. Third, we aim to determine whether *cis* interactions between inhibitory receptor LILRB1 and HLA molecules can regulate NK-cell activation. LILRB1 binding to MHC molecules

has previously been proposed as a mechanism of regulating self-MHC sensitivity thresholds, but it is unclear if this interaction can actually occur *in situ*. In collaboration with structural biologists we will investigate whether the *cis* interaction must occur in pseudo-*trans* way (i.e., a *trans* binding orientation facilitated by bending/folding of the plasma membrane) or if significant conformational changes are required to the structures.

Although each aim involves a different lymphocyte receptor that forms *cis* interactions using distinct mechanisms, our central goal is to quantify each of them using the same biophysical approach. Using FCCS we can ask: does *cis* binding occur in the steady state in live cells, and, if so, to what exact level? Does the presence of a competing (*trans*) ligand have any effect? Can we forcibly disrupt the interaction by, for example, site-specific mutagenesis, and does this have functional consequences?

2. Methods and materials

Project-specific methods are listed at the start of each respective chapter and only techniques used generally are described here. Protocols for the methods performed by collaborators were generously shared and include: FLIM-FRET (NYU), flow-FRET (NYU), TOXGREEN assay (NYU), *in vivo* work (NYU), protein production (Oxford Biochemistry), structure determination (Oxford Biochemistry) and the NFAT-GFP reporter assay (Oxford Biochemistry). For all protocols, reagents were sourced from Thermo Fisher Scientific unless otherwise stated.

2.1 Cell culture

All cell lines were purchased from ATCC with the exception of the B16-Ova melanoma line, which was a gift from S. Feske. Human embryonic kidney 293T (HEK293T) cells and B16-Ova cells were cultured in complete D10 medium (Dulbecco's Modified Eagle Medium [DMEM], 10% fetal bovine serum [FBS], 1% penicillin/streptomycin); Jurkat E6.1 T cells were cultured in complete R10 medium (Roswell Park Memorial Institute 1640 [RPMI-1640] medium, 10% FBS, 1% penicillin/streptomycin, 2% L-glutamine, 25 mM 4-(2-hydroxyethyl)-1-piperazineethanesulfonic acid [HEPES]); Baby hamster kidney 21 (BHK-21) cells were grown in complete E10 medium (Eagle's Minimum Essential Medium [EMEM], 10% FBS, 1% penicillin/streptomycin. Cells were maintained at a density of 0.5-1 million cells per ml at 37°C, 5% CO_2 and grown for a maximum of 20 passages before new vials were thawed.

2.2 Flow cytometry

Flow cytometry was used to assess cells for the expression of surface or intracellular molecules and bead-supported bilayers for the degree of fluorescent protein tethering.

For cells, 5×10^5 cells were washed in flow cytometry buffer (phosphate-buffered saline [PBS], 1% FBS, 0.05% sodium azide) before fixation in 4% paraformaldehyde [PFA] and overnight staining with antibodies at 4°C. For detecting intracellular molecules, the cells were prepared in permeabilization buffer (PBS, 0.5% saponin, 1% FBS) prior to staining. For analysis of protein expression, samples were stained with antibodies against: mouse (m)PD-1 (PE-RMP1-14, BioLegend), human (h)PD-1 (PE-EH12.2H7, BioLegend or recombinant Pembrolizumab), Lck (PE-3A5, Santa Cruz Biotechnology), mCD4 (PE-H129.19, BioLegend), hCD4 (PE-RPA-T4, BioLegend), h-αβTCR (PE-IP26, BioLegend) or hMHC-I (PE-W6/32, BioLegend).

For beads, samples were prepared according to published protocols[165]. In brief, 5 µm silica beads (Bangs Laboratories) were washed with PBS and SLBs formed by incubating with DOPC liposomes supplemented with 12.5% DOGS-NTA. Bead-supported SLBs (BSLBs) were washed in HEPES-buffered saline (HBS) supplemented with 1% human serum album (HSA; HBS/HSA buffer), blocked with 100 µm $NiSO_4$ in 5% bovine serum albumin (BSA) for 20 minutes. BSLBs were then loaded with fluorescent His-tagged proteins for 30 minutes before a final washing step was performed. To relate bilayer density with protein concentrations, residual fluorescence was calibrated against fluorescent microspheres with known MESF (molecules of equivalent soluble fluorescence) values (Bangs Laboratories).

Samples were washed in flow buffer immediately before acquisition on an LSRFortessa™ X-20 (BD Biosciences). Analysis was performed using FlowJo software v10 (Treestar).

2.3 Cloning

Several different constructs were generated for imaging and sFCS experiments performed in chapters 3-6. With the exception of CD8α, CD80, CD86 and PD-1 constructs (gifted from E. Philips), all plasmids were generated through subcloning of mammalian codon-optimized GeneArt fragments using MluI/BamHI restriction digest and ligation (cloning enzymes from NEB) into a recipient pHR vector[166] containing a C-terminal mEGFP or mCherry2 tag (Michael Davidson, Addgene #54767 and #54517). All constructs were verified by Sanger-based sequencing (Source Bioscience).

2.4 Supported lipid bilayers

SLBs were generated through the liposome deposition method with in-house lipid production by S. Valvo (Dustin lab)[167]. Small unilamellar vesicles (SUVs) of DOPC supplemented with 12.5% 1,2-dioleoyl-sn-glycero-3-[(N-(5-amino-1-carboxypentyl)iminodiacetic acid)succinyl (DGS-NTA; Avanti Polar Lipids) were flowed onto clean glass coverslips affixed with adhesive six-lane chambers (sticky-Slide VI 0.4, ibidi) for 20 minutes and then washed with HBS supplemented with 0.1% HSA (Merck-Millipore) to remove excess liposomes. SLBs were then blocked with 5% BSA and 100 µM $NiSO_4$ in PBS for another 20 minutes before washing. Bilayers were functionalized with recombinant, His-tagged proteins produced in-house by L. Chen, H. Rada, T. Harrison or S. Chamberlain.

For chapter 4, the proteins used were: ICAM-1-Alexa Fluor (AF) 405, anti-CD3ε (UCHT1-Fab) or murine pMHC (H-2Kb + SIINFEKL peptide, MBL), and PD-L1-AF647. For chapter 5, the proteins used were: UCHT1-Fab and CD58 (both unlabeled). For chapter 6, the proteins used were: ICAM-1, pMHC-AF647 (HLA-A2 + SLLMWITQV peptide, gifted from E. Jenkins) and RIFIN-AF647 (variable domains). Protein densities were adjusted using calibration curves of bead-SLBs loaded either with fluorescently labelled proteins or unlabeled

proteins stained with antibodies, with reference to calibration beads with known fluorophore densities (Bangs Laboratories). For Fc triggering of NK cells, the human PfRH5-targeting R5.016 antibody[168] (IgG1) was coupled to the SLBs using His-tagged PfRH5 at a concentration of 100 nM. For succinimidyl ester labeling, 100 µg protein was labeled with the appropriate fluorophore using NHS Ester kits. Labeling was performed overnight followed by purification of the protein with a PD SpinTrap G-25 (Cytiva) and overnight dialysis with GeBaFlex tubes (8 kDa MWCO, Generon) at 4°C.

2.5 Microscopy and image acquisition

Imaging samples were prepared by seeding 50,000 HEK293T or Jurkat cells on chambered glass coverslips (µ-Slide #1.5H, ibidi) the day before transfection with 100 ng of plasmid DNA. Cells were then grown for a further 24 hours before imaging to allow expression and maturation of fluorescent proteins (FPs)[169]. Fluorescence images (for micrographs) and intensity fluctuations (for FCS) were acquired on an inverted confocal LSM (Zeiss 780i, Carl Zeiss) equipped with a 40x C-Apochromat 1.2 numerical aperture (NA) water-immersion FCS objective. Fluorescence was collected onto the hybrid GaAsP detectors (Channel S, photon-counting mode). Samples were excited with a 488 nm Argon laser (for mEGFP) and a 594 nm He-Ne laser (for mCherry2) using a 488/594 dichroic and the pinhole set to 1 AU. At the start of each day of experiments, point-FCS measurements were performed on a dye solution (20 nM Alexa Fluor 488) to calibrate the system by optimizing the counts per molecule when setting the correction collar and adjusting the position of the pinhole. Fluorescence line-scans for sFCS were acquired by repeated measurement of a 52-pixel line (digital zoom 40x) at maximum scanning speed (3.94 µs dwell time and 2081 Hz line frequency) for 10^5 cycles resulting in a total measurement time of ~48s. Images were exported as .czi files and line-scans exported as .lsm5 files.

Images were processed with ImageJ (v1.53n, NIH)[170]. Fluorescent cell area was measured by merging the mEGFP and mCherry2 channels and thresholding with Otsu's algorithm[171] to determine the region-of-interest (ROIs). ROI areas were tabulated using the 'Analyze particles' function

2.6 sFCCS and image processing

Confocal .lsm5 files were correlated using the open-source FoCuS_scan software[172]. The cross-correlation quotient (*q*) was calculated as the CCF amplitude relative to the ACF amplitude at G_0 (refs. [173,174]), *i.e.*

$$q = \frac{G_{\mathrm{cc}}(\tau_0)}{\min\left(G_{\mathrm{mEGFP}}(\tau_0), G_{\mathrm{mCherry2}}(\tau_0)\right)}$$

Where G_{cc} indicates the CCF amplitude and G_{mEGFP}/$G_{mCherry2}$ indicate the respective ACFs. If the fitted CCF amplitude was equal to the lower limit of the fitting parameters (0.001), the average of the first five raw CCF values was used instead.

The size of the 488 nm observation volume was calibrated using the solution of Alexa Fluor 488, which has a known diffusion coefficient of 435 $\mu m^2/s$ (see ref. [175]), using the equation:

$$\omega^2 = D \times 4 \times t_{xy}$$

Where ω is the beam waist radius, D is the diffusion coefficient and t_{xy} is the average transit time. ω_{594} (0.266 µm) was calibrated using ω_{488} (0.235 µm) and the diffusion coefficient of the tandem mEGFP-mCherry2 construct.

Fluorescent images were acquired using the same photon-counting settings as for line-scan measurements but at slower frequencies (~12s per 512 x 512 frame) to highlight cell morphologies.

3. Establishing the FCS method for correlative measurements

3.1 Introduction

Principles of fluorescence correlation spectroscopy (FCS)

FCS is a form of fluorescence fluctuation analysis originally established in the 1970s to observe chemical reactions in solution[176,177] but since extended to the study of many different physiochemical processes including triplet-state fluorescence[178], rotational diffusion[179], photobleaching[180] and, perhaps most popularly, diffusion in biological systems[181]. There are two major principles at work with modern FCS that make it particularly versatile as a biophysical tool. First, each process that leads to variation in fluorescence at a given timescale will be reflected in the auto-correlation function (ACF) at that same timescale. This is the basis for the auto-correlation analysis used widely to provide information about molecular dynamics and concentrations[182], though other algorithms are available[183–185]. Secondly, the dimensions of the confocal volume from which the fluorescence signal is collected (typically smaller than 0.5 µm x 0.5 µm x 2 µm) corresponds to a femtoliter-sized volume[186]. Together, these features allow users of FCS to probe single-molecule dynamics and behaviors normally inaccessible with standard, diffraction-limited microscopes. A swathe of developments in commercial turn-key instrumentation and genetically-encodable labels has brought FCS to the front of modern biophysics, allowing for *in situ* measurements of mobility, oligomerization, concentration, anomalous diffusion and molecular interactions[187,188]. Although many of these properties can be accessed with other biophysical methods, like single-particle tracking (SPT) and Förster resonance energy transfer (FRET), FCS has the added advantage of providing them all in a single measurement.

In conventional pFCS, the confocal volume is 'parked' at one location and fluctuations are sampled only at this point in space through continuous excitation of the observation spot. However, in biological systems this approach suffers in signal quality, and several attempts have been made to improve and extend the method. These include scanning-(s)FCS (scanning along a line[189] or circle[190] to reduce photobleaching), imaging-(im)FCS (continuous widefield illumination of a square area)[191], stimulated emission depletion (STED)-FCS (depleting the detection volume to measure nanoscale anomalous diffusion)[192], pair-correlation FCS (providing directional dynamics)[193], inverse FCS (analyzing the densely labeled medium surrounding unlabeled particles)[194], single plane illumination FCS (measuring fluctuation along and through a light sheet)[195] and space-mapped multiplexing FCS (collecting and comparing fluorescence collected simultaneously along a line)[196].

sFCS and imaging FCS

sFCS and imFCS were both originally proposed and applied in a live-cell setting to study membrane proteins[197,198], which diffuse significantly slower than cytoplasmic proteins and are therefore both less likely to enter the observation area (posing sampling issues) and have a longer retention time (causing photobleaching). Both methods involve increasing the number of observation pixels (improving sampling) and can be performed at lower laser powers compared to pFCS (reducing light exposure). In imaging FCS, all the pixels of an image subarray (*e.g.,* 16x16 pixels) are illuminated and acquired simultaneously using widefield methods. In sFCS, the pixels of a predetermined line (typically 52-128 pixels) are acquired sequentially using a laser scanning microscope. For many years, the large sample size provided by imaging FCS came at the cost of a greatly reduced temporal sensitivity[199], initially limited to diffusion events slower than 1 $\mu m^2/s$. The advent of detector technologies that are both fast and sensitive—electron-multiplying charge-coupled devices (EMCCDs) and scientific complementary metal oxide semiconductor (sCMOS) cameras—has enabled imaging FCS to reach speeds and resolutions sufficient for spectroscopy of biological macromolecules[174].

However, to optimize the sensitivity of the system an illumination method with good z-sectioning such as total internal reflection fluorescence (TIRF) or light-sheet is normally necessary, while sFCS can be performed on conventional confocal microscopes which are simpler to access and operate[200,201]. The main advantages of imFCS is in biological systems either where spatial information is needed (*i.e.,* where parameter maps are meaningful) or with spatial heterogeneity (*i.e.,* so spatial filters can be applied).

There are also hybrid scanning-imaging FCS approaches like Raster image correlation spectroscopy (RICS)[202], in which images of the whole sample are generated through line-scanning in a Raster pattern. Since each pixel is collected at a known time in a defined pattern, this information can be used to extract additional temporal information. Unlike imaging FCS, which correlates pixels between images, RICS correlates pixels along the Raster line within a single image and can therefore measure processes too fast for imaging FCS. However, temporal resolution is anisotropic and the need for pixel averaging in practice means that spatial resolution is generally limited. Like sFCS and imaging FCS, RICS can also be performed simultaneously on differentially labeled particles to detect molecular cross-correlation[203].

It is worth noting the distinction between imaging FCS and image correlation spectroscopy (ICS), the latter of which was originally developed to study spatial correlation across an entire image but at a single point in time[204]. Such correlations were used to characterize the distribution and composition of large cell-surface protein clusters but could not be used to measure dynamics[205]. Similar to how temporal-focused pFCS was eventually extended in space (leading to sFCS and imFCS), advancements in detector technology led to the extension of spatial-focused ICS in time (leading to temporal ICS [TICS] and spatiotemporal ICS [STICS]). Although naming conventions have sown some confusion, and there is now considerable overlap in the biological applications for these methods, ICS and its variants are normally performed with video-rate resolution (~30 ms), thus being better suited for probing slowly moving species[206]. For a provenance of these methods, see **Figure 3.1a**.

Cross-correlation

In dual-color FCS, *i.e.,* fluorescence cross-correlation spectroscopy (FCCS), emissions from two spectrally distinct fluorophores are collected and separated simultaneously and can be analyzed to detect interactions. FCCS experiments yield three correlation functions: one ACF from each dye and a single cross-correlation function (CCF). The CCF amplitude is proportional to the fraction of heterodimeric particles detected, and the decay time reflects their mobility. Applications of dual-color FCCS in living systems has seen mixed results. Measurements of cytoplasmic proteins were very successful, yielding important information on the prerequisites of Ca^{2+}-dependent protein-binding[207] and transcription factor heterodimer formation[208]. Studies of membrane receptors, like bacterial cholera toxin[209] and interleukin receptors[210], produced less clear results due in part to low apparent protein mobility and cross-correlation curves of poor quality, suggesting that these data may need to be interpreted carefully. A general drawback of FCCS is that there are several sources of signal deterioration in the amplitude of the CCF stemming either from optical aberrations (*e.g.,* misalignment of the two confocal volumes) or from photophysical properties of the dyes[211]. Without proper controls, these differences can lead to poor CCFs and to significant underestimations of heterotypic protein/protein interactions. In principle, FCCS experiments are not restricted to just two colors since cross-correlations can be calculated for any number of ACF pairs in a sample. Practical constraints on optical filtering and dye overlap, however, have limited multi-color FCCS to experiments with extremely bright Qdots[212]. Only very recently, in 2021, has a study managed to demonstrate four-color FCCS in live cells using spectral detectors and custom-written analysis software[213].

3.2 Methods

pFC(C)S and sFC(C)S

For the details of the optical LSM setup used for sFCS and pFCS, see Methods **Section 2.5**. Prior to each day of experiments, the pinhole was calibrated and the objective correction collar adjusted with a solution of Alexa Fluor 488. FCS was performed by locating dim cells in the 'Live' mode of the Acquisition pane and a homogenously fluorescent area was selected at the basal cell surface. Then, for pFCS, the FCS module was used to acquire and correlate 3x 10 second measurements which were exported to FoCuS software for fitting[201]. For sFCS, after a cell was selected the zoom was set to 40x and 100.000 frames of 52-pixel line was acquired continuously before exporting for correlation externally.

For processing, the first 20% of sFCS intensity traces were cropped remove the most pronounced bleaching and a mono-exponential photobleaching correction (PBC) was applied to correct for decays in the fluorescence time-series as per guidelines[201,211,214]. Carpets were than inspected for the presence of fluorescence artefacts, which most commonly manifest as very bright/dim edges or intrusion of bright clusters that disrupt the auto-correlation analysis. If the artefactual pixels represented <30% of the total carpet, these were filtered out and the remainder of pixels exported and averaged for fitting. Otherwise, the entire carpet was discarded.

pFCS and sFCS curves were fitted identically with the exception of the fitting range which was 10^{-2} to 10^{3} for pFCS and 10^{1} to 10^{4} for sFCS. Diffusion dynamics were fitted with a one-component 2D diffusion model and a Levenberg-Marquardt algorithm from the lmfit python library (https://lmfit.github.io/lmfit-py/) used to optimize parameters to this model[201]. The anomalous diffusion parameter (*alpha1*) was kept fixed at 1 (*i.e.,* no anomalous diffusion was expected) and the correlation amplitude (*Gn0*) was set to vary between 0.001 and 1. All others parameters were allowed to vary. Quality of fits was assessed both by inspecting the overlay of the fit and the correlation curve and then by checking that residuals were randomly

distributed. Fits that exhibited bleaching, systematically deviating residuals or had chi^2 values over 0.05 were excluded[211]. Curves, fits and diffusion parameters were then exported for further analysis and plotting. For the analysis of diffusion mode, the shape of transit time histograms was analyzed statistically using MLE, as described before[215]. This approach specifically differentiates free from hindered diffusion through fitting of histograms: freely diffusing molecules produce distributions with a lognormal shape and nanoscale hindrance introduce a second transit time component, resulting in a double-lognormal shape[216]. To perform this analysis, sFCCS curves were processed as described above except that no spatial averaging was performed, and each pixel was instead fitted individually and transit times were directly subject to frequency analysis. MLE was used to calculate the most likely model for the data employing the Bayesian Information Criterion (BIC), assigning free or hindered diffusion for a given transit time histogram. The code for this analysis can be found at https://github.com/Faldalf/sFCS_BTS. For an extensive protocols paper describing pFCS/sFCS calibration, acquisition, curve fitting and processing, see ref.[211].

imFCS

Imaging FCS was performed on an Olympus cellTIRF-4Line system running cellSENS Dimension software v.2.3 (Olympus) using a 150x (NA 1.45) oil objective. mEGFP-expressing cells were illuminated with a 488 nm laser line and a 16x16 subarray was cropped to basal area of a cell membrane. Intensity frames were acquiring by imaging this inset for 20.000 frames at a camera rate of 10 ms and .tiff files exported to the ImFCS plugin. Files were processed according to recommended guidelines including a polynomial (4-order) PBC and error pixel filtering (typically <5%). As these processing steps were sufficient to produce quality curves, as judged in the same way as for pFCS/sFCS above, binning was not required to improve signal quality. Weighted non-linear least squares (NLS) fitting was used to calculate ACFs with all parameters allowed to float[217,218].

3.3 Results

3.3.1 Comparing pFCS, sFCS and imaging FCS

We set out to compare the suitability of pFCS, sFCS and imFCS (**Figure 3.1b**) for characterizing protein diffusion in the cell membrane. Since mEGFP and mCherry2 are currently the best fluorescent protein (FP) pair for measuring interactions[219], and mEGFP is the brighter fluorophore[220], we began by generating a fluorescent construct that would diffuse freely in the membrane. The transmembrane helix of CD4 was C-terminally linked to mEGFP (SP-$CD4_{TM}$-mEGFP) and this construct placed under a viral SFFV promoter in the pHR plasmid for transfection into HEK293T cells. HEKs are ideal cells for biophysical studies as they readily express foreign genetic material and form large and flat adherent contacts when grown on glass coverslips[219]. pFCS and sFCS measurements were acquired on a confocal LSM while imFCS was performed on a TIRF system (see **Sections 2.5 and 3.2** for experimental details).

pFCS can be performed using commercial LSM operating software with in-built routines that produce intensity traces and ACFs in real-time during imaging. The primary advantage of using pFCS is that experiments can be acquired, visualized and inspected very fast and in quick succession (acquisition time: 10 seconds, processing time: N/A, fitting time: ~5 seconds). On-board signal correlation is inflexible, however, and these routines do not offer options to process intensity traces for signal improvement (**Figure 3.1c**). The easiest way to acquire high-quality ACFs with pFCS is simply to inspect each curve as it is being generated, rejecting curves that cannot be fitted or fall below a fitting score (*e.g.,* typical X^2 cut-off = 0.05)[201].

sFCS analyses are not yet available on commercial instruments and intensity traces acquired on laser-scanning microscopes (LSMs) need to be exported, converted and loaded into third-party software like FoCuS[201,221]. It is therefore more cumbersome than pFCS (acquisition time: 50 seconds, processing time: ~120 seconds, fitting time: ~30 seconds). The

benefit is that each measurement can typically yield useful correlation curves through a combination of cropping, photobleaching correction (PBC) and line-averaging (**Figure 3.1c**). The degree of post-processing required varies depending on the sample, but as a general principle the fewest steps of data processing should be taken that produce good fits[201,211]. We found that, for membrane protein diffusion, sampling a wide range of fluorophore expression levels required a combination of all three processing options. To ensure all samples could be compared, they were all processed in the same manner (for details see **Section 3.2**).

Similar to sFCS, imFCS processing and analysis must be performed post-acquisition using external software packages like the imFCS plugin for ImageJ developed by the Wohland group at NUS[222]. imFCS files are recorded as image stacks of typically 16x16 pixels that are simultaneously processed, correlated and fitted. Although more time-intensive than sFCS analyses (acquisition time: 200 seconds, processing time: ~180 seconds, fitting time: ~30 seconds), imFCS offers more post-processing options including four different photobleaching corrections, binning, pixel filtering and building of parameter maps (**Figure 3.1c**). Thus, although both sFCS and imFCS are significantly slower to execute in practice than pFCS, they provide significantly more information density per unit of experiment time (imFCS: ~0.62 pixels per second, sFCS: ~0.26 pixels per second, pFCS: ~0.07 pixels per second) with a greater probability of obtaining biologically meaningful data in a given measurement.

To compare the three methods, intensity traces were acquired of the same mEGFP-expressing HEK293T sample prepared in triplicate. For sFCS and imFCS, fluctuation measurements were then processed according to the recommended guidelines[201,222]. In each case, ACFs typical of membrane protein diffusion were obtained and fitted (**Figure 3.1c**) and diffusion parameters extracted for comparison (**Figure 3.1d**). We found that, while diffusion coefficients agreed between measurements, the average number of particles detected per pixel (N(FCS)) was much lower when measured by pFCS compared to either sFCS or imFCS. This is consistent with the lack of bleaching correction, leading to a gross underestimation of the number of diffusing proteins. Fewer detected particles leads to poorer ACFs and greater

errors, reflected in the standard deviations for diffusion coefficients. Additionally, the large sample sizes of sFCS and imFCS also led to greater statistical precision as seen when errors are plotted as standard error of the mean (SEM) rather than standard deviation (SD) (**Figure 3.1d**). Overall, these experiments demonstrated the validity of all three methods in assessing protein diffusion in the plasma membrane of live cells, and highlighted the advantages of multiplexing-based approaches over conventional single-point FCS.

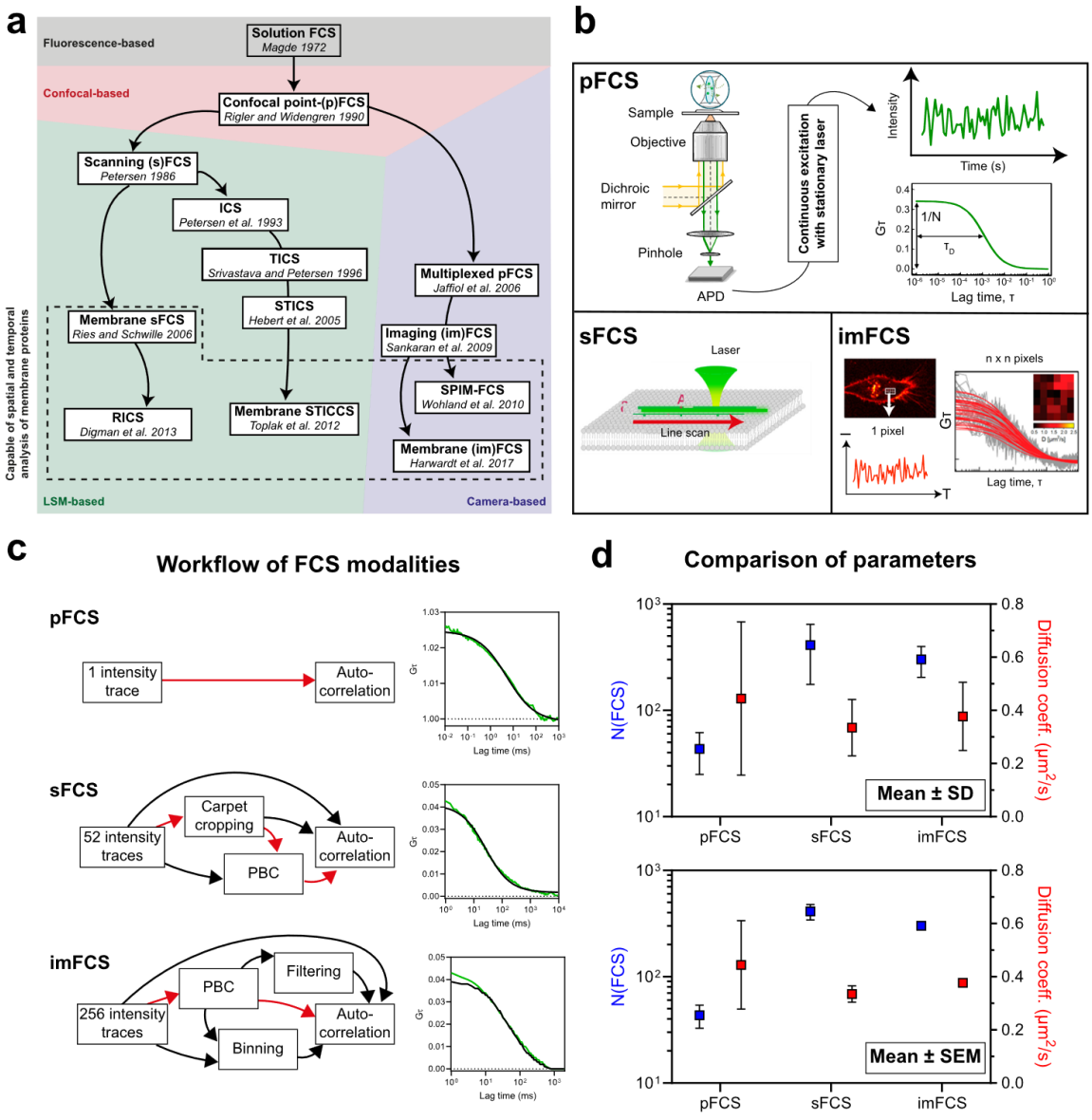


Figure 3.1 **Comparisons of point-FCS (pFCS), scanning-FCS (sFCS) and imaging FCS (imFCS). a.** A provenance of FCS, indicating the different paths that have been taken to develop techniques suitable for measuring membrane protein diffusion (dotted box). **b.** Schematic of the three methods tested in this chapter, adapted from ref.[223]. **c.** Workflow from acquisition of intensity traces to auto-correlating. For sFCS and imFCS, the respective software allows for photobleaching correction (PBC) and signal improvement through either cropping (sFCS) or binning of adjacent pixels (imFCS). The red arrows indicate the analysis pathways used here. The highest-quality ACF for each method is shown on the right. **d**. A comparison of particle density (N(FCS)) and diffusion coefficients extracted from each method, depicted as the means with error bars indicating the standard deviation (SD) in the top panel and standard error of the mean (SEM) in the bottom panel. ACFs from three cells were aggregated for each measurement.

3.3.2 Cross-correlation measurements

For cross-correlation measurements, fluctuations from two different fluorophores in the sample are collected, separated and correlated together to obtain the ACFs and CCFs[224]. For LSM acquisition, fluorescence was collected using a 488/594 nm main beam splitter (MBS) and a hybrid GaAsP detector. The TIRF microscope (a cellTIRF4-line) used for this study was not equipped with a dual-emission image splitter, invalidating this system for cross-correlation measurements since acquisition of multiple colors required mechanical switching of the filter wheel.

To benchmark measurements, a tandem membrane-bound mEGFP-mCherry2 control was generated and expressed in HEK293T cells. The sample was then excited with both 488 nm and 594 nm laser lines simultaneously for both pFCCS and sFCCS (**Figure 3.2a,b**). Cross-correlation quotients were calculated for each ACF (individually for pFCS, spatially averaged for sFCS) to determine the fraction of heterodimeric mEGFP-mCherry2 particles detected (**Figure 3.2c**). In both cases, the CCF amplitudes were lower than either ACF amplitude which indicated that a large fraction of molecules were fluorescent in only a single color. However, the calculated *q* values from pFCCS were also significantly lower (0.26 ± 0.07) than from sFCCS (0.54 ± 0.06). This suggested significant signal deterioration in pFCCS that further decreased the number of fluorescent heterodimers detected. To ensure that the correlation detected between fluorochromes was due to *bona fide* coincidence and not spectral cross-talk, control samples were prepared in parallel. When mEGFP- or mCherry2-only expressing cells were measured under dual-laser excitation, minimal fluorescence was detected in the channel lacking its corresponding fluorophore and attempts to correlate this signal yielded no ACF and thus no CCF (**Figure 3.2d**). In addition, an autofluorescence control (*i.e.,* untreated cells) produced no correlation in any channel, confirming the sensitivity of the sFCS system. We concluded that sFCS was suitable for correlative measurements in live cells, balancing sufficiently rapid measurements to study protein dynamics with greatly improved signal quality to detect co-diffusing molecules.

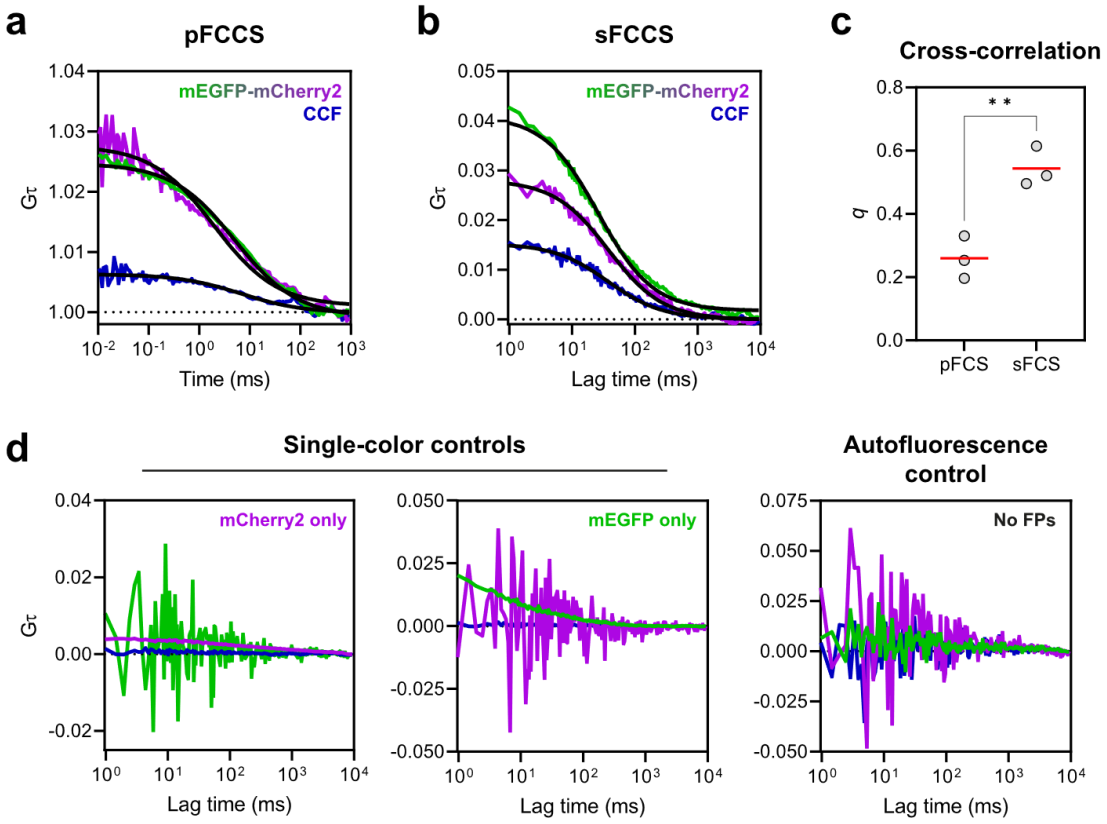


Figure 3.2 **Cross-correlation measurements performed by pFCS and sFCS. a.** and **b.** FCCS measurements of a tandem mEGFP-mCherry2 construct acquired in **a)** point-acquisition or **b)** scanning-acquisition modes. Correlation functions are depicted in colors and fits are shown as solid black lines. **c.** Cross-correlation quotients (*q*) for each method. Each circle indicates a *q* value calculated from one cell. Significance was assessed with an unpaired t test. **d**. Offset controls were performed using sFCS on cells expressing either fluorophore (single-color) or no fluorophores (autofluorescence). One representative set of correlation curves are shown from measurements of four cells for each control condition.

3.3.3 Membrane environment affects diffusion behavior

In FCS, the average concentration of fluorophores in the observation volume needs to remain constant over the time-course of measurement. We wanted to compare diffusion measurements at the apical (top) and basal (bottom) surfaces of our cultured HEK293T cells to determine if the membrane environment impacted diffusion. Although the apposition of the basal surface to a stiff glass substrate might slow or trap diffusing molecules[225], the heterogeneity of the apical surface could cause movement of the membrane within the measurement window[226,227].

Transmembrane-mEGFP fluctuations were acquired either at apical or basal membranes of the same cells and compared (**Figure 3.3a**). Intensity traces were processed identically but yielded vastly different correlation carpets (**Figure 3.3b**), with long 'streaks' appearing in the apical measurements only, indicative of slowly diffusing species. This produced an average ACF which was poorly fitted compared to basal measurements (**Figure 3.3c**). Particle and diffusion parameters from each condition were then extracted and compared, left unaveraged to display the full range (**Figure 3.3d**). N(FCS) was not significantly different between conditions, suggesting that the density of particles detected was approximately equal, but mEGFP molecules diffused significantly slower at the top of the cell compared to the bottom. This difference is presumably because of irregular surface topography at the top of cell (*i.e.,* membrane ruffles[228]) which caused the appearance of longer ACFs. Membrane surface irregularities could have this effect this either through directly slowing/constraining mEGFP diffusion or by stacking/folding of membrane layers in the z-axis, causing locally increased mEGFP coincidence. The fact that a similar number of fluorophores were detected at the bottom of the cell compared to the top suggests the former. The relatively uniform diffusion at the bottom of the cell is probably because adherent cells grow through secreted components and focal adhesions, establishing a gap between the basal surface of the cell and the glass substrate that allows free diffusion.

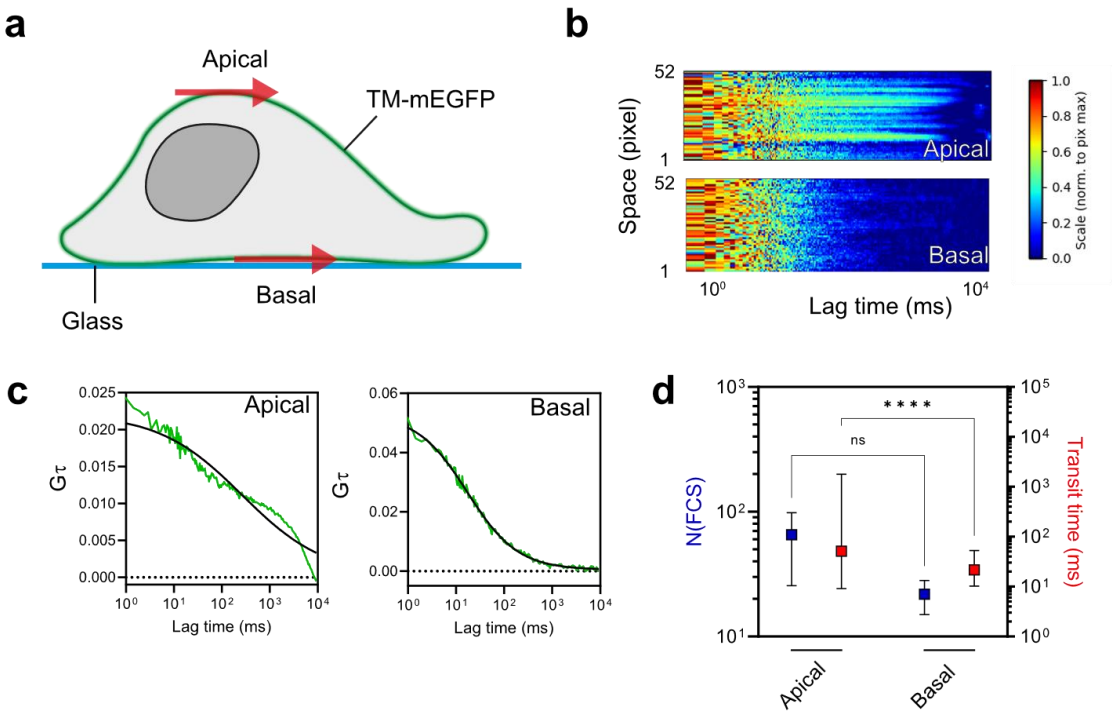


Figure 3.3 **Positioning of the sFCS line-scan affects measurement quality. a.** Schematic of the line-scan positions (red) in a side-on view of a HEK293T cell spread atop a glass surface. **b.** Correlation carpets on mEGFP ACFs represented in heatmap with color indicating auto-correlation amplitude. **c.** The spatially averaged ACF from all 52 pixels shown in **b** plotted as a single ACF (green) and fitted in FoCuS software (black). **d.** Parameters from the apical and basal measurements with boxes depicting the median with error bars indicating range. Significance was assessed with a one-way ANOVA.

3.4 Discussion

3.4.1 sFCS balances rapid and multiplexed acquisition

A major goal of modern microscopy is to break the diffraction barrier, circumventing the limitations of optical physics to study molecules at scale. Truly super-resolved methods achieve this typically either through mapped localization (SMLM) or structured illumination (SIM) but these techniques provide limited information on molecular movement as samples are either immobile (*i.e.,* chemically fixed) or imaged at a very low temporal resolution (*i.e.,* significantly slower than the diffusion of proteins)[229]. FCS represents a relatively straightforward biophysical tool for accessing molecular-level information on diffraction-limited systems without the need for laborious sample preparation, acquisition or reconstruction protocols[211]. A unique example of an imaging method that combines sub-diffraction spatial resolution with molecular dynamics is STED-FCS[230]. In STED, the shape of the excitation beam is optically manipulated to confine the fluorescent signal to a smaller area (~30 nm diameter). STED-FCS can thus provide super-resolved imaging of diffusive processes, revealing nanoscale behaviors that are inherently averaged in confocal FCS. However, the requirement for high laser powers to create the STED excitation 'donut' means that FPs cannot be used and only very bright organic dyes are sufficiently photostable to track diffusion[231].

In this chapter, we systematically compared three different implementations of FCS to probe membrane protein dynamics and interactions, a challenging problem in the general study of biomolecular diffusion[232]. Although pFCS was the only method that could generate ACFs in real-time, side-by-side with intensity trace acquisition, multiplexing methods (sFCS/imFCS) generated more precise diffusion parameters. We noted, in addition, that while imFCS required extensive PBC (*i.e.,* with pixels often exhibiting no detectable auto-correlation until a polynomial correction was applied), sFCS was much less reliant on processing. This difference was presumably because of the reduced light exposure when samples were imaged using LSM compared to TIRF, when the entire field-of-view is continuously illuminated.

Despite imFCS producing a higher total number of pixels per sample, both methods produced comparable diffusion coefficients indicating no substantial advantage of sampling more than ~50 pixels per cell. The primary strength of imFCS and related methods remains in the parsing of diffusion data into parameters maps, combining spatial and temporal information in one image. While this may be useful in understanding heterogeneity in other biological systems, it was not relevant to our samples which exhibited homogeneous membrane fluorescence.

3.4.2 New technologies enable correlative measurements

In biophysical studies of protein oligomerization and conformation, it is often assumed that all proteins expressed with a genetically encoded FP tag become fluorescent. However, there are several processes that contribute to the appearance of 'dark' FPs (*i.e.,* translated but non-fluorescent) including: maturation efficiency[233], folding issues[234], persistence of dark states[235,236] and 'flickering'[237]. For convenience, these factors are combined into a single metric, the apparent fluorescence probability (p_f), which can be determined via, for example, N&B analysis (see *e.g.,* Table S1 in ref.[219]). Previous attempts at performing cross-correlation measurements in biological membranes[238,239], show limited and noisy CCF amplitudes mainly because most red FPs like mRuby, mCardinal and mScarlet never fluoresce, with p_f values ranging from 0.2 to 0.4. The development of mCherry2[240] with a much higher p_f heralded the possibility of a greatly improved dynamic range for FCCS. In combination with mEGFP (average p_f = 0.77 from ref.[219]), the upper limit on the probability of detecting fluorescent heterodimers increases from 0.32 (mCherry p_f = 0.41) to 0.54 (mCherry2 p_f = 0.71).

In performing cross-correlation measurements of a tandem control, which would produce the maximal fluorescence co-incidence possible, we noted that *q* values were significantly lower when measured by pFCCS compared to sFCCS. Given the significant photobleaching that occurs in pFCCS—and the different photostability of the two FPs[241]—it is likely that bleaching caused a considerable and unequal loss of fluorescence, leading to

underestimation of the fraction of heterodimeric particles. Prior pFCCS measurements of a covalent (albeit cytosolic) mEGFP-mCherry2 tandem molecule reported a *q* value of approximately 0.33[219], suggesting that, although our pFCCS assay had room for improvement, it would be unlikely to reach the theoretical limit of 0.54. In contrast, when the tandem was measured with sFCCS the resulting *q* value was in exact agreement with the theoretical p_f, indicating that it was fully capable of detecting virtually all of the dual-fluorescent fluorophores present in the sample. Overall, our data demonstrated the utility of sFCCS for measuring membrane protein interactions with three important advancements over traditional pFCCS: 1) increased chance of encountering a fluorescent protein by sampling multiple pixels, 2) 50-fold reduced bleaching per pixel by laser scanning and 3) post-processing steps to eliminate faulty ACFs and improve the average signal-to-noise ratio.

4. PD-1 dimerization drives inhibitory signaling

4.1 Introduction

Co-stimulation and co-inhibition

The two-signal model for activation of naïve T cells posits that both a primary, antigen-derived stimulus (via cognate peptide-loaded major histocompatibility complex [pMHC]) and a secondary, danger-derived signal (via co-stimulatory receptors) are required for full T-cell activation and deployment of effector functions. This paradigm has expanded with the discovery of co-stimulatory receptors that negatively regulate T cell receptor (TCR) signaling (*i.e.,* co-inhibitory receptors) and it is now clear that T cells express a very broad repertoire of receptors defined by whether they transduce positive (*e.g.,* CD28, inducible T-cell costimulator [ICOS], CD2) or negative (*e.g.,* PD-1, cytotoxic T-lymphocyte-associated protein 4 [CTLA-4], lymphocyte-activation gene 3 [LAG3]) regulatory signals, collectively referred to as 'co-signaling' molecules[242]. TCR ligation in the absence of any co-signaling cues results in anergy[243].

Co-signaling molecules are primarily of the immunoglobulin superfamily (IgSF), tumor necrosis factor receptor (TNFR) and integrin receptor families. Two of the best-studied examples of co-stimulation and co-inhibition are CD28 and PD-1, respectively, both of which are IgSF proteins. CD28 is expressed constitutively on naïve T cells and provides essential signals for cell growth and expansion during activation, primarily through PI3K-Akt mediated signaling. PD-1, in contrast, is absent from the surface of most T cells but is upregulated on antigen-exposed cells within 24 hours of stimulation, countering the signals of co-stimulation[244]. Inhibitory receptors are immunological brakes, serving as immune checkpoints that effector T cells must pass through in order to keep serving their functions. PD-1

expression normally declines after a few days but persistently high levels of PD-1 have been associated with a dysfunctional T-cell state described as 'exhaustion'—although the exact molecular definition of this subset is debated[245].

PD-1: structure, function and oligomeric state

The crystal structure of PD-1 was solved in 2004, revealing how the monomeric receptor ectodomain consists of a single V-set Ig domain perched atop a single-pass transmembrane helix[246]. Although PD-1 is not an extracellular dimer like CD28 (ref.[247]), both receptors are thought to engage their ligands (CD80/86 for CD28, PD-L1/2 for PD-1) monovalently, eliciting signals through intracellular phosphotyrosine motifs. In the case of PD-1, signaling requires both an inhibitory (ITIM) and a switch (ITSM) tyrosine motif which become phosphorylated on triggering and recruit a non-receptor tyrosine phosphatase, SHP-2. SHP-2 recruitment is general feature of inhibitory receptor signaling as it has a broad substrate selectivity and antagonizes signaling in several pathways downstream of, for example, TCR and CD28 signaling including PI3K-Akt, Ras-MAPK, and PLC-γ (reviewed in detail in ref.[248]).

PD-1-deficiency in mice results in profound tolerance defects and accelerated autoimmunity[249,250]. This and other observations spurred the development of PD-1-based therapeutics and biologics, as relieving immune checkpoints like PD-1 could ameliorate inhibited or exhausted T cells and promote anti-tumor immunity. 'Checkpoint inhibitors', primarily monoclonal anti-PD-1/PD-L1 antibodies, have seen spectacular success as immunotherapeutics for the treatment of many types of cancer[251]. However, since checkpoint inhibition is only effective in subsets of patients and there are significant risks of immune-related adverse events, there is broad interest in improving our mechanistic understanding of checkpoint receptor signaling.

Co-signaling receptors that dimerize constitutively (*e.g.,* CD28, ICOS, CTLA-4) do so through a covalent disulfide bond in their extracellular domains, identified clearly in both

functional and structural analyses[252–254]. No such linkages are seen in the structures of PD-1 and its ligands, suggesting that they exist as monomers at the cell surface[246,255]. In 2019, however, Mahoney and colleagues reported the characterization of a secretory PD-L1 (secPD-L1) splice variant which could dimerize in solution and inhibited T cells more potently than a recombinant, monomeric form of the protein[256]. Although PD-1 can bind PD-L1 as a monomer, the increased activity of this secreted dimer suggested that PD-1 receptors might signal more strongly as a dimer. Several co-signaling receptors have been reported to form physiologically important heterodimers in *cis*, including PD-L1/CD80 and PD-L1/PD-1[122,257] but homodimerization of cell-surface PD-1 has not been explored.

4.2 Methods

Biophysical assays

FLIM-FRET samples were prepared by seeding 10^6 BHK cells on glass coverslips and transfecting them with mEGFP- and mCherry2-tagged for 24 hours. Cells were then washed with PBS, fixed in 4% PFA, mounted on glass coverslips and baked at 37°C for 1 hour prior to imaging. Samples were imaged using a Nikon TiE wide-field fluorescence microscope with a 60X Plan-Apo/NA 1.4 oil immersion objective. FLIM was measured using the frequency domain (*i.e.,* not requiring a pulsed laser or curve fitting) using a Lambert Instruments LIFA module attached to the Nikon TiE microscope. For each condition, three individual experiments were performed and a total of at least 60 cells were imaged. FRET efficiency was calculated as 1–(experimental lifetime / (lifetime of mEGFP component with an empty vector)).

For flow-FRET, CFP- and YFP-tagged constructs were first transfected into ExpiCHO-S cells using Lipofectamine 3000 for 40 hours. Then, cells were analyzed in a BD LSRII flow cytometer using 407 nm (violet) and 488 nm (blue) lasers for excitation. YFP fluorescence was measured using a 530/30 detector off of the blue laser. CFP fluorescence was measured using a 450/50 detector off of the violet laser. The $FRET^+$ fraction was determined by first gating on

CFP^+ YFP^+ cells and then by selecting cells that were emitting in the 530/30 detector off the violet laser, as described elsewhere[258]. Data was analyzed using FlowJo™ 10 software.

Jurkat 2E4 cells

Parental Jurkat E6.1 cells were grown as described in **Section 2.1**. To create the 2E4 PD-$1^{-/-}$ cell line, Jurkats were electroporated (AMAXA) with a combination of two CRISPR RNA guides to *PDCD1* (CACGAAGCTCTCCGATGTGT and GCGTGACTTCCACATGAGCG) in pSpCas9(BB)-2A-GFP plasmids (PX458, GenScript). Electroporated cells were transiently rendered GFP^+ and single-cell sorted 48 hours post-transfection. Screening for the loss of PD-1 expression following anti-CD3/CD28 overnight stimulation which identified the 2E4 clone. PD-1 expression was rescued using lentiviral gene delivery by co-transfecting a transfer pHR plasmid (containing wild-type or mutant PD-1 genes) with psPAX2 and pMD2.G in HEK293T cells using Lipofectamine 3000. Three days after transfections, lentiviral particles were harvested, 0.45 µm filtered and added to the 2E4 cells. Re-expression of PD-1 was verified by flow cytometry.

TOXGREEN

The TOXGREEN assay for transmembrane domain dimerization in *E. coli* was performed at stationary phase as described before[259]. In brief, various transmembrane domains were PCR amplified with NheI and BamHI flanking restriction sites and cloned into the pccGFPKAN plasmid (AddGene #73649). MM39 bacteria (AddGene strain #42894) were transformed with these plasmids as well as with pccGFP-GpA (AddGene plasmid #73651), pccGFP-GpA-G83I (AddGene plasmid #73650), and pccGFPKAN as the no TM control. Transformed colonies were grown in 3 mL LB media for 16 hours at 37°C with shaking. 300 µL of culture was loaded into a 96-well black-walled clear bottom plate. Plates were read using a fluorescence multi well plate reader (EnVision Multilabel Plate Reader) with an excitation wavelength of 485 nm

and fluorescence emission at 512 nm along with an OD reading at 600 nm for normalization. Results were further normalized by subtracting the average of the no TM control followed by normalization to the GpA positive control.

In vivo experiments

Female PD-1$^{-/-}$ mice were purchased from Jackson Laboratory (028276 – B6.Cg-Pdcd1$^{tm1.1Shr}$/J). OT-1^{+}, UBC-GFP^{+} male mice were provided by Susan Schwab (NYU). These mice were bred, and subsequent pups were back crossed to PD-1$^{-/-}$ females to generate PD-1$^{-/-}$, OT-1^{+}, GFP^{+} mice. Hemizygous RIP-mOVA male was purchased from Jackson Laboratory (005431 – C57BL/6-Tg(Ins2-TFRC/OVA)296Wehi/WehiJ) and crossed to WT N6 females. Female pups confirmed to be hemizygous for the RIP-mOVA transgene were used in T1D experiments.

To engineer murine cells to express mutated PD-1 receptors, OT-1 T cells were isolated from the spleen and lymph nodes of the PD-1$^{-/-}$ mice and purified by positive selection with MACS anti-CD8 magnetic beads according to manufacturer's protocol (Miltenyi Biotech) and grown in medium consisting of RPMI-1640, 10% FBS, 4mM glutamine, 50 μM β-mercaptoethanol and 20 mM HEPES. To rescue PD-1 expression, T cells were activated overnight with anti-CD3/CD28 and transduced by spin-infection with retroviral particles with 10 μg/mL polybrene (Sigma). Spin infection was performed by centrifugation at 850g at 32°C for 1.5 h. Retroviruses were produced in the same way as for lentiviruses except using the MSCV-IRES-Thy1.1 retroviral vector in Plat-E cells. T cells were supplemented with human IL-2 (Peprotech, 100 U/mL) for 2 days prior to use.

For the B16-Ova tumor model, 2 x 10^5 B16-Ova cells were injected into 8-9-week-old WT Black 6 mice on day -10. On day zero, 5 x 10^6 retrovirally transduced GFP^{+}, OT-1 T cells were injected IV. Tumor growth was measured for 18 days following adoptive transfer or until death/tumor volume exceeding 2000 mm^3.

For the RIP-mOVA T1D model, $1x10^6$ OT-1 cells were adoptively transferred via tail vein injection into hemizygous RIP-mOVA mice 7-12 weeks of age. Blood glucose measurements were taken daily from the tail tip using the AimStrip Plus glucose meter. Mice were considered diabetic if blood glucose readings were above 250 mg/dL for >2 days.

4.3 Results

4.3.1 Intermolecular PD-1 interactions in *cis* at the cell surface

Scanning-fluorescence cross-correlation spectroscopy (sFCCS), established in **Chapter 3**, was used to determine whether intermolecular PD-1 interactions could be detected at the cell surface. We benchmarked these experiments using three control conditions: CD8α/CD8α as a constitutive dimer[260], CD80/CD80 as a dynamic dimer[261,262], and non-interacting CD80/CD86 as a negative control[263]. To ensure that any interactions observed were not the result of signaling-mediated clustering[264], adaptor protein binding or cytoskeletal tethering, the cytosolic domains of all constructs were truncated to leave a minimal stop transfer sequence and a short linker.

sFCCS measurements indicated no correlation between CD80-mEGFP and CD86-mCherry2, confirming the absence of interaction between these molecules. In contrast, PD-1 produced robust homodimerization on par with that of the CD8αα positive control (**Figure 4.1a**), indicating the formation of stable dimers. CD80 dimerization exhibited more cell-to-cell variability, indicating perhaps that its ability to dimerize was dependent on surface expression levels. To validate these findings, we turned to two orthogonal measures of receptor proximity: fluorescence lifetime imaging (FLIM)-FRET and flow-FRET. In FLIM-FRET, changes in the distance between acceptor and donor can be detected through differences in the fluorescence lifetime of the donor, with lifetime decreasing with increased donor-acceptor proximity. While conventional intensity-based FRET is sensitive to variations in expression level or local

crowding effects, FLIM-FRET is internally calibrated and therefore independent of fluorophore concentration[265] (**Figure 4.1b**). In flow-FRET, protein proximity is detected using flow cytometry to detect bulk energy transfers from CFP- to YFP-tagged molecules[266]. The advantage of flow-FRET is that false-positive events (*i.e.,* YFP excitation by the 405 nm laser) can be gated out, increasing the sensitivity of the system[267] (**Figure 4.1c**). In each case, the calculated FRET efficiency (E) was compared to the *q* value from sFCCS, both measures representing the fraction of heterodimers forming. Both methods revealed the same trends as detected using sFCCS, confirming that PD-1 homodimerized at significant levels in mammalian cells.

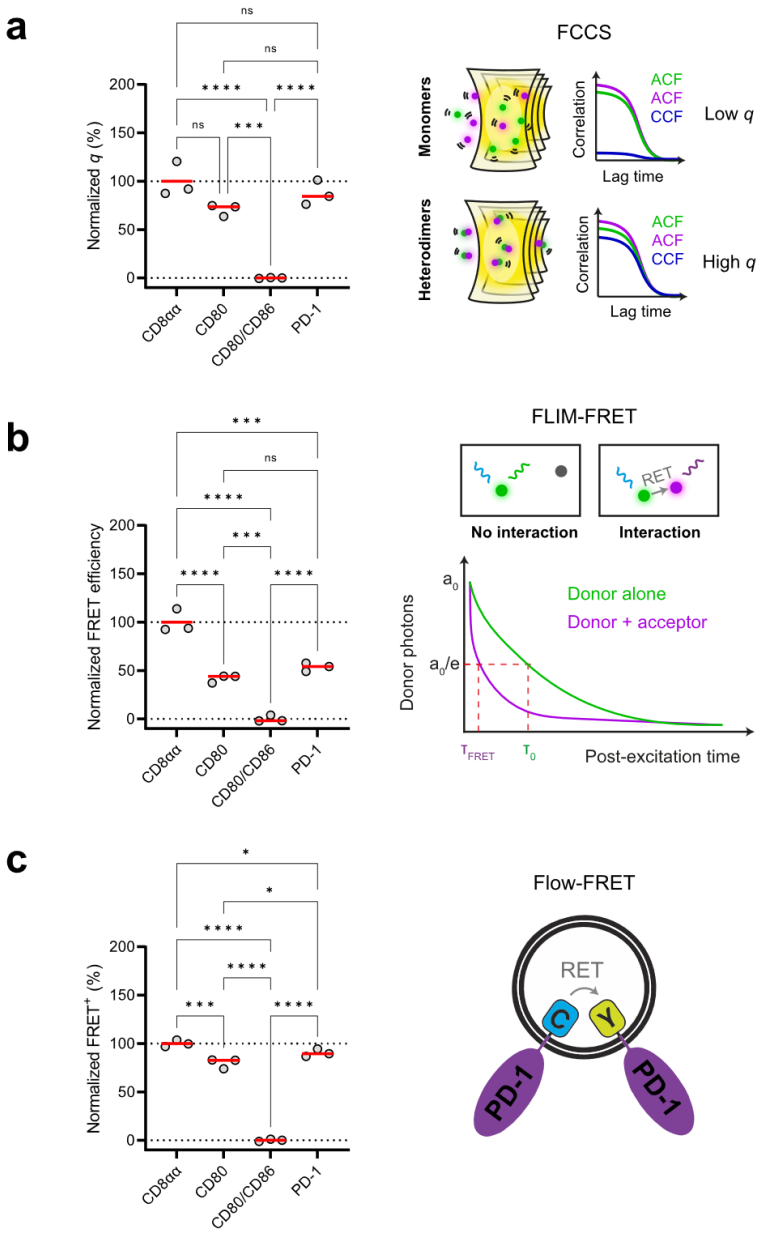


Figure 4.1 **Robust PD-1 dimerization at the cell surface. a.** sFCCS measurements in HEK293Ts expressing mEGFP- or mCherry2-tagged constructs. The *q* values were min-max normalized to the positive (CD8αα) and negative (CD80/86) control conditions. **b.** FRET efficiency between EGFP- and mCherry2-tagged constructs was calculated from fluorescence lifetime measurements in BHK cells, normalized to the same controls as in **a**. **c.** Flow-FRET measurements of CHO cells transfected with CFP- or YFP-tagged constructs, normalized as in **a**. In all panels, each circle indicates the mean readout value from one replicate measurement (*i.e.,* one day of experiments) for each condition. Significance was assessed with a one-way ANOVA and Tukey's test for multiple comparisons.

4.3.2 Transmembrane-driven dimerization

Receptor *cis* interactions can be driven through either the ectodomain or transmembrane domains, the latter being important for the formation of some RTK dimers, for example[268,269]. Since the PD-1 ectodomain lacks the ability to dimerize in solution, and the dimerization observed in cell membranes did not require the cytosolic domain, we hypothesized that PD-1 dimerization was driven exclusively by transmembrane residues. To identify these amino acids, we performed an unbiased Trp scan[270] through the 23-residue transmembrane helix under the assumption that the bulky indole group would disrupt the closely stacked interactions normally required for dimerization. To rapidly screen the effects of the mutated PD-1 residues we used a high-throughput interaction assay, TOXGREEN. This assay is a variation on the genetic dimerization assay, TOXCAT, in which a transmembrane region of interest is fused to a fragment of the prokaryotic ToxR protein and dimerization detected with a reporter gene, chloramphenicol acetyl transferase (CAT). In TOXGREEN, dimerization is assayed through superfolder (sf)GFP fluorescence and can therefore be measured efficiently in a 96-well plate format[271] (**Figure 4.2a**). The scanning mutagenesis strategy revealed that Trp substitution near the helical N-terminus reduced dimerization, but that the same substitution near the C-terminus strengthened it (**Figure 4.2b**). The ability of these constructs to dimerize was benchmarked against the transmembrane domain of a known prokaryotic dimer, glycophorin A (GpA), which can be disrupted with a single G83I point mutation[271]. These data confirmed that PD-1/PD-1 *cis* interactions could be driven by the transmembrane helix. An important corollary of the fact that mutations could either increase or decrease dimerization is that, at least when expressed in a bacterial inner membrane, PD-1 exists in a monomer/dimer equilibrium that is weighted towards dimers.

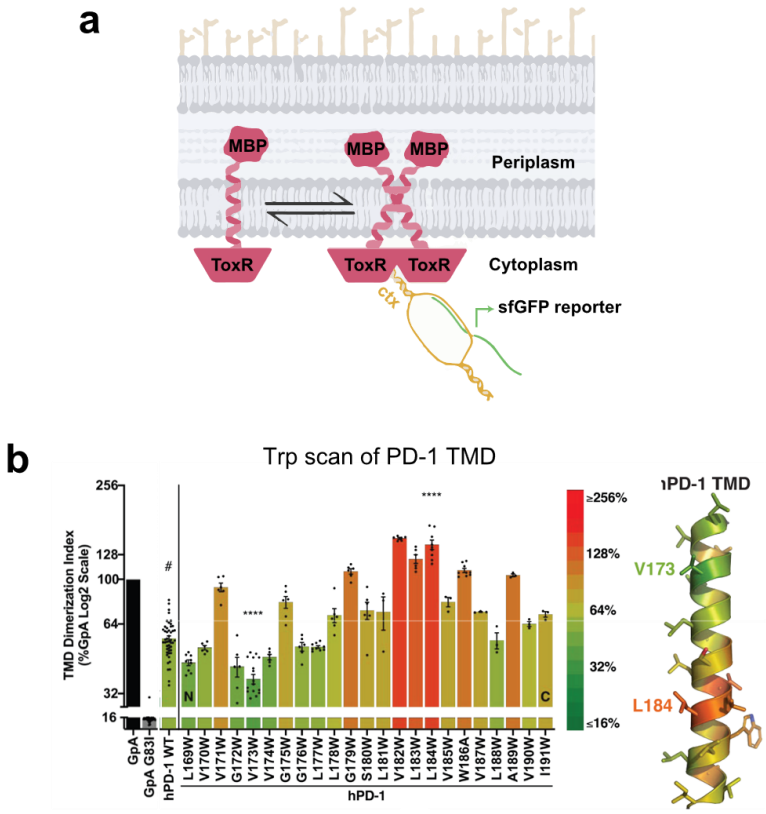


Figure 4.2 **TOXGREEN assays reveal key transmembrane domain residues that drive PD-1 dimerization. a.** Schematic of the prokaryotic TOXGREEN assay in which a transmembrane region of interest is expressed between a periplasmic maltose binding protein (MBP) and cytoplasmic ToxR domain that, upon dimerization, drives sfGFP expression via a *ctx* promoter. **b.** A systematic mutagenesis scan of the PD-1 transmembrane domain reveals two key residues that significantly increase (L184W) or decrease (V173W) dimerization when substituted with Trp. The heatmap indicates percentage change relative to the GpA control (100%). Each point indicates a measurement of one well. Significance was assessed with a one-way ANOVA compared to the WT control (#) with Tukey's test for multiple comparisons. The position of these residues at the N- or C-terminal ends of the helix are depicted in a structural representation on the right.

To validate the TOXGREEN-identified mutations in mammalian cells, we returned to sFCCS and FLIM-FRET to measure dimerization of mutant PD-1 proteins. Although mutation near the helix N-terminus (V173W) significantly reduced dimerization, similar to the results of the bacterial assay, the C-terminal mutation (L184W) did not significantly increase dimerization tendency (**Figure 4.3**). This effect could be due to the differences in composition between eukaryotic and bacterial membranes since our FCCS data suggested that PD-1 dimerized strongly in HEK293Ts, leaving L184W little room to improve upon an efficient interaction. We noted that, although PD-1 dimerization was readily detected using FLIM-FRET, it was always significantly lower than the constitutively dimerizing control CD8αα (**Figure 4.1b and Figure 4.3b**). Reasons for this discrepancy are considered in **Section 4.4.1.**

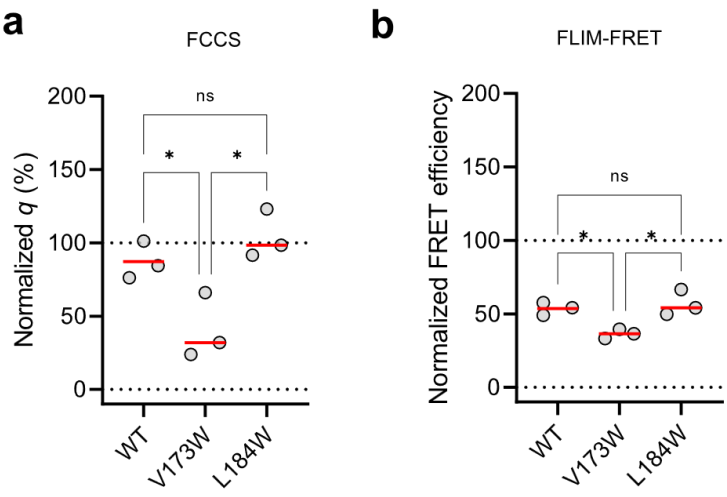


Figure 4.3 **Biophysical validation of hPD-1 mutations that modulate dimerization. a.** and **b.** FCCS measurements (**a**) or FLIM-FRET measurements (**b**) as performed in Figure 4.1 but with the point mutations identified in the TOXGREEN assay for testing in mammalian cells. Measurements were normalized to the positive (CD8αα) and negative (CD80/CD86) controls shown in **Figure 4.1**. Significance was assessed with a one-way ANOVA and Tukey's test for multiple comparisons.

4.3.3 PD-1 dimers inhibit T-cell function

To determine the effects of PD-1 dimerization on T cell signaling, we employed protein-functionalized supported lipid bilayers (SLBs) to investigate PD-1 signaling in Jurkat T cells. Sustained signaling through the TCR leads to formation of a specialized junction called the immune synapse, a radially symmetric and organized structure[272]. Synapse formation was triggered using SLBs presenting ICAM-1 and anti-CD3ε Fab (UCHT1), which is sufficient to establish a conventional synapse[273], with PD-L1 added to elicit inhibitory signals. To control receptor dimerization, CRISPR/Cas9 was used to delete endogenous *PDCD1* (forming the 2E4 line) and PD-1 expression was rescued with vectors encoding either wild-type (WT), low-dimerization (V173W) or high-dimerization (L184W) forms of the proteins (**Figure 4.4a**). TIRF imaging of Jurkats incubated on these bilayers showed that the ability of PD-1 to dimerize correlated with an increased recruitment of PD-L1 and SHP-2 to the synapse (**Figure 4.4b,c,d**). Since PD-1 signaling occurs through SHP-2 recruitment[274], this suggested that increased PD-1 dimerization would also lead to reduced phosphotyrosine levels and this was confirmed through anti-phosphotyrosine staining (**Figure 4.4b,e**). These data support a model in which transmembrane-domain driven PD-1 dimerization serves to limit T-cell function by inhibiting signaling in the synapse.

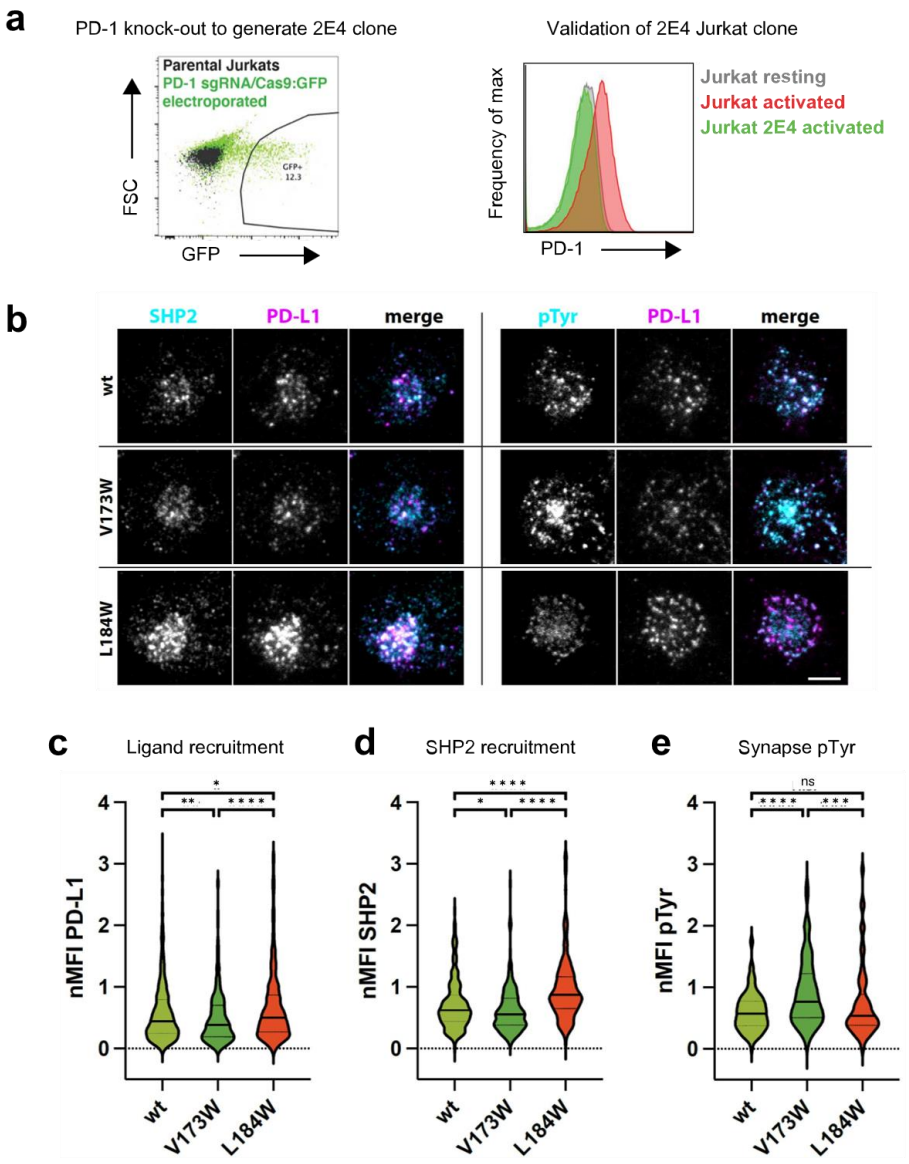


Figure 4.4 **PD-1 dimerization drives inhibitory signaling in Jurkat T cells. a.** Generation of a Jurkat clone (2E4) that lacks endogenous PD-1 using CRISPR/Cas9. Cells that received the electroporated Cas9/RNP complex were sorted on GFP positivity (left). When stimulated, Jurkat 2E4 cells are unable to upregulate PD-1 unlike the parental Jurkat E6.1 cells (right). **b.** TIRF images of T cell/SLB synapses using Jurkat 2E4 cells in which PD-1 expression was rescued with wild-type (wt) or mutant (V173W or L184W) proteins. The bilayers were decorated with ICAM-1, UCHT-1 and PD-L1 to mimic APCs. Scale bars = 5 µm. **c., d.** and **e.** An impaired ability of PD-1 to dimerize correlated with (**c**) diminished ligand recruitment, (**d**) decreased SHP-2 recruitment and (**e**) increased synaptic phosphotyrosines levels. Solid lines indicate median and dotted lines indicate quartiles. pTyr = phosphotyrosine.

To extend these findings to T-cell operation *in vivo* in models of disease, we first identified the murine equivalents of dimerization-altering mutations L184W and V173W. Using the same TOXGREEN-based Trp scan, L186W and G172W were found to cause the greatest changes in dimerization index for the transmembrane domain of mouse PD-1 (**Figure 4.5a**). In parallel, PD-1 null (PD-$1^{-/-}$) mice were bred with OT-1 transgenic mice to generate mice reactive to ovalbumin peptide (pOva) but deficient in PD-1. Then, PD-$1^{-/-}$ OT-1 $CD8^+$ T cells were isolated and retrovirally rescued with WT or mutant receptors to use for adoptive transfer experiments, allowing us to alter the dimerization capability of PD-1 *in vivo* (**Figure 4.5b**). To examine PD-1 function in the context of cancer, we used an anti-PD-1-responsive syngeneic tumor model based on B16 melanoma expressing ovalbumin (Ova)[275]. We found that mice transduced with PD-$1^{-/-}$ OT-1 cells (empty vehicle control) exhibited clear delays in tumor progression compared to the no transfer control, consistent with the strong anti-tumor activity of effector $CD8^+$ cytotoxic T lymphocytes (CTLs) that lack a critical checkpoint inhibitor (**Figure 4.5c**). Transfer of cells expressing WT PD1 molecules into the B16-Ova model confirmed that PD-1-sufficient OT-1 T cells were less effective at delaying tumor growth than PD-$1^{-/-}$ cells, in line with the inhibitory action of PD-1 signaling. We then observed that the L186W and G172W point mutations produced remarkable improvements or impairments to controlling tumor growth, respectively, compared to WT (**Figure 4.5c**), indicating that T-cell signaling *in vivo* could be modulated by the ability of PD-1 to dimerize.

Next, we attempted to determine whether the converse effect could be detected in the functional restriction of T cells when they are overly destructive—T-cell autoimmunity—using a murine model of type I diabetes (T1D), where PD-1 is important for tolerance in pancreatic islets[276]. Similar to the B16 work, we found that receptor dimerization could be linked directly to disease onset (**Figure 4.5d**). T1D was modelled in the well-established RIP-mOVA system in which mice have a membrane-bound *OVA* gene under the control of rat insulin promoter[277]. Mice that were adoptively transferred with pOva-reactive PD-$1^{-/-}$ OT-1 $CD8^+$ T cells developed rapid-onset T1D while their littermates remained disease-free, confirming the normal role T

cells in islet destruction. As expected, rescuing PD-1 expression with the WT form of the protein led to delayed-onset T1D and this effect was significantly hastened if dimerization was impaired (PD-1-G172W), similar to the PD-$1^{-/-}$ control. In contrast, the time to disease onset was significantly improved when the inhibitory signaling capacity was increased (PD-1-L186W), thus providing a direct link between PD-1 dimerization and disease control (**Figure 4.5d**). Together, our *in vivo* results confirm the established function of PD-1 as a strong antagonizer of $CD8^+$ CTL effector activity, as expected, and that normal activity levels could be fine-tuned through receptor dimerization.

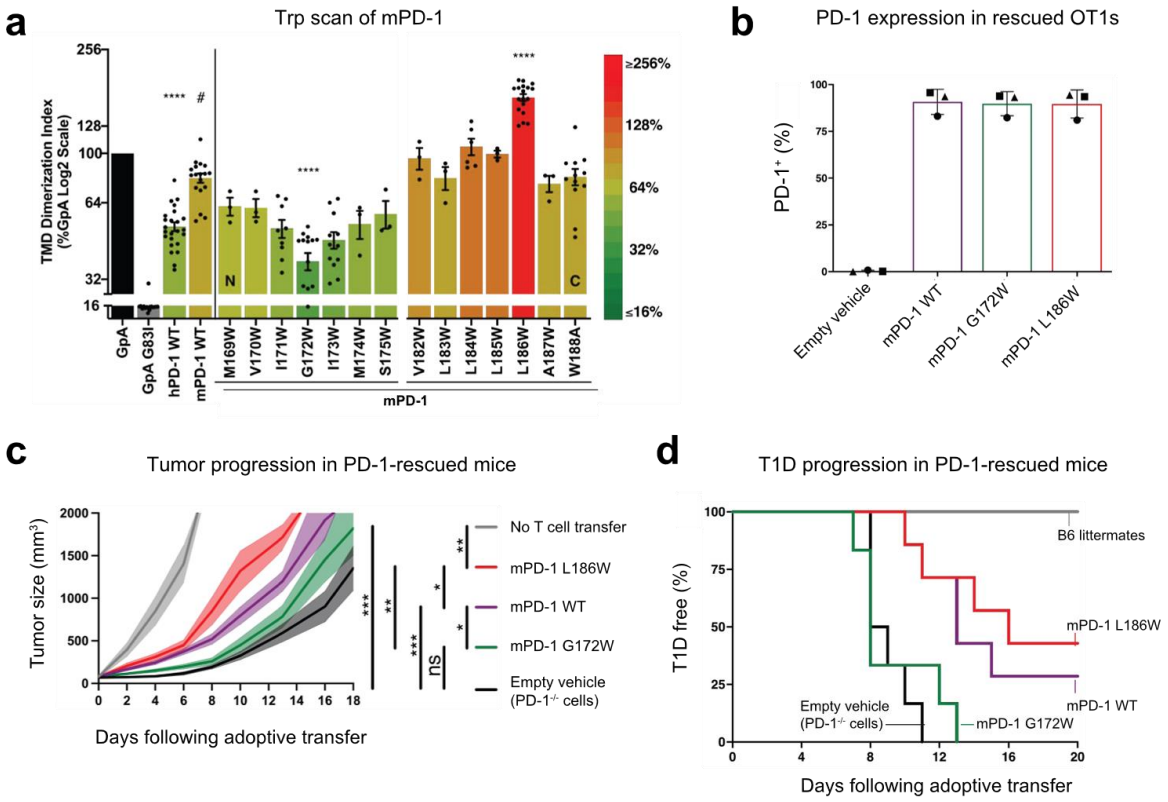


Figure 4.5 **Functional modulation of T cells in models of cancer and autoimmune disease through controlling PD-1 dimerization. a.** Trp scanning mutagenesis to reveal the murine equivalents of dimerization-altering mutations using the TOXGREEN assay (hV173W = mG172W; hL184W = mL186W). **b.** Flow cytometry analysis of PD-1$^{-/-}$ OT-1 cells retrovirally transduced either with an empty vector or WT/mutant forms of PD-1 show that PD-1 expression is restored at equivalent frequencies. Each symbol indicates a replicate measurement. **c.** Spider chart of tumor progression in the B16 melanoma model with adoptive transfer of T cells without PD-1 (black), PD-1 G172W (green), PD-1 WT (purple), PD-1 L186W (red) or no T cells (gray). The solid lines indicate cumulative tumor growth with shaded regions indicating the SEM. Significance was tested by two-way ANOVA. **c.** Kaplan-Meyer plot of diabetes-free mice in a RIP-mOVA model adoptively transferred with OT-1s as above alongside B6 littermates which remained disease free. PD-1 dimerization correlates with increased progression to T1D (*i.e.,* reduced T-cell activity due to increased PD-1 signaling).

4.4 Discussion

This chapter presents evidence that wild-type PD-1 molecules form non-covalent homodimers mediated by transmembrane interactions, and that dimerization is important for normal signaling of the receptor. The initial detection of PD-1 dimers with sFCCS was validated with two orthogonal FRET-based measurements: FLIM- and flow-FRET. A mutagenesis strategy was used to reveal that PD-1 dimerization is substantial but incomplete under normal, ligand-free conditions (*i.e.,* weighted towards dimers), and that specific mutations could be made to inhibit or promote dimerization. These mutations were then used to show how PD-1 dimerization was important for the normal function of the inhibitory receptor during synapse formation *in vitro* and functional inhibition of T cells *in vivo*, both in the inability to clear tumor burdens (B16 melanoma model) and in self-reactive disease (RIP-mOva model).

4.4.1 Biophysical techniques reveal cell-surface *cis* interactions

Because PD-1 dimerizes through non-covalent interactions buried in the membrane, previous studies aimed at determining receptor stoichiometry with conventional methods like crystallography (*i.e.,* involving truncated ectodomains)[246] or Western blots (*i.e.,* boiled in detergent)[278] indicated PD-1 was monomeric. *In situ* measurements of interactions that may be transient or unstable can be challenging, since artefacts of the labeling process or acquisition can alter the native state of protein complexes. Comparisons with multiple, orthogonal methods were therefore needed to determine the stoichiometry in its native environment. The three biophysical assays used in this chapter have complementary strengths and weaknesses, summarized in **Table 1**. For instance, the measurement time per cell is 10^6 times longer in sFCCS (~48 s) compared to flow-FRET (50 µs), providing the former with greater statistical precision per cell and the latter with much higher throughput and sampling power. Conversely, flow-FRET is sensitive to crowding effects (false-positive signals from non-interacting, coinciding fluorophores) that are not present in FLIM-FRET since lifetime

measurements are insensitive to local concentrations. FRET is also dependent on fluorophore orientation, and expression of FRET probes in biological membranes, which are intrinsically anisotropic, may lead to non-specific signals. FCCS is independent of fluorophore orientation, however, and the general agreement between all three methods provides strong evidence that PD-1 is mostly dimeric at the cell surface.

Table 1. Advantages and disadvantages of biophysical interaction assays

	FCCS	FLIM-FRET	Flow-FRET
Pros	Live cells Orientation-independent	Concentration-independent No acceptor excitation	Live cells High throughput
Cons	Slow Low throughput	Fixed cells Orientation-dependent	Orientation-dependent Crowding effects

While FRET relies on energy transfer between physically proximal fluorophores, FCCS only reports on statistically coincident signals through the cross-correlation curve and thus the two methods use different calculations to estimate the interacting fraction of proteins in the sample. As a consequence, they may not scale linearly with the fraction of heterodimers present and may be affected differently by bleaching effects (*e.g.,* in FLIM-FRET the acceptor is not excited and therefore less likely to bleach while in FCCS any bleaching of either fluorophore leads to loss of cross-correlation). To control for these differences, we included biological controls in our measurements of surface proteins known to occupy different positions on the 'dimerization spectrum': obligate CD8αα dimers exhibited both high FRET efficiency and q while co-expression of non-interacting CD80 and CD86 produced no significant FRET or q signals, indicating successful detection of receptor dimerization, at least within the experimental range covered by our controls.

We noted that, despite the general agreement between methods of significant PD-1 dimerization, FLIM-FRET reported a consistently lower dimer occupancy than either of the two

other methods. The difference compared to flow-FRET is especially unexpected as both methods rely on the same physical principle and are covalently linked to FPs in the same way, which should make the FRET distance identical. However, FLIM-FRET was the only method that required fixation of the cells and this may have impacted the readout either directly (*e.g.,* fixatives weakly stabilizing the monomeric form) or indirectly (*e.g.,* fixing PD-1 to other molecules and slightly disfavoring homodimerization).

A caveat of these experiments is that they are all performed in cell lines with truncated PD-1 proteins and it may be that physiological expression of PD-1 alters its ability to dimerize (*e.g.,* through differences in membrane composition or cytoskeletal tethering). Flow-FRET is best suited to address this problem because of the ability to label endogenously expressed proteins with external labels, extending dimerization measurements to primary cells—these efforts are currently underway. An important consideration is whether labelling moieties, like dye-conjugated Fab fragments, might interfere with the native ability of the receptors to dimerize. This may be especially disruptive to non-covalent dimers and caution is needed to ensure that labeling does not bias measurements. Since dimerization is not driven by the ectodomain this problem may be solved by testing and comparing several different site-specific (*i.e.,* epitope-mapped) labels.

4.4.2 Generalizing transmembrane-driven interactions

The result that PD-1 dimers could be detected at the cell surface between cytosolically-truncated proteins hinted at a role for the transmembrane domain in driving *cis* interactions. Two key residues in the transmembrane helix, identified by scanning Trp mutagenesis, were revealed as affecting PD-1/PD-1 interactions inside the membrane; dimerization was increased by V173/G172 and decreased by L184/L186 (residues indicated as human/mouse). It might be that the N-terminal valine/glycine residues need to be small for tight packing and

that tryptophan is disrupting the coiled-coil interaction, while the C-terminal leucine residues provide an important hydrophobic interaction which is improved by the tryptophan.

A key question going forward is whether other co-signaling proteins or their ligands dimerize at appreciable levels. Two obvious candidates are PD-L1 and PD-L2 which, like PD-1, have mainly been considered monomeric[279,280]. Although secPD-L1 contains a disulfide bond, its cysteine residue is encoded in the exon which is spliced for the transmembrane domain, indicating that the conventional membrane-bound form of PD-L1 is unable to express with an extracellular disulfide[256]. PD-L1 interacts in *cis* with other co-signaling proteins via its ectodomain[276,281], and dimerization of the ligand could explain how these heterotypic *cis* interactions work by competing for a limited pool of free (*i.e.,* monomeric) PD-L1, thus reducing binding to PD-1 in *trans*. The biophysical methods employed in this chapter will be useful to investigate dimerization that occurs only at the cell surface.

4.4.3 A new paradigm for PD-1 signaling

The functional data presented in this chapter confirm the well-documented effects of PD-1 in potently inhibiting immune responses[282,283], and further demonstrate the importance of non-covalent dimerization as part of normal PD-1 signaling in the functional inhibition of T cells. Although both the extracellular ligand-binding domain and intracellular signaling pathways of PD-1 have been extensively studied, it is uncertain how exactly signaling passes through the membrane. Our results imply that dimerization is important for enhancing the inhibitory effect of PD-1 signaling, but this could either be at the ligand-binding stage (*e.g.,* increased avidity for PD-L1) or at the signal transduction stage (*e.g.,* altered binding to SHP-2). The latter scenario is supported by a recent report describing the formation of PD-1 dimers through the tandem SH2 domain of SHP-2, which act to ‘fasten’ two receptor molecules together through their ITSM domains[284]. Constitutive PD-1 dimerization likely enhances signaling by increasing the avidity for the bidentate binding of a SHP-2 to PD-1 molecules at the surface.

The ability of the transmembrane helix to modulate the PD-1 signaling threshold may prove useful in fine-tuning signaling in therapeutic receptors engineered to treat disease, like chimeric antigen receptors (CARs). Although increasingly complex CARs have been generated to improve the efficacy of treatments, the CAR transmembrane domain remains the least studied part of the recombinant receptor[285]. Manipulating CAR sensitivity through transmembrane domain-mediated oligomerization could provide an additional regulatory mechanism independent of the extracellular single-chain variable fragment (scFv) domain or intracellular signaling motifs. The therapeutic value of controlling PD-1 signaling through manipulating *cis* interactions has been described before[286] and our results provide a clear and testable mechanism of doing this to modulate T-cell activity in humans, potentially enhancing cancer immunotherapy or alleviating autoimmune disease.

5. Reconsidering the kinase occupancy of T-cell coreceptors

5.1 Introduction

CD4 and CD8 coreceptors

CD4 and CD8 are IgSF (immunoglobulin superfamily) proteins expressed primarily by cells of the helper and cytotoxic T-cell lineages, respectively, and assist the (T cell receptor) TCR in recognizing weak agonistic ligands[140]. Both coreceptors are typical type I transmembrane proteins that consist of an major histocompatibility complex (MHC)-binding ectodomain (CD4 to class II; CD8 to class I) connected directly to the transmembrane helix which is followed by a short cytoplasmic tail without inherent structure[287]. This flexible C-terminus contains the dicysteine sequence that interacts with Lck[288,289], a motif unique to these proteins. CD4 and CD8 have few structural similarities, however, suggesting that in order to function they need simply to bind MHC proteins and to associate stably with cytoplasmic Lck. CD4 is a monomer comprising four V- and C-set IgSF domains whereas CD8 is an obligate heterodimer of α and β subunits each with a single V-set IgSF domain perched on top of a long and heavily O-glycosylated 'stalk' that connects to the plasma membrane[290]. CD8 can also exist as a homodimer of α subunits but this form of protein binds less Lck[291] and cannot substitute for CD8αβ[292] suggesting it does not function as a T-cell coreceptor *in vivo*.

Both coreceptors bind to their MHC ligands with affinities that are extraordinarily low compared to the typical range for leukocyte surface proteins[293]. CD8αβ and CD8αα bind to MHC-I with a 3D dissociation constant (K_D) of 100-200 μM[294,295]. The 3D K_D for CD4 binding to MHC-II is unknown; surface plasmon resonance (SPR) measurements have thus far failed to reveal the binding constant between soluble forms of these proteins suggesting a lower limit

of 2.5 mM[296]. The 2D K_D for the CD4-MHC class II interaction can be measured in contacts established by the CD2-CD48 adhesion system[297]. Based on the 2D K_D and the estimated confinement length, the interaction has an approximate 3D K_D of 5.1 mM, or one of the weakest specific protein/protein interactions measured to date, at least for receptor/ligand binding[298]. The relevance of such weak binding in antigen recognition and discrimination is one reason why the mechanism of coreceptor-mediated signal amplification has been intensely debated[140].

Lck ($p56^{Lck}$) kinase

Lck was first identified as an overexpressed Src-family kinase in a retrovirally-induced murine T-cell leukemia under the names 'lymphocyte specific kinase' (lsk)[299] and 'T-cell kinase' (tck)[300] which were merged to Lck shortly thereafter[301]. It is comprised of five regions: an N-terminal SH4 domain which tethers Lck to the plasma membrane through lipid modifications[302], a coreceptor-binding Zn^{2+} clasp motif[303], an SH3 domain which binds proline-rich sequences, an SH2 domain which binds phosphotyrosines, and a C-terminal kinase domain. The canonical view of Lck regulation is that the phosphorylation states of two key tyrosine residues, Y394 (activatory) and Y505 (inhibitory), control the catalytic activity of the enzyme; Lck would therefore be least active in the $Lck^{Y394/pY505}$ form, most active in the $Lck^{pY394/Y505}$ form and 'primed' in any of the intermediary states[304]. Y394 can be auto-phosphorylated and is therefore not thought to play a major role in kinase activation[305]. However, Y505 is primarily dephosphorylated by CD45, a large transmembrane phosphatase originally described as a negative regulator of TCR signaling because it dephosphorylates TCR immunoreceptor tyrosine-based activation motifs (ITAMs)[306]. CD45 has therefore been ascribed both a positive and negative regulatory role in the initiation of TCR signaling[307,308]. The solution to this paradox is probably explained mainly by the substrate affinity of the phosphatase, since CD45 has a 20-fold higher activity for CD3-ITAMs than Lck-Y505 (ref.[309]).

Coreceptor/Lck interactions

The interactions of CD4 and CD8 with Lck are significantly stronger than their interactions with MHC proteins, with solution dissociation constants of 400 and 800 nM, respectively[310]. The first efforts to quantify the amount of Lck that coreceptors were coupled to (referred to hereafter as occupancy) were mainly focused on CD4, being monomeric and existing only in one form. *In vitro* pulldowns suggested that CD4/Lck occupancy was high (~90%) in mature T cells[311] but lower in thymocytes (25-50%)[312]. Recently, however, claims have emerged that these early reports had underestimated occupancy[313,314]. Using a new variant of immunoprecipitation (IP), called flow cytometric co-IP (FC-IP; see **Section 1.3.1**), these studies suggest CD4/Lck occupancy is very low both in thymocytes (6%-17%)[314,315] and mature T cells (37%)[315]. Thus, a definitive answer to coreceptor/Lck occupancy remains elusive and requires calibrated measurements to be made in the native context at which these proteins are normally expressed *i.e.,* at the mammalian plasma membrane.

5.2 Methods

Co-immunoprecipitation (co-IP)

Carboxylate-modified latex (CML) beads were conjugated to anti-mCD4 (clone RM4-4, BioLegend) or anti-mCD8β (clone 53-5.8, BioLegend) according to published protocols[316]. Thymocytes were isolated from 6-week-old wild-type B6 mice using a 70 µm cell strainer (BD Biosciences), and for each condition 10^7 thymocytes were lysed in 50 µl of lysis buffer (1% NP-40S, 50 mM Tris pH 7.4, 150 mM NaCl, Protease Inhibitor Cocktail (Sigma-Aldrich)) for 30 minutes at 4°C. For Zn^{2+} chelation, cells were either pre-treated with 5 mM TPEN for 15 minutes or 5 mM EDTA was added to the lysis buffer. Lysates were then incubated with 75,000 antibody-conjugated CML beads for 3 hours at 4°C on a vertical rotating wheel. Beads were washed 5x by pelleting and resuspending in lysis buffer (200 µl) before staining with PE-conjugated antibodies against either Lck (3A5, SCBT, F/P = 1.29), mCD4 (H129.19,

BioLegend, F/P = 1.04), mCD8α (53-6.7, BioLegend, F/P = 1.36) or rat CD48 as a negative control (OX45, BioLegend) for 40 minutes at 2 µg/ml at 4°C. Residual bead fluorescence after washing was measured by flow cytometry and geometric mean fluorescence intensities (geometric mean fluorescence intensities; gMFIs) determined using FlowJo. Occupancy was determined as the ratio of background-subtracted Lck gMFI to coreceptor gMFI adjusted for F/P ratios.

Genetic engineering of Jurkat E6.1 cells

CRISPR-Cas9 was used to ablate the expression of human (h) TCR, CD4 and Lck from Jurkat T cells. Guides for the hTCRα, hTCRβ and hCD4 were designed as previously described[317]. For hLck, guides were designed and selected for high specificity with minimal off target activity using Benchling (hg38 reference genome). Complementary oligonucleotides with appropriate overhangs were annealed and ligated into the LentiCRISPRv2 plasmid (Addgene #52961) using the dual BsmBI restriction sites[318]. Guides used are indicated in **Table 2**. Lentiviruses were produced by combining the transfer plasmid (pHR) with packaging plasmids (pMDG-VSVG and pCMV-dR8.91) into human embryonic kidney 293T (HEK293T) cells using GeneJuice® (Novagen) as described before[319]. After three days, the supernatant was 0.45 µm-filtered and added directly to 10^6 Jurkat cells. Negative selection was applied with 1 µg/ml puromycin (Sigma-Aldrich) for seven days and protein expression examined using flow cytometry.

Table 2. CRISPR guides for gene ablation in Jurkat cells.

Target gene	gRNA sequence
hTCRα (TRAV8-4*01)	GTTGCACCTCAGCAGAACCA
hTCRβ (TRBV12-3*01)	TATCCAGTCACCCCGCCATG
hCD4	GGCAAGGCCACAATGAACCG
hLck	CCATTATCCCATAGTCCCAC

mCD4 and mLck were stably expressed in Jurkat$^{hCD4/hLck-}$ cells using lentiviral gene delivery. mCD4 cDNA was obtained by PCR amplification of a splenic cDNA library provided by M. Vuong (Davis lab) and mLck cDNA was a gift from J. Pettman (Davis lab). For mLck^{CS}, the C20S and C23S mutations were incorporated into a long 5' primer. All inserts were then subcloned into the pHR-SIN lentivirus transfer plasmid backbone and verified by sequencing (Source Bioscience).

Approximating CD4 and Lck expression levels

Physiological surface densities of CD4 and Lck were approximated by converting absolute expression levels (molecules/cell) reported elsewhere. These values were obtained and averaged from studies using fluorescent beads[314,320–322], Western blots[323,324] or tandem mass spectrometry[325,326]. The average lymphocyte cell surface area (≈ 565 μm^2) was calculated assuming a 5 μm spherical radius and multiplied by a correction factor of 1.8 to account for surface roughness ($A = 4\pi \times r^2 \times 1.8$)[327,328]. This gave average surface densities of ~380 molecules/μm^2 for CD4 and ~630 molecules/μm^2 for Lck. The latter assumes that all Lck is surface-bound and is therefore an upper estimate.

Ca^{2+} release assay

For calcium-triggering experiments, CultureWell 50-well silicon covers (Grace Bio-Labs) were cut and placed on piranha and plasma cleaned coverslips (25 mm, thickness no. 1.5; VWR). A 98:2 mixture of POPC (1-palmitoyl-2-oleoyl-sn-glycero-3-phosphocholine)-DGS-NTA(1,2-dioleoyl-sn-glycero-3-[(N-(5-amino-1-carboxypentyl)iminodiacetic acid)succinyl])-Ni^{2+} vesicles was added to each well at a final concentration of 0.5 mg/ml (10 μl) and left for 1 hour at room temperature. Wells were washed by removing and adding 5 μl PBS five times before adding CD58 and UCHT1 Fab. Then, 5×10^5 Jurkat^{TCR+} or Jurkat^{TCR-} cells were resuspended in 100 μl of supplement-free RPMI with 25 μg/ml of Fluo-4 dye and incubated at 37°C for 10 minutes.

Cells and SLBs were washed in complete R10 medium pre-warmed to 37°C immediately before use. Cells were washed twice and SLBs were washed ten times by adding and removing 5 µl complete R10 medium. Cells were gently dropped onto the SLB and imaged every second for 10 minutes using a 10x magnification objective to simultaneously acquire 10^2-10^3 cells. Fluo-4 was excited using an argon 488 nm laser. Calcium imaging was performed on a Zeiss LSM880 inverted confocal scanning microscope. Cells were analyzed using a custom MATLAB code, as described before[329].

5.3 Results

5.3.1 Biochemical measurements of coreceptor/Lck occupancy

There is little disagreement between reported values of coreceptor/Lck occupancies measured using co-IP (**Figure 5.1a**). Co-IPs are conventionally performed in buffers that contain chelating agents, such as ethylenediaminetetraacetic acid (EDTA), to inhibit metalloprotease activity[330]. However, EDTA is also known to disrupt Zn^{2+}-dependent coreceptor/Lck association[331] and we hypothesized that this might lead to underestimation of occupancy which could explain some of the disagreements between past reports. To test this idea, we attempted to replicate the findings of Stepanek *et al.* using bulk thymocytes in place of sorted DP thymocytes[314]. Because the vast majority (>80%) of thymocytes are double-positive (DP)[332], we expected this assay to yield low occupancies for CD4/Lck (*i.e.,* 6-17%) as reported before[314,315]. Instead, we found that CD4 was effectively saturated with kinase with the addition of EDTA having no effect, implying that the detergent-solubilized CD4/Lck micelles were resistant to Zn^{2+} chelation under these conditions (**Figure 5.1b**). Pre-treatment of cells with millimolar amounts of a membrane-permeable Zn^{2+} chelator, *N*,*N*,*N′*,*N′*-tetrakis(2-pyridinylmethyl)-1,2-ethanediamine (TPEN), which disrupts the CD4/Lck interaction *in vitro*[333,334], reduced the occupancy by ~40%. A similar effect was seen for the substantial occupation of CD8αβ by Lck (~55%) in the untreated condition which was reduced in the

presence of TPEN treatment of live cells, but not EDTA treatment of lysates (**Figure 5.1b**). This confirmed that sequestering Zn^{2+} *in situ* could disrupt the coreceptor/Lck clasp, but the residual association of precipitated proteins suggested either incomplete Zn^{2+} chelation by TPEN or the Zn^{2+}-independent association of coreceptors and Lck captured in detergent micelles during lysis.

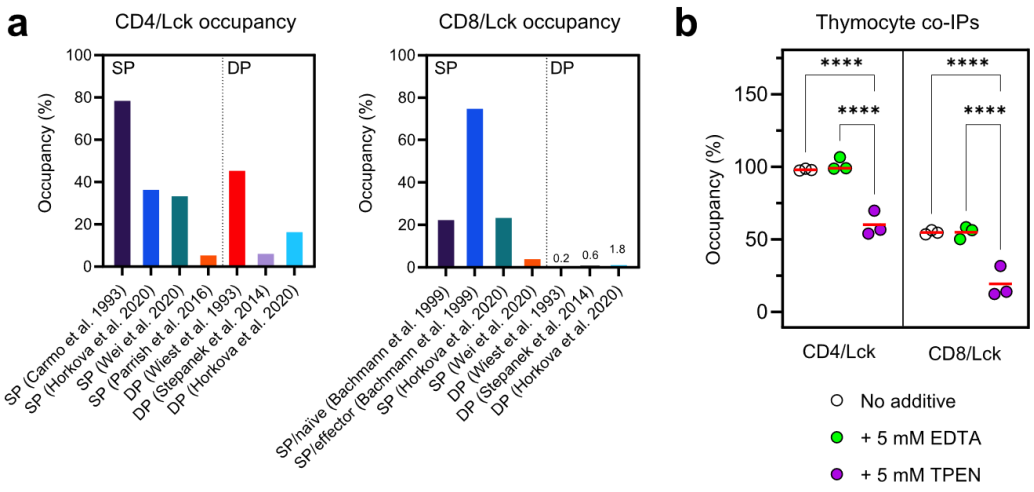


Figure 5.1 **CD4/Lck and CD8/Lck occupancies in SP and DP cells in the thymus and periphery. a.** Literature values of coreceptor/Lck occupancies in both SP T cells (left columns) and DP (right columns) thymocytes for both CD4 and CD8αβ[311,312,314,315,335–337]. All instances of SP measurements are from peripheral naïve T cells with the exception of Bachmann *et al.* 1999 which distinguished naïve T cells from effector T cells generated 7 days post-infection in an LCMV model. **b.** FC-IP measurements of coreceptor/Lck occupancies in bulk (unsorted) thymocytes reveal that CD4 is saturated with Lck while CD8αβ/Lck occupancy is ~55%. Both complexes are partially sensitive to Zn^{2+} chelation with TPEN (membrane-permeable) but not EDTA (membrane-impermeable). Each circle indicates a mean value from one mouse. Significance was assessed with a one-way ANOVA using Tukey's test for multiple comparisons. SP = single-positive, DP = double-positive, LCMV = lymphocytic choriomeningitis virus.

To determine if the partially dissociated complexes were the result of non-specific interactions, we used a lentiviral CRISPR and gene delivery system to replace endogenous hCD4 and hLck proteins in Jurkat T cells with mCD4 and mLck (**Figure 5.2a**). This provided an easily expandable cell line for performing FC-IP measurements with the same reagents as for the original experiments with primary murine cells. Similarly, we observed a high CD4/Lck occupancy for the wild-type interaction irrespective of EDTA treatment but TPEN substantially dissociated the complex (**Figure 5.2b**). To confirm whether this assay was sensitive to the complete dissolution of the CD4/Lck clasp, we expressed a clasp-defective version of Lck with the two clasp cysteines mutated to serine ($Lck^{C20S,C23S}$ or simply Lck^{CS}) and found that no Lck precipitated, consistent with previous data showing that the clasp is essential for coreceptor binding[338]. Although TPEN was only partially chelating Zn^{2+} in this assay, our results indicated that the high occupancies observed in thymocytes were not an artefact of the *in vitro* solubilization method. However, contrary to our expectations, the recent reports of low coreceptor occupancies cannot be explained by the presence of EDTA, motivating the use of biophysical methods to characterize coreceptor/Lck *cis* binding without having to grapple with potential solubilization and lysis artefacts.

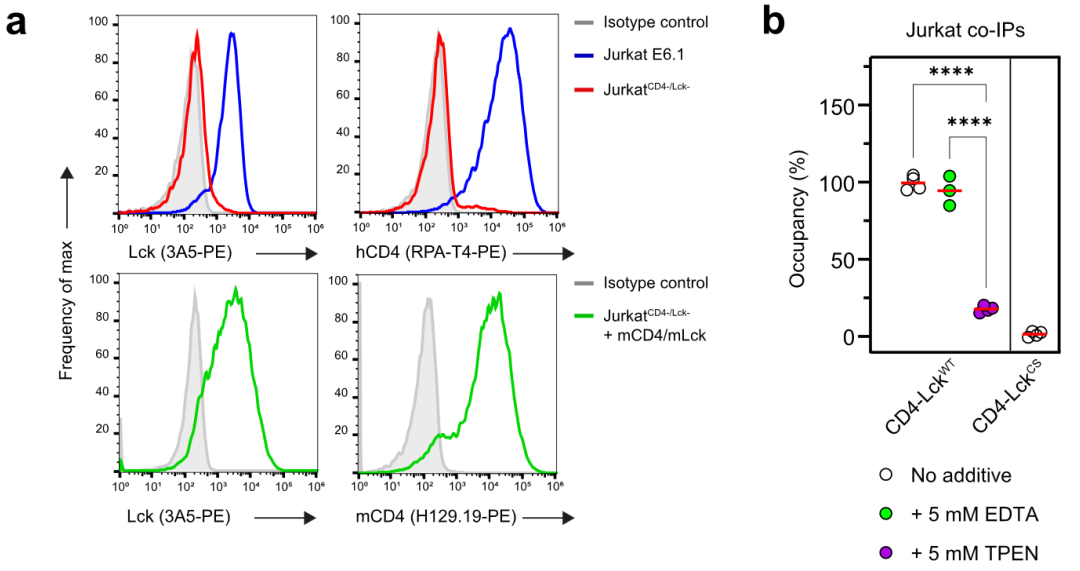


Figure 5.2 **CD4/Lck occupancy in Jurkat CD4⁺ T cells measured with FC-IP**. **a.** Creation of a polyclonal cell line of Jurkat T cells in which endogenous hCD4/hLck genes were deleted with CRISPR-Cas9 (top plots) and replaced with mCD4/mLck (bottom plots). **b.** FC-IP measurements of the murine-engineered Jurkat cells using the same reagents (*i.e.,* the same stock of beads and antibodies) showing saturating levels of CD4/Lck that are sensitive to TPEN but not EDTA. A mutant Lck protein with a deficient Zn^{2+}-binding clasp (Lck^{CS}) shows a complete loss of Lck co-precipitation in the pulldown, indicating that the assay is specific. Each circle indicates a replicate experiment. Significance was assessed with a one-way ANOVA using Tukey's test for multiple comparisons.

5.3.2 Analysis of CD4/Lck occupancy in live cells

The best prior estimate of *in situ* CD4/Lck occupancy comes from a biophysical study of the valency of TCR triggering components[339]. In this report, CD4 oligomerization (likely weak dimerization) observed when the coreceptor is expressed alone was abolished completely either when: 1) the intracellular domain of CD4 is deleted or 2) Lck is co-transfected with CD4. This implies that it is the CD4 clasp which mediates weak homodimerization and, when Lck is present, the coreceptor is invariably saturated with kinase making it entirely monomeric at the cell surface. However, absolute measurements of occupancy have been challenging to determine because of the inherent difficulty of calibrating live-cell experiments, and models of TCR triggering that incorporate these molecules have therefore relied on assumptions like: only coreceptor-bound Lck is relevant to triggering[340], coreceptor/Lck interactions are saturated in the relevant timeframe[341] or that co-IP studies reflect the *in vivo* stoichiometries[314].

To perform precise measurements of CD4/Lck occupancy, we used scanning fluorescence cross-correlation spectroscopy (sFCCS) to monitor the co-diffusion of coreceptors with Lck molecules at the plasma membrane. Full-length human CD4 and Lck constructs were expressed with mCherry2 and mEGFP, respectively, in HEK293T cells for sFCCS analysis (**Figure 5.3a**). Additionally, we generated several control conditions to ensure that our measurements were specific to coreceptor/Lck binding. First, CD4 was co-expressed Lck^{CS}, in which the clasp cysteines are mutated to serine to abolish the interaction[342], hypothesizing that this would control for clasp-independent association of Lck with CD4 (as suggested before[343]). Second, Lck was swapped for Fyn, a Src-family kinase that is structurally similar to Lck and phosphorylates many of the same substrates[344] but cannot interact with coreceptors[345]. The purpose of this control was to ensure that CD4 did not associate non-specifically with membrane-anchored kinases in, for example, GPI-enriched lipid domains[346]. Third, Lck^{CS} was co-expressed in both colors. These constructs would have intact and identical lipid modifications and would control for non-specific association of proteins in membrane microdomains[347], although the existence of such compartments remains

controversial[348]. To determine whether all proteins expressed at physiologically relevant levels, we used the calibrated size of the confocal volume to determine fluorophore density and found it similar to the normal densities of CD4 and Lck (**Figure 5.3b**; see **Section 5.2** for details of this estimation).

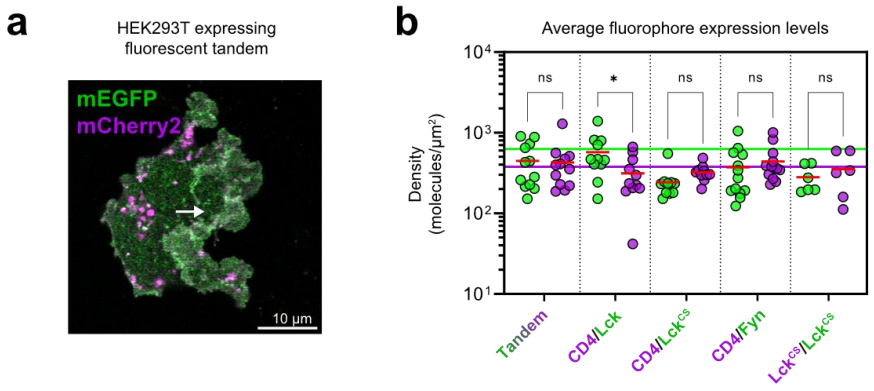


Figure 5.3 **sFCCS measurements of CD4-mCherry2 and Lck-mEGFP in HEK293T cells. a.** Exemplary confocal LSM image of a HEK293T cell expressing a tandem mEGFP-mCherry2 fluorescent protein (FP) construct linked to the membrane acquired in photon-counting mode. The white line indicates a typical position of a line-scanning measurement in a flat, homogenous area of the cell with equivalent fluorescence in both channels. **b.** Fluorophore density measurements of constructs used for this chapter with the faint solid lines indicating the approximate native expression density of CD4 (purple) and Lck (green) on T cells, see **Section 5.2**. All constructs expressed at physiological levels, although the efficiency of Lck expression was affected by its ability to bind CD4. Significance within conditions (*i.e.,* mEGFP vs. mCherry2 only) was assessed with a one-way ANOVA using Tukey's test for multiple comparisons.

To obtain occupancies, we then calculated the cross-correlation quotient (*q*) and normalized it to the tandem control to compensate for differences in fluorophore properties (folding, maturation, bleaching, *etc.*). CD4 bound wild-type Lck with a very high *q* value (96% ± 8%), indicating that essentially all CD4 was co-diffusing with Lck (**Figure 5.4a,b**). To rule out effects of non-specific association, we compared *q* to the negative controls but found that none of these conditions produced detectable cross-correlation. This confirmed that the high CD4/Lck occupancy was wholly dependent on an intact Zn^{2+} clasp structure formed between the coreceptor and the kinase (**Figure 5.4b**).

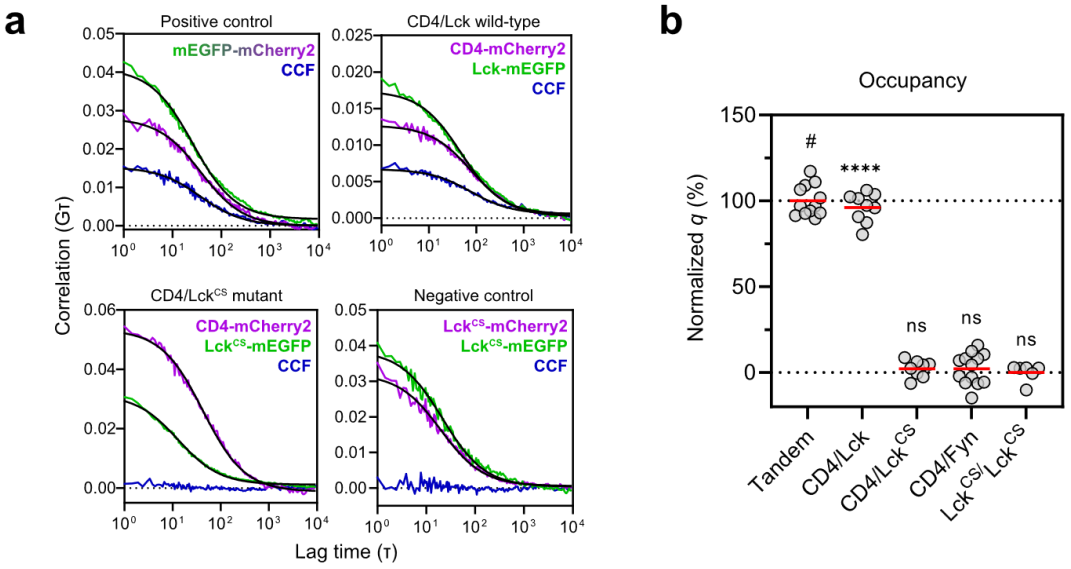


Figure 5.4 **CD4 and Lck co-diffuse stoichiometrically in a Zn^{2+}-clasp-dependent manner at the surface of live cells. a.** Representative line-averaged ACFs and CCFs from a single cell from wild-type (CD4/Lck), mutant (CD4/Lck^{CS}), positive control (tandem mEGFP-mCherry2) and negative control (Lck^{CS}/Lck^{CS}) conditions. The high CCF amplitude of the wild-type CD4/Lck condition is equivalent to the co-diffusion in the positive control. **b.** Quantification of the co-diffusion min-max normalized to the positive (100% co-diffusion) and negative (0% co-diffusion) controls. Each circle indicates a spatially averaged CCF/ACF ratio from one cell, with measurements pooled from triplicate transfections. Significance was assessed with a one-way ANOVA using Tukey's test for multiple comparisons to the tandem control (#). ACF = auto-correlation function, CCF = cross-correlation function.

Lipid-anchored proteins like Lck diffuse faster than fully embedded transmembrane proteins, according to classical models of biological membrane diffusion[349,350]. The high CD4/Lck occupancy predicts that bound Lck would move significantly slower than free Lck by virtue of being attached to the membrane via the coreceptor. To test this, we used sFCCS to determine the diffusion coefficients of CD4/Lck, CD4/Lck^{CS}, and CD4 or Lck expressed alone (**Figure 5.5a,b**). When co-expressed, CD4 and wild-type Lck exhibited similar diffusion coefficients (Lck = 0.29 ± 0.05 μm^2/s, CD4 = 0.21 ± 0.05 μm^2/s), which increased significantly upon mutation of the Lck clasp (Lck^{CS} = 0.97 ± 0.29 μm^2/s, CD4 = 0.33 ± 0.07 μm^2/s), indicating that disrupting the interaction increased the diffusion rates of both CD4 and Lck. In the case of CD4, this diffusion was comparable to when the protein was expressed alone (0.39 ± 0.11 μm^2/s) (**Figure 5.5b**). When Lck was expressed alone its diffusion speed was significantly reduced compared to Lck^{CS} (0.64 ± 0.15 μm^2/s), possibly because of Lck homodimerization through the clasp as others have suggested previously[351] (**Figure 5.5a**). Our diffusion coefficients are within a similar range to those reported previously using other methods (0.52 μm^2/s for CD4-eGFP, 1.16 μm^2/s for Lck-PAmCherry)[352,353]. Differences between the diffusion values may be attributed to the sampling issues of performing FCS in heterogeneous and undulating plasma membranes[354–356]. In summary, the changes in diffusion determined with sFCCS support the conclusion that the bulk of CD4 molecules co-diffuse with Lck in the steady state.

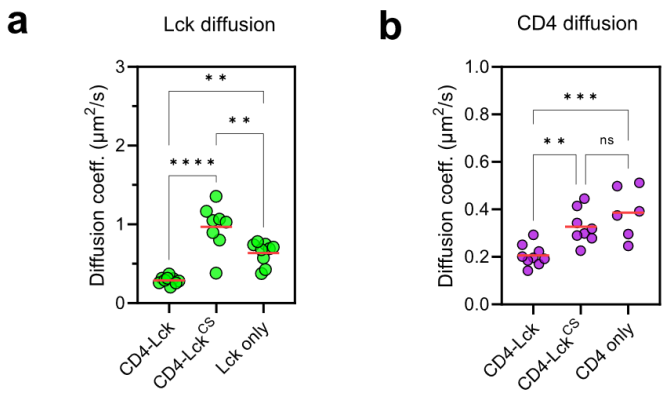


Figure 5.5 **Increases in diffusion speed on CD4/Lck dissociation.** Diffusion coefficients of Lck (**a**) and CD4 (**b**) when co-expressed as wild-type proteins (CD4/Lck), as a mutant pair (CD4/Lck^{CS}) and when expressed alone. For both CD4 and Lck, diffusion speed increases significantly upon disruption of the Zn^{2+} clasp comparable, in the case of CD4, to when the protein diffuses alone. When Lck was expressed alone it diffused significantly slower than Lck^{CS}, suggesting that the kinase was being slowed through weak clasp-dependent homodimerization. Significance was assessed with a one-way ANOVA using Tukey's test for multiple comparisons.

5.3.3 The CD4 amphipathic helix contributes to Lck association

Early mutagenesis studies that introduced systematic mutations or truncations into the C-terminus of CD4 suggested that there might be additional elements in the cytosolic region of the coreceptor which contribute to binding Lck[342,357,358]. The most significant of these motifs was a stretch of residues from Arg406 to Ser415 with hydrophobic amino acids positioned at every 3-4 residues interspersed by polar/neutral residues, the deletion of which results in an almost complete loss of Lck association[359]. This alternating hydrophobic-polar/neutral repeat is characteristic of an amphipathic α-helix where one side is positively charged and the other is hydrophobic[360]. In 2003, the structure of this amphipathic helix was determined by nuclear magnetic resonance (NMR), revealing how it packs together with a similar but much shorter helix in Lck to form a hydrophobic core 'nested' above the bound Zn^{2+} ion tetrahedrally coordinated by four cysteine residues (two from each molecule)[361]. Although the original experiments appeared to suggest a major role for this amphipathic helix in CD4/Lck binding, the deletion of the residues encoding the helix would also result in a truncated protein where the clasp-binding CQCP motif is shifted up towards the membrane. To distinguish the contribution of the helix itself from displacement of the clasp cysteines, we created a mutant CD4 construct in which the residues encoding the amphipathic helix were mutated to $(Gly\text{-}Ser)_n$ repeat of equivalent length (CD4Δhelix), replacing the secondary structure element with a flexible linker (**Figure 5.6a**). We also generated several control conditions in which the palmitoylation sites (CD4Δpalm), the membrane-proximal basic-rich region (BRR; CD4Δbrr), or the flexible C-terminal 'tail' (CD4Δtail) were converted to GS linkers. Both CD4 palmitoylation and the BRR are proposed to target the coreceptor to ordered lipid domains but have no involvement in binding to Lck[362,363] while the role of the flexible, unstructured C-terminus in associating with Lck is disputed[342,359,364]. Finally, as a negative control, we converted the clasp cysteines to serines ($CD4^{CS}$) to abolish binding entirely[365]. All of these mutant constructs were then expressed alongside wild-type Lck in HEK293T cells, as before (**Figure 5.6b**). As expected, CD4Δpalm and CD4Δbrr constructs showed no deficiency in their

ability to bind Lck compared to wild-type, and conversely, $CD4^{CS}$ exhibited no detectable co-diffusion with Lck (**Figure 5.6c**). However, mutation of the amphipathic helix produced a remarkable drop (27%) in kinase occupancy and a double BRR-helix mutant (CD4ΔbrrΔhelix) yielded similar results (28%), indicating that the α-helix specifically contributes to almost a third of the ability of the coreceptor to maintain a high CD4/Lck occupancy. Finally, mutation of the flexible tail produced a small (14%) decrease in occupancy (**Figure 5.6c**). This disordered C-terminus is absent from the CD4/Lck NMR structure but may be involved in stabilizing the clasp by interacting with proximal elements of Lck.

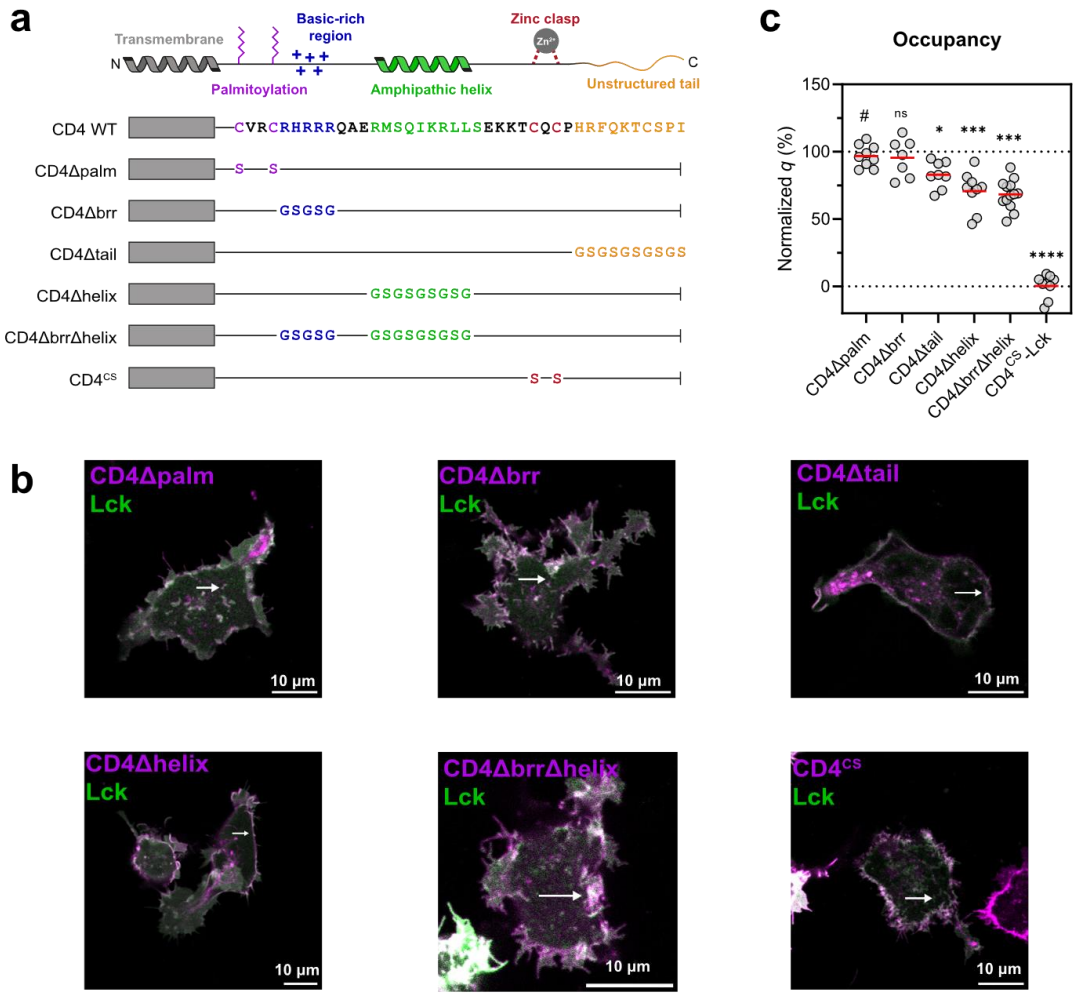


Figure 5.6 **A panel of CD4 mutants to probe secondary structure elements in the CD4 ICD in associating with Lck. a.** Sequences and mutations of the CD4 mutants used for these experiments, in which one or more regions of interest (indicated in color) as replaced with flexible GS linkers of equivalent length. **b.** Exemplary confocal LSM micrographs of HEK293T cells expressing each of the CD4 constructs (mCherry2) with Lck (mEGFP). The white arrow indicates the approximate position of a line-scan recorded on each cell. **c.** Occupancy measurements determined by sFCCS for each of the CD4 mutants and wild-type Lck-mEGFP, normalized to controls in the same manner as **Figure 5.4**. Each circle indicates an averaged ratio from one cell. Significance was assessed with a one-way ANOVA using Tukey's test for multiple comparisons. LSM = laser-scanning microscope.

To confirm that effects on occupancy were not due to inadvertent effects on mobility or expression of these constructs, we used sFCCS to check the diffusion speed and density across conditions. None of the CD4 constructs diffused significantly faster than CD4Δpalm, except when Lck-binding was abolished in the $CD4^{CS}$ condition (**Figure 5.7a**), as expected from similar experiments in **Figure 5.5**. In addition, each construct expressed at levels similar to wild-type (dotted line), demonstrating no changes in expression efficiency (**Figure 5.7b**). Overall, these results demonstrate that the Zn^{2+} clasp is necessary but insufficient for the formation of high-occupancy CD4/Lck complexes, requiring the amphipathic α-helix for fully stoichiometric binding. The significance of the finding that mutation of the clasp but not the helix is unable to bind any Lck is revisited later, in **Section 5.4.2**.

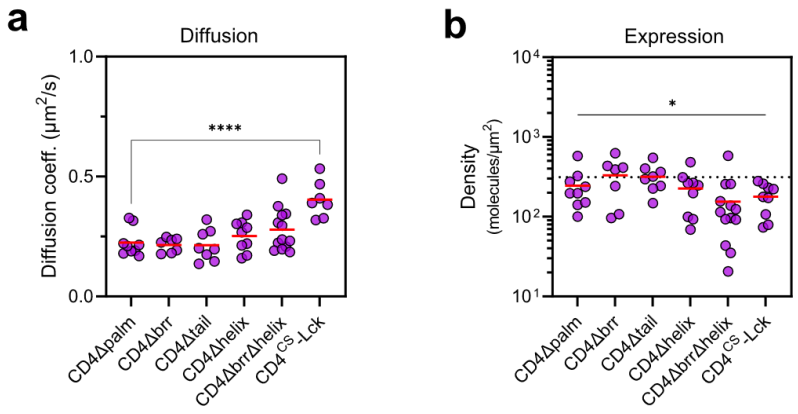


Figure 5.7 **Mutation of the CD4 intracellular domains did not substantially alter protein diffusion or surface density. a.** Diffusion coefficients for the mutant CD4 constructs were not significantly different from the CD4Δpalm control except for $CD4^{CS}$, which diffused much faster due to the loss of Lck-binding. **b.** Surface expression levels of the fluorescent proteins were not significantly different across conditions. Each circle indicates a spatially averaged measurement from one cell. Significance was assessed with a one-way ANOVA using Tukey's test for multiple comparisons. Only the significant comparison in (**a**) is shown, while in (**b**) none of the pairwise comparisons were significant.

5.3.4 Competition for Lck in dual coreceptor-expressing cells

CD8/Lck interactions are weaker than CD4/Lck interactions in both pulldowns[314,315,366] and when assayed as isolated polypeptides using isothermal titration calorimetry[361], suggesting that CD8αβ binds Lck less efficiently than CD4. However, the ratio of CD4/Lck to CD8/Lck occupancies varies considerably between studies (1.5-7.4 for single-positive [SP] cells[315,366] and 1.8-11.3 for DP cells[314,315]), suggesting that relative difference between CD4 and CD8 is not precisely known. Therefore, we co-transfected CD8α, CD8β-mCherry2 and Lck-mEGFP into HEK293T cells and used sFCCS to estimate the CD8αβ/Lck occupancy at 59% ± 10% (**Figure 5.8a**). Fewer CD8αβ dimers bound Lck than CD4, consist with the kinetic studies, but occupancy was still much higher than in previous co-IPs[314,315]. This also suggested that, when co-expressed in the same cells, the coreceptors might compete for Lck if it is present in limited amounts. To this we, generated coreceptor dual-expressing cells (either CD4-mCherry2 with non-fluorescent CD8α and CD8β or CD8β-mCherry2 with non-fluorescent CD8α and CD4) co-transfected with equivalent amounts of Lck-mEGFP, and measured the coreceptor/Lck *q* under each condition (**Figure 5.8b**). The average occupancies of both CD4/Lck (57% ± 20%) and CD8αβ/Lck (37% ± 20%) were substantially reduced compared to when a single coreceptor was expressed (*cf.* 96% for CD4/Lck [**Figure 5.4b**], 59% for CD8αβ/Lck [**Figure 5.8a**]), implying that all the available Lck was partitioned between coreceptors when the kinase was a limiting factor (Lck^{Low}). We hypothesized, therefore, that increasing Lck levels in excess of CD4 and CD8 (Lck^{High}) would reverse this trend, restoring the coreceptor/Lck equilibrium to that of cells with just one coreceptor. These measurements proved technically challenging because increased mEGFP expression led, in most cases, to cell brightness beyond the detection range for single-molecule fluctuations. Nonetheless, in the narrow range of cells yielding suitable fluctuation curves, increased Lck-mEGFP expression levels yielded average occupancy values comparable to those of single coreceptor-expressing HEKs for both CD4 (88% ± 23%) and CD8αβ (60% ± 12%) (**Figure 5.8b**), albeit with higher experimental uncertainties. These results suggested that Lck expression levels could regulate coreceptor

occupancy, and that, on average, CD4 outcompeted CD8αβ under limiting Lck. To corroborate this statistically, Lck^{Low} and Lck^{High} measurements were pooled and linear regression used to analyze the relationship between the amount of excess Lck (*i.e.,* the Lck/coreceptor density ratio) and occupancy (**Figure 5.8c**). Although there was no statistical link between CD4/Lck *q* and the Lck/coreceptor ratio (R^2 = 0.001, p = 0.83), CD8/Lck *q* increased significantly with excess Lck (R^2 = 0.38, p < 0.0001). At low Lck concentrations, CD4 has a higher probability of being occupied by Lck than CD8αβ and it is only when the Lck levels begin exceeding both coreceptors (Lck/coreceptor ratio ≥ 2) that CD8αβ/Lck approaches the occupancy observed in cells expressing CD8αβ alone. Together, our results indicate that the coreceptor/Lck equilibrium in dual coreceptor-expressing cells is sensitive to relative Lck levels.

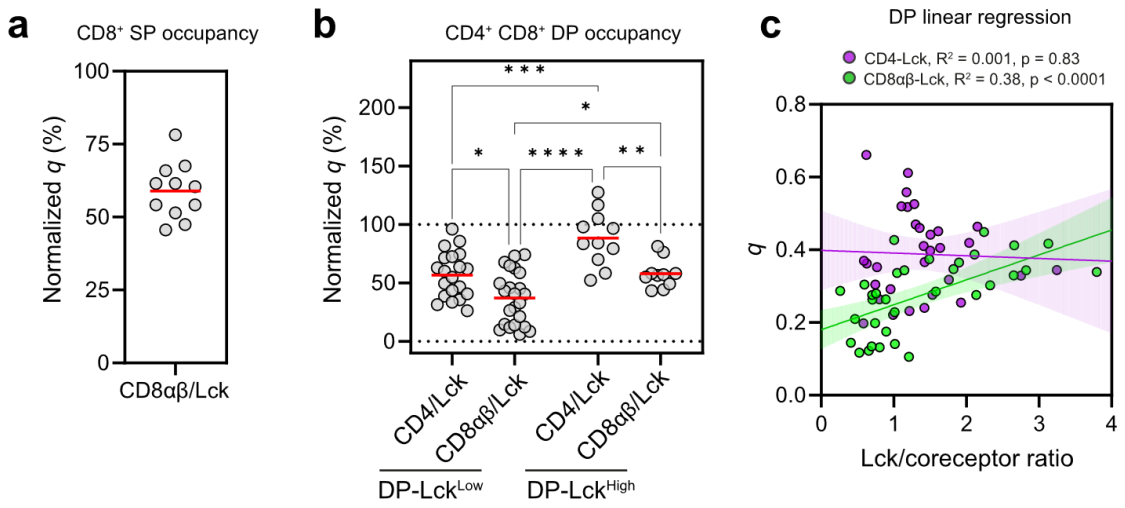


Figure 5.8 **Coreceptor/Lck occupancy is regulated by Lck availability in dual coreceptor-expressing cells. a.** CD8ab/Lck occupancy in single coreceptor-expressing HEK293Ts measured by sFCCS. Cross-correlation was measured between CD8β-mCherry2 and Lck-mEGFP. Unlabeled CD8α was added to the transfection mixture as without the α chain, mCherry2 fluorescence was retained intracellularly and did not reach the membrane. **b.** CD4/Lck or CD8/Lck occupancies in HEK293T cells expressing relatively low or high levels of Lck. Significance was assessed with a one-way ANOVA using Tukey's test for multiple comparisons. **c.** Linear regression between relative Lck levels and coreceptor/Lck *q* for all measured cells (*i.e.,* pooled Lck^{Low} and Lck^{High} values). Each circle indicates a spatially averaged measurement from one cell.

5.3.5 TCR triggering does not affect CD4/Lck occupancy

The experiments described thus far in **Chapter 4** were designed to test coreceptor/Lck interactions in a heterologous cellular system, devoid of any T cell-specific signaling factors. However, early hypotheses for coreceptor functions suggested that the activities of CD4 and CD8αβ could be controlled by TCR signaling[367] potentially through regulating kinase occupancy[368]. To determine whether coreceptor/Lck occupancy would change as a result of TCR phosphorylation and signaling, we transfected CD4-mCherry2 and Lck-mEGFP into Jurkat$^{CD4-/Lck-}$ T-cells (generated for the FC-IP experiments described in **Section 5.3.1**) and incubated them at 37°C on supported lipid bilayers (SLBs) functionalized with the small adhesion protein CD58, which establishes contact areas with a uniform intermembrane spacing of ~12.8 ± 1.4 nm based on measurements from interfaces formed by the similar rat CD2-CD48 interaction[369]. CD58 was necessary for the formation of suitably stable cell/SLB contacts, as the cells would otherwise migrate and drift[370], introducing movement artefacts into the fluctuation analysis[355,356,371]. Then, to activate the cells through TCR engagement, anti-CD3ε Fabs were tethered to the SLBs alongside CD58 (**Figure 5.9a**, 'activated'). To control for the basal level of activation that occurs through the CD58 condition alone ('primed'), owed to ligand-independent TCR triggering[372,373], we also generated TCR-deficient Jurkat$^{CD4-/Lck-}$ cells (Jurkat^{TCR-}) using CRISPR/Cas9 (**Figure 5.9a**, 'non-stimulated'). The diminished signaling capacity of Jurkat^{TCR-} cells was verified by Ca^{2+} flux measurements when placed onto SLBs decorated with both UCHT1 and CD58 (**Figure 5.9c**).

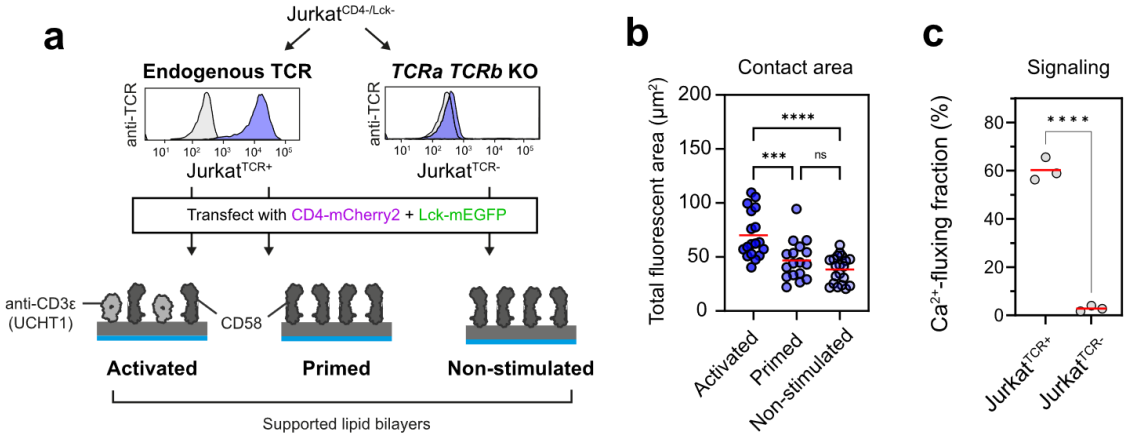


Figure 5.9 **Signaling-competent and -deficient Jurkat T cells on supported lipid bilayers. a.** Jurkat$^{CD4-/Lck-}$ cells were split into TCR-CRISPR'd (Jurkat^{TCR-}) and non-CRISPR'd (Jurkat^{TCR+}) pools, transfected with CD4-mCherry2 and Lck-mEGFP and incubated on protein-functionalized SLBs. To generate the 'activated' and 'primed' condition, Jurkat^{TCR+} cells were placed on UCHT1/CD58 bilayers and CD58-only bilayers, respectively. To generate the 'non-stimulated' condition, Jurkat^{TCR-} cells were placed onto CD58-only bilayers. **b.** The average spreading area of cells in each condition was approximated using the total (mCherry2 + mEGFP) fluorescent area, with activated cells spreading significantly more than either primed or non-stimulated cells. Each circle indicates the area of one Jurkat T cell, all imaged on the same day of experiments. Significance was assessed with a one-way ANOVA using Tukey's test for multiple comparisons. **c.** The signaling deficiency of Jurkat^{TCR-} cells was validated through Ca^{2+} flux measurements on UCHT1/CD58 bilayers, performed by Ed Jenkins. Each circle indicates one replicate bulk analysis of several hundreds of cells and significance was assessed with an unpaired t test.

We noticed, additionally, that Jurkat^{TCR-} cells did not spread in the characteristic manner of activated T cells on SLBs. This difference was confirmed by measuring the total fluorescent area (*i.e.,* the area containing either CD4 or Lck) at the plane of contact with the SLB, and the average area was found to be significantly increased in activated condition compared to either the primed or non-stimulated setting (**Figure 5.9b**). Then, to determine occupancies, CD4/Lck interactions were analyzed by performing sFCCS in the Jurkats that had formed stable contacts within 10 minutes of incubation (**Figure 5.10a**, white arrows). The cross-correlation analysis produced very high CD4/Lck *q* values in all conditions (activated: 96% ± 14%, primed: 92% ± 10%, non-stimulated: 85% ± 15%), virtually identical to the occupancies measured in HEK293T cells (**Figure 5.10b**). In conclusion, our results show that the high CD4/Lck occupancy observed in our assays is not an artefact of heterologous expression and agrees with our FC-IP data with Jurkat T-cells expressing murine proteins (**Figure 5.2b**), suggesting that CD4 and Lck are coupled stoichiometrically in both humans and mice.

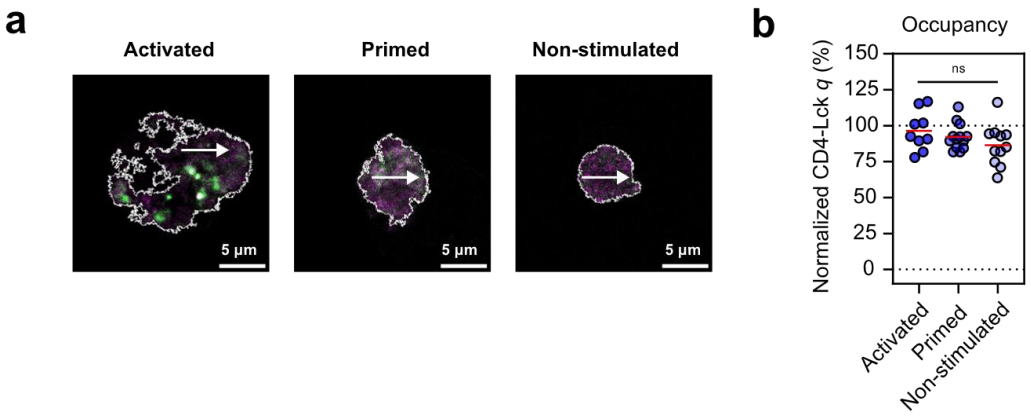


Figure 5.10 **sFCCS indicates high-occupancy CD4/Lck complexes are not disrupted by early TCR signaling. a.** Representative confocal images of a single Jurkat T cell expressing CD4-mCherry2 (purple) and Lck-mEGFP (green) in each of the three signaling conditions, with the cell outline in solid white. The white arrow indicates the approximate position of a line-scan in sFCCS measurements of the cells. **b.** CD4/Lck occupancy measurements normalized to the controls in Figure 5.4. Each circle indicates a spatially averaged CCF/ACF ratio from one cell. Significance was assessed with a one-way ANOVA and no comparisons were significantly different.

Single-molecule imaging experiments have shown that both CD4 and Lck can form small, nanoscale clusters within minutes of TCR triggering[374,375], in part through confinement in CD2 nanodomains[376]. To combine the brightness and diffusion data derived from the sFCS experiments, we generated bivariate (brightness + transit time) histograms allowing us to visualize fluorophore oligomerization (*i.e.,* photon counts per molecule or brightness[219]) and diffusion (*i.e.,* log-transformed transit time) simultaneously (**Figure 5.11a**). These weighted scatter plots provide insights into molecular organization based on where clusters appear on the graph; singular, fast-moving species would appear in the bottom left while large, slow clusters would appear in the top right. This approach revealed two important things about the diffusing populations: first, that both protein populations were largely homogenous in each condition (*i.e.,* all data points were clustered together) and two, that brightness values were increased slightly in the activated conditions compared to the non-signaling setting. Although CD4/Lck microclusters were observed in the Jurkat T cells, we were unable to perform FCS measurements in these spots as there were insufficient single-molecule fluctuations due to high brightness. Outside of these microclusters, we observed no significant changes in bulk diffusion between conditions, suggesting no changes in diffusion speed of either protein as a result of TCR activation diffuse significantly faster or slower (**Figure 5.11a**). However, previous studies show that the diffusion mode of Lck becomes 'trapped' or hindered only in activated T cells[211,377,378]. We therefore analyzed the transit time histograms of Lck using maximum likelihood estimation (MLE) calculation to determine if the histogram was best represented by a model for free or hindered diffusion[216,379]. Using MLE analysis, we found that Lck exhibited free (lognormal) diffusion in the primed and non-stimulated state and trapped (double-lognormal) diffusion in the activated condition only (**Figure 5.11b**). In summary, our results indicated that early TCR signaling has no effect on the high coreceptor/Lck occupancy, but does lead to changes in nanoscale organization in the form of transient hindrances of Lck, in agreement with past results using single-molecule microscopy[378,380].

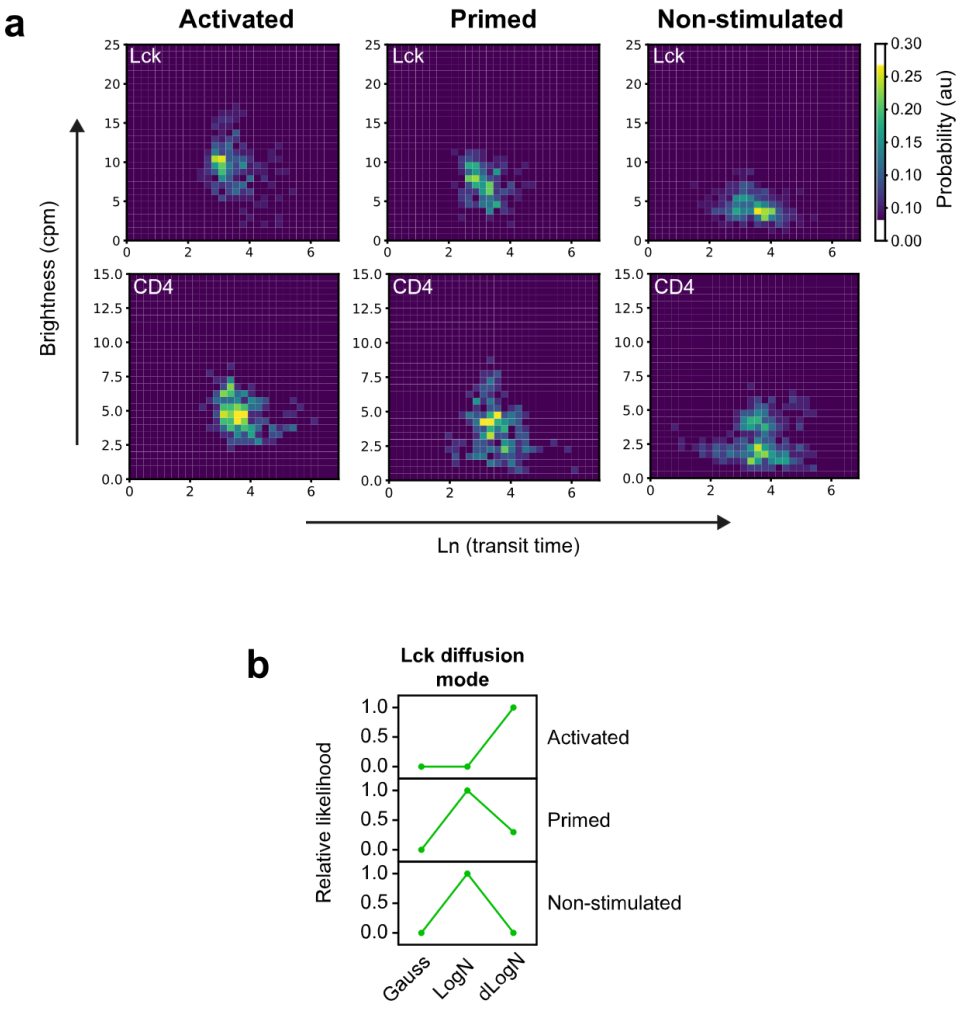


Figure 5.11 **Statistical analysis of CD4/Lck diffusion and oligomerization. a.** Brightness-transit histograms of pooled ACFs from all pixels in all cells represented as a heatmap. Bulk brightness of both CD4 and Lck increases with the degree of cell activation, suggesting signaling-specific oligomerization of both proteins. Transit times are not significantly altered between signaling conditions of either CD4 or Lck. **b.** Analysis of Lck diffusion modes using MLE to determine if the transit times best fit a free diffusion profile (logN) or hindered diffusion profile (dLogN), performed by Falk Schneider. Free Lck diffusion dominates in the non-stimulated and primed state, with diffusion shifting to hindered upon engagement of the TCR in the activated state.

5.4 Discussion

The results presented in this chapter describe the use of sFCCS to determine coreceptor/Lck occupancy *in situ* and is, to our knowledge, the first ever calibrated measurement of these proteins at the surface of live cells. Our biophysical measurements of HEK293T cells and Jurkats expressing human proteins are consistent with our FC-IP measurements of mouse thymocytes and Jurkats engineered to express murine proteins, and collectively suggest that, under most conditions, CD4 and CD8αβ are substantially occupied by Lck.

5.4.1 Discrepancies between past reports of occupancy

Our initial motivation to reproduce the recent FC-IP experiments was to determine whether commonly-used chelating agents could explain the discrepancy between recent reports of a low CD4/Lck occupancy[314,315,337,381] and older studies showing ample (but often unquantified) amounts of Lck associated with CD4 pulldowns in both primary T cells[311,312,382,383], transfected cell lines[364,384,385] and *in vitro* incubations[365]. The result that an excess of EDTA had no effect on occupancy measurements in our FC-IP experiments (**Figure 5.1b, Figure 5.2b**) reveals that chelating agents would have had little effect on the variation between studies, contrary to our expectations. TPEN, a membrane-permeable Zn^{2+} chelator not used in lysis buffers, reduced the occupancies by different amounts for CD4/Lck and CD8αβ which could indicate different amounts of TPEN-resistant complexes in the precipitates.

It is, at present, unclear why our results differ so profoundly from those of previous reports using FC-IP. One clue that points to a problem with reproducibility is a difference in CD4/Lck occupancy in DP thymocytes reported by the same group, conducted in the same laboratories, with wild-type mice from the same animal facility: 6% in one study[314] and 17% in another[315] (both with small margins of error). With this in mind, it seems the most likely explanation for these inconsistencies is differences in experimental conditions. For example,

serum-free buffers that contain Ca^{2+} can cause Zn^{2+} efflux from mammalian cells[386] and this alone could disrupt the coreceptor/Lck clasp[387]. Another possibility is excessive dilution effects due to large (~1 ml) washing volumes, as described in the original FC-IP protocol[316], which may shift the equilibrium of precipitated complexes towards dissociation. Additionally, assuming typical on-rates[388], a kinetic analysis suggests that coreceptor/Lck interactions have relatively short half-lives (~17s for CD4-Lck, ~8s for CD8-Lck)[140] and components of the complex might be lost at different rates post-washing. It is easy to envisage how experimental factors like lysis buffer composition, washing procedure and prolonged delays between pulldown and readout could all affect the measured occupancy, but these details rarely reported in full[314–316]. The variability in results using FC-IP methods suggest that experiments need to be rigorously controlled in order to obtain reproducible results, and should ideally be correlated with *in situ* methods.

5.4.2 Analysis of CD4 C-terminal secondary structure elements

By combining our sFCCS platform with a traditional mutagenesis approach we were able to dissect the individual contributions of the CD4 ICD to Lck-binding, with the major observation being that the Zn^{2+} clasp cysteines and amphipathic helix are both necessary for the stoichiometric binding of CD4 to Lck. The kinase occupancies of helix-deficient CD4 and wild-type CD8αβ are not dissimilar (73% and 59%, respectively), suggesting that the amphipathic helix of CD4 is a major contributor to the differential coupling of the coreceptors to Lck. A study published at the time of writing, which performed a similar mutagenesis screen but using *in vitro* membrane fractionation, corroborates our finding that the CD4 helix contributes to the CD4/Lck association[389]. Although their results suggest the mutation of the helix is more disruptive to CD4/Lck binding (~77% reduction) than ours (~27% reduction), an important point of difference is that the fractionation method used by this group has also yielded a very low occupancy in a prior study[337], suggesting that measurements are being made on a destabilized complex. Since a helix-sufficient, clasp-deficient mutant CD4 protein was completely unable

to bind Lck in our experiments, we hypothesize that CD4/Lck binding occurs first via Zn^{2+}-dependent clasp formation which is then stabilized by the folding and apposition of the two amphipathic helixes, one from each protein, to form the hydrophobic core. Simulations of polypeptide folding kinetics might provide insights into the energy landscape of coreceptor/Lck Zn^{2+} clasp formation, and differences between the coreceptors in this respect[361].

Why are the occupancies of helix-deficient CD4 (73%) and CD8αβ (59%) not exactly the same? Using the mutagenesis screen, we also identified a small contribution of the flexible C-terminal 'tail' of CD4 (**Figure 5.6**). If binding contributions are assumed to be additive this implies that a version of CD4 lacking both the helix (27% reduction) and the tail (14% reduction) would bind Lck at an occupancy of around 59% (*i.e.,* identical to CD8αβ) although this needs to be verified experimentally. A recent phylogenetic analysis[389] has revealed an unexpectedly conserved stretch of residues within the flexible tail of CD4 (HRΦQK; where Φ is a large non-polar residue) which is absent in CD8α[140] and is a strong candidate for further investigation. Together, this would suggest that, while the Zn^{2+} clasp is essential for the initial attachment of coreceptors to Lck, only CD4 is capable of forming additional stabilizing interactions (through mainly the helix) which allows the formation of high-occupancy complexes at the cell surface.

5.4.3 Coreceptor occupancy in positive and negative selection

How do our results relate to the roles of the coreceptors in thymic development, where they are co-expressed prior to lineage commitment[390]? The 'Lck availability' model posits that the coreceptors sequester Lck to prevent signaling by non-MHC ligands and relies inherently on both CD4 and CD8αβ having high kinase occupancies[134,391]. The 'coreceptor scanning' model, in contrast, suggests that both coreceptor proteins bind Lck at low capacity to effect differential signal amplification based on pMHC dwell times[314,315]. The high kinase occupancy observed in our experiments with dual coreceptor-expressing cells is compatible with 'Lck availability'

but not with ‘coreceptor scanning’, suggesting that low coreceptor/Lck occupancy is not a primary mechanism for antigen discrimination. As Lck is generally thought to be expressed in excess of both coreceptors[314,332,392–396], it is difficult to envision signaling mechanisms that would constrain occupancy below that dictated by their association at equilibrium. In addition, a comprehensive analysis of TCR/pMHC binding studies shows that the increase in TCR sensitivity afforded by coreceptors comes at the cost of a reduction in discriminatory power rather than increasing it[397]. As mentioned in **Section 1.2.2**, the current view is that both thymocytes and T cells discriminate between agonists and non-agonists through one of two mechanisms. Either the TCR and coreceptor are intrinsically mechanosensitive, differentiating between ligands based on the types of molecular bonds they form[398] or antigen discrimination depends only on receptor dwell-time at phosphatase-depleted regions of T cell/APC contact[399,400].

5.4.4 Coreceptor/Lck interactions during early TCR signaling

TCR triggering, often studied using artificial antigen-presenting surfaces, results in rapid re-organization of the interface between the T cell and the antigen-bearing substrate driven primarily by biophysical properties of protein binding, density and membrane distance[401–404]. The organizational heterogeneity of an immune synapse poses a challenge for line-averaged sFCS measurements in which the concentration of fluorophores needs to remain constant in the observation region (a straight 5 µm line) over the course of a measurement. Thus, to reduce the complexity of the system, we isolated Jurkat T cells into different signaling states using a combination of genetic engineering (to control the presence of the TCR) and supported lipid bilayers (to confine the T-cell membrane to a single focal plane).

No substantial differences were found in coreceptor/Lck occupancy between the non-stimulated, primed and activated conditions suggesting that these complexes are durable and readily available prior to and during TCR triggering. An important caveat of our measurements

is that, due to the need to detect single-molecule fluctuations, we were unable to analyze the small, bright protein clusters which formed in the activated condition. Our measurements were therefore constrained to the molecules which remained more homogenously distributed throughout the surface. Despite this active bias toward looking only at proteins displaying diffusion as the basis for intensity fluctuations, we still detected increased brightness in the activated and primed conditions. Thus, TCR signaling changed the bulk oligomerization of CD4/Lck throughout the interface. Although brightness had in both cases increased approximately two-fold from the non-stimulated state, the oligomeric state cannot easily be correlated with the increase in apparent brightness. A pure population of dimers would be difficult to deconvolve from, for example, a mixture of monomers, dimers, trimers and tetramers[219]. However, given that CD4/Lck complexes are monomeric by default (*i.e.,* in the absence of signaling)[339], the most probable scenario is that a small number of higher-order oligomers formed during initial TCR signaling amidst a majority of monomers, similar to results from TCCD measurements of the TCR[405].

Class I- and class II-restricted TCRs signal identically despite binding different ligands[406,407]. We would therefore expect that Jurkat$^{CD4-/Lck-}$ transfectants of CD8α, CD8β-mCherry2 and Lck-mEGFP would model class I-restricted TCR signaling sufficiently to determine CD8αβ/Lck occupancy as was done for CD4/Lck in this chapter. *In vitro* assays have shown that CD8/Lck occupancy is stable up to 24 hours post T-cell activation[366], reinforcing the idea that coreceptors remain stably bound to Lck. A caveat of these results is that cells were stimulated in an antigen-unspecific manner (anti-CD3 Fabs for the results of this chapter; anti-CD3/anti-CD28 beads for ref.[[366]]) and we cannot rule out that triggering of the TCR by cognate pMHC molecules could affect coreceptor/Lck interactions. Biochemical studies show that phorbol 12-myristate 13-acetate (PMA)-mediated stimulation of cell lines produces a rapid loss of Lck from anti-CD4 Western blots[408], suggesting that further studies are needed to determine how exactly coreceptors are internalized and/or recycled following TCR triggering and whether this impacts their association with Lck at the cell surface.

6. Malaria antigens and host LILRB1/HLA *cis* interactions

6.1 Introduction

Variant surface antigens (VSAs) of falciparum malaria

Malaria is a parasitic disease caused by five different species of *Plasmodium* protozoans, of which falciparum malaria causes almost all deaths globally[409]. *P. falciparum* has a complex life cycle, transferring between human hosts and mosquito vectors, and can exist in at least five different stages within these organisms during the phases of replication, infection and transmission. Several molecules that are essential to this life cycle are also targets of the adaptive immune response, and the parasite has therefore evolved the ability to express hundreds of variants of these antigens[410]. These include the *var* genes, which encode the endothelium-binding PfEMP1 proteins, the *rif* genes and the *stevor* genes. The *rif* genes were first identified in the 1980s as extensively repeating DNA elements at subtelomeric regions of the genome[411,412] and subsequent sequencing revealed that the repetitive interspersed families of polypeptides (RIFIN) family was the largest of the malaria surface antigens with over 150 members[413]. Although the function of the highly polymorphic RIFINs remains largely unknown, the fact that they are expressed at the surface of infected erythrocytes, that they undergo antigenic variation and that they are correlated with severe disease all suggest the direct involvement of RIFINs with binding to host factors and promoting virulence[414].

Binding of RIFINs to inhibitory human receptors

In 2017, screening of infected erythrocytes against a recombinant library of inhibitory immune receptors revealed that a subset of RIFINs bound to either leukocyte-associated immunoglobulin-like receptor 1 (LAIR1) or leukocyte Ig-like receptor subfamily B member 1

(LILRB1) and could dampen the effector functions of primary B cells and immortalized NK cells *in vitro*[415]. This suggested that some RIFINs could function by triggering inhibitory signaling pathways in the host, providing the parasite with the means to evade clearance by the immune system. Antibodies containing small LAIR1 or LILRB1 inserts in the Fab domain were subsequently crystallized which could bind these RIFINs[416,417], hypothesized to have developed as a mechanism to counter the ability of parasites to exploit inhibitory signaling in the host. Since these insertions were first detected in public antibodies from healthy adults in malaria-endemic regions[418], this novel mechanism of interchromosomal DNA transposition was suggested to be a general feature of antibody diversification to control malaria infections.

However, as discussed in **Section 1.2.3**, there is evidence that LILRB1 would, at least in the absence of *trans* ligands, bind to major histocompatibility complex (MHC) class I proteins in *cis* at the cell surface. This fact raises a central question: how would RIFINs overcome this potential 'masking' of LILRB1 to depress the function of immune cells? There are three potential solutions to this problem: RIFINs could either 1) elicit non-canonical signaling through binding to a composite LILRB1/MHC-I surface or 2) directly mimic the binding mode of MHC-I molecules that normally bind LILRB1 in *trans* or 3) trigger signaling through LILRB1 in a conformationally agnostic manner.

6.2 Methods

Protein purification, characterization and structure determination

LILRB1 D1D2 (amino acids 1-198) and RIFIN variable regions (PF3D7_1254800 and PF3D7_1373400, amino acids 165-274) were cloned into a pET15b vector together with an N-terminal 6xHis tag. The G234R mutation was incorporated by site-directed mutagenesis. Constructs were transformed into BL21 (DE3) competent *Escherichia coli* (NEB), with expression induced at an optical density at 600 nm of 0.6 by adding isopropyl β-D-1-thiogalactopyranoside (IPTG) to a final concentration of 1 mM. Proteins were purified from

inclusion bodies as previously described[415] by solubilization in 6 M guanidine HCl, immobilization on an IMAC column with Ni^{2+}-NTA resin, refolding with flash dilution into 1 M L-arginine and purification by size-exclusion chromatography using a Superdex 75 10/300 (GE Healthcare) column. LILRB1 D1-D4 and D3-D4 (amino acids 1-394 and 199-394, respectively) were purified in a similar manner, but without refolding, directly from day 5 supernatants of transfected HEK293F cells.

Circular dichroism (CD) experiments were conducted using a Jasco J815 CD spectrophotometer. The proteins were desalted using PD-10 columns (GE Healthcare) and were adjusted to a concentration of 0.25 mg/ml. A spectrum was taken at 20 °C between 260 nm and 190 nm using a 1 mm path length with measurements taken every 0.5 nm. A baseline determined using buffer alone was subtracted from the protein spectra and ten equivalent spectra were averaged together.

Surface plasmon resonance experiments were carried out using a Biacore T200 instrument (GE Healthcare). LILRB1 constructs were coupled to a CM5 chip by amine coupling and concentration series of RIFINs were flowed over this chip at 30 µl/min. After each run, the chip was regenerated using 10 mM glycine pH 2.5 for 30 seconds. Data were analyzed using the BiaEvaluation software (v.1.0) for kinetic analysis and Prism (v.8.2.1) for equilibrium analysis.

For structure determination, LILRB1 D1D4 and the RIFIN variable regions were combined to a 1:1 molar ratio and incubated for 1 hour before purification of the complex by size-exclusion chromatography (GE Healthcare). Crystallization trials were carried out using vapor diffusion in sitting drops and crystals obtained after 10 days. Crystals were collected, cryo-cooled in liquid nitrogen and scattering data collected at the Proxima-1 beamline at SOLEIL at a wavelength of 0.97857 Å. The structure was solved by molecular replacement using Phaser MR (v.2.8.3)[419], with the individual domains of LILRB1 (from PDB accession codes 6EWA and 4LL9) used as four separate search models.

NFAT-GFP reporter assay

The GFP reporter assay was conducted as previously described[415]. The LILRB1 reporter cells were mouse T cell hybridomas that were stably transfected with NFAT-GFP, Flag-tagged DAP12 and a fusion of the extracellular domain of LILRB1 with the transmembrane and intracellular domains of paired immunoglobulin-like receptor β (PILRβ). The transmembrane and cytoplasmic domains of PILRβ were used to induce GFP via the DAP12 adaptor molecule in the reporter cells. Recombinant RIFINs were immobilized on a 96-well plate and cultured with 10^5 reporter cells for 16 hours before GFP expression was analyzed using flow cytometry.

NK cell handling

Primary human NK cells were isolated from leukocyte cones provided by UK National Health Service Blood and Transplant (NHSBT) using the RosetteSep Human NK Cell Enrichment Cocktail (StemCell Technologies). Use of leukapheresis products at the University of Oxford was approved by the Non-Clinical Issue division of the National Health Service (REC 11/H/11/7). LILRB1 expression was assessed with rabbit anti-LILRB1 (abcam, EPR21007) followed by Alexa Fluor 647-conjugated F(ab)′2 anti-rabbit (ThermoFisher Scientific, A-27040). For imaging experiments, NK cells were resuspended in complete R10 medium and used on the same day, within 2 hours of isolation.

SLBs and TIRF imaging

SLBs were prepared as described in **Section 2.4**. SLBs were prewarmed to 37 °C and 10^6 primary NK cells were infused into each lane. Samples were incubated for 30 min at 37 °C and 5% CO2 and then fixed with warm 4% paraformaldehyde in PHEM buffer (60 mM PIPES, 25 mM HEPES, 10 mM EGTA, 2 mM $MgCl_2$, pH 7.4) for 15 min. For LILRB1 staining, to enhance receptor detection, cells were permeabilized with 0.1% saponin in PHEM buffer for

20 min, then washed and blocked with 100 mM glycine and 5% BSA overnight. For LILRB1 staining, two non-blocking antibodies against LILRB1 (abcam, EPR21007 and EPR11256) were diluted in PHEM buffer containing 0.02% saponin and 3% BSA and added to the samples for 1 hour before washing. For perforin staining, cells were left unpermeabilized and stained using anti-perforin conjugated to Alexa Fluor 488 (BioLegend, dG9) was diluted in PHEM buffer with 0.02% saponin and 3% BSA and added to samples for 1 h before washing.

For details of the TIRF imaging setup, see **Section 3.2**. Cells were illuminated with 488 nm, 561 nm and 640 nm lasers and images analyzed using ImageJ v1.5.2. Cell boundaries were defined based on segmented ('Otsu' algorithm in ImageJ) reflection images and all pixels in the contact area used to calculate the MFI. Pearson's correlation coefficient (PCC) values were calculated for each cell contact using the Coloc2 plugin to perform pixel intensity correlations between channels.

6.3 Results

6.3.1 Structural characterization of a LILRB1-binding RIFIN

The extracellular regions of RIFINs consist of conserved N-terminal domains and variable C-terminal domains[420,421]. To solve the structure of a specific RIFIN shown to bind LILRB1 (PF3D7_1254800)[415], different fragments of the ectodomain were generated and assessed for expression. Although both the truncated constant and variable regions could be expressed, only the variable region exhibited binding to LILRB1 by surface plasmon resonance (SPR) (**Figure 6.1a**). The full-length ectodomain did not express in a folded form. The solution affinity of the variable domain for LILRB1 was 570 nM, around ten-fold higher than LILRB1/MHC-I interactions (K_D = 2-7 µM)[422]. In subsequent work, the recombinant RIFINs correspond only to the variable C-terminal domains.

Co-crystals of the monomeric variable domain with the extracellular domain of LILRB1 diffracted to 3.0 Å and the structure was built by molecular replacement with reference to a previous LILRB1 structure (PDB ID: 6EWA). The RIFIN variable domain consists of three main helices connected by extensive loops that form small helical segments (**Figure 6.1b**), binding to LILRB1 at the hinge between its D1 and D2 domains (**Figure 6.1c**). To distinguish this particular RIFIN based on its binding mode, it was named RBL1D2 (RIFIN that binds LILRB1 at D1-D2). We next compared the binding mode of RBL1D2 with the endogenous ligand for LILRB1, MHC-I β_2m, using a crystal structure of human leukocyte antigen (HLA)-A2 bound to LILRB1 domains D1 and D2, aligning the two complexes at the D1-D2 hinge[423] (**Figure 6.1d,e**). This comparison revealed that RBL1D2 and MHC-I share a highly similar binding interface, comprising a short loop supported mainly by backbone-mediated hydrogen bonds to the receptor, despite being structurally unrelated. The interaction surface areas were also similar, with 750 Å^2 for RBL1D2 and 833 Å^2 for β_2m. This indicates that RBL1D2 is able to mimic the molecular binding mode of class I proteins, and achieves ten-fold higher affinity despite lacking any significant structural similarity.

To confirm that the binding interface identified in the crystal was involved with LILRB1 binding, we introduced a point mutation (G234R) into RBL1D2 designed to sterically disrupt the receptor-binding interface with a bulky side chain (**Figure 6.1f**). SPR analyses showed no detectable binding of the RBL1D2^{G234R} to LILRB1 (**Figure 6.1g**), although circular dichroism (CD) confirmed it retained the same secondary structure content as the wild-type RBL1D2 (**Figure 6.1h**).

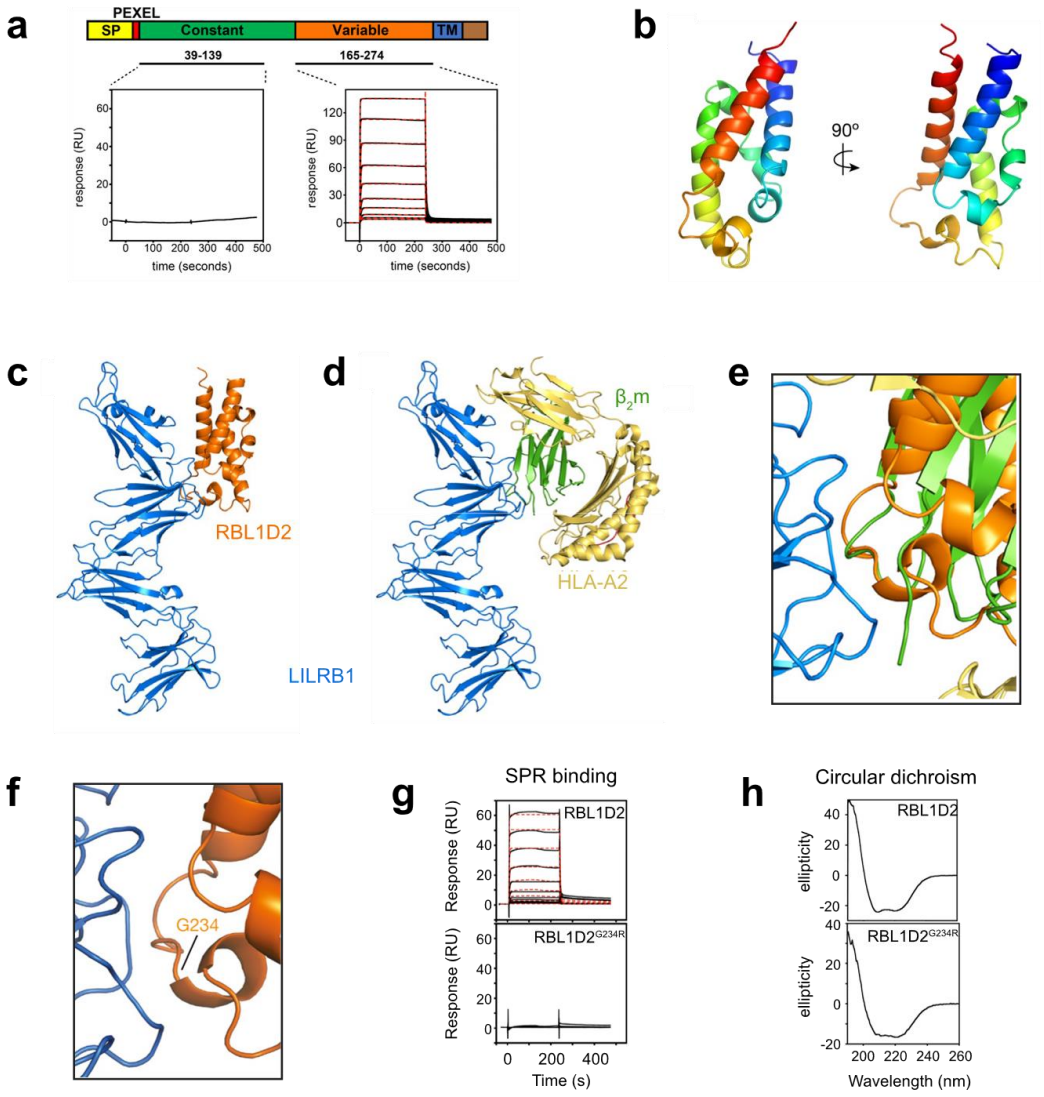


Figure 6.1 **Structural characterization of a LILRB1-binding RIFIN. a.** Schematic depiction of RIFIN protein architecture with SPR binding curves of isolated constant (green) and variable (orange) domains interacting with the ectodomain of host receptor LILRB1. **b.** Ribbon representation of the RIFIN variable domain shown in a 'spectrum' coloring scheme from N-terminus (blue) to C-terminus (red). **c.** and **d.** Structural comparison of how LILRB1 binds its malarial (RBL1D2, **c**) and host (HLA-A2, **d**) ligands using the same D1-D2 hinge interface. **e.** Overlay of the receptor-binding loops of RBL1D2 and β_2m, colored as in **c** and **d**. **f.** Location of Gly234 in the RBL1D2 binding loop which is substituted with Arg to create RBL1D2^{G234R}. **g** and **h.** Biophysical characterization of the G234R mutation indicates a loss of LILRB1-binding via SPR (**g**) without major disruption to secondary structure content via CD (**h**).

6.3.2 RIFIN binding produces functional inhibition of NK cells

Next, we assessed whether soluble RBL1D2 could induce signaling in the plate-based reporter system which was used in the initial identification of the LILRB1/RBL1D2 interaction[415]. When LILRB1^{+} reporter cells were stimulated with wild-type RBL1D2 proteins, strong activation of green fluorescent protein (GFP) expression was detected (**Figure 6.2a**) whereas mutation of the RIFIN (G234R) or substitution with a non-LILRB1-binding RIFIN (PF3D7_1254200) abolished the GFP signal. This experiment confirmed that a recombinant form of RBL1D2 could elicit signaling in a reporter assay, and demonstrated that the interface observed in the crystal was responsible for triggering LILRB1-mediated signal transduction.

To understand whether activation of a receptor in a cell line would translate to functional depression of lymphocyte effector function, we turned to total internal reflection fluorescence (TIRF) imaging of the supported lipid bilayer (SLB) platform introduced in **Section 4.3.3**. Because NK cells have recently been reported to be important in controlling blood-stage malaria through antibody-mediated cellular cytotoxicity[424,425], we isolated primary NK cells from healthy human donors and confirmed LILRB1 expression by flow cytometry (**Figure 6.2b**). Immune synapse formation was triggered by tethering human IgG1 (Fab-side down) and ICAM-1 to the SLBs, mimicking the contacts formed between NKs and their infected target cells. Then, equal densities of RBL1D2 or RBL1D2^{G234R} were coupled to the bilayers before incubating with freshly-isolated NK cells. As a negative control, we also infused SLBs with equivalent densities of HLA-A2 to block antibody-dependent cellular cytotoxicity (ADCC). After 30 minutes of synapse formation, cells were fixed and stained for LILRB1, to determine whether the receptor was recruited to cytotoxic synapses, and perforin, as a marker for NK-cell degranulation. Both MHC-I and RBL1D2 showed an enriched recruitment to synapses which, in the case of the RIFIN, was diminished when the LILRB1-binding site was mutated (RBL1D2^{G234R}) (**Figure 6.1c,d**). Additionally, both MHC-I and RBL1D2 showed significantly increased colocalization with LILRB1 compared to RBL1D2^{G234R}, indicating that recruitment was specific to the ability to bind LILRB1 (**Figure 6.1e**). Finally, we found that

perforin secretion was blocked in the presence of MHC-I or wild-type, but not mutant, RBL1D2 (**Figure 6.1f**). The distribution of the perforin deposits was heterogeneous and punctate, as seen in prior studies[426–428], probably indicating that the pore-forming protein was being released as a mixture of both soluble monomers[429] and the proteinaceous particles discovered recently[430,431]. Thus, recruitment of RBL1D2 to the synapses of NK cells, requiring a specific LILRB1-binding site on the RIFIN, inhibited secretion of cytotoxic perforin.

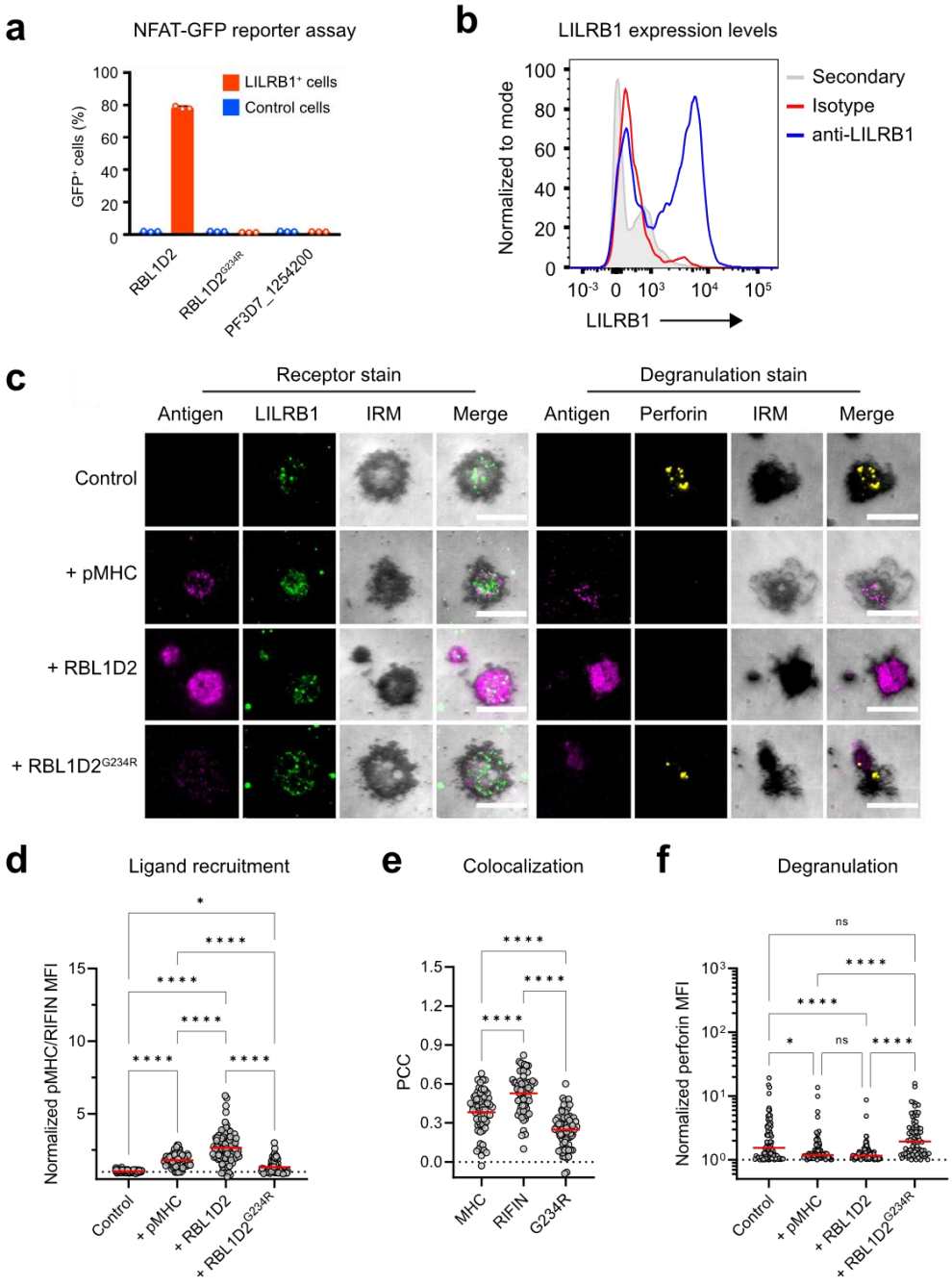


Figure 6.2 **RBL1D2 induces LILRB1-mediated signaling and inhibits NK cell activity**. **a.** Soluble RBL1D2 produces GFP transcription in LILRB1^{+} reporter cells but not LILRB1^{-} controls cells. This effect is abolished through mutation of the receptor-binding loop (G234R) or using a RIFIN that does not bind LILRB1 (PF3D7_1254200, ligand unknown). **b.** Characterization of LILRB1 expression on NK cells in healthy donor PBMCs. **c.** TIRF imaging micrographs of NK cells deposited on SLBs coated with hIgG1 and ICAM-1 (control) and one of three LILRB1 ligands: pMHC, RBL1D2 or RBL1D2^{G234R}. Scale bar = 10 µm. **d.** Quantification of recruited fluorescence in the NK/SLB contact area for pMHC or

RIFINs. **e.** Colocalization between LILRB1 and its ligands quantified with Pearson's correlation coefficient (PCC). **f.** Perforin release in each of the indicated conditions. Each circle in **a** indicates one repeated measurement. Each circle in **d**, **e** and **f** indicates measurements from one cell. Significance was assessed with a one-way ANOVA with Tukey's test for multiple comparisons.

6.3.3 MHC-I/LILRB1 *cis* interactions are modulated by RIFINs

In 2021, the Lanzavecchia group reported the structure of an antibody containing a LILRB1 D3-D4 insert bound to its RIFIN antigen (PF3D7_1373400)[432], establishing a second group of LILRB1-binding RIFINs. Although this new protein, RBL1D3 (RIFIN that binds LILRB1 at D3), appears structurally similar to RBL1D2, it binds LILRB1 very differently. RBL1D2 binds at the endogenous β_2m-binding loop (D1-D2 hinge), while RBL1D3 is expected to engage a small interface at the apex of the D3 domain largely occluded by D2 when the receptor extends out from the surface. This suggested that LILRB1 would have to adopt distinct conformations to interact with each antigen: RBL1D2 would effectively mimic a normal *trans* ligand while RBL1D3 could only bind if the upper D1-D2 domains were folded away from the lower D3-D4 domains. Crystallization of the RBL1D3/LILRB1 complex confirmed this idea, revealing a dramatic bend between the D2 and D3 domains of LILRB1 which forces the receptor into a horseshoe shape[433] (**Figure 6.3a**).

To determine whether receptor bending was a prerequisite for binding of RBL1D3 or if, perhaps, the RIFIN could itself induce bending of the extended conformer (*e.g.,* via the long receptor-binding loops[432]), we then generated structural mutants of LILRB1. Based on the existing bent and extended models, we engineered disulfide bonds at select locations to lock the ectodomain rigidly in either the extended ($LILRB1^{ext}$) or bent ($LILRB1^{bent}$) conformation (**Figure 6.3b**). Then, recombinant RIFINs were tethered to an SPR chip and binding assays performed with soluble $LILRB1^{WT}$, $LILRB1^{ext}$ and $LILRB1^{bent}$ to screen for interactions (**Figure 6.3c**). RBL1D2 was found to bind all forms of LILRB1 similarly, while RBL1D3 bound

preferentially to LILRB1^{bent}, at intermediate levels to LILRB1^{WT} and not at all to LILRB1^{ext} (**Figure 6.3c**). This hierarchy of binding agreed with the structural predictions that the RBL1D3 epitope on the receptor would be hidden in the extended conformer of the protein. We noted that the kinetics of RBL1D3/LILRB1 binding (k_{on} = 2×10^4 M^{-1} s^{-1}, k_{off} = 0.025 s^{-1}) were much slower compared to RBL1D2/LILRB1 binding (k_{on} = 10^6 M^{-1} s^{-1}, k_{off} = 0.3 s^{-1}). This could suggest a scenario in which RBL1D3 binding is inherently slow because it requires the receptor to switch a less favorable bent form, although the effective half-lives (confinement times) in a membrane are likely to be more similar because of RBL1D2 rebinding to LILRB1.

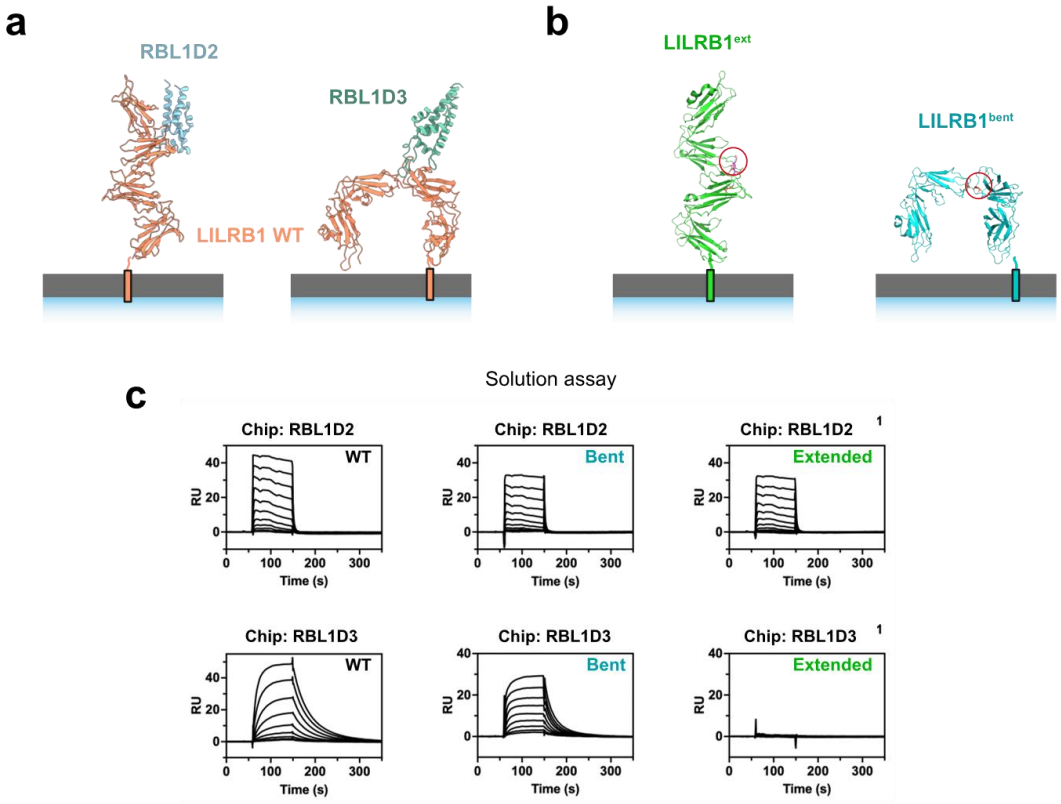


Figure 6.3 **A LILRB1 D3-binding RIFIN interacts with a bent receptor. a.** Comparative structures of RBL1D2 and RBL1D3 bound to LILRB1, showing significant conformational bending in the latter only. **b.** Structural representation of the conformationally-locked LILRB1 mutants with the elongated form in green (LILRB1^{ext}) and bent form in blue (LILRB1^{bent}). The red circle indicates the position of the disulfide bonds introduced to lock the structures. **c.** SPR binding assays of LILRB1^{WT}, LILRB1^{bent} and LILRB1^{ext} interacting with either RBL1D2 (top) or RBL1D3 (bottom) conjugated to the chip. RBL1D2 binds all three receptors, indicating that the mutations do not interfere with the receptor-binding ability of the antigen. Notably, while RBL1D2 is still able to bind LILRB1^{bent} (presumably because the interaction occurs in solution) while RBL1D3 cannot bind LILRB1^{ext} (in agreement with the structural requirement for the receptor to bend to expose its RBL1D3-binding epitope).

The β_2m-binding loop of LILRB1 is located at the apex of the receptor, preventing it from binding to endogenous MHC-I on the same cell when in the extended conformation[120]. In contrast, the bent form of the receptor shown here (and hypothesized to exist almost 15 years ago[120]) positions the binding loop at the exact height for *cis* binding, implying a clear structure-function relationship for the ability of LILRB1 to bind ligands in different orientations. To test this, we performed sFCCS measurements as described before by transiently co-expressing the relevant constructs with C-terminal mEGFP (LILRB1$^{WT/ext/bent}$) or mCherry2 (single-chain trimer HLA-A2)[434] tags. Additionally, for the experiments in this chapter, HEK293T cells deficient in β_2m (HEK293T$^{\beta 2m-/-}$) were used to ensure depletion of endogenous MHC-I molecules which could otherwise have interfered by competing for *cis* binding to LILRB1. Using this assay, we confirmed the *cis* interaction of LILRB1^{WT} with MHC-I at an average density of 167 and 234 molecules/μm^2, respectively (**Figure 6.4**). In addition, LILRB1^{bent} displayed increased association with MHC-I and LILRB1^{ext} did not bind MHC-I at all. By normalizing LILRB1^{WT}/MHC-I *q* to that of the conformationally-locked mutants, we calculated that ~40% of LILRB1^{WT} molecules were bound to MHC-I in this system. Thus, our assay was sensitive to LILRB1/MHC *cis* binding and could validate the mutations that altered the conformation of the receptor.

The results of the SPR assays shown earlier indicated that RBL1D2 and RBL1D3 might have different effects on LILRB1/MHC-I heterodimers on the cell surface. While D2-binding RIFINs would compete with and disrupt *cis* interactions, resulting in stabilization of extended conformers of LILRB1, D3-binding RIFINs favor the bent conformer leading to increased LILRB1/MHC-I *cis* interactions. In order to test these predictions, we repeated the sFCCS experiments in the presence of recombinant RIFINs (**Figure 6.4**). As a control we included a pan-HLA antibody (W6/32)[435] which binds a composite β_2m/α-chain interface[436] and should therefore block the *cis* interaction wholly. As expected, addition of either W6/32 or RBL1D2 to the cells resulted in similarly diminished LILRB1/MHC-I cross-correlation, trending

towards an abolished *cis* interaction even when compared to the modest *q* of the wild-type receptor. On the other hand, RBL1D3 had the opposite effect, significantly increasing *q*.

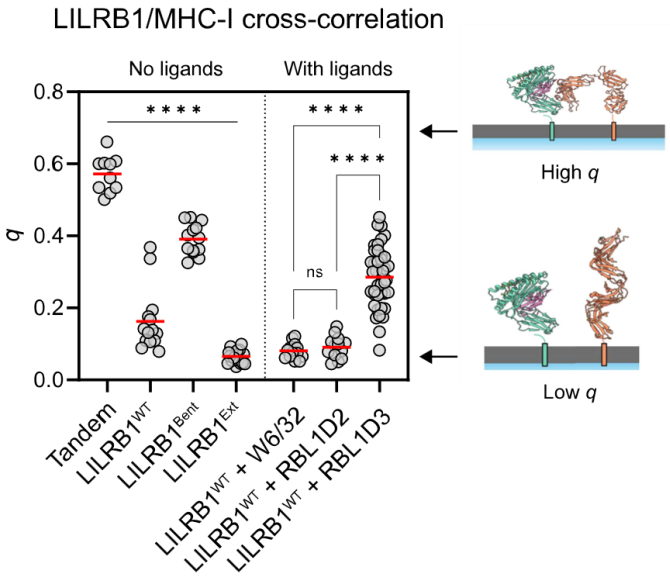


Figure 6.4 ***Cis* measurements of LILRB1/MHC-I interactions with sFCCS.** sFCCS of LILRB1 and MHC-I (expressed as a single-chain trimer) with either wild-type (WT) or mutant receptor molecules (left) or wild-type interactions either with an anti-HLA antibody (W6/32), RBL1D2 and RBL1D3 (right). Each indicate an sFCCS measurements from one cell. Significance was assessed with a one-way ANOVA followed by Tukey's test for multiple comparisons.

The different binding modes of the two RIFINs, and their resulting effects on LILRB1/MHC-I *cis* interactions, suggested that they might produce different functional effects. We originally intended to compare them by disrupting endogenous LILRB1 expression in NK cells and express transgenes encoding the bent or extended receptors instead. As both lentiviral and electroporation-based CRISPR approaches failed to generate an efficient LILRB1 knock-out, we repeated the functional SLB assay depicted in **Figure 6.2** with primary NK cells expressing wild-type LILRB1 (**Figure 6.5a**). These experiments showed clearly that RBL1D3 is recruited to NK-cell synapses at significantly increased levels compared to RBL1D2 (**Figure 6.5b**) and

perforin staining revealed that it also acted more potently to inhibit cells (**Figure 6.5c**). Thus, while both RIFINs shared a similar structure and bound to the same receptor, they produced different functional effects based purely on differences in binding location and/or kinetics.

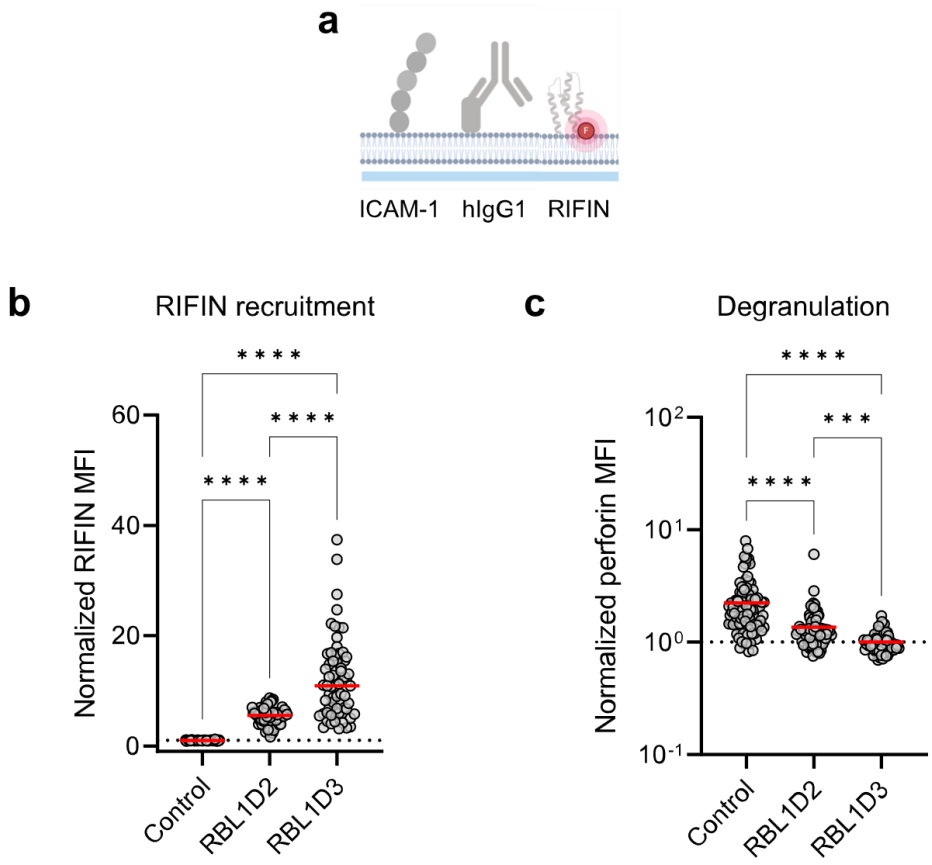


Figure 6.5 **Functional effects of RBL1D2 vs. RBL1D3 on primary NK cells in the bilayer assay. a.** Cartoon depiction of the bilayer composition showing ICAM-1 and hIgG1 to induce degranulation (unlabeled) + a labelled RIFIN (either RBL1D2 or RBL1D3). **b.** and **c.** The functional SLB assay was used to compare the effects of RBL1D2 and RBL1D3 on the same donor cells with readouts of **b)** RIFIN-AF647 recruitment and **c)** perforin deposition measured with antibody staining. At equivalent densities, RBL1D3 was recruited significantly more to NK synapses compared to RBL1D2 and produced a greater inhibitory effect via LILRB1. Each circle indicates a measurement from one NK cell. Significance was assessed with a one-way ANOVA followed by Tukey's test for multiple comparisons.

6.4 Discussion

The RIFIN family is by far the largest of the malarial VSAs[437] and yet the function of these proteins on infected erythrocytes was largely unknown, until recently[421]. The discovery of RIFINs that bind human immune receptors[415,418] suggests a major role for these parasite-encoded proteins in manipulating host immune cells by triggering inhibitory signaling pathways. In this section, we describe the molecular and functional characterization of two different RIFIN proteins, RBL1D2 and RBL1D3, in their ability to bind host receptor LILRB1. As this receptor has been suggested to bind HLA-I proteins in *cis*[145], we used sFCCS to confirm and quantify this *cis* interaction before determining whether the two RIFINs altered the equilibrium between the monomeric and heterodimeric forms of LILRB1. Finally, to study the functional effects of RIFIN proteins we employed reductionist signaling assays. Functional effects of *rif* family members have been difficult to study *in vivo*: anti-RIFIN antibodies have been identified in malaria-infected individuals but it is unclear if they correlate with protection[438] and none of the murine models of malaria express *rif* genes[439]. In our system, we were able to study the effects of single RIFINs presented on flat bilayers as infected erythrocyte mimetics and quantify their inhibitory effects on NK cells.

6.4.1 RIFIN variable domains form novel α-helical bundles

Initial topological predictions suggested that variable region of RIFINs might be exposed on the surface of the infected erythrocyte while the conserved region remained in the cytoplasm, anchored between two transmembrane helices[440]. This view was later revised with improved topology prediction algorithms indicating that both the variable and constant regions would be extracellular[441] (*i.e.,* exposed to the immune system) but a role for the constant region has yet to be identified. In the study that first identified RIFIN/LILRB1 binding, *P. falciparum*-infected erythrocytes bound better to LILRB1 when they expressed full-length RIFIN over just the isolated variable region[415]. Although the constant region did not interact appreciably with the

receptor (and is not required for LILRB1 binding in solution), it may be involved with supporting the trafficking or folding of the variable region at the erythrocyte surface. From a structural side, neural network-based prediction tools like AlphaFold[442] may be helpful to determine the architecture of the constant region, potentially providing clues as to its role. Functionally, the importance of these domains could be determined through controlled human malaria infections (CHMIs)[443] using a *P. falciparum* strain like 3D7 engineered expressing clonal RIFINs, comparing disease progression between full-length and truncated constructs.

The structures of two variable RIFIN ectodomains presented here both consist of a small hydrophobic bundle of slanted α-helices connected by extensive loops. Although other *P. falciparum* proteins are also built from small helical scaffolds[444], their topology differs from that of RBL1D2 and RBL1D3. Interestingly, two recent structures of LAIR1-binding RIFINs share the same basic architecture[445,446], suggesting that this type of helical bundle represents a small, novel protein fold used, to our knowledge, only by RIFIN proteins. These comparisons indicate that there is no clear structure-function relationships for the RIFINs identified so far since they bind distinct conformational epitopes with similar tertiary structures. This is consistent with other subclasses of malarial surface antigens like PfEMP1s which are under selection pressure to maintain functional binding while exhibiting extensive sequence variation to evade adaptive immune responses[447].

6.4.2 Supported lipid bilayer mimetics of infected erythrocytes

The nuclear factor of activated T-cells (NFAT)-GFP reporter assay developed by Saito and colleagues[415] proved useful in testing and validating the recombinantly produced RIFIN fragments but it is not without caveats. The main drawback is that the antigen is presented immobilized on a solid substrate and in a random orientation, rather than laterally mobile and in specific orientation like how surface-bound ligands would normally be recognized. To address this, we adapted the SLB system used to study T-cell signaling in **Chapters 4** and **5**

for NK cells, as they have been implicated in controlling parasite replication in the early phases of blood-stage malaria[448]. Functional studies of NK cells using SLBs have been performed before with both MHC class I polypeptide–related sequence A (MICA) stimulation[431] and anti-CD16[449] but given the functional importance of ADCC to trigger NK-mediated lysis of *P. falciparum*-infected target cells[450] we ensured that human IgG1 molecules were anchored to the SLB in an orientation permissive to Fc receptor triggering.

Although the imaging assay showed clear recruitment of LILRB1 and its ligands to cytotoxic synapses, the colocalization between receptors and ligands was less obvious owing, in part, to the different distributions of fluorescence: LILRB1 puncta were scattered across the synapse, dim MHC-I molecules clustered around the lytic central supramolecular activation cluster (cSMAC)[451] while a dense carpet of RIFINs was recruited to the entire interface. This is partially because ligands were directly conjugated to fluorescent dyes while the receptor was labelled with primary/secondary antibodies which may produce some non-specific staining. To quantify colocalization in a manner that was insensitive to these differences in intensity and offset (*i.e.,* background) we used Pearson's correlation coefficient (PCC)[452,453]. The fact that LILRB1/MHC PCC was significantly lower than LILRB1/RBL1D2 PCC suggested that MHC-I molecules in the bilayer were binding to surface receptors other than LILRB1, consistent with NK cells expressing a wide variety of MHC-I-specific receptors[83]. When RBL1D2^{G234R} was introduced into the SLBs, almost no protein was recruited to the synapse but the residual amount of fluorescence produced a substantial, non-zero colocalization with LILRB1. This could either represent very weak, residual binding activity of RBL1D2^{G234R} not detectable by SPR or the non-specific trapping of protein in the bilayer underneath the NK cell. The fact that RBL1D2^{G234R} produced no significant reduction in degranulation compared to the control suggested that the latter was the case and that the mutant RIFIN was effectively inert.

There are three main caveats of the SLB system used in this assay to mimic erythrocytes. First, as mentioned, the density of RIFINs on infected erythrocytes is unknown.

There is some evidence that the products of the *rif* genes, like those of the *var* genes, undergo clonal switching[454], suggesting that only one RIFIN might be present on a given infected erythrocyte at a time. Quantitative flow cytometry on parasite lines that express single RIFINs[415] may be useful in determining the absolute RIFIN density *in situ*. Second, to adhere the NK cells to our SLBs we used ICAM-1, a typical adhesion protein used to mimic antigen presenting cells. However, mature erythrocytes express ICAM-4 and CD58 as adhesion proteins[455] which have different extracellular spacings, altering the lateral organization of proteins at the NK/SLB interface[456]. Third, the stiffness of the glass coverslip on which the SLB is deposited is several orders of magnitude greater than that of eukaryotic cell membranes[457,458]. Recreating the erythrocyte surface might require technologies that more closely mimic soft physiological membranes, such as gel-supported bilayers[458].

6.4.3 Bending over backwards to bind RIFINs

Only two previous reports have directly shown the binding of LILR family proteins to MHC-I in *cis* in live cells. Masuda *et al.* reported data suggesting an association between LILRB2 and HLA molecules in immortalized basophils[459] while Mori *et al.* demonstrated that both LILRB1 and LILRB2 on osteoclasts can interact with MHC-I on the same cells[145]. Although not explicitly calculated in the latter study, the normalized (Förster resonance energy transfer) FRET efficiency of LILRB1/MHC-I heterodimers was ca. 43%, in very close agreement with our calibrated measurements of 40%. As LILRB1 is expressed broadly on T cells, B cells, NK cells, macrophages and monocytes[141], we assume that its *cis* interactions will occur widely across LILRB1-expressing leukocytes. Only a small number of additional receptors other than LILRB1/2 have been tested for binding MHC-I molecules in *cis*[120]. A systematic screen developed specifically to test for receptor/MHC-I interactions within the same membrane may help broaden this list, advancing our understanding of how surface receptors sense both classical and non-classical class I proteins of the HLA system.

On the comparison of RIFINs, our initial hypothesis, based mainly on the kinetic data, was that RBL1D2 would be a more potent inhibitor than RBL1D3 simply because it binds both conformers with a fast on-rate while RBL1D3 only binds one (LILRB1^{bent}) and with a slow on-rate. However, the situation in solution will be different to that of the physiological contact between an NK cell and an infected erythrocyte, where RBL1D2 would be unlikely to access the bent form of LILRB1. This is primarily because the intermembrane gap would have to be much smaller (~50Å)[433] than the distance spanned by most leukocyte receptor/ligand complexes[460,461] and, in addition, because binding would be competitively inhibited in *cis* by endogenous MHC-I, expressed at high surface levels[462]. RBL1D3, although it can only interact with LILRB1^{bent}, binds with slow on- and off-rates. This means that, when RBL1D3 eventually binds to a bent receptor (a state presumably stabilized by endogenous MHC-I), it would be able to remain bound much longer than RBL1D2. Coupled with the fact that there is no competition for ligand-binding in *trans*—as erythrocytes do not express MHC genes[463]—RBL1D3 is practically conformationally agnostic, transducing inhibitory signals better than RBL1D2, which can only engage extended receptors. Our prediction that RBL1D3 was the better inhibitor was borne out by our imaging assay comparing the consequences of binding D2 vs. D3 on NK degranulation *ex vivo*.

Of the three possible models of RIFIN binding to LILRB1 discussed in **Section 6.1**, two appear to be used: RBL1D2 mimics a normal *trans* ligand while RBL1D3 will eventually signal through both conformers and is thus conformation-independent. These observations offer a clue to the evolutionary family history of RBL1D2 and RBL1D3. We speculate that RBL1D2 could have evolved first to mimic the binding of MHC-I molecules to LILRB1—effectively disguising infected erythrocytes as healthy self—but that this inhibition could be relieved by host immune cells upregulating surface MHC-I to 'mask' more LILRB1. As a counter strategy, the parasite subsequently evolved the RBL1D3 family of receptor-binding RIFINs to allow them to signal through LILRB1 even when in the bent conformer. Although convincing evidence of this hypothesis does not yet exist, it is supported by our SLB assays

showing that RBL1D3 is recruited more strongly to the synapse despite a similar affinity for the receptor (RBL1D2 K_D = 1 µM; RBL1D3 K_D = 700 nM). It is striking that RBL1D2 recruitment is halved compared to RBL1D3 since this is precisely consistent with a scenario in which RBL1D2 binds approximately half as many receptors as RBL1D3.

7. General discussion

Signal transduction through lymphocyte receptors remains an active area of interest for molecular immunologists, in part because of the powerful translational benefits of understanding, harnessing and redirecting lymphocyte effector activity[464–466]. Much is known about the basic biology of the receptors of T cells, B cells and NK cells including their structural layouts[467–470], how signals are transmitted through the membrane[471–475] and which signaling pathways are activated as result[63,89,104,109]. Although many receptors are known to oligomerize or cluster when triggered, their organization in the 'resting' state (*i.e.,* in the absence of stimuli) has been a subject of debate. For instance, controversy surrounding the oligomeric state of G protein-coupled receptors (GPCRs)[476] and the T cell receptor (TCR)[477,478] was resolved only relatively recently through the careful development and application of cutting-edge fluorescence methods sensitive enough to probe *bona fide* protein organization[339,479–482]. The physiological relevance of *cis* interactions is the most recent instalment in this series of questions about the molecular organization of lymphocyte receptors[121]. In a similar manner, this thesis adapts and implements a conventional form of fluorescence fluctuation spectroscopy—fluorescence correlation spectroscopy (FCS)—to measure different forms of receptor interactions within the plane of the cell membrane. Scanning fluorescence cross-correlation spectroscopy (sFCCS), which combines the dynamics of biophysical methods like fluorescence recovery after photobleaching (FRAP) and Förster resonance energy transfer (FRET) with the near-molecular resolution of super-resolved imaging, is used to identify and quantitate *cis*-interacting proteins at the surface of live cells. Functional assays are used demonstrate the relevance of these interactions in T-cell and NK-cell signaling, and reveal how *cis* interactions can be important for normal receptor function and bypassed by pathogens when ordinary signaling is hijacked.

7.1 Summary of findings

Biophysical studies of lymphocyte receptor *cis* interactions have, thus far, only been performed using intensity-based FRET measurements[122,123,145,483]. Although this form of FRET remains popular due to being accessible with conventional, turn-key equipment, it suffers generally from drawbacks as discussed in **Section 1.3.2**. Fluorescence cross-correlation spectroscopy (FCCS) overcomes two important limitations of bulk-FRET particularly relevant for membrane proteins: it is both independent of dipole orientation and much less sensitive to crowding effects at physiological densities while still achievable with standard laser-scanning microscopes (LSMs). However, few reports have attempted conventional FCCS studies of protein interactions in physiological membranes (*i.e.,* not in artificial bilayers[484,485] or reconstituted membrane-derived vesicles[486]), presumably because bleached signals often result in correlation curves of moderate to low quality[487–490]. The results of this thesis explore a different approach to adapt FCCS for the study of membrane proteins to specifically probe *cis* interactions. In **Chapter 3**, different modalities of fluorescence correlation spectroscopy (FCS) were compared to determine which of pFCS, sFCS and imFCS was best suited to study membrane protein dynamics. Although sFCS and imFCS both produced significantly increased signal quality and sampling compared to pFCS, sFCS was faster and less harsh on samples and was therefore chosen for further studies of membrane protein interactions. The key findings are summarized below.

In the first part of **Chapter 4,** the specificity of sFCCS was confirmed through cross-validation to FRET-based approaches (fluorescence lifetime imaging [FLIM]-FRET and flow-FRET) applied to the novel phenomenon of programmed cell death protein 1 (PD-1) homodimerization. The second part of **Chapter 4** demonstrated the functional relevance of this interaction in *in vitro* signaling and *in vivo* functional experiments.

In **Chapter 5**, sFCCS was extended to heterotypic *cis* interactions between surface receptors and their non-ligand interaction partner: CD4 or CD8αβ binding to Lck kinase at the

inner leaflet of the plasma membrane. This resolved a long-standing controversy about the nature of coreceptor/kinase occupancy arising from incongruent reports from biochemistry experiments. *In situ* measurements reveal how coreceptors are wholly occupied by Lck, which has important implications both for models of T-cell antigen discrimination and cell fate decisions made during thymopoiesis.

Lastly, in the last half of **Chapter 6**, previously reported homotypic *cis* interactions between an inhibitory NK receptor (leukocyte Ig-like receptor subfamily B member 1 [LILRB1]) and major histocompatibility complex (MHC) class I molecules were confirmed and quantified with sFCCS. The hijacking of this interaction by malarial variant surface antigens (VSAs), members of the RIFIN family characterized in the first half of **Chapter 6**, was then demonstrated. This revealed how parasite-encoded molecules had evolved to mimic host signals and suggested that they could also overcome 'masking' of their ligands by the immune system.

7.2 Defining lymphocyte receptor *cis* interactions

The experimental study of protein *cis* interactions remains a challenge. Structural methods allow for the direct visualization of protein/ligand *cis* heterodimers but steps must be taken that these are clearly distinguishable from *trans* ligand complexes, especially in the case of homotypic interactions. The biases of crystallography towards ordered, high-affinity interaction between soluble molecules[491] also favor more 'conventional' *cis* interactions *i.e.,* mediated by a well-defined interface between ectodomains, like for the LILRB1/MHC-I heterodimer. *In vitro* studies are powerful for the detection and identification of proteins—and were originally used to identify the receptors central to each chapter[492–494]—but their use for characterizing *cis* interactions is also prejudiced. Methods that extract protein complexes from their native environments and stabilize them in solution heavily favor stable interactions that are able to resist coming apart during extensive solubilization and washing steps required to purify

material from crude mixtures[495]. Finally, determining the relevance of receptor *cis* interactions requires clear evidence. Functional studies need to balance how closely the experimental systems approximates physiology (*e.g., in vivo* versus *ex vivo*) without compromising the interpretation of results (*e.g.,* clearly identifying *cis* ligand binding), and this can be challenging to execute in practice.

When the concept of *cis* interactions was first introduced, the standard definition was given as a receptor capable binding to the same protein ligand presented either in *cis* or in *trans* (*e.g.,* LILRs binding to MHC molecules)[120,121]. Our results reframe this definition and suggest that any interaction can be considered a *cis* interaction if it occurs in the plane of the membrane and has some functional consequence. Thus, if receptor dimerization is transient and regulatory, as is the case with RTKs, cytokine receptors and PD-1, it counts as a *cis* interaction. Conversely, obligate receptor dimers are effectively monovalent (*e.g.,* CD28) as changes in oligomeric state cannot occur and thus do not affect ligand binding or signaling. The different classes of *cis* interactions will require different methods to study and, as discussed above, not all methods are equally suitable for measuring, for example, *cis* binding between purified ectodomains versus intramembrane coiled-coiled interactions between hydrophobic helices. In this final section of the thesis, we will compare and contrast the three different *cis*-interacting receptors examined here (PD-1, coreceptors and LILRB1) in the context of 1) structure determination, 2) *in vitro* analysis and 3) evidence for functional importance.

7.2.1 Structural biology and the ‘tyranny of the lattice’

LILRB1/MHC interactions

The results presented in **Chapter 6** demonstrate a clear structure-function relationship between the conformation of LILRB1 and its ability to engage MHC-I proteins in *cis* or *trans*. The requirement for LILRB1 to swing down at the D2-D3 hinge to bind membrane-proximal

MHC-I was first speculated in a review article from over a decade ago[120] yet a structural model of this complex is still not available. However, a comparison between this hypothetical complex[120] and our schematic of how LILRB1 would have to bind to bind MHC-I in *cis* (**Figure 1.4**) reveal a drastic bending of the receptor that is almost identical. Further investigation is warranted to determine whether a trimolecular complex can form between RIFIN that binds LILRB1 at D3 (RBL1D3) and the LILRB1/MHC-I *cis* heterodimer.

All of the binding interactions studied in **Chapter 6** are mediated by globular protein domains that bind one another with a relatively high affinity. This allowed us to use structural biology both directly (to visualize the complexes) and analytically (using structure-guided design) to study the effects of receptor conformation on binding preference. The observation that RIFIN variable regions binds to their receptors via a well-defined interface[432,496,497] also helped to resolve how exactly the parasite hijacks host signaling pathways using protein scaffolds that are structurally distinct from the endogenous ligands of immune receptors[498,499]. It is worth noting that no reports have thus far succeeded in solving the structure of a RIFIN constant region and so its molecular structure remains enigmatic. So far, the only clue as to its structure comes from circular dichroism (CD) analysis of a purified constant region which suggests that it might be intrinsically disordered. Solution-based structural methods like nuclear magnetic resonance (NMR) will be helpful to test this hypothesis and may provide additional clues on function.

Coreceptor/Lck interactions

Like LILRB1/MHC interactions, binding of Lck kinase to the T cell coreceptors occurs outside the plasma membrane through non-covalent interactions between well-defined residues. While LILRB1/MHC interactions occur extracellularly, coreceptor/Lck binding, explored in **Chapter 5**, occurs at the inner leaflet of the plasma membrane via a Zn^{2+}-stabilized motif. The only structural data available on these complexes come from an NMR study, which

demonstrated that the polypeptide regions that make up the Zn^{2+} clasp are largely unstructured in isolation and only adopt secondary structure elements upon binding[361]. As far as we know, these Zn^{2+}-binding dicysteine motifs are unique not only among cell-surface receptors but across Zn^{2+}-coordinating protein domains too[500]. The high selectivity of these interactions has even inspired their adaptation for biochemical engineering[501,502].

There are two structural features of the coreceptor/Lck clasp that remain open to investigation. First, what is the role of lipid palmitoylation groups upstream of the clasp? Our data suggest these modifications are not required to stabilize the complex. Other studies have shown that palmitoylation is important for targeting of proteins to plasma membrane domains with a specialized lipid composition—so-called membrane-ordered domains—but it is unclear why both proteins would need to be targeted in this way given that they interact at a high occupancy. Second, what is the function of CD4's amphipathic helix in the co-folding of the complex? Clearly this helix is dispensable for binding to Lck as both CD4Δhelix and CD8αβ can interact with the kinase, albeit at different occupancies. Further investigation using, for example, molecular dynamics simulations may aid our understanding of how coreceptor/Lck clasps form and what role the helix plays in stabilizing the interaction.

PD-1 *cis* interactions

Non-covalent PD-1 dimers, mediated as they are by residues buried in the membrane, probably represent the most challenging class of *cis* interaction to determine structurally. Current structures of PD-1 consist only of ectodomain fragments, and direct visualization of the transmembrane and cytosolic regions will require insights from membrane protein structural studies like crystallography of protein nanodiscs[503], lipidic cubic phase technology[504] or solid-state NMR[505]. Cryogenic electron microscopy (cryo-EM), which has been successful at solving the structure of multiple vitrified receptor complexes[506–508], might also be applicable to PD-1 dimers if the complex is large enough. To aid with sample homogeneity, the dimer

could be stabilized with appropriate mutations or by chemical cross-linking. It would be interesting to see if there are any external factors that contribute to the propensity of the transmembrane helices to interact, such as the direct involvement of lipids as seen in some GPCRs[509], ion pumps[510] and the TCR[508].

7.2.1 Assaying *cis* binding *in vitro*

Coreceptor/Lck interactions

Biochemistry has revealed much about how lymphocyte receptors bind to, and signal through, peripheral membrane proteins including, for example, the recruitment of SH2-containing proteins to receptor tyrosine kinases (RTKs)[511], G proteins to GPCRs[512], signal transducers and activator of transcriptions (STATs) to Janus kinases[513] and Src-family kinases to antigen receptors[89,104]. Since these interactions are sequestered underneath the cell membrane, unavailable to extracellular probes, biophysical assays are generally limited to studies in cell lines with chimeric fusion proteins that fluoresce. Although *in vitro* approaches like co-IPs are valuable in that they can be used with primary cell samples, the requirement for membrane lysis, solubilization and washing may alter the native state of proteins. This problem has been shown before for post-translational modification state—disagreements between Lck phosphorylation states[514,515]—but also applies to complex stoichiometry[314,315], as we discussed in **Chapter 5**. This emphasizes the caution that must be exercised when making inferences about native protein states from *in vitro* assays alone, especially for transmembrane or integral membrane proteins which exist in specific lipid environments that are unlikely to be reconstituted fully by detergents[516].

Why do our flow-cytometric immunoprecipitation (FC-IP) results differ so profoundly from those of Stepanek and Horkova *et al*? In **Section 5.4.1** we discuss several potential sources of experimental error and a key factor is probably dilution effects. The law of mass action dictates that the equilibrium stability of a receptor/ligand complex depends on the

concentration of its constituent components[517]. Since membrane-embedded complexes are probably shielded from this effect by detergents to some extent, this could explain why similar assays have produced such drastically different results over the years. In this study, washing volumes and steps were strictly kept at the minimum level recommended in the protocol[316] that still produced clean and sharp peaks on fluorescence histograms. This may have enabled us to reproduce values from *in situ* assays.

LILRB1/MHC interactions

The arguments for why LILRB1/MHC-I *cis* interactions are amenable to study with traditional structural methods also apply to *in vitro* techniques: interactions occur between well-defined interfaces with relatively strong binding. This feature allows the purified protein complexes to be quality-controlled prior to crystallization trials (*e.g.,* size exclusion chromatography [SEC]). *In vitro* analyses of parasite proteins are more challenging for the simple reason that the translation and trafficking machinery normally responsible for the production of RIFINs is absent in the Expi293F™ cells used in this study[518]. To overcome this, truncated fragments of the RIFIN variable domains were instead tested for their ability to express and fold. This approach yielded the two RIFINs described in **Chapter 6**, allowing for *in vitro* (*e.g.,* SEC and surface plasmon resonance [SPR]) analysis of RIFIN/receptor binding, verifying the effects of binding-deficient RIFIN mutants, and testing of the conformational LILRB1 mutants.

PD-1 *cis* interactions

Initially, *in vitro* assays of the isolated PD-1 ectodomain failed to find any evidence of a homotypic interaction[519]. This is consistent with the evidence presented in **Chapter 4** showing that dimerization is driven by transmembrane residues, and cannot occur between isolated ectodomains. How, then, could PD-1 dimers be studied *in vitro*? Previously, molecular analyses of receptor dimers have been performed with chemical cross-linking and sucrose-

gradient ultracentrifugation[520]. As discussed above, these approaches might alter the native state of inter-helical interactions. The TOXGREEN assay introduction in **Section 4.3.2** indicates that dimerization is substantial yet incomplete, suggesting that it could be sensitive to the membrane environment that surrounds the hydrophobic helix. A caveat of this assay is that the helices are expressed in a bacterial inner membrane and not a mammalian one. *In silico* analyses by molecular dynamics, assembling a model of the PD-1 helix into a representative simulation of a mammalian membrane, may be needed to capture a snapshot of the PD-1 dimer outside living systems.

7.2.2 Are receptor *cis* interactions physiologically relevant?

PD-1 *cis* interactions

The results of **Chapter 4** demonstrate clearly how intermolecular *cis* interactions at the cell surface are integral to the normal function of a lymphocyte receptor. The discovery that full-length PD-1 molecules could interact without ligands in model cell lines suggested two different models of PD-1 activity. Either dimerization was part of the normal receptor triggering process (*i.e.,* conducive to inhibitory signaling) or PD-1 dimers acted to block triggering (*i.e.,* hindering inhibitory signaling) and were disrupted by ligand-binding. The functional experiments with Jurkat T cells expressing engineered PD-1 molecules demonstrated conclusively that dimerization was important for normal receptor function. While the molecular basis for dimerization-dependent signaling is still unknown, the discovery of this phenomenon suggests that it might be therapeutically tractable to manipulate PD-1 dimerization with biologics. Bispecific antibodies that would simultaneously engage the PD-1 ectodomain and another receptor might disrupt dimers and attenuate inhibitory signaling[521]. This approach to antagonizing PD-1 may be helpful in co-administration regimes designed to stifle PD-1 and cytotoxic T-lymphocyte-associated protein 4 (CTLA-4) signaling simultaneously in cancer treatment[522]. Conversely, developing PD-1 agonists on the same principle (*i.e.,* using small

molecules or drugs to hold PD-1 in a dimeric state) could reduce the threshold for inhibitory signaling and alleviate pathologies like rheumatic or diabetic disease. Blocking anti-PD-1 antibodies have mainly been developed as signal-inhibiting reagents (*i.e.,* checkpoint inhibitors) but re-examining candidates for their ability to promote PD-1 dimerization might prove fruitful. A recent preprint demonstrated the development of deep-learning based models for *de novo* design of small protein binders, including for PD-1, which may prove very helpful in the targeted development of oligomerization-state specific therapeutics[523]. A complete understanding of how receptor dimerization is linked to signaling will require further characterization of the system, as the TOXGREEN assay suggests that wild-type PD-1 dimerizes at a substantial yet submaximal level. Chimeric PD-1 proteins with transmembrane helices that are constitutively monomeric (*e.g.,* CD4) or dimeric (*e.g.,* GpA) would be useful in testing the extremes of PD-1 signaling and aid in the rational design of PD-1 therapies.

Coreceptor/Lck interactions

The results of **Chapter 5** reveal how the T-cell coreceptors associate with Lck at high stoichiometry when expressed at the surface of live cells. Lck association in *cis* is indispensable for coreceptor function and *in vitro* experiments have shown that T cells expressing truncated coreceptor molecules unable to bind Lck have diminished antigen sensitivity[524,525]. Our data are consistent with the current view of how CD4 and CD8αβ are thought to work, called the 'coreceptor recruitment' or two-step model[526,527]. According to this mechanism, signal propagation from the TCR occurs via 1) incipient phosphorylation of the ligand-bound receptor by free Lck, followed very rapidly by 2) the co-recruitment of a coreceptor/Lck complex through bidentate interactions with TCR/pMHC. Bidentate binding is important since having extracellular (coreceptor/MHC) and intracellular (Lck/phosphotyrosines) interactions occur simultaneously increases the avidity of coreceptor recruitment greatly, corresponding to a 30- to 40-fold increase in the rate at which the TCR

can be phosphorylated in mathematical models[341]. The provenance of the two-step model and the theories it supersedes have recently been reviewed in ref.[[140]].

In T-cell development, CD4 and CD8αβ have long been considered to 'program' thymocytes towards appropriately-restricted effector lineages (*i.e.,* ensuring that T_H-destined cells are $CD4^+$ and CTL-destined cells are $CD8^+$), although direct experimental evidence has been difficult to come by. Recently, using unique 'FlipFlop' mice, Shinzawa and colleagues were able to functionally reverse T-cell development by switching around the *Cd4* and *Cd8* genes in their respective loci[528]. Remarkably, $CD4^+$ cells which still received MHC-II-restricted signals became cytotoxic and $CD8^+$ cells which received MHC-I-restricted signals became helper cells. This proves conclusively that it is the duration of coreceptor expression, as determined by *cis*-regulatory genetic elements, rather than their physical structure or signaling capacity that dictates lineage fates. We speculate that, during the early stages of signaling before changes in *CD4* and *CD8* transcription occur, the higher CD4/Lck occupancy versus that for CD8αβ compensates for the very low affinity of CD4/MHC II interactions[341] helping it match the signals generated by CD8αβ during thymopoiesis.

LILRB1/MHC interactions

Although prior studies indicate that LILRB1 binds to MHC-I in *cis*[145,529], our measurements in **Chapter 6** are the first to verify this with human proteins. These previous reports also indicate that the role of this *cis* interaction is to mask LILRB1, decreasing the sensitivity of the receptor to *trans* ligand. If this is a general principle, this would be significant because LILRB1 is broadly expressed on human immune cells[141] and would be engaged in *cis* interactions everywhere. Many other receptor families, including cytokine receptors, nervous system receptors and metabolic receptors, have been proposed to bind HLA proteins in *cis*[530]. However, many of these associations were inferred from weak co-precipitation with HLA, and at times artificially stabilized with chemical cross-linking[531]. As discussed by Ruggiero and Springer[531], the lack

of a standardized approach to measuring class I *cis* interactions has sown some confusion and led to conflicting results. Methods capable of probing the formation of *cis* interactions in live cells, like sFCCS, will be important for the categorical distinction of *bona fide* interactions from experimental artefacts.

Results of the preliminary imaging assay revealed that RBL1D3 is more potent inhibitor of NK cells than RIFIN that binds LILRB1 at D1-D2 (RBL1D2), consistent with the *cis* model of LILRB1 interactions that we posited in **Section 6.3.3**. While this suggests that RIFIN-mediated inhibition is linked to whether or not receptor binding is conformation-agnostic, the implication that signaling through LILRB1 can be regulated by MHC-I interaction in *cis* has yet to be proven. One simple way to achieve this is by expressing LILRB1-Cis or LILRB1-Trans mutants in NK cells and measuring changes in cytotoxicity towards target cells. We hypothesize that killing will be increased when the receptor is bent (reduced sensing of target MHC-I) and decreased when the receptor is extended (improved sensing of target MHC-I), compared to wildtype. MHC-deficient cells *(e.g.,* K562 cells) could be used as a control to confirm that the conformation of the receptor is linked to MHC expression in *trans*.

What questions remain open about RIFIN-mediated modulation of immune cells? First, it would be prudent to test the effects of antibodies in the systems we have established. Several studies have identified anti-RIFIN antibodies in individuals from malaria-endemic countries[418,432,450] which mediate opsonization of infected erythrocytes. It is unknown if these antibodies block RIFINs from binding to their host receptors or simply tag the infected erythrocyte for destruction via lysis[450] or phagocytosis[532]. Second, a high-throughput, CRISPR-based screening approach could be used to characterize the human receptors of the remaining RIFINs, and might even reveal novel receptors of the malaria parasite. A similar analysis could be applied to the subtelomeric variant open reading frame polypeptides (STEVORs), another enigmatic family of VSAs[533], which would reveal the full complement of host-parasite interactions mediated by these antigens and provide clues as to which of these provide a selective advantage to the parasite. Third, the regulation of *rif* genes should be

investigated to determine whether the RIFINs, like the *P. falciparum* erythrocyte membrane protein 1s (PfEMP1s), undergo clonal switching[534]. While populations of infected erythrocytes from a single individual express multiple RIFINs[535], it is unclear if a single parasite-harboring erythrocyte can simultaneously bind to multiple receptors. This could be investigated with single-cell mass cytometry of cultured 3D7 parasites using metal-conjugated receptor tetramers. A comprehensive characterization of RIFINs, their binding partners and the host signaling pathways they activate would broaden our understanding both of parasite biology and receptor signal transduction. Since *cis* interactions at lymphocyte membranes may be more common than previously appreciated, it is possible that further mechanisms of how malaria has evolved to hijack *cis*-interacting proteins could be revealed.

7.3 Concluding remarks

The results presented in this work describe a new implementation of fluorescence correlation spectroscopy to study the interactions of lymphocyte receptors with their binding partners in *cis*. Two physiologically important instances of *cis*-binding for inhibitory molecules (PD-1 and LILRB1) were characterized and functionally validated, emphasizing how immune cell signaling can either by 'poised' or 'masked' by protein/protein interactions that occur between molecules present on the surface of the same cell. We were also able to resolve the controversy surrounding the kinase occupancy of T-cell coreceptors through quantifying coreceptor/Lck *cis* binding. This work showed that both CD4 and CD8αβ are associated with an abundance of Lck, and suggested that the differences between them might be important when Lck levels are limiting. Our work highlights the importance of trying to observe molecular interactions *in situ* and contributes to a more complete picture of lymphocyte receptor signal transduction.

Bibliography

1. Arber, W. & Linn, S. DNA modification and restriction. *Annual Review of Biochemistry* vol. 38 467–500 Preprint at https://doi.org/10.1146/annurev.bi.38.070169.002343 (1969).

2. Mojica, F. J. M., Juez, G. & Rodriguez-Valera, F. Transcription at different salinities of Haloferax mediterranei sequences adjacent to partially modified PstI sites. *Mol Microbiol* **9**, 613–621 (1993).

3. Koonin, E. V. & Makarova, K. S. Origins and evolution of CRISPR-Cas systems. *Philosophical Transactions of the Royal Society B: Biological Sciences* vol. 374 Preprint at https://doi.org/10.1098/rstb.2018.0087 (2019).

4. Hedges, S. B., Blair, J. E., Venturi, M. L. & Shoe, J. L. A molecular timescale of eukaryote evolution and the rise of complex multicellular life. *BMC Evol Biol* **4**, 1–9 (2004).

5. Dupuis, M. È., Villion, M., Magadán, A. H. & Moineau, S. CRISPR-Cas and restriction-modification systems are compatible and increase phage resistance. *Nat Commun* **4**, 1–7 (2013).

6. Desjardins, M., Houde, M. & Gagnon, E. Phagocytosis: The convoluted way from nutrition to adaptive immunity. *Immunological Reviews* vol. 207 158–165 Preprint at https://doi.org/10.1111/j.0105-2896.2005.00319.x (2005).

7. Bilej, M., De Baetselier, P. & Beschin, A. Antimicrobial Defense of the Earthworm. *Folia Microbiol (Praha)* **45**, 283–300 (2000).

8. Cooper, E. L. Evolution of immune systems from self/not self to danger to artificial immune systems (AIS). *Physics of Life Reviews* vol. 7 55–78 Preprint at https://doi.org/10.1016/j.plrev.2009.12.001 (2010).

9. Erwin, D. H. Early metazoan life: Divergence, environment and ecology. *Philosophical Transactions of the Royal Society B: Biological Sciences* vol. 370 Preprint at https://doi.org/10.1098/rstb.2015.0036 (2015).

10. Iwasaki, A. & Medzhitov, R. Control of adaptive immunity by the innate immune system. *Nat Immunol* **16**, 343–353 (2015).

11. Schmid-Hempel, P. Immune defence, parasite evasion strategies and their relevance for 'macroscopic phenomena' such as virulence. *Philosophical Transactions of the Royal Society B: Biological Sciences* **364**, 85–98 (2009).

12. Janeway, C. A. Approaching the asymptote? Evolution and revolution in immunology. in *Cold Spring Harbor Symposia on Quantitative Biology* vol. 54 1–13 (1989).

13. Kärre, K., Ljunggren, H. G., Piontek, G. & Kiessling, R. Selective rejection of H-2-deficient lymphoma variants suggests alternative immune defence strategy. *Nature* **319**, 675–678 (1986).

14. Xing, Y. & Hogquist, K. A. T-Cell Tolerance: Central and Peripheral. *Cold Spring Harb Perspect Biol* **4**, 1–15 (2012).

15. Wang, L., Wang, F. S. & Gershwin, M. E. Human autoimmune diseases: A comprehensive update. *Journal of Internal Medicine* vol. 278 369–395 Preprint at https://doi.org/10.1111/joim.12395 (2015).

16. Mills, D. B. The origin of phagocytosis in Earth history. *Interface Focus* **10**, (2020).

17. Desjardins, M., Houde, M. & Gagnon, E. Phagocytosis: The convoluted way from nutrition to adaptive immunity. *Immunological Reviews* vol. 207 158–165 Preprint at https://doi.org/10.1111/j.0105-2896.2005.00319.x (2005).

18. Janeway, C. A. Approaching the asymptote? Evolution and revolution in immunology. in *Cold Spring Harbor Symposia on Quantitative Biology* vol. 54 1–13 (1989).

19. Ljunggren, H. G. & Kärre, K. In search of the 'missing self': MHC molecules and NK cell recognition. *Immunol Today* **11**, 237–244 (1990).

20. Netea, M. G. *et al.* A guiding map for inflammation. *Nature Immunology* vol. 18 826–831 Preprint at https://doi.org/10.1038/ni.3790 (2017).

21. Allen, R. J. & Waclaw, B. Bacterial growth: A statistical physicist's guide. *Reports on Progress in Physics* vol. 82 016601 Preprint at https://doi.org/10.1088/1361-6633/aae546 (2019).

22. Medzhitov, R., Preston-Hurlburt, P. & Janeway, C. A. A human homologue of the Drosophila toll protein signals activation of adaptive immunity. *Nature* **388**, 394–397 (1997).

23. Hansson, G. K. & Edfeldt, K. Toll to be paid at the gateway to the vessel wall. *Arteriosclerosis, Thrombosis, and Vascular Biology* vol. 25 1085–1087 Preprint at https://doi.org/10.1161/01.ATV.0000168894.43759.47 (2005).

24. Medzhitov, R. Toll-like receptors and innate immunity. *Nature Reviews Immunology* vol. 1 135–145 Preprint at https://doi.org/10.1038/35100529 (2001).

25. Kagan, J. C. & Barton, G. M. Emerging principles governing signal transduction by Pattern-Recognition receptors. *Cold Spring Harb Perspect Biol* **7**, a016253 (2015).

26. Iwasaki, A. & Medzhitov, R. Control of adaptive immunity by the innate immune system. *Nat Immunol* **16**, 343–353 (2015).

27. Raulet, D. H. Missing self recognition and self tolerance of natural killer (NK) cells. *Semin Immunol* **18**, 145–150 (2006).

28. Colonna, M. *et al.* A common inhibitory receptor for major histocompatibility complex class I molecules on human lymphoid and myelomonocytic cells. *Journal of Experimental Medicine* **186**, 1809–1818 (1997).

29. Boehm, T. *et al.* Evolution of Alternative Adaptive Immune Systems in Vertebrates. *Annu Rev Immunol* **36**, 19–42 (2018).

30. Pamcer, Z. *et al.* Somatic diversification of variable lymphocyte receptors in the agnathan sea lamprey. *Nature* **430**, 174–180 (2004).

31. Flajnik, M. F. A cold-blooded view of adaptive immunity. *Nature Reviews Immunology* vol. 18 438–453 Preprint at https://doi.org/10.1038/s41577-018-0003-9 (2018).

32. Flajnik, M. F. & Kasahara, M. Origin and evolution of the adaptive immune system: Genetic events and selective pressures. *Nature Reviews Genetics* vol. 11 47–59 Preprint at https://doi.org/10.1038/nrg2703 (2010).

33. Klein, J. & O'hUigin, C. Composite origin of major histocompatibility complex genes. *Curr Opin Genet Dev* **3**, 923–930 (1993).

34. Kaufman, J. The new W family reconstructs the evolution of MHC genes. *Proceedings of the National Academy of Sciences of the United States of America* vol. 119 e2122079119 Preprint at https://doi.org/10.1073/pnas.2122079119 (2022).

35. Wieczorek, M. *et al.* Major histocompatibility complex (MHC) class I and MHC class II proteins: Conformational plasticity in antigen presentation. *Frontiers in Immunology* vol. 8 292 Preprint at https://doi.org/10.3389/fimmu.2017.00292 (2017).

36. Shiku, H. *et al.* Expression of T cell differentiation antigens on effector cells in cell mediated cytotoxicity in vitro. Evidence for functional heterogeneity related to the surface phenotype of T cells. *Journal of Experimental Medicine* **141**, 227–241 (1975).

37. Cantor, H. & Boyse, E. A. Regulation of Cellular and Humoral Immune Responses by T-cell Subclasses. *Cold Spring Harb Symp Quant Biol* **41**, 23–32 (1977).

38. Kwak, K., Akkaya, M. & Pierce, S. K. B cell signaling in context. *Nat Immunol* (2019) doi:10.1038/s41590-019-0427-9.

39. Orenstein, W. A., Seib, K., Graham-Rowe, D. & Berkley, S. Contemporary vaccine challenges: Improving global health one shot at a time. *Science Translational Medicine* vol. 6 Preprint at https://doi.org/10.1126/scitranslmed.3009848 (2014).

40. Eberl, G., Colonna, M., Santo, J. P. D. & McKenzie, A. N. J. Innate lymphoid cells: A new paradigm in immunology. *Science* vol. 348 Preprint at https://doi.org/10.1126/science.aaa6566 (2015).

41. Krangel, M. S. Mechanics of T cell receptor gene rearrangement. *Current Opinion in Immunology* vol. 21 133–139 Preprint at https://doi.org/10.1016/j.coi.2009.03.009 (2009).

42. Jung, D., Giallourakis, C., Mostoslavsky, R. & Alt, F. W. Mechanism and control of V(D)J recombination at the immunoglobulin heavy chain locus. *Annual Review of Immunology* vol. 24 541–570 Preprint at https://doi.org/10.1146/annurev.immunol.23.021704.115830 (2006).

43. Sun, J. C. & Lanier, L. L. NK cell development, homeostasis and function: Parallels with CD8+ T cells. *Nature Reviews Immunology* vol. 11 645–657 Preprint at https://doi.org/10.1038/nri3044 (2011).

44. Klein, L., Kyewski, B., Allen, P. M. & Hogquist, K. A. Positive and negative selection of the T cell repertoire: What thymocytes see (and don't see). *Nature Reviews Immunology* vol. 14 377–391 Preprint at https://doi.org/10.1038/nri3667 (2014).

45. Arstila, T. P. *et al.* A direct estimate of the human αβ T cell receptor diversity. *Science (1979)* **286**, 958–961 (1999).

46. Klein, L., Kyewski, B., Allen, P. M. & Hogquist, K. A. Positive and negative selection of the T cell repertoire: What thymocytes see (and don't see). *Nature Reviews Immunology* vol. 14 377–391 Preprint at https://doi.org/10.1038/nri3667 (2014).

47. Van Laethem, F. *et al.* Lck availability during thymic selection determines the recognition specificity of the T cell repertoire. *Cell* **154**, 1326 (2013).

48. Shinzawa, M. *et al.* Reversal of the T cell immune system reveals the molecular basis for T cell lineage fate determination in the thymus. *Nat Immunol* **23**, 731–742 (2022).

49. Besnard, M., Padonou, F., Provin, N., Giraud, M. & Guillonneau, C. Aire deficiency, from preclinical models to human apeced disease. *DMM Disease Models and Mechanisms* vol. 14 Preprint at https://doi.org/10.1242/DMM.046359 (2021).

50. Venanzi, E. S., Melamed, R., Mathis, D. & Benoist, C. The variable immunological self: Genetic variation and nongenetic noise in Aire-regulated transcription. *Proc Natl Acad Sci U S A* **105**, 15860–15865 (2008).

51. Palmer, E. Negative selection - Clearing out the bad apples from the T-cell repertoire. *Nature Reviews Immunology* vol. 3 383–391 Preprint at https://doi.org/10.1038/nri1085 (2003).

52. Surh, C. D. & Sprent, J. T-cell apoptosis detected in situ during positive and negative selection in the thymus. *Nature* **372**, 100–103 (1994).

53. Rothenberg, E. V., Moore, J. E. & Yui, M. A. Launching the T-cell-lineage developmental programme. *Nat Rev Immunol* **8**, 9–21 (2008).

54. Lebien, T. W. & Tedder, T. F. B lymphocytes: How they develop and function. *Blood* **112**, 1570–1580 (2008).

55. Nemazee, D. Mechanisms of central tolerance for B cells. *Nature Reviews Immunology* vol. 17 281–294 Preprint at https://doi.org/10.1038/nri.2017.19 (2017).

56. Sun, J. C. & Lanier, L. L. NK cell development, homeostasis and function: Parallels with CD8+ T cells. *Nature Reviews Immunology* vol. 11 645–657 Preprint at https://doi.org/10.1038/nri3044 (2011).

57. Saravia, J., Chapman, N. M. & Chi, H. Helper T cell differentiation. *Cellular and Molecular Immunology* vol. 16 634–643 Preprint at https://doi.org/10.1038/s41423-019-0220-6 (2019).

58. Saravia, J., Chapman, N. M. & Chi, H. Helper T cell differentiation. *Cellular and Molecular Immunology* vol. 16 634–643 Preprint at https://doi.org/10.1038/s41423-019-0220-6 (2019).

59. Shevach, E. M. & Thornton, A. M. tTregs, pTregs, and iTregs: Similarities and differences. *Immunol Rev* **259**, 88–102 (2014).

60. Zhang, N. & Bevan, M. J. CD8+ T Cells: Foot Soldiers of the Immune System. *Immunity* vol. 35 161–168 Preprint at https://doi.org/10.1016/j.immuni.2011.07.010 (2011).

61. Bluestone, J., Mackay, C., O'Shea, J. & Stockinger, B. The functional plasticity of T cell subsets. *Nat Rev Immunol* **9**, 811–816 (2009).

62. De Silva, N. S. & Klein, U. Dynamics of B cells in germinal centres. *Nat Rev Immunol* **15**, 137–148 (2015).

63. Kwak, K., Akkaya, M. & Pierce, S. K. B cell signaling in context. *Nat Immunol* (2019) doi:10.1038/s41590-019-0427-9.

64. Raulet, D. H. Interplay of natural killer cells and their receptors with the adaptive immune response. *Nat Immunol* **5**, 996–1002 (2004).

65. Huang, J. *et al.* A Single peptide-major histocompatibility complex ligand triggers digital cytokine secretion in CD4+ T Cells. *Immunity* **39**, 846–857 (2013).

66. Natkanski, E. *et al.* B cells use mechanical energy to discriminate antigen affinities. *Science (1979)* **340**, 1587–1590 (2013).

67. Courtney, A. H., Lo, W. L. & Weiss, A. TCR Signaling: Mechanisms of Initiation and Propagation. *Trends in Biochemical Sciences* vol. 43 108–123 Preprint at https://doi.org/10.1016/j.tibs.2017.11.008 (2018).

68. Smith-Garvin, J. E., Koretzky, G. A. & Jordan, M. S. T cell activation. *Annu Rev Immunol* **27**, 591–619 (2009).

69. Dal Porto, J. M. *et al.* B cell antigen receptor signaling 101. *Mol Immunol* **41**, 599–613 (2004).

70. Barten, R., Torkar, M., Haude, A., Trowsdale, J. & Wilson, M. J. Divergent and convergent evolution of NK-cell receptors. *Trends Immunol* **22**, 52–57 (2001).

71. Carrillo-Bustamante, P., Keşmir, C. & de Boer, R. J. The evolution of natural killer cell receptors. *Immunogenetics* vol. 68 3–18 Preprint at https://doi.org/10.1007/s00251-015-0869-7 (2016).

72. Gaud, G., Lesourne, R. & Love, P. E. Regulatory mechanisms in T cell receptor signalling. *Nat Rev Immunol* **18**, 485–497 (2018).

73. Zinkernagel, R. M. & Doherty, P. C. Restriction of in vitro T cell-mediated cytotoxicity in lymphocytic choriomeningitis within a syngeneic or semiallogeneic system. *Nature* **248**, 701–702 (1974).

74. Dong, D. *et al.* Structural basis of assembly of the human T cell receptor–CD3 complex. *Nature* **573**, 546–552 (2019).

75. Sušac, L. *et al.* Structure of a fully assembled tumor-specific T cell receptor ligated by pMHC. *Cell* **185**, 3201-3213.e19 (2022).

76. Yin, L. *et al.* A single T cell receptor bound to major histocompatibility complex class I and class II glycoproteins reveals switchable TCR conformers. *Immunity* **35**, 23–33 (2011).

77. Übelhart, R. *et al.* Responsiveness of B cells is regulated by the hinge region of IgD. *Nat Immunol* **16**, 534–543 (2015).

78. Tolar, P. & Pierce, S. K. Unveiling the B cell receptor structure. *Science (1979)* **377**, 819–820 (2022).

79. Wong, W. K., Leem, J. & Leem, J. Comparative Analysis of the CDR Loops of Antigen Receptors. *Front Immunol* **10**, 2454 (2019).

80. Tan, J. *et al.* A LAIR1 insertion generates broadly reactive antibodies against malaria variant antigens. *Nature* **529**, 105–109 (2016).

81. Hsieh, F. L. & Higgins, M. K. The structure of a LAIR1-containing human antibody reveals a novel mechanism of antigen recognition. *Elife* **6**, (2017).

82. Barten, R., Torkar, M., Haude, A., Trowsdale, J. & Wilson, M. J. Divergent and convergent evolution of NK-cell receptors. *Trends Immunol* **22**, 52–57 (2001).

83. Carrillo-Bustamante, P., Keşmir, C. & de Boer, R. J. The evolution of natural killer cell receptors. *Immunogenetics* vol. 68 3–18 Preprint at https://doi.org/10.1007/s00251-015-0869-7 (2016).

84. Hirayasu, K. & Arase, H. Functional and genetic diversity of leukocyte immunoglobulin-like receptor and implication for disease associations. *Journal of Human Genetics* vol. 60 703–708 Preprint at https://doi.org/10.1038/jhg.2015.64 (2015).

85. Cosman, D. *et al.* A novel immunoglobulin superfamily receptor for cellular and viral MHC class I molecules. *Immunity* **7**, 273–282 (1997).

86. Harrison, T. E. *et al.* Structural basis for RIFIN-mediated activation of LILRB1 in malaria. *Nature* (2020) doi:10.1038/s41586-020-2530-3.

87. Thill, P. A., Weiss, A. & Chakraborty, A. K. Phosphorylation of a Tyrosine Residue on Zap70 by Lck and Its Subsequent Binding via an SH2 Domain May Be a Key Gatekeeper of T Cell Receptor Signaling In Vivo. *Mol Cell Biol* **36**, 2396–2402 (2016).

88. Smith-Garvin, J. E., Koretzky, G. A. & Jordan, M. S. T cell activation. *Annu Rev Immunol* **27**, 591–619 (2009).

89. Courtney, A. H., Lo, W. L. & Weiss, A. TCR Signaling: Mechanisms of Initiation and Propagation. *Trends in Biochemical Sciences* vol. 43 108–123 Preprint at https://doi.org/10.1016/j.tibs.2017.11.008 (2018).

90. Mariuzza, R. A., Agnihotri, P. & Orban, J. The structural basis of T-cell receptor (TCR) activation: An enduring enigma. *Journal of Biological Chemistry* **295**, 914–925 (2020).

91. Schamel, W. W. A. *et al.* Coexistence of multivalent and monovalent TCRs explains high sensitivity and wide range of response. *Journal of Experimental Medicine* **202**, 493–503 (2005).

92. Lillemeier, B. F. *et al.* TCR and Lat are expressed on separate protein islands on T cell membranes and concatenate during activation. *Nat Immunol* **11**, 90–96 (2010).

93. Santos, A. M. *et al.* Capturing resting T cells: The perils of PLL. *Nature Immunology* vol. 19 203–205 Preprint at https://doi.org/10.1038/s41590-018-0048-8 (2018).

94. Annibale, P., Vanni, S., Scarselli, M., Rothlisberger, U. & Radenovic, A. Quantitative Photo Activated Localization Microscopy: Unraveling the effects of photoblinking. *PLoS One* **6**, e22678 (2011).

95. Burgert, A., Letschert, S., Doose, S. & Sauer, M. Artifacts in single-molecule localization microscopy. *Histochem Cell Biol* **144**, 123–131 (2015).

96. James, J. R. *et al.* Single-molecule level analysis of the subunit composition of the T cell receptor on live T cells. *Proc Natl Acad Sci U S A* **104**, 17662–17667 (2007).

97. James, J. R. *et al.* The T cell receptor triggering apparatus is composed of monovalent or monomeric proteins. *Journal of Biological Chemistry* **286**, 31993–32001 (2011).

98. Rossboth, B. *et al.* TCRs are randomly distributed on the plasma membrane of resting antigen-experienced T cells. *Nat Immunol* **19**, 821–827 (2018).

99. Brameshuber, M. *et al.* Monomeric TCRs drive T cell antigen recognition. *Nat Immunol* **19**, 487–496 (2018).

100. Hong, J. *et al.* A TCR mechanotransduction signaling loop induces negative selection in the thymus. *Nat Immunol* **19**, 1379–1390 (2018).

101. Fernandes, R. A. *et al.* A cell topography-based mechanism for ligand discrimination by the T cell receptor. *Proc Natl Acad Sci U S A* **116**, 14002–14010 (2019).

102. Brownlie, R. J. & Zamoyska, R. T cell receptor signalling networks: Branched, diversified and bounded. *Nature Reviews Immunology* vol. 13 257–269 Preprint at https://doi.org/10.1038/nri3403 (2013).

103. Kurosaki, T., Shinohara, H. & Baba, Y. B cell signaling and fate decision. *Annual Review of Immunology* vol. 28 21–55 Preprint at https://doi.org/10.1146/annurev.immunol.021908.132541 (2010).

104. Dal Porto, J. M. *et al.* B cell antigen receptor signaling 101. *Mol Immunol* **41**, 599–613 (2004).

105. Treanor, B. B-cell receptor: From resting state to activate. *Immunology* vol. 136 21–27 Preprint at https://doi.org/10.1111/j.1365-2567.2012.03564.x (2012).

106. Depoil, D. *et al.* CD19 is essential for B cell activation by promoting B cell receptor-antigen microcluster formation in response to membrane-bound ligand. *Nat Immunol* **9**, 63–72 (2008).

107. Harwood, N. E. & Batista, F. D. Early events in B cell activation. *Annual Review of Immunology* vol. 28 185–210 Preprint at https://doi.org/10.1146/annurev-immunol-030409-101216 (2010).

108. Vivier, E., Nunès, J. A. & Vély, F. Natural killer cell signaling pathways. *Science (1979)* **306**, 1517–1519 (2004).

109. Vivier, E., Nunès, J. A. & Vély, F. Natural killer cell signaling pathways. *Science (1979)* **306**, 1517–1519 (2004).

110. Gismondi, A. *et al.* Impaired natural and CD16-mediated NK cell cytotoxicity in patients with WAS and XLT: Ability of IL-2 to correct NK cell functional defect. *Blood* **104**, 436–443 (2004).

111. Razi, N. & Varki, A. Masking and unmasking of the sialic acid-binding lectin activity of CD22 (Siglec-2) on B lymphocytes. *Proc Natl Acad Sci U S A* **95**, 7469–7474 (1998).

112. Collins, B. E. *et al.* Masking of CD22 by cis ligands does not prevent redistribution of CD22 to sites of cell contact. *Proc Natl Acad Sci U S A* **101**, 6104–6109 (2004).

113. Collins, B. E. *et al.* High-Affinity Ligand Probes of CD22 Overcome the Threshold Set by cis Ligands to Allow for Binding, Endocytosis, and Killing of B Cells. *The Journal of Immunology* **177**, 2994–3003 (2006).

114. Nitschke, L. CD22 and Siglec-G: B-cell inhibitory receptors with distinct functions. *Immunol Rev* **230**, 128–143 (2009).

115. Zhao, Y. *et al.* PD-L1:CD80 Cis-Heterodimer Triggers the Co-stimulatory Receptor CD28 While Repressing the Inhibitory PD-1 and CTLA-4 Pathways. *Immunity* **51**, 1059-1073.e9 (2019).

116. Held, W. & Mariuzza, R. A. Cis-trans interactions of cell surface receptors: biological roles and structural basis. *Cellular and Molecular Life Sciences* **68**, 3469–3478 (2011).

117. Held, W. & Mariuzza, R. A. Cis interactions of immunoreceptors with MHC and non-MHC ligands. *Nature Reviews Immunology* vol. 8 269–278 Preprint at https://doi.org/10.1038/nri2278 (2008).

118. Li, B. *et al.* Cis interactions between CD2 and its ligands on T cells are required for T cell activation. *Sci Immunol* **7**, eabn6373 (2022).

119. Zhao, Y. *et al.* Antigen-Presenting Cell-Intrinsic PD-1 Neutralizes PD-L1 in cis to Attenuate PD-1 Signaling in T Cells. *Cell Rep* **24**, 379-390.e6 (2018).

120. Held, W. & Mariuzza, R. A. Cis interactions of immunoreceptors with MHC and non-MHC ligands. *Nature Reviews Immunology* vol. 8 269–278 Preprint at https://doi.org/10.1038/nri2278 (2008).

121. Held, W. & Mariuzza, R. A. Cis-trans interactions of cell surface receptors: biological roles and structural basis. *Cellular and Molecular Life Sciences* **68**, 3469–3478 (2011).

122. Zhao, Y. *et al.* PD-L1:CD80 Cis-Heterodimer Triggers the Co-stimulatory Receptor CD28 While Repressing the Inhibitory PD-1 and CTLA-4 Pathways. *Immunity* **51**, 1059-1073.e9 (2019).

123. Li, B. *et al.* Cis interactions between CD2 and its ligands on T cells are required for T cell activation. *Sci Immunol* **7**, eabn6373 (2022).

124. Sharma, P. & Allison, J. P. Immune checkpoint targeting in cancer therapy: Toward combination strategies with curative potential. *Cell* vol. 161 205–214 Preprint at https://doi.org/10.1016/j.cell.2015.03.030 (2015).

125. Mahoney, K. M. *et al.* A secreted PD-L1 splice variant that covalently dimerizes and mediates immunosuppression. *Cancer Immunology, Immunotherapy* **68**, 421–432 (2019).

126. Patsoukis, N., Wang, Q., Strauss, L. & Boussiotis, V. A. Revisiting the PD-1 pathway. *Sci Adv* **6**, (2020).

127. Zhang, X. *et al.* Structural and functional analysis of the costimulatory receptor programmed death-1. *Immunity* **20**, 337–347 (2004).

128. Zak, K. M. *et al.* Structure of the Complex of Human Programmed Death 1, PD-1, and Its Ligand PD-L1. *Structure* **23**, 2341–2348 (2015).

129. Janeway, C. A. Accessories or coreceptors? *Nature* **335**, 208–210 (1988).

130. Rudd, C. E. CD4, CD8 and the TCR-CD3 complex: a novel class of protein-tyrosine kinase receptor. *Immunology Today* vol. 11 400–406 Preprint at https://doi.org/10.1016/0167-5699(90)90159-7 (1990).

131. Mørch, A. M., Bálint, Š., Santos, A. M., Davis, S. J. & Dustin, M. L. Coreceptors and TCR Signaling – the Strong and the Weak of It. *Frontiers in Cell and Developmental Biology* vol. 8 1147 Preprint at https://doi.org/10.3389/fcell.2020.597627 (2020).

132. Li, Q. J. *et al.* CD4 enhances T cell sensitivity to antigen by coordinating Lck accumulation at the immunological synapse. *Nat Immunol* **5**, 791–799 (2004).

133. Artyomov, M. N., Lis, M., Devadas, S., Davis, M. M. & Chakraborty, A. K. CD4 and CD8 binding to MHC molecules primarily acts to enhance Lck delivery. *Proceedings of the National Academy of Sciences* **107**, 16916–16921 (2010).

134. Van Laethem, F. *et al.* Lck availability during thymic selection determines the recognition specificity of the T cell repertoire. *Cell* **154**, 1326 (2013).

135. Carmo, A. M., Mason, D. W. & Beyers, A. D. Physical association of the cytoplasmic domain of CD2 with the tyrosine kinases p56lck and p59fyn. *Eur J Immunol* **23**, 2196–2201 (1993).

136. Wiest, D. L. *et al.* Regulation of T cell receptor expression in immature CD4+CD8+ thymocytes by p56lck tyrosine kinase: basis for differential signaling by CD4 and CD8 in immature thymocytes expressing both coreceptor molecules. *Journal of Experimental Medicine* **178**, 1701–1712 (1993).

137. Stepanek, O. *et al.* Coreceptor scanning by the T cell receptor provides a mechanism for T cell tolerance. *Cell* **159**, 333–345 (2014).

138. Parrish, H. L., Deshpande, N. R., Vasic, J. & Kuhns, M. S. Functional evidence for TCR-intrinsic specificity for MHCII. *Proc Natl Acad Sci U S A* **113**, 3000–3005 (2016).

139. Kappes, D. J. CD4 and CD8: Hogging All the Lck. *Immunity* vol. 27 691–693 Preprint at https://doi.org/10.1016/j.immuni.2007.11.002 (2007).

140. Mørch, A. M., Bálint, Š., Santos, A. M., Davis, S. J. & Dustin, M. L. Coreceptors and TCR Signaling – the Strong and the Weak of It. *Frontiers in Cell and Developmental Biology* vol. 8 1147 Preprint at https://doi.org/10.3389/fcell.2020.597627 (2020).

141. Colonna, M. *et al.* A common inhibitory receptor for major histocompatibility complex class I molecules on human lymphoid and myelomonocytic cells. *Journal of Experimental Medicine* **186**, 1809–1818 (1997).

142. Mori, Y. *et al.* Inhibitory Immunoglobulin-Like Receptors LILRB and PIR-B Negatively Regulate Osteoclast Development. *The Journal of Immunology* **181**, 4742–4751 (2008).

143. Saito, F. *et al.* Immune evasion of Plasmodium falciparum by RIFIN via inhibitory receptors. *Nature* **552**, 101–105 (2017).

144. Razi, N. & Varki, A. Masking and unmasking of the sialic acid-binding lectin activity of CD22 (Siglec-2) on B lymphocytes. *Proc Natl Acad Sci U S A* **95**, 7469–7474 (1998).

145. Mori, Y. *et al.* Inhibitory Immunoglobulin-Like Receptors LILRB and PIR-B Negatively Regulate Osteoclast Development. *The Journal of Immunology* **181**, 4742–4751 (2008).

146. Buzas, E. I. The roles of extracellular vesicles in the immune system. *Nature Reviews Immunology* 1–15 Preprint at https://doi.org/10.1038/s41577-022-00763-8 (2022).

147. Hayashida, K., Bartlett, A. H., Chen, Y. & Park, P. W. Molecular and cellular mechanisms of ectodomain shedding. *Anatomical Record* vol. 293 925–937 Preprint at https://doi.org/10.1002/ar.20757 (2010).

148. Pettmann, J., Santos, A. M., Dushek, O. & Davis, S. J. Membrane ultrastructure and T cell activation. *Frontiers in Immunology* vol. 9 2152 Preprint at https://doi.org/10.3389/fimmu.2018.02152 (2018).

149. Anderson, N. G. Co-immunoprecipitation. Identification of interacting proteins. *Methods in Molecular Biology* **88**, 35–45 (1998).

150. Schrum, A. G. *et al.* High-sensitivity detection and quantitative analysis of native protein-protein interactions and multiprotein complexes by flow cytometry. *Sci STKE* **2007**, pl2 (2007).

151. Pattnaik, P. Surface plasmon resonance: Applications in understanding receptor-ligand interaction. *Applied Biochemistry and Biotechnology* vol. 126 79–92 Preprint at https://doi.org/10.1385/abab:126:2:079 (2005).

152. Cooper, M. A. Advances in membrane receptor screening and analysis. *Journal of Molecular Recognition* vol. 17 286–315 Preprint at https://doi.org/10.1002/jmr.675 (2004).

153. Dunn, K. W., Kamocka, M. M. & McDonald, J. H. A practical guide to evaluating colocalization in biological microscopy. *American Journal of Physiology - Cell Physiology* vol. 300 723–742 Preprint at https://doi.org/10.1152/ajpcell.00462.2010 (2011).

154. Manzo, C. & Garcia-Parajo, M. F. A review of progress in single particle tracking: From methods to biophysical insights. *Reports on Progress in Physics* **78**, 124601 (2015).

155. Orte, A., Clarke, R. & Klenerman, D. Single-molecule two-colour coincidence detection to probe biomolecular associations. *Biochemical Society Transactions* vol. 38 914–918 Preprint at https://doi.org/10.1042/BST0380914 (2010).

156. Kenakin, T. The mass action equation in pharmacology. *Br J Clin Pharmacol* **81**, 41–51 (2016).

157. Algar, W. R., Hildebrandt, N., Vogel, S. S. & Medintz, I. L. FRET as a biomolecular research tool — understanding its potential while avoiding pitfalls. *Nat Methods* **16**, 815–829 (2019).

158. Algar, W. R., Hildebrandt, N., Vogel, S. S. & Medintz, I. L. FRET as a biomolecular research tool — understanding its potential while avoiding pitfalls. *Nat Methods* **16**, 815–829 (2019).

159. Datta, R., Heaster, T. M., Sharick, J. T., Gillette, A. A. & Skala, M. C. Fluorescence lifetime imaging microscopy: fundamentals and advances in instrumentation, analysis, and applications. *J Biomed Opt* **25**, 1 (2020).

160. Roy, R., Hohng, S. & Ha, T. A practical guide to single-molecule FRET. *Nature Methods* vol. 5 507–516 Preprint at https://doi.org/10.1038/nmeth.1208 (2008).

161. Magde, D., Elson, E. & Webb, W. W. Thermodynamic fluctuations in a reacting system measurement by fluorescence correlation spectroscopy. *Phys Rev Lett* **29**, 705–708 (1972).

162. Krieger, J. W. *et al.* Imaging fluorescence (cross-) correlation spectroscopy in live cells and organisms. *Nat Protoc* **10**, 1948–1974 (2015).

163. Mørch, A. M. & Schneider, F. Investigating diffusion dynamics and interactions with scanning fluorescence correlation spectroscopy (sFCS). in *Methods in Molecular Biology* (eds. Baldari, C. T. & Dustin, M. L.) In press (Springer, 2023).

164. Schwille, P. & Haustein, E. Fluorescence correlation spectroscopy. *A tutorial for the Biophysics Textbook Online (BTOL)* (2002).

165. Céspedes, P. F. *et al.* T-cell trans-synaptic vesicles are distinct and carry greater effector content than constitutive extracellular vesicles. *Nat Commun* **13**, 1–18 (2022).

166. Zufferey, R., Nagy, D., Mandel, R. J., Naldini, L. & Trono, D. Multiply attenuated lentiviral vector achieves efficient gene delivery in vivo. *Nat Biotechnol* **15**, 871–875 (1997).

167. Dustin, M. L., Starr, T., Varma, R. & Thomas, V. K. Supported planar bilayers for study of the immunological synapse. *Curr Protoc Immunol* **Chapter 18**, 18.13.1-18.13.35 (2007).

168. Alanine, D. G. W. *et al.* Human Antibodies that Slow Erythrocyte Invasion Potentiate Malaria-Neutralizing Antibodies. *Cell* **178**, 216-228.e21 (2019).

169. Dunsing, V. *et al.* Optimal fluorescent protein tags for quantifying protein oligomerization in living cells. *Sci Rep* **8**, 1–12 (2018).

170. Schindelin, J. *et al.* Fiji: An open-source platform for biological-image analysis. *Nature Methods* vol. 9 676–682 Preprint at https://doi.org/10.1038/nmeth.2019 (2012).

171. Otsu, N. A Threshold Selection Method from Gray-Level Histograms. *IEEE Trans Syst Man Cybern* **SMC-9**, 62–66 (1979).

172. Waithe, D. *et al.* Optimized processing and analysis of conventional confocal microscopy generated scanning FCS data. *Methods* **140–141**, 62–73 (2018).

173. Bacia, K., Kim, S. A. & Schwille, P. Fluorescence cross-correlation spectroscopy in living cells. *Nat Methods* **3**, 83–89 (2006).

174. Krieger, J. W. *et al.* Imaging fluorescence (cross-) correlation spectroscopy in live cells and organisms. *Nat Protoc* **10**, 1948–1974 (2015).

175. Petrášek, Z. & Schwille, P. Precise measurement of diffusion coefficients using scanning fluorescence correlation spectroscopy. *Biophys J* **94**, 1437–1448 (2008).

176. Magde, D., Elson, E. L. & Webb, W. W. Fluorescence correlation spectroscopy. II. An experimental realization. *Biopolymers* **13**, 29–61 (1974).

177. Magde, D., Elson, E. & Webb, W. W. Thermodynamic fluctuations in a reacting system measurement by fluorescence correlation spectroscopy. *Phys Rev Lett* **29**, 705–708 (1972).

178. Widengren, J., Mets, Ü. & Rigler, R. Fluorescence correlation spectroscopy of triplet states in solution: A theoretical and experimental study. *Journal of Physical Chemistry* **99**, 13368–13379 (1995).

179. Ehrenberg, M. & Rigler, R. Rotational brownian motion and fluorescence intensify fluctuations. *Chem Phys* **4**, 390–401 (1974).

180. Widengren, J. & Rigler, R. Mechanisms of photobleaching investigated by fluorescence correlation spectroscopy. *Bioimaging* **4**, 149–157 (1996).

181. Kim, S. A., Heinze, K. G. & Schwille, P. Fluorescence correlation spectroscopy in living cells. *Nat Methods* **4**, 963–973 (2007).

182. Hink, M. A. Fluorescence correlation spectroscopy. *Methods in Molecular Biology* **1251**, 135–150 (2014).

183. Priest, D. G., Solano, A., Lou, J. & Hinde, E. Fluorescence fluctuation spectroscopy: An invaluable microscopy tool for uncovering the biophysical rules for navigating the nuclear landscape. *Biochemical Society Transactions* vol. 47 1117–1129 Preprint at https://doi.org/10.1042/BST20180604 (2019).

184. Elson, E. L. Fluorescence correlation spectroscopy: Past, present, future. *Biophysical Journal* vol. 101 2855–2870 Preprint at https://doi.org/10.1016/j.bpj.2011.11.012 (2011).

185. Digman, M. A. & Gratton, E. Lessons in fluctuation correlation spectroscopy. *Annu Rev Phys Chem* **62**, 645–668 (2011).

186. Rigler, R. & Mets, U. Diffusion of single molecules through a Gaussian laser beam. in *Laser Spectroscopy of Biomolecules* vol. 1921 239 (SPIE, 1993).

187. Schneider, F., Colin-York, H. & Fritzsche, M. Quantitative Bio-Imaging Tools to Dissect the Interplay of Membrane and Cytoskeletal Actin Dynamics in Immune Cells. *Frontiers in Immunology* vol. 11 1–13 Preprint at https://doi.org/10.3389/fimmu.2020.612542 (2021).

188. Digman, M. A. & Gratton, E. Lessons in fluctuation correlation spectroscopy. *Annu Rev Phys Chem* **62**, 645–668 (2011).

189. Petersen, N. O. Scanning fluorescence correlation spectroscopy. I. Theory and simulation of aggregation measurements. *Biophys J* **49**, 809–815 (1986).

190. Gunther, G., Jameson, D. M., Aguilar, J. & Sánchez, S. A. Scanning fluorescence correlation spectroscopy comes full circle. *Methods* vols 140–141 52–61 Preprint at https://doi.org/10.1016/j.ymeth.2018.01.023 (2018).

191. Sankaran, J., Manna, M., Guo, L., Kraut, R. & Wohland, T. Diffusion, transport, and cell membrane organization investigated by imaging fluorescence cross-correlation spectroscopy. *Biophys J* **97**, 2630–2639 (2009).

192. Kastrup, L., Blom, H., Eggeling, C. & Hell, S. W. Fluorescence fluctuation spectroscopy in subdiffraction focal volumes. *Phys Rev Lett* **94**, 178104 (2005).

193. Digman, M. A. & Gratton, E. Imaging barriers to diffusion by pair correlation functions. *Biophys J* **97**, 665–673 (2009).

194. Wennmalm, S., Thyberg, P., Xu, L. & Widengren, J. Inverse-fluorescence correlation spectroscopy. *Anal Chem* **81**, 9209–9215 (2009).

195. Wohland, T., Shi, X., Sankaran, J. & Stelzer, E. H. K. Single Plane Illumination Fluorescence Correlation Spectroscopy (SPIM-FCS) probes inhomogeneous three-dimensional environments. *Opt Express* **18**, 10627 (2010).

196. Baum, M., Erdel, F., Wachsmuth, M. & Rippe, K. Retrieving the intracellular topology from multi-scale protein mobility mapping in living cells. *Nat Commun* **5**, 1–12 (2014).

197. Ruan, Q., Cheng, M. A., Levi, M., Gratton, E. & Mantulin, W. W. Spatial-temporal studies of membrane dynamics: Scanning fluorescence correlation spectroscopy (SFCS). *Biophys J* **87**, 1260–1267 (2004).

198. Sankaran, J., Manna, M., Guo, L., Kraut, R. & Wohland, T. Diffusion, transport, and cell membrane organization investigated by imaging fluorescence cross-correlation spectroscopy. *Biophys J* **97**, 2630–2639 (2009).

199. Bag, N. & Wohland, T. Imaging fluorescence fluctuation spectroscopy: New tools for quantitative bioimaging. *Annu Rev Phys Chem* **65**, 225–248 (2014).

200. Waithe, D. Open-source browser-based software simplifies fluorescence correlation spectroscopy data analysis. *Nature Photonics* vol. 15 790–791 Preprint at https://doi.org/10.1038/s41566-021-00876-x (2021).

201. Waithe, D. *et al.* Optimized processing and analysis of conventional confocal microscopy generated scanning FCS data. *Methods* **140–141**, 62–73 (2018).

202. Rossow, M. J., Sasaki, J. M., Digman, M. A. & Gratton, E. Raster image correlation spectroscopy in live cells. *Nat Protoc* **5**, 1761–1774 (2010).

203. Digman, M. A., Wiseman, P. W., Horwitz, A. R. & Gratton, E. Detecting protein complexes in living cells from laser scanning confocal image sequences by the cross correlation raster image spectroscopy method. *Biophys J* **96**, 707–716 (2009).

204. Petersen, N. O., Höddelius, P. L., Wiseman, P. W., Seger, O. & Magnusson, K. E. Quantitation of membrane receptor distributions by image correlation spectroscopy: concept and application. *Biophys J* **65**, 1135–1146 (1993).

205. Keating, E., Nohe, A. & Petersen, N. O. Studies of distribution, location and dynamic properties of EGFR on the cell surface measured by image correlation spectroscopy. *European Biophysics Journal* **37**, 469–481 (2008).

206. Bag, N. & Wohland, T. Imaging fluorescence fluctuation spectroscopy: New tools for quantitative bioimaging. *Annu Rev Phys Chem* **65**, 225–248 (2014).

207. Kim, S. A., Heinzet, K. G., Waxham, M. N. & Schwille, P. Intracellular calmodulin availability accessed with two-photon cross-correlation. *Proc Natl Acad Sci U S A* **101**, 105–110 (2004).

208. Baudendistel, M., Müller, G., Waldeck, W., Angel, P. & Langowski, J. Two-hybrid fluorescence cross-correlation spectroscopy detects protein-protein interactions in vivo. *ChemPhysChem* **6**, 984–990 (2005).

209. Bacia, K., Majoul, I. V. & Schwille, P. Probing the endocytic pathway in live cells using dual-color fluorescence cross-correlation analysis. *Biophys J* **83**, 1184–1193 (2002).

210. Vámosi, G. *et al.* IL-2 and IL-15 receptor α-subunits are coexpressed in a supramolecular receptor cluster in lipid rafts of T cells. *Proc Natl Acad Sci U S A* **101**, 11082–11087 (2004).

211. Mørch, A. M. & Schneider, F. Investigating diffusion dynamics and interactions with scanning fluorescence correlation spectroscopy (sFCS). in *Methods in Molecular Biology* (eds. Baldari, C. T. & Dustin, M. L.) In press (Springer, 2023).

212. Burkhardt, M., Heinze, K. G. & Schwille, P. Four-color fluorescence correlation spectroscopy realized in a grating-based detection platform. *Opt Lett* **30**, 2266 (2005).

213. Dunsing, V., Petrich, A. & Chiantia, S. Multi-color fluorescence fluctuation spectroscopy in living cells via spectral detection. *Elife* **10**, 1–33 (2021).

214. Schneider, F., Sych, T., Eggeling, C. & Sezgin, E. Influence of nanobody binding on fluorescence emission, mobility, and organization of GFP-tagged proteins. *iScience* **24**, 101891 (2021).

215. Schneider, F. *et al.* Statistical Analysis of Scanning Fluorescence Correlation Spectroscopy Data Differentiates Free from Hindered Diffusion. *ACS Nano* **12**, 8540–8546 (2018).

216. Schneider, F. *et al.* Statistical Analysis of Scanning Fluorescence Correlation Spectroscopy Data Differentiates Free from Hindered Diffusion. *ACS Nano* **12**, 8540–8546 (2018).

217. Sankaran, J., Shi, X., Ho, L. Y., Stelzer, E. H. K. & Wohland, T. ImFCS: A software for Imaging FCS data analysis and visualization. *Opt Express* **18**, 25468 (2010).

218. NUS. Imaging FCS - a plugin for ImageJ. 56 (2019).

219. Dunsing, V. *et al.* Optimal fluorescent protein tags for quantifying protein oligomerization in living cells. *Sci Rep* **8**, 1–12 (2018).

220. Lambert, T. J. FPbase: a community-editable fluorescent protein database. *Nature Methods* vol. 16 277–278 Preprint at https://doi.org/10.1038/s41592-019-0352-8 (2019).

221. Waithe, D. Open-source browser-based software simplifies fluorescence correlation spectroscopy data analysis. *Nature Photonics* vol. 15 790–791 Preprint at https://doi.org/10.1038/s41566-021-00876-x (2021).

222. Sankaran, J., Shi, X., Ho, L. Y., Stelzer, E. H. K. & Wohland, T. ImFCS: A software for Imaging FCS data analysis and visualization. *Opt Express* **18**, 25468 (2010).

223. Yu, L. *et al.* A Comprehensive Review of Fluorescence Correlation Spectroscopy. *Frontiers in Physics* vol. 9 110 Preprint at https://doi.org/10.3389/fphy.2021.644450 (2021).

224. Schwille, P., Meyer-Almes, F. J. & Rigler, R. Dual-color fluorescence cross-correlation spectroscopy for multicomponent diffusional analysis in solution. *Biophys J* **72**, 1878–1886 (1997).

225. Bufi, N. *et al.* Human primary immune cells exhibit distinct mechanical properties that are modified by inflammation. *Biophys J* **108**, 2181–2190 (2015).

226. Fradin, C., Abu-Arish, A., Granek, R. & Elbaum, M. Fluorescence correlation spectroscopy close to a fluctuating membrane. *Biophys J* **84**, 2005–2020 (2003).

227. Gesper, A. *et al.* Variations in Plasma Membrane Topography Can Explain Heterogenous Diffusion Coefficients Obtained by Fluorescence Correlation Spectroscopy. *Front Cell Dev Biol* **8**, 767 (2020).

228. Adler, J., Shevchuk, A. I., Novak, P., Korchev, Y. E. & Parmryd, I. Plasma membrane topography and interpretation of single-particle tracks. *Nature Methods* vol. 7 170–171 Preprint at https://doi.org/10.1038/nmeth0310-170 (2010).

229. Turkowyd, B., Virant, D. & Endesfelder, U. From single molecules to life: microscopy at the nanoscale. *Analytical and Bioanalytical Chemistry* vol. 408 6885–6911 Preprint at https://doi.org/10.1007/s00216-016-9781-8 (2016).

230. Eggeling, C. *et al.* Direct observation of the nanoscale dynamics of membrane lipids in a living cell. *Nature* **457**, 1159–1162 (2009).

231. Sezgin, E. *et al.* Measuring nanoscale diffusion dynamics in cellular membranes with super-resolution STED–FCS. *Nat Protoc* **14**, 1054–1083 (2019).

232. Ries, J. & Schwille, P. New concepts for fluorescence correlation spectroscopy on membranes. *Physical Chemistry Chemical Physics* vol. 10 3487–3497 Preprint at https://doi.org/10.1039/b718132a (2008).

233. Balleza, E., Kim, J. M. & Cluzel, P. Systematic characterization of maturation time of fluorescent proteins in living cells. *Nat Methods* **15**, 47–51 (2018).

234. Pédelacq, J. D., Cabantous, S., Tran, T., Terwilliger, T. C. & Waldo, G. S. Engineering and characterization of a superfolder green fluorescent protein. *Nat Biotechnol* **24**, 79–88 (2006).

235. Haupts, U., Maiti, S., Schwille, P. & Webb, W. W. Dynamics of fluorescence fluctuations in green fluorescent protein observed by fluorescence correlation spectroscopy. *Proc Natl Acad Sci U S A* **95**, 13573–13578 (1998).

236. Schenk, A., Ivanchenko, S., Röcker, C., Wiedenmann, J. & Nienhaus, G. U. Photodynamics of Red Fluorescent Proteins Studied by Fluorescence Correlation Spectroscopy. *Biophys J* **86**, 384–394 (2004).

237. Hendrix, J., Flors, C., Dedecker, P., Hofkens, J. & Engelborghs, Y. Dark states in monomeric red fluorescent proteins studied by fluorescence correlation and single molecule spectroscopy. *Biophys J* **94**, 4103–4113 (2008).

238. Bacia, K., Majoul, I. V. & Schwille, P. Probing the endocytic pathway in live cells using dual-color fluorescence cross-correlation analysis. *Biophys J* **83**, 1184–1193 (2002).

239. Vámosi, G. *et al.* IL-2 and IL-15 receptor α-subunits are coexpressed in a supramolecular receptor cluster in lipid rafts of T cells. *Proc Natl Acad Sci U S A* **101**, 11082–11087 (2004).

240. Shen, Y., Chen, Y., Wu, J., Shaner, N. C. & Campbell, R. E. Engineering of mCherry variants with long Stokes shift, red-shifted fluorescence, and low cytotoxicity. *PLoS One* **12**, e0171257 (2017).

241. Lambert, T. J. FPbase: a community-editable fluorescent protein database. *Nature Methods* vol. 16 277–278 Preprint at https://doi.org/10.1038/s41592-019-0352-8 (2019).

242. Chen, L. & Flies, D. B. Molecular mechanisms of T cell co-stimulation and co-inhibition. *Nature Reviews Immunology* vol. 13 227–242 Preprint at https://doi.org/10.1038/nri3405 (2013).

243. Schwartz, R. H., Mueller, D. L., Jenkins, M. K. & Quill, H. T-cell clonal anergy. in *Cold Spring Harbor Symposia on Quantitative Biology* vol. 54 605–610 (1989).

244. Chen, L. & Flies, D. B. Molecular mechanisms of T cell co-stimulation and co-inhibition. *Nature Reviews Immunology* vol. 13 227–242 Preprint at https://doi.org/10.1038/nri3405 (2013).

245. Blank, C. U. *et al.* Defining 'T cell exhaustion'. *Nat Rev Immunol* **19**, 665–674 (2019).

246. Zhang, X. *et al.* Structural and functional analysis of the costimulatory receptor programmed death-1. *Immunity* **20**, 337–347 (2004).

247. Evans, E. J. *et al.* Crystal structure of a soluble CD28-Fab complex. *Nat Immunol* **6**, 271–279 (2005).

248. Sharpe, A. H. & Pauken, K. E. The diverse functions of the PD1 inhibitory pathway. *Nature Reviews Immunology* vol. 18 153–167 Preprint at https://doi.org/10.1038/nri.2017.108 (2018).

249. Nishimura, H., Nose, M., Hiai, H., Minato, N. & Honjo, T. Development of lupus-like autoimmune diseases by disruption of the PD-1 gene encoding an ITIM motif-carrying immunoreceptor. *Immunity* **11**, 141–151 (1999).

250. Nishimura, H. & Honjo, T. PD-1: An inhibitory immunoreceptor involved in peripheral tolerance. *Trends in Immunology* vol. 22 265–268 Preprint at https://doi.org/10.1016/S1471-4906(01)01888-9 (2001).

251. Sharma, P. & Allison, J. P. Immune checkpoint targeting in cancer therapy: Toward combination strategies with curative potential. *Cell* vol. 161 205–214 Preprint at https://doi.org/10.1016/j.cell.2015.03.030 (2015).

252. Linsley, P. S. *et al.* Binding stoichiometry of the cytotoxic T lymphocyte-associated molecule-4 (CTLA-4): A disulfide-linked homodimer binds two CD86 molecules. *Journal of Biological Chemistry* **270**, 15417–15424 (1995).

253. Greene, J. A. L. *et al.* Covalent dimerization of CD28/CTLA-4 and oligomerization of CD80/CD86 regulate T cell costimulatory interactions. *Journal of Biological Chemistry* **271**, 26762–26771 (1996).

254. Hutloff, A. *et al.* ICOS is an inducible T-cell co-stimulator structurally and functionally related to CD28. *Nature* **397**, 263–266 (1999).

255. Martin-Orozco, N., Wang, Y.-H., Yagita, H. & Dong, C. Cutting Edge: Programed Death (PD) Ligand-1/PD-1 Interaction Is Required for CD8 + T Cell Tolerance to Tissue Antigens. *The Journal of Immunology* **177**, 8291–8295 (2006).

256. Mahoney, K. M. *et al.* A secreted PD-L1 splice variant that covalently dimerizes and mediates immunosuppression. *Cancer Immunology, Immunotherapy* **68**, 421–432 (2019).

257. Sugiura, D. *et al.* Restriction of PD-1 function by cis-PD-L1/CD80 interactions is required for optimal T cell responses. *Science (1979)* **364**, 558–566 (2019).

258. Banning, C. *et al.* A flow cytometry-based FRET assay to identify and analyse protein-protein interactions in living cells. *PLoS One* **5**, e9344 (2010).

259. Armstrong, C. R. & Senes, A. Screening for transmembrane association in divisome proteins using TOXGREEN, a high-throughput variant of the TOXCAT assay. *Biochim Biophys Acta Biomembr* **1858**, 2573–2583 (2016).

260. Robson MacDonald, H., Schreyer, M., Howe, R. C. & Bron, C. Selective expression of CD8α (Ly-2) subunit on activated thymic γ/δ cells. *Eur J Immunol* **20**, 927–930 (1990).

261. Schwartz, J. C. D., Zhang, X., Fedorov, A. A., Nathenson, S. G. & Almo, S. C. Structural basis for co-stimulation by the human CTLA-4/B7-2 complex. *Nature* **410**, 604–608 (2001).

262. Zhang, X., Schwartz, J. C. D., Almo, S. C. & Nathenson, S. G. Crystal structure of the receptor-binding domain of human B7-2: Insights into organization and signaling. *Proc Natl Acad Sci U S A* **100**, 2586–2591 (2003).

263. Ikemizu, S. *et al.* Structure and dimerization of a soluble form of B7-1. *Immunity* **12**, 51–60 (2000).

264. Patsoukis, N. *et al.* Interaction of SHP-2 SH2 domains with PD-1 ITSM induces PD-1 dimerization and SHP-2 activation. *Commun Biol* **3**, 1–13 (2020).

265. Datta, R., Heaster, T. M., Sharick, J. T., Gillette, A. A. & Skala, M. C. Fluorescence lifetime imaging microscopy: fundamentals and advances in instrumentation, analysis, and applications. *J Biomed Opt* **25**, 1 (2020).

266. Siegel, R. M. *et al.* Measurement of molecular interactions in living cells by fluorescence resonance energy transfer between variants of the green fluorescent protein. *Sci Signal* **2000**, (2000).

267. Banning, C. *et al.* A flow cytometry-based FRET assay to identify and analyse protein-protein interactions in living cells. *PLoS One* **5**, e9344 (2010).

268. Finger, C., Escher, C. & Schneider, D. The single transmembrane domains of human receptor tyrosine kinases encode self-interactions. *Sci Signal* **2**, (2009).

269. Lemmon, M. A. & Schlessinger, J. Cell signaling by receptor tyrosine kinases. *Cell* vol. 141 1117–1134 Preprint at https://doi.org/10.1016/j.cell.2010.06.011 (2010).

270. Sharp, L. L., Zhou, J. & Blair, D. F. Features of MotA proton channel structure revealed by tryptophan-scanning mutagenesis. *Proc Natl Acad Sci U S A* **92**, 7946–7950 (1995).

271. Armstrong, C. R. & Senes, A. Screening for transmembrane association in divisome proteins using TOXGREEN, a high-throughput variant of the TOXCAT assay. *Biochim Biophys Acta Biomembr* **1858**, 2573–2583 (2016).

272. Monks, C. R. F., Freiberg, B. A., Kupfer, H., Sciaky, N. & Kupfer, A. Three-dimensional segregation of supramolecular activation clusters in T cells. *Nature* **395**, 82–86 (1998).

273. Bunnell, S. C. *et al.* T cell receptor ligation induces the formation of dynamically regulated signaling assemblies. *Journal of Cell Biology* **158**, 1263–1275 (2002).

274. Yokosuka, T. *et al.* Programmed cell death 1 forms negative costimulatory microclusters that directly inhibit T cell receptor signaling by recruiting phosphatase SHP2. *Journal of Experimental Medicine* **209**, 1201–1217 (2012).

275. Curran, M. A., Montalvo, W., Yagita, H. & Allison, J. P. PD-1 and CTLA-4 combination blockade expands infiltrating T cells and reduces regulatory T and myeloid cells within B16 melanoma tumors. *Proc Natl Acad Sci U S A* **107**, 4275–4280 (2010).

276. Martin-Orozco, N., Wang, Y.-H., Yagita, H. & Dong, C. Cutting Edge: Programed Death (PD) Ligand-1/PD-1 Interaction Is Required for CD8 + T Cell Tolerance to Tissue Antigens. *The Journal of Immunology* **177**, 8291–8295 (2006).

277. Kurts, C. *et al.* Constitutive class I-restricted exogenous presentation of self antigens in vivo. *Journal of Experimental Medicine* **184**, 923–930 (1996).

278. Vibhakar, R., Juan, G., Traganos, F., Darzynkiewicz, Z. & Finger, L. R. Activation-induced expression of human programmed death-1 gene in T- lymphocytes. *Exp Cell Res* **232**, 25–28 (1997).

279. Lázár-Molnár, E. *et al.* Crystal structure of the complex between programmed death-1 (PD-1) and its ligand PD-L2. *Proc Natl Acad Sci U S A* **105**, 10483–10488 (2008).

280. Zak, K. M. *et al.* Structure of the Complex of Human Programmed Death 1, PD-1, and Its Ligand PD-L1. *Structure* **23**, 2341–2348 (2015).

281. Sugiura, D. *et al.* Restriction of PD-1 function by cis-PD-L1/CD80 interactions is required for optimal T cell responses. *Science (1979)* **364**, 558–566 (2019).

282. Nishimura, H., Nose, M., Hiai, H., Minato, N. & Honjo, T. Development of lupus-like autoimmune diseases by disruption of the PD-1 gene encoding an ITIM motif-carrying immunoreceptor. *Immunity* **11**, 141–151 (1999).

283. Nishimura, H. & Honjo, T. PD-1: An inhibitory immunoreceptor involved in peripheral tolerance. *Trends in Immunology* vol. 22 265–268 Preprint at https://doi.org/10.1016/S1471-4906(01)01888-9 (2001).

284. Patsoukis, N. *et al.* Interaction of SHP-2 SH2 domains with PD-1 ITSM induces PD-1 dimerization and SHP-2 activation. *Commun Biol* **3**, 1–13 (2020).

285. Sterner, R. C. & Sterner, R. M. CAR-T cell therapy: current limitations and potential strategies. *Blood Cancer Journal* vol. 11 1–11 Preprint at https://doi.org/10.1038/s41408-021-00459-7 (2021).

286. Patsoukis, N., Wang, Q., Strauss, L. & Boussiotis, V. A. Revisiting the PD-1 pathway. *Sci Adv* **6**, (2020).

287. Leahy, D. J. A structural view of CD4 and CD8. *The FASEB Journal* **9**, 17–25 (1995).

288. Veillette, A., Bookman, M. A., Horak, E. M. & Bolen, J. B. The CD4 and CD8 T cell surface antigens are associated with the internal membrane tyrosine-protein kinase p56lck. *Cell* **55**, 301–308 (1988).

289. Barber, E. K., Dasgupta, J. D., Schlossman, S. F., Trevillyan, J. M. & Rudd, C. E. The CD4 and CD8 antigens are coupled to a protein-tyrosine kinase (p56(lck)) that phosphorylates the CD3 complex. *Proc Natl Acad Sci U S A* **86**, 3277–3281 (1989).

290. Li, Y., Yin, Y. & Mariuzza, R. A. Structural and biophysical insights into the role of CD4 and CD8 in T cell activation. *Frontiers in Immunology* vol. 4 206 Preprint at https://doi.org/10.3389/fimmu.2013.00206 (2013).

291. Rybakin, V., Clamme, J. P., Ampudia, J., Yachi, P. P. & Gascoigne, N. R. J. CD8αα and-αβ isotypes are equally recruited to the immunological synapse through their ability to bind to MHC class i. *EMBO Rep* **12**, 1251–1256 (2011).

292. Cheroutre, H. & Lambolez, F. Doubting the TCR Coreceptor Function of CD8αα. *Immunity* vol. 28 149–159 Preprint at https://doi.org/10.1016/j.immuni.2008.01.005 (2008).

293. Davis, S. J. *et al.* The nature of molecular recognition by T cells. *Nat Immunol* **4**, 217–224 (2003).

294. Wyer, J. R. *et al.* T cell receptor and coreceptor CD8αα bind peptide-MHC independently and with distinct kinetics. *Immunity* **10**, 219–225 (1999).

295. Leishman, A. J. *et al.* T cell responses modulated through interaction between CD8αα and the nonclassical MHC class I molecule, TL. *Science (1979)* **294**, 1936–1939 (2001).

296. Jönsson, P. *et al.* Remarkably low affinity of CD4/peptide-major histocompatibility complex class II protein interactions. *Proceedings of the National Academy of Sciences* **113**, 5682–5687 (2016).

297. Dustin, M. L. *et al.* Low affinity interaction of human or rat T cell adhesion molecule CD2 with its ligand aligns adhering membranes to achieve high physiological affinity. *Journal of Biological Chemistry* **272**, 30889–30898 (1997).

298. Sukenik, S., Ren, P. & Gruebele, M. Weak protein-protein interactions in live cells are quantified by cell-volume modulation. *Proc Natl Acad Sci U S A* **114**, 6776–6781 (2017).

299. Marth, J. D., Peet, R., Krebs, E. G. & Perlmutter, R. M. A lymphocyte-specific protein-tyrosine kinase gene is rearranged and overexpressed in the murine T cell lymphoma LSTRA. *Cell* **43**, 393–404 (1985).

300. Voronova, A. F. & Sefton, B. M. Expression of a new tyrosine protein kinase is stimulated by retrovirus promoter insertion. *Nature* **319**, 682–685 (1986).

301. Voronova, A. F., Adler, H. T. & Sefton, B. M. Two lck transcripts containing different 5' untranslated regions are present in T cells. *Mol Cell Biol* **7**, 4407–4413 (1987).

302. Bijlmakers, M. J. J. E., Isobe-Nakamura, M., Ruddock, L. J. & Marsh, M. Intrinsic signals in the unique domain target p56(lck) to the plasma membrane independently of CD4. *Journal of Cell Biology* **137**, 1029–1040 (1997).

303. Rudd, C. E., Anderson, P., Morimoto, C., Streuli, M. & Schlossman, S. F. Molecular interactions, T-cell subsets and a role of the CD4/CD8:p56lck complex in human T-cell activation. *Immunol Rev* **111**, 225–266 (1989).

304. Gaud, G., Lesourne, R. & Love, P. E. Regulatory mechanisms in T cell receptor signalling. *Nat Rev Immunol* **18**, 485–497 (2018).

305. Yamaguchi, H. & Hendrickson, W. A. Structural basis for activation of human lymphocyte kinase Lck upon tyrosine phosphorylation. *Nature* **384**, 484 (1996).

306. Williams, A. F. & Barclay, A. N. *Handbook of Experimental Immunology*. (Blackwell Scientific Publishing, 1986).

307. Hui, E. & Vale, R. D. In vitro membrane reconstitution of the T-cell receptor proximal signaling network. *Nat Struct Mol Biol* **21**, 133–142 (2014).

308. Courtney, A. H. *et al.* CD45 functions as a signaling gatekeeper in T cells. *Sci Signal* **12**, (2019).

309. Hui, E. & Vale, R. D. In vitro membrane reconstitution of the T-cell receptor proximal signaling network. *Nat Struct Mol Biol* **21**, 133–142 (2014).

310. Kim, P. W., Sun, Z. Y. J., Blacklow, S. C., Wagner, G. & Eck, M. J. A zinc clasp structure tethers Lck to T cell coreceptors CD4 and CD8. *Science (1979)* **301**, 1725–1728 (2003).

311. Carmo, A. M., Mason, D. W. & Beyers, A. D. Physical association of the cytoplasmic domain of CD2 with the tyrosine kinases p56lck and p59fyn. *Eur J Immunol* **23**, 2196–2201 (1993).

312. Wiest, D. L. *et al.* Regulation of T cell receptor expression in immature CD4+CD8+ thymocytes by p56lck tyrosine kinase: basis for differential signaling by CD4 and CD8 in immature thymocytes expressing both coreceptor molecules. *Journal of Experimental Medicine* **178**, 1701–1712 (1993).

313. Horkova, V. *et al.* Dynamics of the Coreceptor-LCK Interactions during T Cell Development Shape the Self-Reactivity of Peripheral CD4 and CD8 T Cells. *Cell Rep* **30**, 1504-1514.e7 (2020).

314. Stepanek, O. *et al.* Coreceptor scanning by the T cell receptor provides a mechanism for T cell tolerance. *Cell* **159**, 333–345 (2014).

315. Horkova, V. *et al.* Dynamics of the Coreceptor-LCK Interactions during T Cell Development Shape the Self-Reactivity of Peripheral CD4 and CD8 T Cells. *Cell Rep* **30**, 1504-1514.e7 (2020).

316. Schrum, A. G. *et al.* High-sensitivity detection and quantitative analysis of native protein-protein interactions and multiprotein complexes by flow cytometry. *Sci STKE* **2007**, pl2 (2007).

317. Yang, H. *et al.* HLA-E-restricted, Gag-specific CD8+T cells can suppress HIV-1 infection, offering vaccine opportunities. *Sci Immunol* **6**, (2021).

318. Shalem, O. *et al.* Genome-scale CRISPR-Cas9 knockout screening in human cells. *Science (1979)* **343**, 84–87 (2014).

319. Chang, V. T. *et al.* Initiation of T cell signaling by CD45 segregation at 'close contacts'. *Nat Immunol* **17**, 574–582 (2016).

320. Takada, S. & Engleman, E. G. Evidence for an association between CD8 molecules and the T cell receptor complex on cytotoxic T cells. *Journal of Immunology* **139**, 3231–3235 (1987).

321. Davis, K. A., Abrams, B., Iyer, S. B., Hoffman, R. A. & Bishop, J. E. Determination of CD4 antigen density on cells: Role of antibody valency, avidity, clones, and conjugation. *Cytometry* **33**, 197–205 (1998).

322. Pannu, K. K., Joe, E. T. & Iyer, S. B. Performance evaluation of quantiBRITE phycoerythrin beads. *Cytometry* **45**, 250–258 (2001).

323. Olszowy, M. W., Leuchtmann, P. L., Veillette, A. & Shaw, A. S. Comparison of p56lck and p59fyn protein expression in thymocyte subsets, peripheral T cells, NK cells, and lymphoid cell lines. *Journal of Immunology* **155**, 4236–40 (1995).

324. Hui, E. *et al.* T cell costimulatory receptor CD28 is a primary target for PD-1-mediated inhibition. *Science (1979)* **355**, 1428–1433 (2017).

325. Hukelmann, J. L. *et al.* The cytotoxic T cell proteome and its shaping by the kinase mTOR. *Nat Immunol* **17**, 104–112 (2016).

326. Voisinne, G. *et al.* Quantitative interactomics in primary T cells unveils TCR signal diversification extent and dynamics. *Nat Immunol* **20**, 1530–1541 (2019).

327. Mege, J. L. *et al.* Quantification of cell surface roughness; a method for studying cell mechanical and adhesive properties. *J Theor Biol* **119**, 147–160 (1986).

328. Dustin, M. L. *et al.* Low affinity interaction of human or rat T cell adhesion molecule CD2 with its ligand aligns adhering membranes to achieve high physiological affinity. *Journal of Biological Chemistry* **272**, 30889–30898 (1997).

329. Lippert, A. H. *et al.* Soft Polydimethylsiloxane-Supported Lipid Bilayers for Studying T Cell Interactions. *Biophys J* **120**, 35–45 (2021).

330. Holmquist, B. & Vallee, B. L. Metal substitutions and inhibition of thermolysin: spectra of the cobalt enzyme. *Journal of Biological Chemistry* **249**, 4601–4607 (1974).

331. Huse, M., Eck, M. J. & Harrison, S. C. A Zn2+ ion links the cytoplasmic tail of CD4 and the N-terminal region of Lck. *Journal of Biological Chemistry* **273**, 18729–18733 (1998).

332. Olszowy, M. W., Leuchtmann, P. L., Veillette, A. & Shaw, A. S. Comparison of p56lck and p59fyn protein expression in thymocyte subsets, peripheral T cells, NK cells, and lymphoid cell lines. *Journal of Immunology* **155**, 4236–40 (1995).

333. Lin, R. S., Rodriguez, C., Veillette, A. & Lodish, H. F. Zinc is essential for binding of p56(lck) to CD4 and CD8α. *Journal of Biological Chemistry* **273**, 32878–32882 (1998).

334. Schwarzenbacher, M. *et al.* Micropatterning for quantitative analysis of protein-protein interactions in living cells. *Nat Methods* **5**, 1053–1060 (2008).

335. Bachmann, M. F. *et al.* Developmental regulation of Lck targeting to the CD8 coreceptor controls signaling in naive and memory T cells. *Journal of Experimental Medicine* **189**, 1521–1529 (1999).

336. Wei, Q. *et al.* Lck bound to coreceptor is less active than free Lck. *Proc Natl Acad Sci U S A* **117**, 15809–15817 (2020).

337. Parrish, H. L., Deshpande, N. R., Vasic, J. & Kuhns, M. S. Functional evidence for TCR-intrinsic specificity for MHCII. *Proc Natl Acad Sci U S A* **113**, 3000–3005 (2016).

338. Turner, J. M. *et al.* Interaction of the unique N-terminal region of tyrosine kinase p56lck with cytoplasmic domains of CD4 and CD8 is mediated by cysteine motifs. *Cell* **60**, 755–765 (1990).

339. James, J. R. *et al.* The T cell receptor triggering apparatus is composed of monovalent or monomeric proteins. *Journal of Biological Chemistry* **286**, 31993–32001 (2011).

340. Artyomov, M. N., Lis, M., Devadas, S., Davis, M. M. & Chakraborty, A. K. CD4 and CD8 binding to MHC molecules primarily acts to enhance Lck delivery. *Proceedings of the National Academy of Sciences* **107**, 16916–16921 (2010).

341. Jönsson, P. *et al.* Remarkably low affinity of CD4/peptide-major histocompatibility complex class II protein interactions. *Proceedings of the National Academy of Sciences* **113**, 5682–5687 (2016).

342. Turner, J. M. *et al.* Interaction of the unique N-terminal region of tyrosine kinase p56lck with cytoplasmic domains of CD4 and CD8 is mediated by cysteine motifs. *Cell* **60**, 755–765 (1990).

343. Schwarzenbacher, M. *et al.* Micropatterning for quantitative analysis of protein-protein interactions in living cells. *Nat Methods* **5**, 1053–1060 (2008).

344. van Oers, N. S. C., Lowin-Kropf, B., Finlay, D., Connolly, K. & Weiss, A. αβ T cell development is abolished in mice lacking both Lck and Fyn protein tyrosine kinases. *Immunity* **5**, 429–36 (1996).

345. Palacios, E. H. & Weiss, A. Function of the Src-family kinases, Lck and Fyn, in T-cell development and activation. *Oncogene* vol. 23 7990–8000 Preprint at https://doi.org/10.1038/sj.onc.1208074 (2004).

346. Cinek, T., Hilgert, I. & Hořejší, V. An alternative way of CD4 and CD8 association with protein kinases of the Src family. *Immunogenetics* **41**, 110–116 (1995).

347. Fragoso, R. *et al.* Lipid raft distribution of CD4 depends on its palmitoylation and association with Lck, and evidence for CD4-induced lipid raft aggregation as an additional mechanism to enhance CD3 signaling. *Journal of Immunology* **170**, 913–21 (2003).

348. Levental, I., Levental, K. R. & Heberle, F. A. Lipid Rafts: Controversies Resolved, Mysteries Remain. *Trends Cell Biol* **30**, 341–353 (2020).

349. Saffman, P. G. & Delbrueck, M. Brownian motion in biological membranes. *Proc Natl Acad Sci U S A* **72**, 3111–3113 (1975).

350. Weiß, K. *et al.* Quantifying the diffusion of membrane proteins and peptides in black lipid membranes with 2-focus fluorescence correlation spectroscopy. *Biophys J* **105**, 455–462 (2013).

351. Davis, A. M. & Berg, J. M. Homodimerization and heterodimerization of minimal Zinc(II)-binding-domain peptides of T-cell proteins CD4, CD8α, and Lck. *J Am Chem Soc* **131**, 11492–11497 (2009).

352. Baker, A. M. *et al.* CD4 interacts constitutively with multiple CCR5 at the plasma membrane of living cells: A fluorescence recovery after photobleaching at variable radii approach. *Journal of Biological Chemistry* **282**, 35163–35168 (2007).

353. Hilzenrat, G. *et al.* Conformational States Control Lck Switching between Free and Confined Diffusion Modes in T Cells. *Biophys J* **118**, 1489–1501 (2020).

354. Sezgin, E. & Schwille, P. Fluorescence techniques to study lipid dynamics. *Cold Spring Harb Perspect Biol* **3**, a009803 (2011).

355. Fradin, C., Abu-Arish, A., Granek, R. & Elbaum, M. Fluorescence correlation spectroscopy close to a fluctuating membrane. *Biophys J* **84**, 2005–2020 (2003).

356. Gesper, A. *et al.* Variations in Plasma Membrane Topography Can Explain Heterogenous Diffusion Coefficients Obtained by Fluorescence Correlation Spectroscopy. *Front Cell Dev Biol* **8**, 767 (2020).

357. Shaw, A. S. *et al.* Short related sequences in the cytoplasmic domains of CD4 and CD8 mediate binding to the amino-terminal domain of the p56lck tyrosine protein kinase. *Mol Cell Biol* **10**, 1853–1862 (1990).

358. Salghetti, S., Mariani, R. & Skowronski, J. Human immunodeficiency virus type 1 Nef and p56lck protein-tyrosine kinase interact with a common element in CD4 cytoplasmic tail. *Proc Natl Acad Sci U S A* **92**, 349–353 (1995).

359. Salghetti, S., Mariani, R. & Skowronski, J. Human immunodeficiency virus type 1 Nef and p56lck protein-tyrosine kinase interact with a common element in CD4 cytoplasmic tail. *Proc Natl Acad Sci U S A* **92**, 349–353 (1995).

360. Giménez-Andrés, M., Čopič, A. & Antonny, B. The many faces of amphipathic helices. *Biomolecules* vol. 8 Preprint at https://doi.org/10.3390/biom8030045 (2018).

361. Kim, P. W., Sun, Z. Y. J., Blacklow, S. C., Wagner, G. & Eck, M. J. A zinc clasp structure tethers Lck to T cell coreceptors CD4 and CD8. *Science (1979)* **301**, 1725–1728 (2003).

362. Popik, W. & Alce, T. M. CD4 receptor localized to non-raft membrane microdomains supports HIV-1 entry. Identification of a novel raft localization marker in CD4. *Journal of Biological Chemistry* **279**, 704–712 (2004).

363. Fragoso, R. *et al.* Lipid raft distribution of CD4 depends on its palmitoylation and association with Lck, and evidence for CD4-induced lipid raft aggregation as an additional mechanism to enhance CD3 signaling. *Journal of Immunology* **170**, 913–21 (2003).

364. Shaw, A. S. *et al.* Short related sequences in the cytoplasmic domains of CD4 and CD8 mediate binding to the amino-terminal domain of the p56lck tyrosine protein kinase. *Mol Cell Biol* **10**, 1853–1862 (1990).

365. Huse, M., Eck, M. J. & Harrison, S. C. A Zn2+ ion links the cytoplasmic tail of CD4 and the N-terminal region of Lck. *Journal of Biological Chemistry* **273**, 18729–18733 (1998).

366. Wei, Q. *et al.* Lck bound to coreceptor is less active than free Lck. *Proc Natl Acad Sci U S A* **117**, 15809–15817 (2020).

367. Xu, H. & Littman, D. R. A kinase-independent function of Lck in potentiating antigen-specific T cell activation. *Cell* **74**, 633–643 (1993).

368. Rudd, C. E. CD4, CD8 and the TCR-CD3 complex: a novel class of protein-tyrosine kinase receptor. *Immunology Today* vol. 11 400–406 Preprint at https://doi.org/10.1016/0167-5699(90)90159-7 (1990).

369. Milstein, O. *et al.* Nanoscale increases in CD2-CD48-mediated intermembrane spacing decrease adhesion and reorganize the immunological synapse. *Journal of Biological Chemistry* **283**, 34414–34422 (2008).

370. Urbančič, I. *et al.* Aggregation and mobility of membrane proteins interplay with local lipid order in the plasma membrane of T cells. *FEBS Lett* **595**, 2127–2146 (2021).

371. Sezgin, E. & Schwille, P. Fluorescence techniques to study lipid dynamics. *Cold Spring Harb Perspect Biol* **3**, a009803 (2011).

372. Kaizuka, Y., Douglass, A. D., Vardhana, S., Dustin, M. L. & Vale, R. D. The coreceptor CD2 uses plasma membrane microdomains to transduce signals in T cells. *Journal of Cell Biology* **185**, 521–534 (2009).

373. Chang, V. T. *et al.* Initiation of T cell signaling by CD45 segregation at 'close contacts'. *Nat Immunol* **17**, 574–582 (2016).

374. Rossy, J., Owen, D. M., Williamson, D. J., Yang, Z. & Gaus, K. Conformational states of the kinase Lck regulate clustering in early T cell signaling. *Nat Immunol* **14**, 82–89 (2013).

375. Yuan, Y. *et al.* Single-molecule super-resolution imaging of T-cell plasma membrane CD4 redistribution upon HIV-1 binding. *Viruses* **13**, 142 (2021).

376. Douglass, A. D. & Vale, R. D. Single-molecule microscopy reveals plasma membrane microdomains created by protein-protein networks that exclude or trap signaling molecules in T cells. *Cell* **121**, 937–950 (2005).

377. Ike, H. *et al.* Mechanism of Lck recruitment to the T-cell receptor cluster as studied by single-molecule-fluorescence video imaging. *ChemPhysChem* **4**, 620–626 (2003).

378. Douglass, A. D. & Vale, R. D. Single-molecule microscopy reveals plasma membrane microdomains created by protein-protein networks that exclude or trap signaling molecules in T cells. *Cell* **121**, 937–950 (2005).

379. Pinkwart, K. *et al.* Nanoscale dynamics of cholesterol in the cell membrane. *Journal of Biological Chemistry* **294**, 12599–12609 (2019).

380. Ike, H. *et al.* Mechanism of Lck recruitment to the T-cell receptor cluster as studied by single-molecule-fluorescence video imaging. *ChemPhysChem* **4**, 620–626 (2003).

381. Lee, M. S. *et al.* Enhancing and inhibitory motifs regulate CD4 activity. *Elife* **2022**, 1–29 (2022).

382. Bonnard, M., Maroun, C. R. & Julius, M. Physical association of CD4 and CD45 in primary, resting CD4+ T cells. *Cell Immunol* **175**, 1–11 (1997).

383. Veillette, A., Bookman, M. A., Horak, E. M. & Bolen, J. B. The CD4 and CD8 T cell surface antigens are associated with the internal membrane tyrosine-protein kinase p56lck. *Cell* **55**, 301–308 (1988).

384. Filipp, D., Leung, B. L., Zhang, J., Veillette, A. & Julius, M. Enrichment of Lck in Lipid Rafts Regulates Colocalized Fyn Activation and the Initiation of Proximal Signals through TCRαβ. *The Journal of Immunology* **172**, 4266–4274 (2004).

385. Lin, R. S., Rodriguez, C., Veillette, A. & Lodish, H. F. Zinc is essential for binding of p56(lck) to CD4 and CD8α. *Journal of Biological Chemistry* **273**, 32878–32882 (1998).

386. Deshpande, C. N. *et al.* Calcium is an essential cofactor for metal efflux by the ferroportin transporter family. *Nat Commun* **9**, 1–10 (2018).

387. Kocyła, A., Czogalla, A., Wessels, I., Rink, L. & Krężel, A. A combined biochemical and cellular approach reveals Zn2+-dependent hetero- and homodimeric CD4 and Lck assemblies in T cells. *bioRxiv* 2022.12.17.520849 (2022) doi:10.1101/2022.12.17.520849.

388. Schlosshauer, M. & Baker, D. Realistic protein-protein association rates from a simple diffusional model neglecting long-range interactions, free energy barriers, and landscape ruggedness. *Protein Science* **13**, 1660–1669 (2004).

389. Lee, M. S. *et al.* Enhancing and inhibitory motifs regulate CD4 activity. *Elife* **2022**, 1–29 (2022).

390. Singer, A., Adoro, S. & Park, J. H. Lineage fate and intense debate: Myths, models and mechanisms of CD4- versus CD8-lineage choice. *Nature Reviews Immunology* vol. 8 788–801 Preprint at https://doi.org/10.1038/nri2416 (2008).

391. Kappes, D. J. CD4 and CD8: Hogging All the Lck. *Immunity* vol. 27 691–693 Preprint at https://doi.org/10.1016/j.immuni.2007.11.002 (2007).

392. Davis, K. A., Abrams, B., Iyer, S. B., Hoffman, R. A. & Bishop, J. E. Determination of CD4 antigen density on cells: Role of antibody valency, avidity, clones, and conjugation. *Cytometry* **33**, 197–205 (1998).

393. Pannu, K. K., Joe, E. T. & Iyer, S. B. Performance evaluation of quantiBRITE phycoerythrin beads. *Cytometry* **45**, 250–258 (2001).

394. Hukelmann, J. L. *et al.* The cytotoxic T cell proteome and its shaping by the kinase mTOR. *Nat Immunol* **17**, 104–112 (2016).

395. Voisinne, G. *et al.* Quantitative interactomics in primary T cells unveils TCR signal diversification extent and dynamics. *Nat Immunol* **20**, 1530–1541 (2019).

396. Hui, E. *et al.* T cell costimulatory receptor CD28 is a primary target for PD-1-mediated inhibition. *Science (1979)* **355**, 1428–1433 (2017).

397. Pettmann, J. *et al.* The discriminatory power of the T cell receptor. *Elife* **10**, (2021).

398. Hong, J. *et al.* A TCR mechanotransduction signaling loop induces negative selection in the thymus. *Nat Immunol* **19**, 1379–1390 (2018).

399. Davis, S. J. & van der Merwe, P. A. The kinetic-segregation model: TCR triggering and beyond. *Nat Immunol* **7**, 803–809 (2006).

400. Fernandes, R. A. *et al.* A cell topography-based mechanism for ligand discrimination by the T cell receptor. *Proc Natl Acad Sci U S A* **116**, 14002–14010 (2019).

401. Krummel, M. F. & Davis, M. M. Dynamics of the immunological synapse: Finding, establishing and solidifying a connection. *Current Opinion in Immunology* vol. 14 66–74 Preprint at https://doi.org/10.1016/S0952-7915(01)00299-0 (2002).

402. James, J. R. & Vale, R. D. Biophysical mechanism of T-cell receptor triggering in a reconstituted system. *Nature* **487**, 64–69 (2012).

403. Dustin, M. L. The immunological synapse. *Cancer Immunology Research* vol. 2 1023–1033 Preprint at https://doi.org/10.1158/2326-6066.CIR-14-0161 (2014).

404. Schmid, E. M. *et al.* Size-dependent protein segregation at membrane interfaces. *Nat Phys* **12**, 704–711 (2016).

405. James, J. R. *et al.* Single-molecule level analysis of the subunit composition of the T cell receptor on live T cells. *Proc Natl Acad Sci U S A* **104**, 17662–17667 (2007).

406. Singh, N. K. *et al.* A class-mismatched TCR bypasses MHC restriction via an unorthodox but fully functional binding geometry. *Nat Commun* **13**, 1–14 (2022).

407. Yin, L. *et al.* A single T cell receptor bound to major histocompatibility complex class I and class II glycoproteins reveals switchable TCR conformers. *Immunity* **35**, 23–33 (2011).

408. Pelchen-Matthews, A., Parsons, I. J. & Marsh, M. Phorbol Ester-induced Downregulation of CD4 is a Multistep Process Involving Dissociation from p56 lck, Increased Association with Clathrin-coated Pits, and Altered Endosomal Sorting. *Journal of Experimental Medicine* **178**, 1209–1222 (1993).

409. Malaria.

410. Wahlgren, M., Goel, S. & Akhouri, R. R. Variant surface antigens of Plasmodium falciparum and their roles in severe malaria. *Nat Rev Microbiol* **15**, 479–491 (2017).

411. Weber, J. L. Interspersed repetitive DNA from Plasmodium falciparum. *Mol Biochem Parasitol* **29**, 117–124 (1988).

412. Gardner, M. J. *et al.* Chromosome 2 Sequence of the Human Malaria Parasite Plasmodium falciparum. *Science (1979)* **282**, 1126–1132 (1998).

413. Gardner, M. J. *et al.* Genome sequence of the human malaria parasite Plasmodium falciparum. *Nature* **419**, 498–511 (2002).

414. Goel, S. *et al.* RIFINs are adhesins implicated in severe Plasmodium falciparum malaria. *Nat Med* **21**, 314–321 (2015).

415. Saito, F. *et al.* Immune evasion of Plasmodium falciparum by RIFIN via inhibitory receptors. *Nature* **552**, 101–105 (2017).

416. Chen, Y. *et al.* Structural basis of malaria RIFIN binding by LILRB1-containing antibodies. *Nature* **592**, 639–643 (2021).

417. Hsieh, F. L. & Higgins, M. K. The structure of a LAIR1-containing human antibody reveals a novel mechanism of antigen recognition. *Elife* **6**, (2017).

418. Tan, J. *et al.* A LAIR1 insertion generates broadly reactive antibodies against malaria variant antigens. *Nature* **529**, 105–109 (2016).

419. McCoy, A. J. *et al.* Phaser crystallographic software. *J Appl Crystallogr* **40**, 658–674 (2007).

420. Bachmann, A. *et al.* A comparative study of the localization and membrane topology of members of the RIFIN, STEVOR and PfMC-2TM protein families in Plasmodium falciparum-infected erythrocytes. *Malar J* **14**, 1–18 (2015).

421. Goel, S. *et al.* RIFINs are adhesins implicated in severe Plasmodium falciparum malaria. *Nat Med* **21**, 314–321 (2015).

422. Wang, Q. *et al.* Structures of the four Ig-like domain LILRB2 and the four-domain LILRB1 and HLA-G1 complex. *Cell Mol Immunol* **17**, 966–975 (2020).

423. Willcox, B. E., Thomas, L. M. & Bjorkman, P. J. Crystal structure of HLA-A2 bound to LIR-1, a host and viral major histocompatibility complex receptor. *Nat Immunol* **4**, 913–919 (2003).

424. Arora, G. *et al.* NK cells inhibit Plasmodium falciparum growth in red blood cells via antibody-dependent cellular cytotoxicity. *Elife* **7**, e36806 (2018).

425. Burrack, K. S., Hart, G. T. & Hamilton, S. E. Contributions of natural killer cells to the immune response against Plasmodium. *Malaria Journal* vol. 18 1–9 Preprint at https://doi.org/10.1186/s12936-019-2953-1 (2019).

426. Rak, G. D., Mace, E. M., Banerjee, P. P., Svitkina, T. & Orange, J. S. Natural Killer cell lytic granule secretion occurs through a pervasive actin network at the immune synapse. *PLoS Biol* **9**, e1001151 (2011).

427. Zheng, P., Bertolet, G., Chen, Y., Huang, S. & Liu, D. Super-resolution imaging of the natural killer cell immunological synapse on a glass-supported planar lipid bilayer. *Journal of Visualized Experiments* (2015) doi:10.3791/52502.

428. Ambrose, A. R., Hazime, K. S., Worboys, J. D., Niembro-Vivanco, O. & Davis, D. M. Synaptic secretion from human natural killer cells is diverse and includes supramolecular attack particles. *Proc Natl Acad Sci U S A* **117**, 23717–23720 (2020).

429. Voskoboinik, I., Whisstock, J. C. & Trapani, J. A. Perforin and granzymes: Function, dysfunction and human pathology. *Nature Reviews Immunology* vol. 15 388–400 Preprint at https://doi.org/10.1038/nri3839 (2015).

430. Balint, Š. *et al.* Supramolecular attack particles are autonomous killing entities released from cytotoxic T cells. *Science (1979)* eaay9207 (2020) doi:10.1126/science.aay9207.

431. Ambrose, A. R., Hazime, K. S., Worboys, J. D., Niembro-Vivanco, O. & Davis, D. M. Synaptic secretion from human natural killer cells is diverse and includes supramolecular attack particles. *Proc Natl Acad Sci U S A* **117**, 23717–23720 (2020).

432. Chen, Y. *et al.* Structural basis of malaria RIFIN binding by LILRB1-containing antibodies. *Nature* **592**, 639–643 (2021).

433. Wang, Q. *et al.* Structures of the four Ig-like domain LILRB2 and the four-domain LILRB1 and HLA-G1 complex. *Cell Mol Immunol* **17**, 966–975 (2020).

434. Yu, Y. Y. L., Netuschil, N., Lybarger, L., Connolly, J. M. & Hansen, T. H. Cutting Edge: Single-Chain Trimers of MHC Class I Molecules Form Stable Structures That Potently Stimulate Antigen-Specific T Cells and B Cells. *The Journal of Immunology* **168**, 3145–3149 (2002).

435. Barnstable, C. J. *et al.* Production of monoclonal antibodies to group A erythrocytes, HLA and other human cell surface antigens-new tools for genetic analysis. *Cell* **14**, 9–20 (1978).

436. Parham, P., Androlewicz, M. J., Brodsky, F. M., Holmes, N. J. & Ways, J. P. Monoclonal antibodies: Purification, fragmentation and application to structural and functional studies of class I MHC antigens. *Journal of Immunological Methods* vol. 53 133–173 Preprint at https://doi.org/10.1016/0022-1759(82)90137-5 (1982).

437. Wahlgren, M., Goel, S. & Akhouri, R. R. Variant surface antigens of Plasmodium falciparum and their roles in severe malaria. *Nat Rev Microbiol* **15**, 479–491 (2017).

438. Turner, L. *et al.* Antibodies against PfEMP1, RIFIN, MSP3 and GLURP are acquired during controlled Plasmodium falciparum malaria infections in naïve volunteers. *PLoS One* **6**, e29025 (2011).

439. Otto, T. D. *et al.* A comprehensive evaluation of rodent malaria parasite genomes and gene expression. *BMC Med* **12**, 1–18 (2014).

440. Kyes, S. A., Rowe, J. A., Kriek, N. & Newbold, C. I. Rifins: A second family of clonally variant proteins expressed on the surface of red cells infected with Plasmodium falciparium. *Medical Sciences* **96**, 9333–9338 (1999).

441. Bultrini, E. *et al.* Revisiting the Plasmodium falciparum RIFIN family: From comparative genomics to 3D-model prediction. *BMC Genomics* **10**, 445 (2009).

442. Jumper, J. *et al.* Highly accurate protein structure prediction with AlphaFold. *Nature* **596**, 583–589 (2021).

443. Duncan, C. J. A. & Draper, S. J. Review: Controlled human blood stage malaria infection: Current status and potential applications. *American Journal of Tropical Medicine and Hygiene* vol. 86 561–565 Preprint at https://doi.org/10.4269/ajtmh.2012.11-0504 (2012).

444. Higgins, M. K. & Carrington, M. Sequence variation and structural conservation allows development of novel function and immune evasion in parasite surface protein families. *Protein Science* **23**, 354–365 (2014).

445. Xu, K. *et al.* Structural basis of LAIR1 targeting by polymorphic Plasmodium RIFINs. *Nat Commun* **12**, 1–8 (2021).

446. Xie, Y. *et al.* Structural basis of malarial parasite RIFIN-mediated immune escape against LAIR1. *Cell Rep* **36**, 109600 (2021).

447. Lau, C. K. Y. *et al.* Structural conservation despite huge sequence diversity allows EPCR binding by the pfemp1 family implicated in severe childhood malaria. *Cell Host Microbe* **17**, 118–129 (2015).

448. Burrack, K. S., Hart, G. T. & Hamilton, S. E. Contributions of natural killer cells to the immune response against Plasmodium. *Malaria Journal* vol. 18 1–9 Preprint at https://doi.org/10.1186/s12936-019-2953-1 (2019).

449. Liu, D. *et al.* Integrin-Dependent Organization and Bidirectional Vesicular Traffic at Cytotoxic Immune Synapses. *Immunity* **31**, 99–109 (2009).

450. Arora, G. *et al.* NK cells inhibit Plasmodium falciparum growth in red blood cells via antibody-dependent cellular cytotoxicity. *Elife* **7**, e36806 (2018).

451. Davis, D. M. & Dustin, M. L. What is the importance of the immunological synapse? *Trends in Immunology* vol. 25 323–327 Preprint at https://doi.org/10.1016/j.it.2004.03.007 (2004).

452. Adler, J. & Parmryd, I. Quantifying colocalization by correlation: The pearson correlation coefficient is superior to the Mander's overlap coefficient. *Cytometry Part A* **77**, 733–742 (2010).

453. Dunn, K. W., Kamocka, M. M. & McDonald, J. H. A practical guide to evaluating colocalization in biological microscopy. *American Journal of Physiology - Cell*

Physiology vol. 300 723–742 Preprint at https://doi.org/10.1152/ajpcell.00462.2010 (2011).

454. Fernandez, V., Hommel, M., Chen, Q., Hagblom, P. & Wahlgren, M. Small, clonally variant antigens expressed on the surface of the Plasmodium falciparum-infected erythrocyte are encoded by the rif gene family and are the target of human immune responses. *Journal of Experimental Medicine* **190**, 1393–1403 (1999).

455. Pretini, V. *et al.* Red blood cells: Chasing interactions. *Frontiers in Physiology* vol. 10 945 Preprint at https://doi.org/10.3389/fphys.2019.00945 (2019).

456. Schmid, E. M. *et al.* Size-dependent protein segregation at membrane interfaces. *Nat Phys* **12**, 704–711 (2016).

457. Bufi, N. *et al.* Human primary immune cells exhibit distinct mechanical properties that are modified by inflammation. *Biophys J* **108**, 2181–2190 (2015).

458. Lippert, A. H. *et al.* Soft Polydimethylsiloxane-Supported Lipid Bilayers for Studying T Cell Interactions. *Biophys J* **120**, 35–45 (2021).

459. Masuda, A., Nakamura, A., Maeda, T., Sakamoto, Y. & Takai, T. Cis binding between inhibitory receptors and MHC class I can regulate mast cell activation. *Journal of Experimental Medicine* **204**, 907–920 (2007).

460. Springer, T. A. Adhesion receptors of the immune system. *Nature* vol. 346 425–434 Preprint at https://doi.org/10.1038/346425a0 (1990).

461. van der Merwe, P. A. & Davis, S. J. Molecular interactions mediating T cell antigen recognition. *Annu Rev Immunol* **21**, 659–684 (2003).

462. Chappell, P. *et al.* Expression levels of MHC class I molecules are inversely correlated with promiscuity of peptide binding. *Elife* **2015**, (2015).

463. Brown, G., Biberfeld, P., Christensson, B. & Mason, D. Y. The distribution of HLA on human lymphoid, bone marrow and peripheral blood cells. *Eur J Immunol* **9**, 272–275 (1979).

464. June, C. H., O'Connor, R. S., Kawalekar, O. U., Ghassemi, S. & Milone, M. C. CAR T cell immunotherapy for human cancer. *Science* vol. 359 1361–1365 Preprint at https://doi.org/10.1126/science.aar6711 (2018).

465. Kontermann, R. E. & Brinkmann, U. Bispecific antibodies. *Drug Discovery Today* vol. 20 838–847 Preprint at https://doi.org/10.1016/j.drudis.2015.02.008 (2015).

466. Xie, G. *et al.* CAR-NK cells: A promising cellular immunotherapy for cancer. *EBioMedicine* vol. 59 102975 Preprint at https://doi.org/10.1016/j.ebiom.2020.102975 (2020).

467. Sundberg, E. J., Li, Y. & Mariuzza, R. A. So many ways of getting in the way: Diversity in the molecular architecture of superantigen-dependent T-cell signaling complexes. *Current Opinion in Immunology* vol. 14 36–44 Preprint at https://doi.org/10.1016/S0952-7915(01)00296-5 (2002).

468. Gao, G. F., Rao, Z. & Bell, J. I. Molecular coordination of αβ T-cell receptors and coreceptors CD8 and CD4 in their recognition of peptide-MHC ligands. *Trends Immunol* **23**, 408–413 (2002).

469. Li, Y. & Mariuzza, R. A. Structural basis for recognition of cellular and viral ligands by NK cell receptors. *Frontiers in Immunology* vol. 5 123 Preprint at https://doi.org/10.3389/fimmu.2014.00123 (2014).

470. Tolar, P. & Pierce, S. K. Unveiling the B cell receptor structure. *Science (1979)* **377**, 819–820 (2022).

471. Duncan, A. L., Song, W. & Sansom, M. S. P. Lipid-dependent regulation of ion channels and g protein-coupled receptors: Insights from structures and simulations. *Annual*

Review of Pharmacology and Toxicology vol. 60 31–50 Preprint at https://doi.org/10.1146/annurev-pharmtox-010919-023411 (2020).

472. Davis, S. J. & van der Merwe, P. A. The kinetic-segregation model: TCR triggering and beyond. *Nat Immunol* **7**, 803–809 (2006).

473. Mariuzza, R. A., Agnihotri, P. & Orban, J. The structural basis of T-cell receptor (TCR) activation: An enduring enigma. *Journal of Biological Chemistry* **295**, 914–925 (2020).

474. Harwood, N. E. & Batista, F. D. Early events in B cell activation. *Annual Review of Immunology* vol. 28 185–210 Preprint at https://doi.org/10.1146/annurev-immunol-030409-101216 (2010).

475. Treanor, B. B-cell receptor: From resting state to activate. *Immunology* vol. 136 21–27 Preprint at https://doi.org/10.1111/j.1365-2567.2012.03564.x (2012).

476. Farran, B. An update on the physiological and therapeutic relevance of GPCR oligomers. *Pharmacological Research* vol. 117 303–327 Preprint at https://doi.org/10.1016/j.phrs.2017.01.008 (2017).

477. Van Der Merwe, P. A., Dunne, P. D., Klenerman, D. & Davis, S. J. Taking T cells beyond the diffraction limit. *Nature Immunology* vol. 11 51–52 Preprint at https://doi.org/10.1038/ni0110-51 (2010).

478. Santos, A. M. *et al.* Capturing resting T cells: The perils of PLL. *Nature Immunology* vol. 19 203–205 Preprint at https://doi.org/10.1038/s41590-018-0048-8 (2018).

479. Felce, J. H., Davis, S. J. & Klenerman, D. Single-Molecule Analysis of G Protein-Coupled Receptor Stoichiometry: Approaches and Limitations. *Trends Pharmacol Sci* **39**, 96–108 (2018).

480. Asher, W. B. *et al.* Single-molecule FRET imaging of GPCR dimers in living cells. *Nat Methods* **18**, 397–405 (2021).

481. Rossboth, B. *et al.* TCRs are randomly distributed on the plasma membrane of resting antigen-experienced T cells. *Nat Immunol* **19**, 821–827 (2018).

482. Brameshuber, M. *et al.* Monomeric TCRs drive T cell antigen recognition. *Nat Immunol* **19**, 487–496 (2018).

483. Zhao, Y. *et al.* Antigen-Presenting Cell-Intrinsic PD-1 Neutralizes PD-L1 in cis to Attenuate PD-1 Signaling in T Cells. *Cell Rep* **24**, 379-390.e6 (2018).

484. Moran-Mirabal, J. M. *et al.* Micrometer-sized supported lipid bilayer arrays for bacterial toxin binding studies through total internal reflection fluorescence microscopy. *Biophys J* **89**, 296–305 (2005).

485. Jenkins, E. *et al.* Reconstitution of immune cell interactions in free-standing membranes. *J Cell Sci* 311399 (2018) doi:10.1101/311399.

486. Schneider, F. *et al.* Diffusion of lipids and GPI-anchored proteins in actin-free plasma membrane vesicles measured by STED-FCS. *Mol Biol Cell* **28**, 1507–1518 (2017).

487. Liu, P. *et al.* Investigation of the dimerization of proteins from the epidermal growth factor receptor family by single wavelength fluorescence cross-correlation spectroscopy. *Biophys J* **93**, 684–698 (2007).

488. Neugart, F. *et al.* Detection of ligand-induced CNTF receptor dimers in living cells by fluorescence cross correlation spectroscopy. *Biochim Biophys Acta Biomembr* **1788**, 1890–1900 (2009).

489. Eckert, A. F. *et al.* Measuring ligand-cell surface receptor affinities with axial line-scanning fluorescence correlation spectroscopy. *Elife* **9**, 1–92 (2020).

490. Lillemeier, B. F. *et al.* TCR and Lat are expressed on separate protein islands on T cell membranes and concatenate during activation. *Nat Immunol* **11**, 90–96 (2010).

491. Dickerson, R. E., Goodsell, D. S. & Neidle, S. '... The tyranny of the lattice ...' *Proc Natl Acad Sci U S A* **91**, 3579–3583 (1994).

492. Ishida, Y., Agata, Y., Shibahara, K. & Honjo, T. Induced expression of PD-1, a novel member of the immunoglobulin gene superfamily, upon programmed cell death. *EMBO Journal* **11**, 3887–3895 (1992).

493. Rudd, C. E. How the Discovery of the CD4/CD8-p56lck Complexes Changed Immunology and Immunotherapy. *Frontiers in Cell and Developmental Biology* vol. 9 107 Preprint at https://doi.org/10.3389/fcell.2021.626095 (2021).

494. Samaridis, J. & Colonna, M. Cloning of novel immunoglobulin superfamily receptors expressed on human myeloid and lymphoid cells: Structural evidence for new stimulatory and inhibitory pathways. *Eur J Immunol* **27**, 660–665 (1997).

495. Anderson, N. G. Co-immunoprecipitation. Identification of interacting proteins. *Methods in Molecular Biology* **88**, 35–45 (1998).

496. Xu, K. *et al.* Structural basis of LAIR1 targeting by polymorphic Plasmodium RIFINs. *Nat Commun* **12**, 1–8 (2021).

497. Xie, Y. *et al.* Structural basis of malarial parasite RIFIN-mediated immune escape against LAIR1. *Cell Rep* **36**, 109600 (2021).

498. Brondijk, T. H. C. *et al.* Crystal structure and collagen-binding site of immune inhibitory receptor LAIR-1: Unexpected implications for collagen binding by platelet receptor GPVI. *Blood* **115**, 1364–1373 (2010).

499. Willcox, B. E., Thomas, L. M. & Bjorkman, P. J. Crystal structure of HLA-A2 bound to LIR-1, a host and viral major histocompatibility complex receptor. *Nat Immunol* **4**, 913–919 (2003).

500. Padjasek, M. *et al.* Structural zinc binding sites shaped for greater works: Structure-function relations in classical zinc finger, hook and clasp domains. *Journal of Inorganic*

Biochemistry vol. 204 110955 Preprint at https://doi.org/10.1016/j.jinorgbio.2019.110955 (2020).

501. Kocyła, A. & Krężel, A. Zinc clasp-based reversible toolset for selective metal-mediated protein heterodimerization. *Chemical Communications* **54**, 13539–13542 (2018).

502. Davis, A. M. & Berg, J. M. Homodimerization and heterodimerization of minimal Zinc(II)-binding-domain peptides of T-cell proteins CD4, CD8α, and Lck. *J Am Chem Soc* **131**, 11492–11497 (2009).

503. Nikolaev, M. *et al.* Integral Membrane Proteins Can Be Crystallized Directly from Nanodiscs. *Cryst Growth Des* **17**, 945–948 (2017).

504. Cherezov, V. Lipidic cubic phase technologies for membrane protein structural studies. *Curr Opin Struct Biol* **21**, 559–566 (2011).

505. Reif, B., Ashbrook, S. E., Emsley, L. & Hong, M. Solid-state NMR spectroscopy. *Nature Reviews Methods Primers* vol. 1 1–23 Preprint at https://doi.org/10.1038/s43586-020-00002-1 (2021).

506. Xie, W., Wucherpfennig, K. & Patel, D. J. A structural platform for B cell receptor signaling. *Cell Research* 1–2 Preprint at https://doi.org/10.1038/s41422-022-00724-9 (2022).

507. Dong, D. *et al.* Structural basis of assembly of the human T cell receptor–CD3 complex. *Nature* **573**, 546–552 (2019).

508. Sušac, L. *et al.* Structure of a fully assembled tumor-specific T cell receptor ligated by pMHC. *Cell* **185**, 3201-3213.e19 (2022).

509. Yeagle, P. L. Non-covalent binding of membrane lipids to membrane proteins. *Biochimica et Biophysica Acta - Biomembranes* vol. 1838 1548–1559 Preprint at https://doi.org/10.1016/j.bbamem.2013.11.009 (2014).

510. Shinoda, T., Ogawa, H., Cornelius, F. & Toyoshima, C. Crystal structure of the sodium-potassium pump at 2.4 Å resolution. *Nature* **459**, 446–450 (2009).

511. Lemmon, M. A. & Schlessinger, J. Cell signaling by receptor tyrosine kinases. *Cell* vol. 141 1117–1134 Preprint at https://doi.org/10.1016/j.cell.2010.06.011 (2010).

512. Weis, W. I. & Kobilka, B. K. The Molecular Basis of G Protein-Coupled Receptor Activation. *Annual Review of Biochemistry* vol. 87 897–919 Preprint at https://doi.org/10.1146/annurev-biochem-060614-033910 (2018).

513. Schindler, C., Levy, D. E. & Decker, T. JAK-STAT signaling: From interferons to cytokines. *Journal of Biological Chemistry* vol. 282 20059–20063 Preprint at https://doi.org/10.1074/jbc.R700016200 (2007).

514. Nika, K. *et al.* Constitutively active lck kinase in T cells drives antigen receptor signal transduction. *Immunity* **32**, 766–777 (2010).

515. Ballek, O., Valečka, J., Manning, J. & Filipp, D. The pool of preactivated Lck in the initiation of T-cell signaling: A critical re-evaluation of the Lck standby model. *Immunol Cell Biol* **93**, 384–395 (2015).

516. Lorent, J. H. *et al.* Plasma membranes are asymmetric in lipid unsaturation, packing and protein shape. *Nat Chem Biol* **16**, 644–652 (2020).

517. Kenakin, T. The mass action equation in pharmacology. *Br J Clin Pharmacol* **81**, 41–51 (2016).

518. Deponte, M. *et al.* Wherever I may roam: Protein and membrane trafficking in P. falciparum-infected red blood cells. *Mol Biochem Parasitol* **186**, 95–116 (2012).

519. Vibhakar, R., Juan, G., Traganos, F., Darzynkiewicz, Z. & Finger, L. R. Activation-induced expression of human programmed death-1 gene in T- lymphocytes. *Exp Cell Res* **232**, 25–28 (1997).

520. Moriki, T., Maruyama, H. & Maruyama, I. N. Activation of preformed EGF receptor dimers by ligand-induced rotation of the transmembrane domain. *J Mol Biol* **311**, 1011–1026 (2001).

521. Labrijn, A. F., Janmaat, M. L., Reichert, J. M. & Parren, P. W. H. I. Bispecific antibodies: a mechanistic review of the pipeline. *Nature Reviews Drug Discovery* vol. 18 585–608 Preprint at https://doi.org/10.1038/s41573-019-0028-1 (2019).

522. Fife, B. T. & Bluestone, J. A. Control of peripheral T-cell tolerance and autoimmunity via the CTLA-4 and PD-1 pathways. *Immunological Reviews* vol. 224 166–182 Preprint at https://doi.org/10.1111/j.1600-065X.2008.00662.x (2008).

523. Watson, J. L. *et al.* Broadly applicable and accurate protein design by integrating structure prediction networks and diffusion generative models. *bioRxiv* 2022.12.09.519842 (2022) doi:10.1101/2022.12.09.519842.

524. Zamoyska, R. *et al.* Inability of CD8α′ polypeptides to associate with p56lck correlates with impaired function in vitro and lack of expression in vivo. *Nature* **342**, 278–281 (1989).

525. Miceli, M. C., Von Hoegen, P. & Parnes, J. R. Adhesion versus coreceptor function of CD4 and CD8: Role of the cytoplasmic tail in coreceptor activity. *Proc Natl Acad Sci U S A* **88**, 2623–2627 (1991).

526. van der Merwe, P. A. & Cordoba, S. P. Late Arrival: Recruiting Coreceptors to the T Cell Receptor Complex. *Immunity* vol. 34 1–3 Preprint at https://doi.org/10.1016/j.immuni.2011.01.001 (2011).

527. Xu, H. & Littman, D. R. A kinase-independent function of Lck in potentiating antigen-specific T cell activation. *Cell* **74**, 633–643 (1993).

528. Shinzawa, M. *et al.* Reversal of the T cell immune system reveals the molecular basis for T cell lineage fate determination in the thymus. *Nat Immunol* **23**, 731–742 (2022).

529. Masuda, A., Nakamura, A., Maeda, T., Sakamoto, Y. & Takai, T. Cis binding between inhibitory receptors and MHC class I can regulate mast cell activation. *Journal of Experimental Medicine* **204**, 907–920 (2007).

530. Ruggiero, F. M. & Springer, S. Homotypic and heterotypic in cis associations of MHC class I molecules at the cell surface. *Current Research in Immunology* vol. 3 85–99 Preprint at https://doi.org/10.1016/j.crimmu.2022.05.001 (2022).

531. Ruggiero, F. M. & Springer, S. Homotypic and heterotypic in cis associations of MHC class I molecules at the cell surface. *Current Research in Immunology* vol. 3 85–99 Preprint at https://doi.org/10.1016/j.crimmu.2022.05.001 (2022).

532. Junqueira, C. *et al.* γδ T cells suppress Plasmodium falciparum blood-stage infection by direct killing and phagocytosis. *Nat Immunol* **22**, 347–357 (2021).

533. Niang, M., Xue, Y. Y. & Preiser, P. R. The Plasmodium falciparum STEVOR multigene family mediates antigenic variation of the infected erythrocyte. *PLoS Pathog* **5**, e1000307 (2009).

534. Fernandez, V., Hommel, M., Chen, Q., Hagblom, P. & Wahlgren, M. Small, clonally variant antigens expressed on the surface of the Plasmodium falciparum-infected erythrocyte are encoded by the rif gene family and are the target of human immune responses. *Journal of Experimental Medicine* **190**, 1393–1403 (1999).

535. Milne, K. *et al.* Mapping immune variation and var gene switching in naive hosts infected with plasmodium falciparum. *Elife* **10**, (2021).